

AD-A261 671



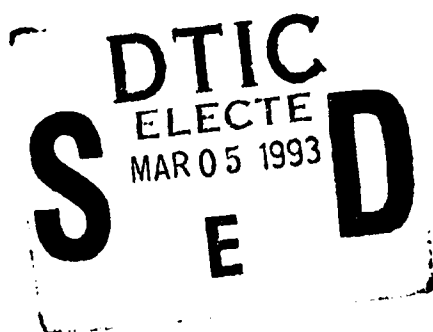
AFOSR-TR93-0077

②

Final Report
Grant #AFOSR-89-0403

INVESTIGATION OF LIQUID SLOSHING IN SPIN-STABILIZED SATELLITES

Joseph R. Baumgarten
Donald R. Flugrad
Richard H. Pletcher



Department of Mechanical Engineering

January 31, 1993

This report has been prepared for the
Air Force Office of Scientific Research

93-04639



ISU-ERI-Ames-93113
Project 3166



engineering research institute

iowa state university

~~DISTRIBUTION STATEMENT~~

Approved for public release
Distribution Unlimited

93 3 4 015

REPORT DOCUMENTATION PAGE

1a. REPORT SECURITY CLASSIFICATION Unclassified			1b. RESTRICTIVE MARKINGS		
2a. SECURITY CLASSIFICATION AUTHORITY			3. DISTRIBUTION / AVAILABILITY OF REPORT Approved for public release; distribution unlimited		
2b. DECLASSIFICATION / DOWNGRADING SCHEDULE			5. MONITORING ORGANIZATION REPORT NUMBER(S) —		
4. PERFORMING ORGANIZATION REPORT NUMBER(S) ISU-ERI-Ames-93113 Project 3166			7a. NAME OF MONITORING ORGANIZATION Air Force Office of Scientific Research (AFOSR)		
6a. NAME OF PERFORMING ORGANIZATION Iowa State University Dept. of Mechanical Engineering		6b. OFFICE SYMBOL (if applicable) NA	7b. ADDRESS (City, State, and ZIP Code) Air Force Office of Scientific Research Directorate of Aerospace Science (AFOSR/NA) Bolling AFB, DC 20332		
6c. ADDRESS (City, State, and ZIP Code) Room 2025 Black Engineering Building Ames, IA 50011		9. PROCUREMENT INSTRUMENT IDENTIFICATION NUMBER AFOSR-89-C403			
8a. NAME OF FUNDING / SPONSORING ORGANIZATION AFOSR		8b. OFFICE SYMBOL (if applicable) NA	10. SOURCE OF FUNDING NUMBERS		
8c. ADDRESS (City, State, and ZIP Code) Bldg. 410 Bolling AFB, DC 20332-6448		PROGRAM ELEMENT NO. 11109F	PROJECT NO. 2302	TASK NO. AS 4302781	WORK UNIT ACCESSION NO.
11. TITLE (Include Security Classification) Investigation of Liquid Sloshing in Spin-Stabilized Satellites (Unclassified)					
12. PERSONAL AUTHOR(S) Baumgarten, Joseph R.; Flugrad, Donald R.; Pletcher, Richard H.					
13a. TYPE OF REPORT Final Report		13b. TIME COVERED FROM 7/1/89 TO 11/30/92		14. DATE OF REPORT (Year, Month, Day) 1993 January 31	
				15. PAGE COUNT 229	
16. SUPPLEMENTARY NOTATION					
17. COSATI CODES			18. SUBJECT TERMS (Continue on reverse if necessary and identify by block number)		
FIELD	GROUP	SUB-GROUP	Coning, nutation, and structural deflection of satellites due to sloshing fluid, fluid-structure interaction		
19. ABSTRACT (Continue on reverse if necessary and identify by block number)					
<p>Several spin-stabilized communication satellites with liquid stores on board have exhibited unstable nutational motion. Liquid sloshing is suspected as the cause of this undesirable behavior. During an initial three year grant period, a test rig was built and instrumented, a rigid body computer model was developed using a pendulum analogy to simulate the sloshing liquid, and computational fluid dynamic (CFD) methods were used to develop a primitive variable numerical algorithm to describe two and three dimensional liquid sloshing.</p> <p>During the current three year grant period, the test rig and rigid body computer model have been used to study the effect of various physical parameter values on the motion, and stability conditions have been determined. The structural mathematical model has been improved by introduction of finite element techniques to account for elastic deformation of the test rig, and an implicit-explicit numerical approach has been implemented to solve the coupled, nonlinear equations of motion.</p> <p>(Continued on reverse side)</p>					
20. DISTRIBUTION / AVAILABILITY OF ABSTRACT <input type="checkbox"/> UNCLASSIFIED/UNLIMITED <input checked="" type="checkbox"/> SAME AS RPT <input checked="" type="checkbox"/> OTIC USERS			21. ABSTRACT SECURITY CLASSIFICATION Unclassified		
22a. NAME OF RESPONSIBLE INDIVIDUAL Donald R. Flugrad			22b. TELEPHONE (Include Area Code) (515) 294-9415		22c. OFFICE SYMBOL NA

19. Two CFD numerical strategies for computing liquid sloshing have been developed. One is based on surface fitting, and the other is based on surface capturing. Both provide solutions to the full three-dimensional unsteady incompressible Navier-Stokes equations which govern the liquid motion.

The structural and CFD software packages have been merged to study the fluid-structure interaction. Several spin-up cases have been computed, and results have been compared with experimental data.

TABLE OF CONTENTS 1

TABLE OF CONTENTS

Accession For	
NTIS CRA&I	<input checked="" type="checkbox"/>
DTIC TAB	<input checked="" type="checkbox"/>
Unannounced	<input type="checkbox"/>
Justification	
By	
Distribution /	
Availability Codes	
Dist	Avail and / or Special
A-1	

ABSTRACT	iii
LIST OF TABLES	ix
LIST OF FIGURES	xi
1. INTRODUCTION	1
1.1 Research Objectives	3
1.2 Status of Research	4
1.3 Publications	7
1.4 List of Research Personnel, Thesis Titles, and Degrees Awarded	10
1.5 Seminars, Presentations, and Laboratory Visits	11
2. RESEARCH IN PROGRESS	15
2.1 Recent Progress in the Surface Fitting Approach	15
2.1.1 Free-surface motion	15
2.1.2 Contact line boundary conditions	18
2.1.3 Code refinement efforts	19
2.2 Recent Progress in the Surface Capturing Approach	21
2.2.1 Formulation of the governing equations	22
2.2.2 Numerical methods	23

2.2.3	Test case results	26
2.2.4	Concluding remarks	28
2.3	Progress in Fluid-Structure Interaction	28
2.3.1	Equipment	28
2.3.2	Calibration	42
2.3.3	Experiments	44
2.3.4	Results	45
2.3.5	Numerical simulation	46
2.3.6	Discussion of results	47
2.3.7	Concluding remarks	48
BIBLIOGRAPHY		59
APPENDIX A. Computer Simulation of a Test Rig to Model Slosh-		
ing in Spin-Stabilized Satellites.		61
APPENDIX B. Motion Study of a Spin-Stabilized Satellite Test Rig.		73
APPENDIX C. A Finite Element/Lagrangian Formulation Dynamic		
Motion Prediction for a Flexible Satellite Simulator with Both		
Rigid and Elastic Bodies		113
APPENDIX D. Modeling of Multibody Flexible Articulated Struc-		
tures with Mutually Coupled Motions: Part I - General Theory.		123
APPENDIX E. Modeling of Multibody Flexible Articulated Struc-		
tures with Mutually Coupled Motions: Part II - Application and		
Results.		135

APPENDIX F. A Sequential Implicit-Explicit Integration Method in Solving Nonlinear Differential Equations from Flexible System Modeling.	147
APPENDIX G. A Primitive Variable, Strongly Implicit Calculation Procedure for Viscous Flows at All Speeds.	155
APPENDIX H. Simulation of Three-Dimensional Liquid Sloshing Flows Using a Strongly Implicit Calculation Procedure.	167
APPENDIX I. A Numerical and Experimental Study of Three- Dimensional Liquid Sloshing in a Rotating Spherical Container. .	205

LIST OF TABLES

Table 2.1:	Description of Equipment	39
------------	------------------------------------	----

LIST OF FIGURES

Figure 2.1:	Control volume within a two-fluid system.	24
Figure 2.2:	Schematic of the broken dam problem.	29
Figure 2.3:	Density interface for the broken dam problem selected times.	30
Figure 2.4:	Velocity field for the broken dam problem selected times. . .	31
Figure 2.5:	Surge front position versus dimensionless time for the broken dam problem.	32
Figure 2.6:	Back wall free surface position versus dimensionless time for the broken dam problem.	33
Figure 2.7:	Schematic of oscillating tank problem.	34
Figure 2.8:	Density interface for selected times: oscillating tank test case.	35
Figure 2.9:	Free surface position versus time for front and back tank walls.	36
Figure 2.10:	The satellite test rig.	37
Figure 2.11:	Strain Gage Conditioning Circuit	40
Figure 2.12:	Photopotentiometer Circuit	41
Figure 2.13:	Data Acquisition Terminal Block Connections	42
Figure 2.14:	Photopotentiometer 1 Calibration	49
Figure 2.15:	Photopotentiometer 2 Calibration	50
Figure 2.16:	Tachometer Calibration	51

Figure 2.17: Photopotentiometer 3 Calibration	52
Figure 2.18: Strain Gage Calibration	53
Figure 2.19: Results of Spin-up of 0 to 30 rpm: trial A.	54
Figure 2.20: Results of Spin-up of 0 to 45 rpm, trial A	55
Figure 2.21: Results of Spin-up of 0 to 60 rpm, trial A	56
Figure 2.22: Comparison of numerical and experimental results of spin-up of 0 to 60 rpm: trial A.	57

1. INTRODUCTION

This final technical report presents a comprehensive summary of the research accomplishments supported by Grant #AFOSR-89-0403 over the period July 1, 1989 to November 30, 1991². The report reviews the objectives of the research in Section 1.1. The status of the research effort is reported in Section 1.2. Section 1.3 of Chapter 1 presents a comprehensive list of written publications resulting from this research effort. Following this, Section 1.4 presents a recapitulation of the advanced degrees awarded, a list of thesis titles, and a history of the professional personnel associated with this grant. Seminars, presented papers, and advisory meetings with Air Force and other DOD laboratories are reviewed in Section 1.5.

Chapter 2 presents some recent progress in the computational fluid dynamics research associated with the study. Some additional work dealing with the modeling of liquid-structure interaction is also described.

Appendix A describes the computer simulation of the test rig using a pendulum analogy to model the sloshing liquid. Also included is a comparison of the results with those obtained by another rigid body dynamic modeling package and from experimental instrumentation of the test rig.

Appendix B discusses the study of the test rig stability which depends on such physical parameters as the masses, inertias and linear dimensions. The work is based

upon experimental results and computer simulations completed using the software package SATELL developed at Iowa State University.

Appendices C, D, and E describe the finite element modeling of the test rig to account for the elastic deformation of the spinning structure in addition to the rigid body motion. A Lagrangian approach was used to develop the equations of motion which include nonlinear relationships for the unknown rigid body motions and linear terms for the relatively small elastic deformations of the members.

Appendix F outlines a sequential implicit-explicit numerical technique developed to solve the system of nonlinear differential equations which describe the rigid body and elastic motions of the structure. The technique employs a Newmark algorithm which is often used in conjunction with finite element methods.

Appendix G describes the basic concepts of the primitive variable coupled strongly implicit solution procedure that was eventually employed in a revised form in the three-dimensional surface fitting sloshing code, SLOSH3D. The version described in Appendix G is applicable to all flow regimes. For use in the simulation of sloshing flows, the scheme of Appendix G was eventually extended to three dimensions and specialized to incompressible flow.

Appendix H contains the first numerical solutions obtained for three-dimensional liquid sloshing using the surface fitting scheme developed under the present grant. The paper also describes the mathematical modeling required to correctly account for the general rotating-nutating motion of the container. Results for five different free surface calculations are presented.

Appendix I presents both experimental and computational results for the sloshing inside a partially filled spherical container undergoing an orbital rotating motion.

Solutions of the unsteady, three-dimensional Navier-Stokes equations for the case of a gradual spin-up from rest are compared with experimental data obtained using a rotating test rig fitted with two partially filled spherical tanks. The numerical solutions were found to compare favorably with the experimental data.

1.1 Research Objectives

This project has involved the study of the dynamics of spin-stabilized satellites carrying sloshing liquid stores. It represents a continuation of work completed during an initial three year funding period from the Air Force Office of Scientific Research. During the previous three year period, a test rig capable of spinning an assembly with two liquid-filled spherical tanks was designed, built and instrumented. Initial experimental runs were completed for a limited number of physical parameter values. In a parallel effort a computer simulation model was developed which treated the sloshing liquid as a two degree-of-freedom pendulum. Numerical results showed good agreement with the empirical data. However, in an attempt to produce an even better mathematical model, an effort was initiated to replace the pendulum analogy by a more exact characterization based upon computational fluid dynamics (CFD). The research conducted during the current three year period has continued the spacecraft dynamic studies started during the initial phase. The objectives of this continuation grant have included:

- To define regions of stability for the existing test rig and to evaluate the effect on stability of such design parameters as tank fill ratios, liquid viscosity, and moments and products of inertia.

- To modify and expand the mathematical model of the satellite simulator to include a finite element analysis of the precessing and deforming structure.
- To identify the fluid reaction on its container (tank) by the dynamic modeling of the sloshing free surface liquid. To fully develop the computational fluid dynamic model of this free surface liquid with its time-varying reaction on the spherical tank.

Development of such a model was undertaken to provide a state-of-the-art representation of the test rig to accurately predict the motion of the system and its various elements and to provide insight into the interactive nature of the structural and liquid components. Such a computational model should provide a valuable tool for the study of parameters and physical phenomena governing the stability and motion of complex space systems.

1.2 Status of Research

Work under the previous AFOSR grant has provided a solid foundation for the current effort. During the previous phase of the research, a test rig was built and instrumented, and a software package (SATELL) was developed to simulate the rigid body motion of the test assembly. A pendulum analogy was used to model the sloshing liquid in that early program. Several numerical simulations were carried out and results were compared with those from another rigid body dynamics package called CAMS. Simulation output was also compared with experimental data for a few select cases (see Appendix A).

Experimental work and numerical simulations using SATELL have continued

during the current research effort. Attention has been focused on stability analysis of the test rig's dynamic motion. Various cases have been studied to determine the influence of physical parameters such as masses, inertias and linear dimensions. Results have verified the conclusion that stable motion for such a system with energy dissipation due to flexible members and/or a sloshing viscous liquid requires spin about the axis of maximum principal moment of inertia. However, certain instances were discovered when that requirement was not sufficient to guarantee stable motion. This was found to be true for both experimental and numerical procedures (see Appendix B).

While the rigid body model provided results that were in general agreement with the experimental data, a more exact model to account for the elastic and rigid body motions was needed to better predict the motion of the assembly. A finite element approach was utilized along with a Lagrangian formulation to develop the equations of motion. Both the rigid body degrees of freedom and the elastic degrees of freedom were considered as unknown generalized coordinates of the entire system in order to accurately reflect the nature of mutually coupled rigid body and elastic motions. Nonlinear coupling terms between the rigid body and elastic motions were fully derived and explicitly expressed in matrix form (see Appendices C, D and E).

The equations developed for the overall rigid plus elastic motion described above contain rigid body motion coordinates that appear in a highly nonlinear fashion along with small elastic motion coordinates that can be handled adequately by linearized relationships. Furthermore, the overall system of equations involves time-varying coefficient matrices which greatly complicate the solution process. A sequential, implicit-explicit integration method is utilized to handle these difficulties. In this

technique, the equation system is first mapped to a subsystem in which the specified generalized coordinates are eliminated. The subsystem is then partitioned into two sets of coupled equations. The set describing elastic motion, which is linear with respect to the elastic generalized coordinates is integrated implicitly. The set governing the rigid body motion, which contains the highly nonlinear coupling terms, is integrated explicitly with back substitution of the elastic kinematic properties determined from the first set of equations. A Newmark algorithm is used to integrate the second order systems of equations directly (see Appendix F).

Two numerical strategies for computing liquid sloshing flows have been pursued under this grant. Both provide a numerical solution to the full three-dimensional unsteady incompressible Navier-Stokes equations which govern the liquid motion. Both schemes utilize primitive variables and an artificial compressibility approach. The schemes differ primarily in the way in which the free surface and the grid are treated.

The most widely tested and "advanced" scheme utilizes "surface fitting" whereby the free surface becomes one of the boundaries of the computational domain. In this approach the grid points are moved after each time step. The computer code based on this approach, SLOSH3D, utilizes a coupled strongly implicit procedure (SIP) to solve the resulting algebraic equations. The basic concept of the primitive variable coupled SIP scheme is discussed in a paper by Chen and Pletcher (see Appendix G). Results from the SLOSH3D code are described in Appendix H and Appendix I.

The second scheme utilizes "surface capturing." The main motivation for pursuing this strategy is that surface capturing does not require a moving, surface conforming grid. Such surface conforming grids become difficult to generate as the free

surface topologies become more complex. In addition, the establishment of a new grid at each time step does require computational resources. The surface capturing permits the calculation of a more general class of flow than with surface fitting. The surface fitting approach allows computation of only the liquid in a container whereas with surface capturing, the flow in both phases, liquid and gas (or vapor) can be resolved. In some applications, information on both phases is desired. This formulation and the results obtained to date are described in Section 2.2.

Calculations of fluid-structure interactions have been successfully carried out. Two codes developed under this grant, STRUCTURE, which calculates the flexible system dynamics, and SLOSH3D, which computes the sloshing motion of the fluid contained in the tank, have been joined into a single unit that enables the transfer of information between the two component modules at each time step of the simulation. Such interactive calculations permit much more realistic predictions of system behavior and are likely to become widely used in design procedures in the future. More details of the formulation and the preliminary results are reported in Section 2.3.

1.3 Publications

Listed below are technical reports previously submitted to the Air Force Office of Scientific Research:

Baumgarten, J.R., Flugrad, D.R., and Pletcher, R.H. (1990). "Investigation of Liquid Sloshing in Spin-Stabilized Satellites," Technical Report No. ISU-ERI-Ames 90410, Iowa State University, Ames, IA.

Baumgarten, J.R., Flugrad, D.R., and Pletcher, R.H. (1991). "Investigation of Liquid Sloshing in Spin-Stabilized Satellites," Technical Report

No. ISU-ERI-Ames 92400, Iowa State University, Ames, IA.

Listed below are technical publications resulting from this work during the current grant:

Chen, K.-H., Kelecý, F.J., and Pletcher, R.H. (1992). "A Numerical and Experimental Study of Three-Dimensional Liquid Sloshing in a Rotating Spherical Container," AIAA-92-0829, presented at the 30th Aerospace Sciences Meeting, Reno, NV.

Chen, K.-H. and Pletcher, R.H. (1991). "A Primitive Variable, Strongly Implicit Calculation Procedure for Viscous Flows at all Speeds," *AIAA Journal*, Vol. 29, No. 8: 1241-1249.

Chen, K.-H. and Pletcher, R.H. (1991). "A Primitive Variable, Strongly Implicit Calculation Procedure," Technical Report Grant No. AFOSR-89-0403, Report No. ISU-ERI-Ames 91401.

Flugrad, D.R. and Obermaier, L.A. (1992). "Computer Simulation of a Test-Rig to Model Liquid Sloshing in Spin-Stabilized Satellites," *ASME Journal of Dynamic Systems, Measurements, and Control*, Vol. 114, No. 4: 689-698.

Kassinis, A.C. and Prusa, J.M. (1990). "A Numerical Model for 3D Viscous Sloshing in Moving Containers," Proceedings of the ASME Winter Annual Meeting, Symposium on Recent Advances and Applications in CFD: pp. 75-86.

Listed below are the papers which have been accepted for publication:

Chen, K.-H. and Pletcher, R.H. (in press). "Simulation of Three-Dimensional Liquid Sloshing Flows Using a Strongly Implicit Calculation Procedure," *AIAA Journal*.

Hill, D.E. and Baumgarten, J.R. (in press). "Control of Spin-Stabilized Spacecraft with Sloshing Fluid Stores," *ASME Journal of Dynamic Systems, Measurements, and Control*.

Xu, J., and Baumgarten, J.R. (1991). "A Finite Element/Lagrangian Formulation of Dynamic Motion Prediction for a Flexible Satellite Simulator with Both Rigid and Elastic Bodies," *Proceedings of the 2nd National Applied Mechanisms and Robotics Conference*, Cincinnati, OH, November 3 - 6, 91AMR-VIIB-5: 1 - 8.

Xu, J., and Baumgarten, J.R. (1992). "Modeling of Flexible Multibody Articulated Structures with Mutually Coupled Motions. Part I: General Theory," *ASME Flexible Mechanisms, Dynamics, and Analysis*, DE-Vol. 47: 411 - 419.

Xu, J., and Baumgarten, J.R. (1992). "Modeling of Flexible Multibody Articulated Structures with Mutually Coupled Motions. Part II: Application and Results," *ASME Flexible Mechanisms, Dynamics, and Analysis*, DE-Vol. 47: 421 - 429.

Xu, J., and Baumgarten, J.R. (1992). "A Sequential Implicit-Explicit Integration Method in Solving Nonlinear Differential Equations from Flexible System Modeling," *ASME Flexible Mechanisms, Dynamics, and Analysis*, DE-Vol. 47: 561 - 566.

Listed below are the papers which are currently under review for publication in the technical literature:

Chen, K.-H., Kelecy, F.J., and Pletcher, R.H. (1992). "A Numerical and Experimental Study of Three-Dimensional Liquid Sloshing in a Rotating Spherical Container," under review by *AIAA Journal Thermophysics and Heat Transfer*.

Schick, T.E. and Flugrad, D.R. (1992). "Motion Study of A Spin-Stabilized Satellite Test Rig," under review by *AIAA Journal of Guidance, Control, and Dynamics*.

1.4 List of Research Personnel, Thesis Titles, and Degrees Awarded

The investigation of rigid body and flexural structure response of the satellite simulator is directed by J.R. Baumgarten and D.R. Flugrad.

J. R. Baumgarten served as principal investigator for the project until his retirement in June 1992. D. R. Flugrad and R. H. Pletcher have served as co-principal investigators and have continued to share that responsibility following Baumgarten's retirement.

J. R. Baumgarten supervised the work of Jiechi Xu, a Ph.D. student who has developed software to model the elastic and dynamic motions of the satellite test rig. This is a particularly difficult problem because of the unspecified rigid body motions of the assembly which are best characterized by nonlinear differential equations coupled with small elastic deformations of the structure which can adequately be described by linear relationships. Flexible components of the structure were modeled by finite element beam members and a sequential implicit-explicit integration technique was developed to solve the combined system of differential equations. He also worked with others on the project in developing a numerical procedure for simulating the interaction between the spinning, elastic structure and the sloshing liquid. Xu is expected to graduate in May 1993. His dissertation is entitled:

Xu, J., (1993). "Dynamic Modeling of Multibody Flexible Structures,"
Ph.D. Thesis, Iowa State University, Ames, IA.

Troy Schick studied the dynamic stability of the satellite test rig. Under the direction of D. R. Flugrad he extended the work of Lisa Obermaier, a former M.S. student who worked on the project during the previous three year grant. Obermaier

developed a computer program named SATELL to simulate the rigid body motion of the test rig using a pendulum analogy to model the sloshing liquid. Schick used that program to run a number of cases to study motion stability of the system based on physical parameters such as masses, inertias and linear dimensions. He was also able to verify expected results experimentally. He graduated in May 1991 and is currently employed by Olin Corporation in Indianapolis, IN. His thesis title is:

Schick, T. E. (1991). "Motion Study of a Spin-Stabilized Satellite Test Rig," M.S. Thesis, Iowa State University, Ames, IA.

Tom Thompson joined the project as a Ph.D. student in 1992. Under D. R. Flugrad's supervision, he has assisted in the experimental work associated with the effort to combine the rigid body/elastic model and the CFD model to study the liquid/structure interaction. He expects to graduate in 1994.

The computational fluid dynamics effort was directed by R. H. Pletcher. He was assisted by Ph.D. students Kuo-Huey Chen, Franklyn Kelecyc, and Babu Sethuraman, Mr. Chen graduated with the Ph.D. in December, 1990. His dissertation was entitled

Chen, K-H. (1990). "A Primitive Variable, Strongly Implicit Calculation Procedure for Two and Three-Dimensional Unsteady Viscous Flows: Applications to Compressible and Incompressible Flows Including Flows with Free Surfaces," Ph.D. Thesis, Iowa State University, Ames, IA.

Mr. Kelecyc expects to complete degree requirements in 1993, and Mr. Sethuraman, in 1994.

1.5 Seminars, Presentations, and Laboratory Visits

J. R. Baumgarten visited Dr. Spencer Wu at AFOSR Bolling AFB in March 1990. The visit coordinated the work of various technical personnel with the mission

of the grant. Baumgarten attended the 1990 Supercomputing Institute at AFSC Kirtland AFB, 21-25 May 1990. He conducted the seminar titled "Tumbling Satellites" at Afdeling Werktuigkunde, K. U. Leuven, Leuven, Belgium on Jan. 15, 1990.

R. H. Pletcher held a seminar titled "Numerical Simulation of Unsteady Viscous Flows" on Jan. 16, 1990 at NASA Lewis Research Center in which he covered the early results of Mr. Chen's calculations. His host was Dr. Meng Liou, Branch Chief, Computational Fluid Mechanics.

Kuo-Huey Chen held a seminar titled "A Primitive Variable Strongly Implicit Calculation Procedure for Two and Three Dimensional Flows " on June 4, 1990 at CFD Research Corporation, Huntsville Alabama.

R.H. Pletcher held the seminar entitled, "Numerical Simulation of Unsteady Viscous Flows" at the University of Alabama, Huntsville, Feb. 15, 1991. Results of liquid sloshing simulations were featured. The seminar was part of the 1991 Propulsion/CFD/Mechanical Engineering Series attended by faculty, students, industrial representatives, and personnel from NASA Marshall Labs. Pletcher visited NASA Lewis Research Center on three occasions to discuss future research in liquid sloshing. He visited NASA Ames Research Center in March 1991 to collaborate on research in turbulence modeling.

D.R. Flugrad and J.R. Baumgarten visited the Federal Microelectronics and Instrumentation Laboratory, Limrick, Ireland in March while participating in the seminar FAIM 91. Drs. Flugrad and Baumgarten both presented lectures on path planning for open chain multiple body mechanisms.

All three principal investigators participated in the 1991 Air Force Office of Scientific Research Contractors Meeting on Structural Dynamics held in Dayton,

Ohio in October of 1991. A presentation of progress and plans was made as a part of the scheduled program.

During July, 1991, R. H. Pletcher presented a seminar on "Recent Results in the Numerical Simulation of Unsteady Viscous Flows" at the NASA Lewis Research Center. In September, 1991, he presented an invited lecture on "Numerical Simulation of Unsteady Viscous Flows" at the Fourth Nobeyama Workshop on Supercomputing and Experiments in Fluid Dynamics, Nobeyama, Japan. In November, 1991, Pletcher presented a seminar at Iowa State University "On the Numerical Solution of the Compressible Navier-Stokes Equations at Very Low Mach Numbers."

In January, 1992, Dr. K.-H. Chen, a former graduate student participant in the present grant, presented a paper describing some of our most recent results, "A Numerical and Experimental Study of Three-Dimensional Liquid Sloshing in a Rotating Spherical Container" at the 1992 Aerospace Sciences meeting in Reno, Nevada.

In November of 1991, Mr. Xu presented a paper entitled "A Finite Element/Lagrangian Formulation of Dynamic Motion Prediction for a Flexible Satellite Simulator with Both Rigid and Elastic Bodies" at the 2nd National Applied Mechanisms and Robotics Conference in Cincinnati, Ohio.

2. RESEARCH IN PROGRESS

The following sections summarize some of the more recent results obtained in the present research program. The first section discusses the progress made in the liquid sloshing calculations using the surface fitting approach. The next section describes recent advances in the surface capturing approach along with some results for two test cases. The last section presents some experimental results obtained from the ISU satellite test rig for the case of a simple orbital spin-up. The experimental data are compared with numerical solutions obtained from a fluid-structure interaction code.

2.1 Recent Progress in the Surface Fitting Approach

Most of the effort in the surface fitting approach has been directed towards eliminating some of the problems with the current code and enhancing its overall capability. The two areas which received the most attention were the handling of the free surface motion and speeding up the code execution particularly through vectorization. Progress in these two areas will be discussed below.

2.1.1 Free-surface motion

A key feature of the free surface fitting approach is that the location and shape of the free surface at each time step is not known beforehand and thus has to be

evaluated as part of the solution. The free-surface location is obtained by solving the equation that states the free-surface kinematic (FSK) condition which is based on the principle that 'particles on the free surface remain on the free surface'.

Knowing the flow solution (the velocity components u, v , and w in the three directions and the density ρ) at all the grid points at a particular point in time, the location of the free surface after one time step must be evaluated. This is done by solving the free surface kinematic equation, which is of the form:

$$\frac{\partial F}{\partial t} = C_1 \frac{\partial F}{\partial x_1} + C_2 \frac{\partial F}{\partial x_2} + S \quad (2.1)$$

where $F = F(x_1, x_2, t)$ is the free-surface function that describes the location/shape of the free-surface. In this equation, coefficients C_1 , C_2 , and the source term S are functions of the flow field and certain other grid related parameters. As we are trying to estimate F at time step ' $n + 1$ ', the flow solution as well as the grid are known only at the current time level, n . Hence the coefficients, C_1 , C_2 and the source term S are also known only at the time level n . In trying to solve for F^{n+1} (superscript denotes time level), these coefficients and the source term are 'lagged' to the previous time level. In short, it can be said that the equation solved was equivalent to

$$\left[\frac{\partial F}{\partial t} \right]^{n+\frac{1}{2}} = [C_1]^n \left[\frac{\partial F}{\partial x_1} \right]^{n+1} + [C_2]^n \left[\frac{\partial F}{\partial x_2} \right]^{n+1} + [S]^n \quad (2.2)$$

In the past, this equation was solved just once to get F^{n+1} . The approach has been modified in the following way: The above procedure of lagging the unknown coefficients is used once to get F^{n+1} . Using the new free-surface information and the subsequently converged flow solution, the coefficients and the source term are evaluated at the new time level $n + 1$. Using the new information, the following

equation was solved to refine F^{n+1} :

$$\begin{aligned}
 \left[\frac{\partial F}{\partial t} \right]^{n+\frac{1}{2}} &= \frac{F^{n+1} - F^n}{\Delta t} \\
 &= \frac{[C_1]^n \left[\frac{\partial F}{\partial x_1} \right]^n + [C_1]^{n+1} \left[\frac{\partial F}{\partial x_1} \right]^{n+1}}{2} \\
 &\quad + \frac{[C_2]^n \left[\frac{\partial F}{\partial x_2} \right]^n + [C_2]^{n+1} \left[\frac{\partial F}{\partial x_2} \right]^{n+1}}{2} + \frac{[S]^n + [S]^{n+1}}{2}
 \end{aligned} \tag{2.3}$$

The system of algebraic equations resulting from approximating the spatial derivatives by appropriate (one-sided or central, depending on the situation) finite difference forms, was solved using a two-dimensional strongly implicit procedure (2DSIP). Terms that did not fall within the 5 point 2DSIP molecule (including terms from previous time level) were moved to the right hand side in the solution algorithm.

This method, which is more like the trapezoidal or Crank-Nicolson time differencing, was expected to give better results as the scheme is closer to being second order accurate in time as compared to the first order accuracy of the old scheme. It should be noted that the above procedure can be repeated (using the latest values of C_1 , C_2 , and S for time level $n + 1$) until the changes in F are small at each time step.

As the location of the free surface determines the amount of liquid in the container, the more accurate scheme is likely to better conserve mass globally. Numerical calculations to date tend to support this idea. For one spin-up calculation, the error between the initial volume of liquid and the final volume was about 10 % when the free surface calculations were done only once per time step. It was found that this

error could be reduced to approximately 4 % when the free surface calculations were done twice per time step, and to slightly below 2 % when the calculations were done four times per time step.

2.1.2 Contact line boundary conditions

The boundary condition used along the line of contact between the free-surface and the solid container wall has been changed to avoid some problems associated with computing higher Reynolds number flows. The grid in the interior of the liquid is generated algebraically so that the grid lines conform to the shape of the free-surface. In other words, the free-surface shape is one of the main factors that determines the placement of interior grid lines.

The free-surface kinematic equation is solved in the interior of the free surface (i.e. the entire free-surface excluding the line of contact between the free-surface and the container wall) and the position of the contact line is estimated through separate procedures. The method that is currently being used is to estimate the contact line such that the condition $\frac{\partial F}{\partial \bar{n}} = 0$ is satisfied. In this condition, \bar{n} denotes a direction normal to the wall of the container. This method ensures that the free-surface is locally normal to the solid wall along the contact line. This is an attempt to avoid grid cells with very sharp corners near the container wall and associated numerical instabilities.

The improved method of solving the free surface kinematic (FSK) equation along with the revised boundary condition has shown much promise. In earlier attempts at trying to solve some severe spin-up cases, the code displayed a tendency to slow down in convergence as time marching continued, and eventually blow up. This

problem was eliminated by using the new approach described above. One spin-up case corresponding to a Reynolds number of 250 has been successfully computed. Further numerical experiments are underway to study the usefulness of this procedure.

2.1.3 Code refinement efforts

Earlier attempts at using the SLOSH3D code to simulate spin-ups of spherical tanks encountered some difficulties beyond a certain range of Reynolds numbers (based on tank radius and linear velocity of tank center). For a particular case ($Re \approx 180$), the calculations suddenly began to diverge, and eventually blew up. Another problem associated with such calculations was a large difference (more than 10%) between the initial volume of the liquid in the tank and the calculated volume after sufficiently large number of time steps.

It was felt that the use of a finer grid might eliminate such problems. A major difficulty associated with grid refinement was that the time taken for the computations began to grow out of control. At that stage, it was realized that enhancing the execution speed of the code was vital to the simulation of finer grid and high Reynolds number cases.

Two different approaches were taken to make the code execution faster. The first one is a direct consequence of the fact that the code was developed to suit the capability of the workstations on which the code was primarily expected to run. These machines had restrictions on the memory size that prohibited the use of finer grids. So, it was decided to use larger memory vector machines like the Cray Y-MP with a code that was different in the following ways:

1. Removing repetitive calculations:

As pointed out earlier, the initial code development was tailored to suit the capability of workstations available on campus which had very limited memory. Hence, as far as possible, the code was based on repetitive generation of the same sets of numbers rather than generating them just once and storing them in large arrays. The enhanced memory on large computers like the Y-MP, permitted switching to larger storage and fewer calculations. This eventually resulted in faster code execution. In fact, a significant speed-up, by a factor of as many as ten times could be achieved by modifying the code along these lines.

2. Vectorization:

The SLOSH3D code uses a three-dimensional coupled strongly implicit procedure (CSIP3D) to solve the system of algebraic equations which results from the finite difference discretization. This CSIP3D routine is a critical and time consuming part of the overall calculations. It was realized that this part of the calculations was responsible for a large fraction of the computer execution time due to high data dependence of the implicit procedure and the consequent time consuming scalar execution loops.

The algorithm was vectorized along surfaces of constant index sums ($i + j + k = \text{constant}$). In other words, the three-dimensional calculations were converted to two dimensions: surfaces containing points whose indices add to the same number. Surfaces were identified by their index sums (ranging from $i + j + k = i_{min} + j_{min} + k_{min}$ to $i + j + k = i_{max} + j_{max} + k_{max}$) and each of these

surfaces contained all the points (one or more) that satisfied the property that their indices add up to a certain constant. Vectorizing the calculations along these lines was possible because of the fact that the calculations (in the CSIP3D procedure) for points lying on any one surface was not dependent on any parameters related to any other point on the same surface. Hence, the calculations for all such points lying on the same surface could be done simultaneously; this results in more vector operations and consequent higher rate of execution. The overall execution speed of the code was increased approximately to about sixteen times the original speed.

2.2 Recent Progress in the Surface Capturing Approach

This section highlights progress made in the development of the surface capturing approach for modeling sloshing flows in moving containers. As discussed in previous reports [4] [5], the primary motivation for pursuing this strategy is that surface capturing does not require a moving, surface-conforming grid, and hence is free of the grid generation problems associated with the surface fitting approach. Moreover, multiple free surfaces and complex surface interactions can be handled without any special treatment.

Initial work on the free surface capturing approach was begun as part of the ongoing satellite propellant sloshing research at Iowa State University. The evolution of the present surface capturing methodology has been documented in the previous annual reports [4] [5]. Many ideas have been tested during the course of the research, with the goal of obtaining a reliable, robust, and accurate computer code. The most significant developments will be discussed in the sections below, along with some

results for two validation test cases

2.2.1 Formulation of the governing equations

Consider a container partially filled with a liquid, the remaining regions being occupied by a gas. If it is assumed that both the liquid and gas behave as isothermal, incompressible fluids, the equations which govern the fluid motion within a discrete control volume Ω intersected by the free surface (Fig. 2.1) can be written as follows:

$$\frac{d}{dt} \int_{\Omega} \rho d\Omega + \oint_S \rho \vec{V} \cdot d\vec{S} = 0 \quad (2.4)$$

$$\frac{d}{dt} \int_{\Omega} \rho \vec{V} d\Omega + \oint_S \rho \vec{V} \vec{V} \cdot d\vec{S} = \int_{\Omega} \rho \vec{B} d\Omega + \oint_S \vec{T} \cdot d\vec{S} + \oint_C \sigma \hat{N} dC \quad (2.5)$$

$$\oint_S \vec{V} \cdot d\vec{S} = 0 \quad (2.6)$$

where ρ is the fluid density, \vec{V} is the velocity vector, \vec{T} is the stress tensor, \vec{B} is the body force acceleration vector, and σ is the surface tension.

Equations 2.4, 2.5, and 2.6 represent, respectively, the conservation of mass, the conservation of momentum, and an incompressibility constraint. Note that the conservation of mass and incompressibility constraint equations become identical away from the interface since the density of each fluid is considered constant.

While the foregoing equations appear unusual at first glance (due to the presence of an equation for density), they do in fact constitute a solvable set of equations given appropriate initial and boundary conditions. Detailed discussions of the mathematical properties of solutions to differential analogs of these equations can be found in

recent works by Simon [12] and Antontsev et. al [2].

It should be noted that the density is considered here to be a *discontinuous* function of space (the discontinuity occurring at the free surface). This comment also applies to other fluid properties such as the viscosity. As a result, the solution of Eq. (2.4) provides a means of locating the free surface through knowledge of the density field.

The inclusion of a surface tension force term into the conservation of momentum equation is valid only for control volumes containing the free surface. Away from the free surface (in the single phase regions) this term will vanish. Therefore, in order for surface tension to be included in the numerical formulation described below, it is necessary to identify the location of the free surface within the computational domain. However, for most of the sloshing problems of interest in the present research, surface tension effects should be small (thus allowing the surface tension force to be neglected from the formulation).

2.2.2 Numerical methods

The numerical algorithms developed to date have employed the finite volume method [1]. In the finite volume method, the computational domain is divided up into a system of non-overlapping control volumes. The dependent variables are assigned values at node points located at the centroids of these control volumes. Numerical approximations of the fluid conservation laws (e.g. Eqs. 2.4 - 2.6) may then be derived for each control volume.

In order to couple the incompressibility constraint with the conservation of mass and momentum equations, the pseudo-compressibility method of Chorin is employed

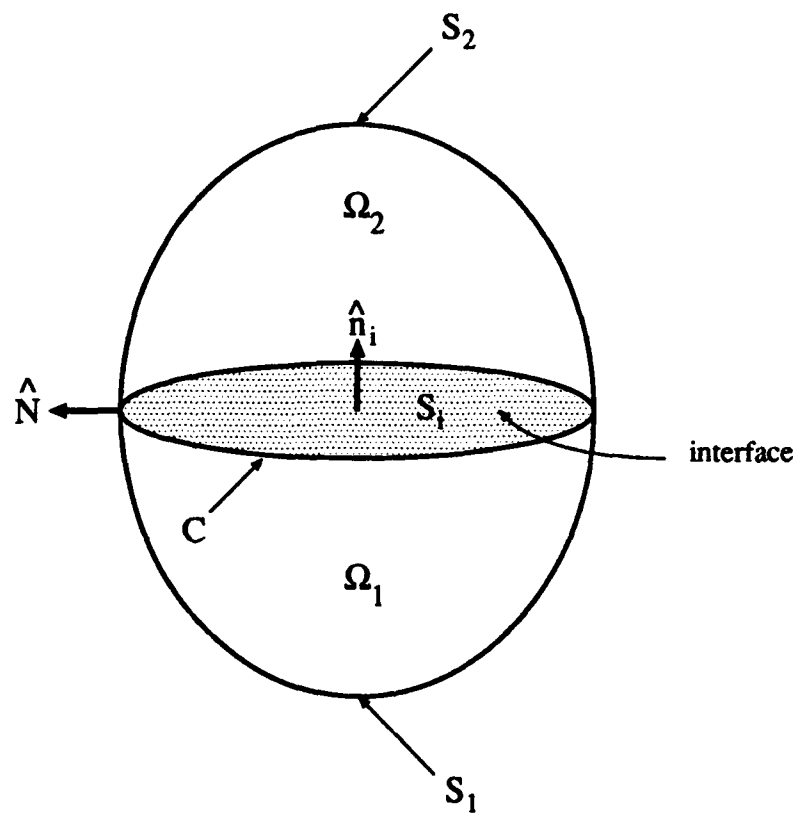


Figure 2.1: Control volume within a two-fluid system.

[6]. The pseudo-compressibility approach adds a fictitious pressure derivative term to Eq. (2.6), yielding

$$\frac{d}{d\tau} \int_{\Omega} P d\Omega + \beta \oint_S \vec{V} \cdot d\vec{S} = 0 \quad (2.7)$$

where β is a constant parameter, and τ is the pseudo-time. It should be noted that the pseudo-time, which has no physical meaning, is essentially an iteration parameter for which

$$\lim_{\tau \rightarrow \infty} \frac{\partial f}{\partial \tau} = 0 \quad (2.8)$$

$$\lim_{\tau \rightarrow \infty} f(\tau) = f(t + \Delta t) \quad (2.9)$$

where f is any flow field variable. Equations (2.8) and (2.9) suggest that the solution at any given future time level $t + \Delta t$ corresponds to a steady state solution in pseudo time. For consistency in the formulation, pseudo-time terms are also added to the other equations. This practice does not affect the solution since all pseudo-time derivatives are required to go to zero at steady state (in pseudo-time).

The discretized equations form a coupled system containing five (in three dimensions) unknowns at each point. The current formulation solves this system using an LU-factored implicit algorithm similar to that of Yoon et. al. [14]. Transient calculations are carried out using a constant physical time step in conjunction with subiteration. The subiterations are needed in order to drive the pseudo-time derivatives to zero, and hence converge the solution at the next physical time level.

2.2.3 Test case results

Results for two test cases are presented in this section. The first test case is the "broken dam" problem [13], which was chosen, primarily due to its use by other authors as a validation case [7] [9] [11], the availability of experimental data [10], and the complex behavior of the flow field and free surface. In the broken dam problem (Fig. 2.2), a rectangular liquid column is initially held up by a thin partition (the dam). At time $t = 0^+$, the partition is removed, thereby allowing the liquid to collapse under the influence of gravity. Of interest for comparison with the experimental data from the literature are the positions of the free surface at the bottom wall (the surge front) and back wall as functions of time.

The case presented here employed a square initial liquid profile of length a placed within a container $5a$ units long by $1.25a$ units high by a units wide. The liquid was assumed to be water and the gas air, both at standard conditions.

In previous calculations of this test case, a three dimensional grid was used. However, as the major flowfield features are principally two dimensional, the decision was made to employ a two dimensional version of the original three dimensional code. This permitted a faster turn around time in the individual calculations (which tended to be quite lengthy due to the nature of the unsteady flowfield).

In order to examine the effect of grid refinement, numerical solutions were computed using three grid sizes of 80×20 , 120×30 , 160×40 control volumes. A constant time step was prescribed for each calculation as follows (time units are dimensionless): 0.01 for the 80×20 grid, 0.0067 for the 120×30 grid, and 0.005 for the 160×40 grid.

Some selected results derived from the computed solutions are presented in Figs.

2.3 - 2.6. Figure 2.3 shows the position of the density interface (free surface) at various times during the transient for the 120×30 grid solution. The corresponding velocity fields are shown in Fig. 2.4. Notice the formation of a large vortex in the vicinity of the free surface due to the shear induced by the motion of the liquid relative to the gas. The free surface profiles are quite similar to those shown in photographs from experiments in Ref. [10].

A more quantitative comparison of the numerical solution with the experimental data is given in Figs. 2.5 and 2.6. Here the position of the free surface along the bottom and back walls of the container are plotted versus non-dimensional time. The agreement between the numerical solution and the experimental data is good considering the uncertainties inherent in the experimental data and the approximations used in the numerical solution.

The second test which was recently attempted is depicted in Fig. 2.7. Here, a two-dimensional, rectangular tank half-filled with water is subjected to a prescribed horizontal, oscillating acceleration. This acceleration is of the form

$$a_x(t) = Ag \sin(\omega t) \quad (2.10)$$

where $A = 0.01$ is an amplitude parameter, g is the acceleration due to gravity, and $\omega = 2\pi f = 5.592 \text{ Hz}$ is the oscillation frequency. The motion of the tank gives rise to a periodic sloshing motion of the water. This case has been studied numerically by Huerta and Lin [8].

The calculations were performed on a 48×64 control volume grid. The time step was set to 0.025 (dimensionless time units), and the calculations carried out for 400 time steps.

Selected plots of the density interface position are presented in Fig. 2.8. The position of the free surface at the front and back walls of the tank is plotted as a function of time in Fig. 2.9. The periodic motion of the water waves is clearly indicated in this figure. Notice that the free surface motions at front and back walls appear to be out of phase with one another.

2.2.4 Concluding remarks

The encouraging results obtained thus far have spurred additional efforts to refine the methodology. Current work is focusing on enhancing the stability, accuracy, and robustness of the method. Application of the method to other test cases and to the satellite propellant sloshing problem will follow.

2.3 Progress in Fluid-Structure Interaction

Experimental measurements of fluid and structural displacement for the case of a simple orbital spin-up from rest were recently obtained on the satellite test rig at Iowa State University. The purpose of these experiments was to provide data for verifying the accuracy of the fluid-structure interaction computer code (STRUCTURE-SLOSH3D). A detailed summary of this work is presented in the sections below.

2.3.1 Equipment

The test rig is shown in Figure 2.10. Its upper body, which emulates an orbiting satellite, is mounted on a universal joint driven by a 1/4-horsepower DC motor through a gear train. In the spin-up tests, a collar was positioned so that the upper body could only rotate about a vertical axis. The two 6-inch-diameter spherical

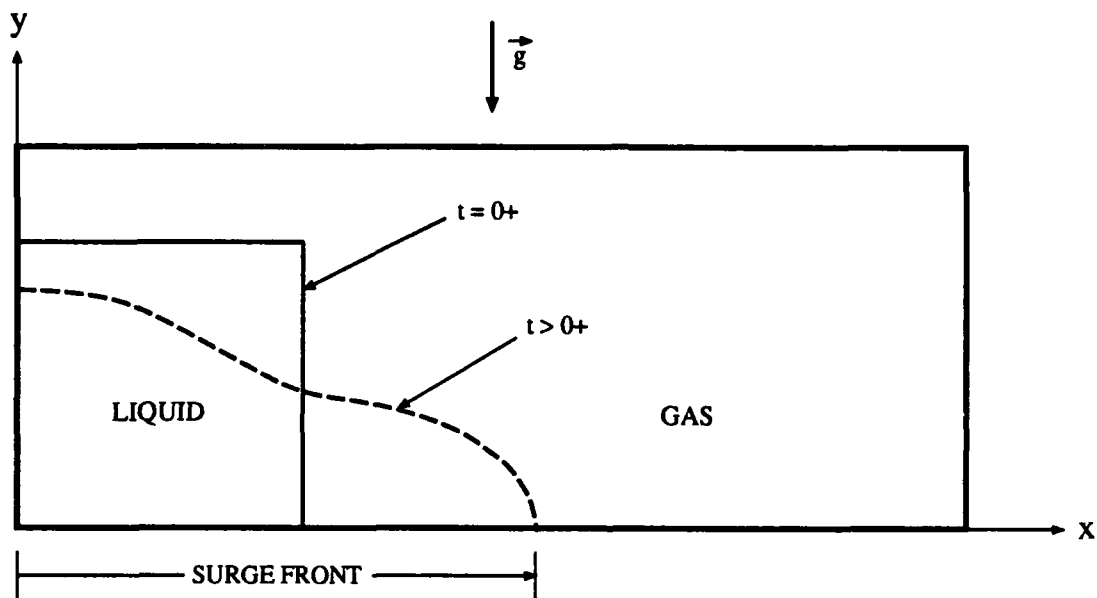


Figure 2.2: Schematic of the broken dam problem.

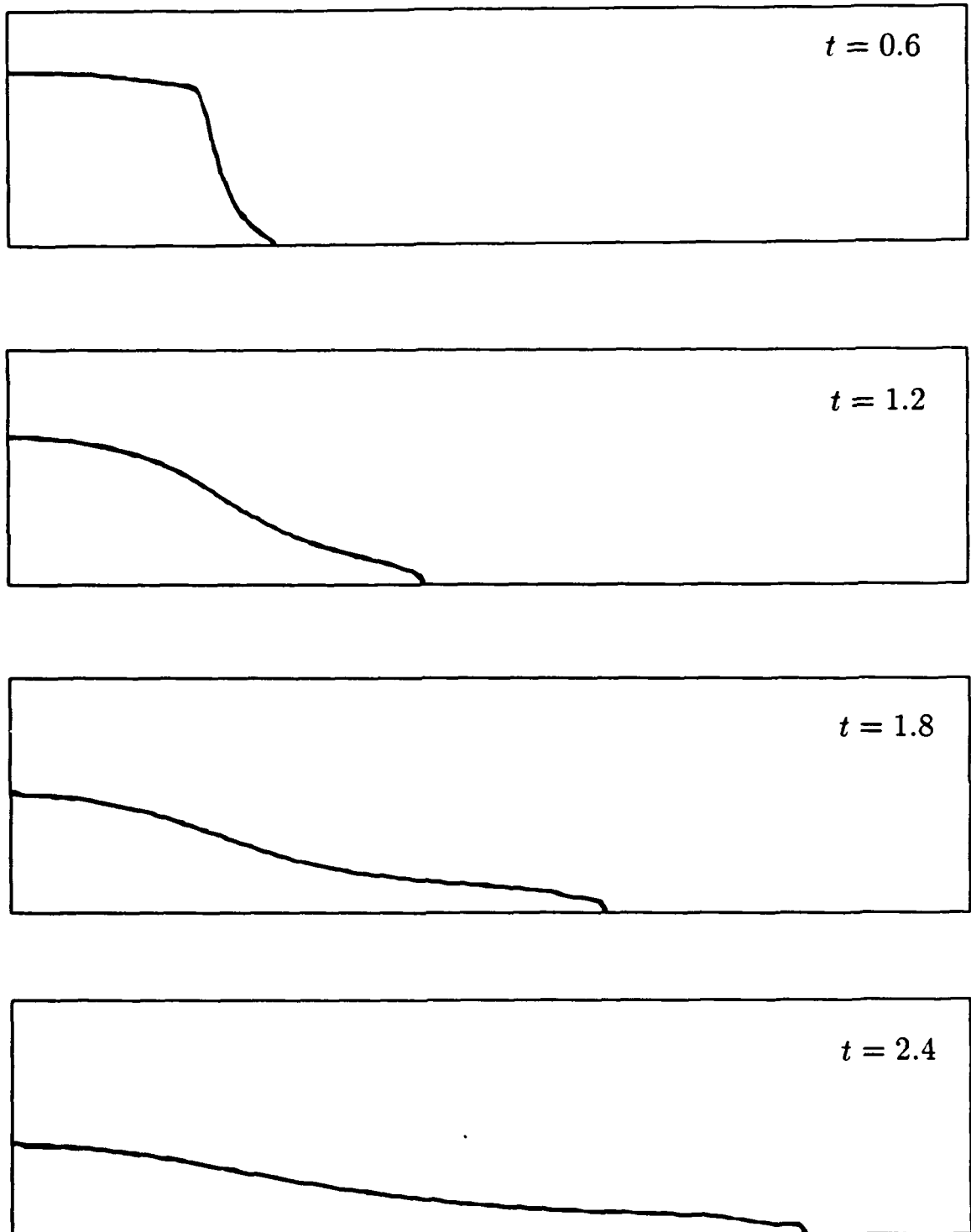


Figure 2.3: Density interface for the broken dam problem; selected times.

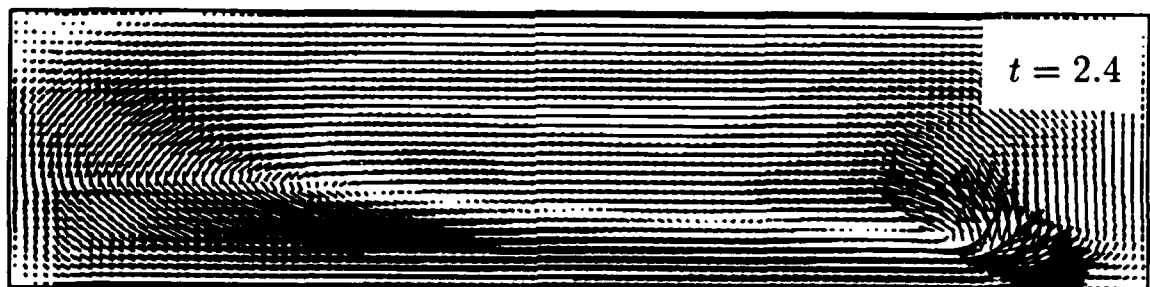
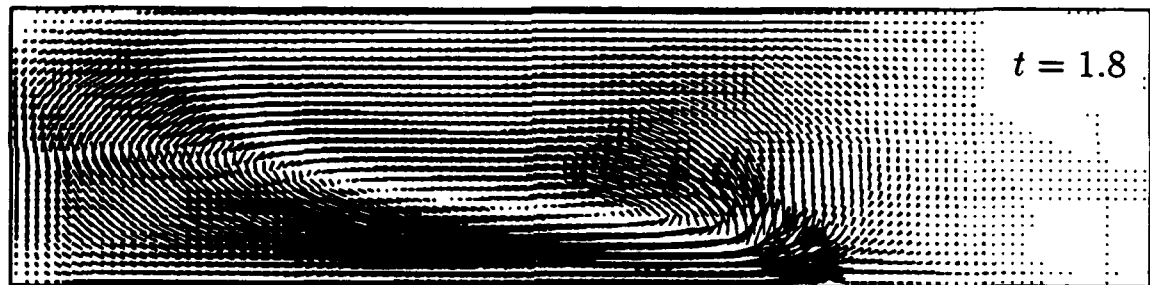
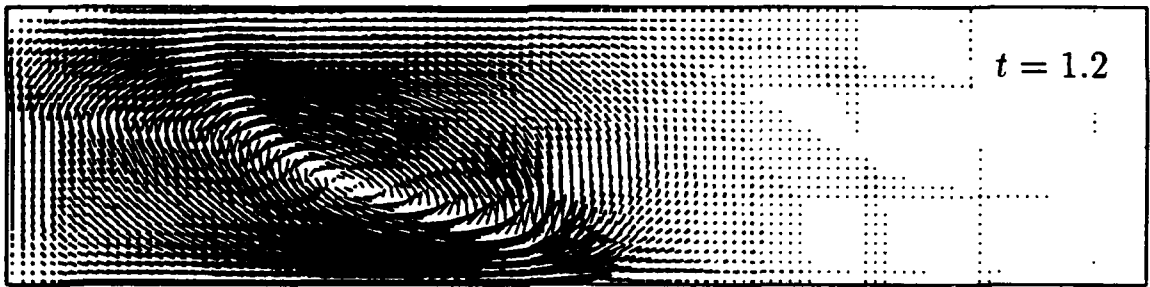
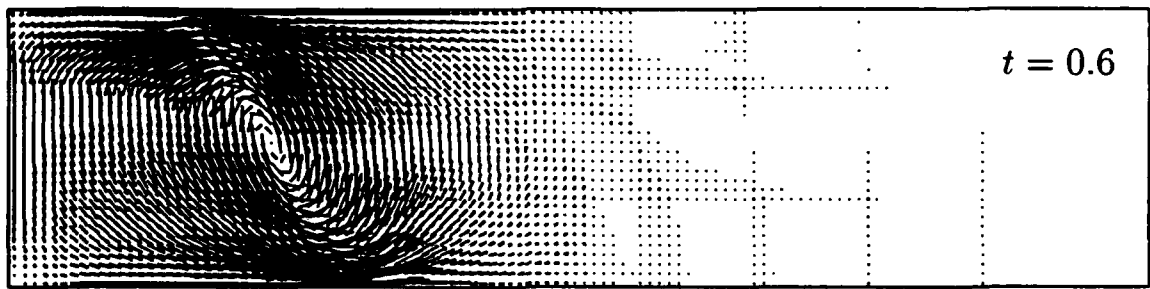


Figure 2.4: Velocity field for the broken dam problem: selected times.

SURGE FRONT POSITION VS TIME BROKEN DAM PROBLEM

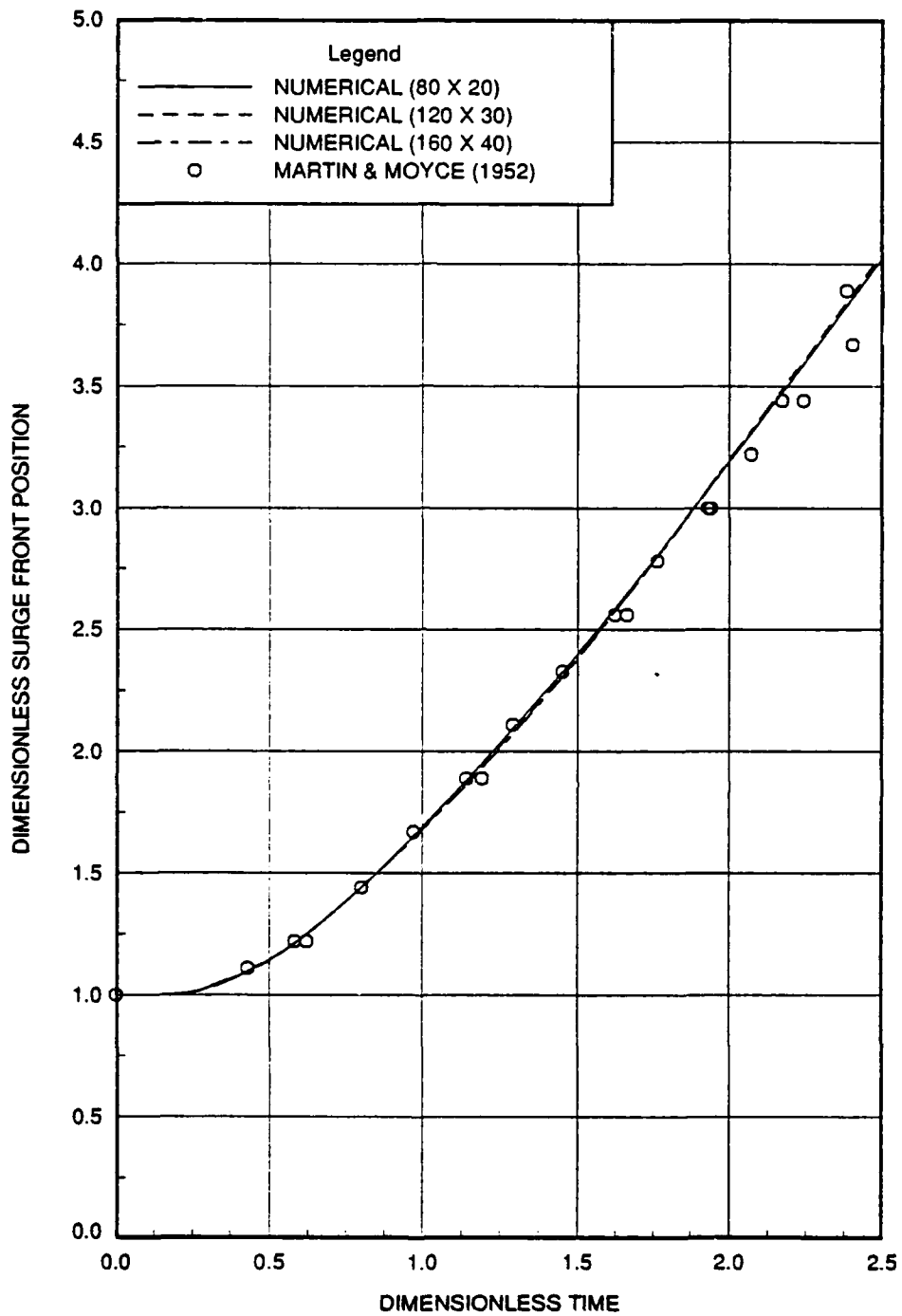


Figure 2.5: Surge front position versus dimensionless time for the broken dam problem.

BACK WALL FREE SURFACE POSITION VS TIME BROKEN DAM PROBLEM

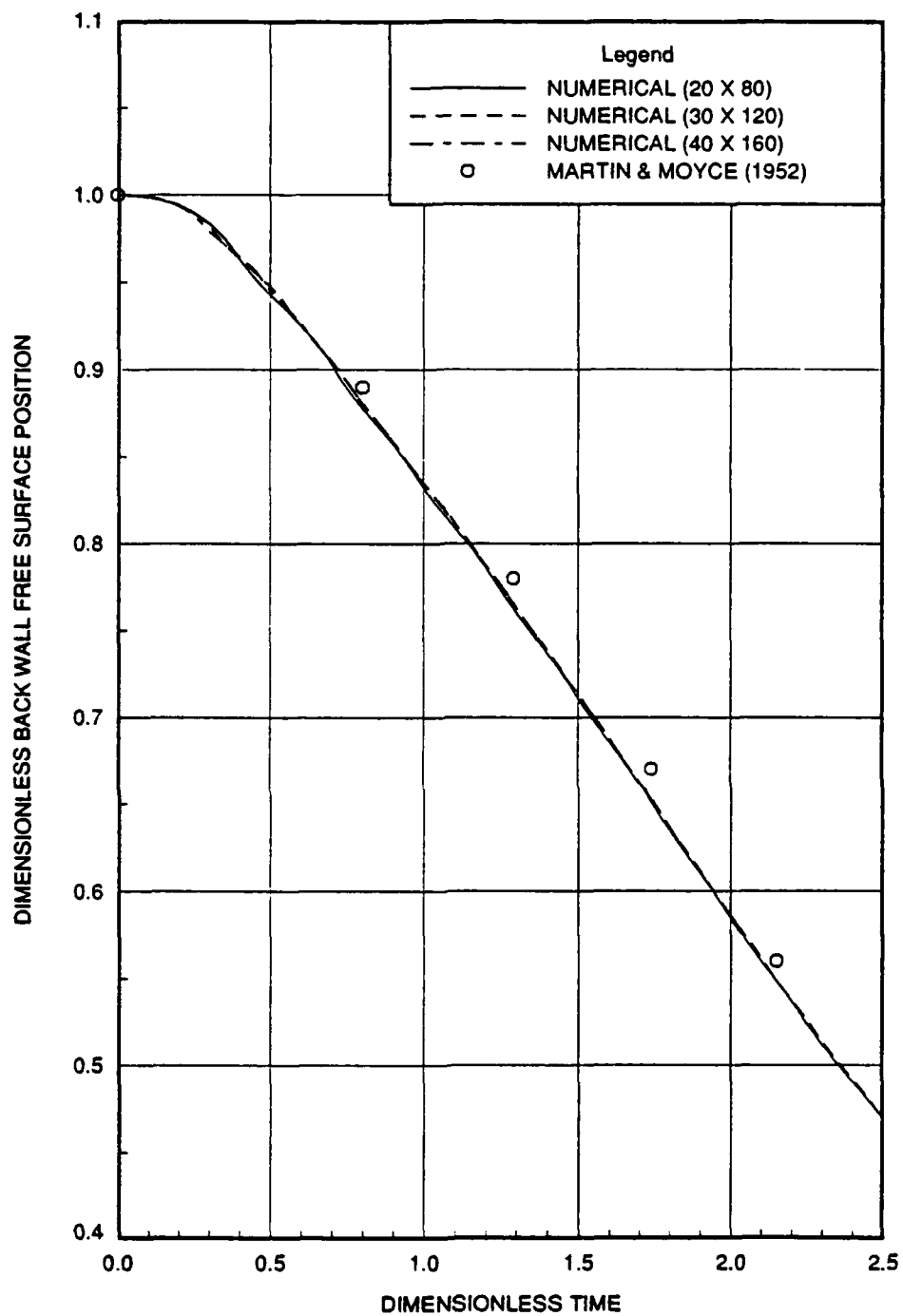


Figure 2.6: Back wall free surface position versus dimensionless time for the broken dam problem.

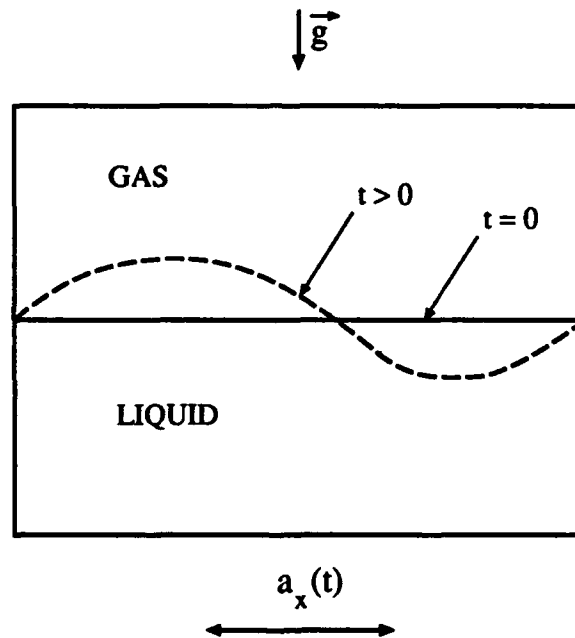


Figure 2.7: Schematic of oscillating tank problem.

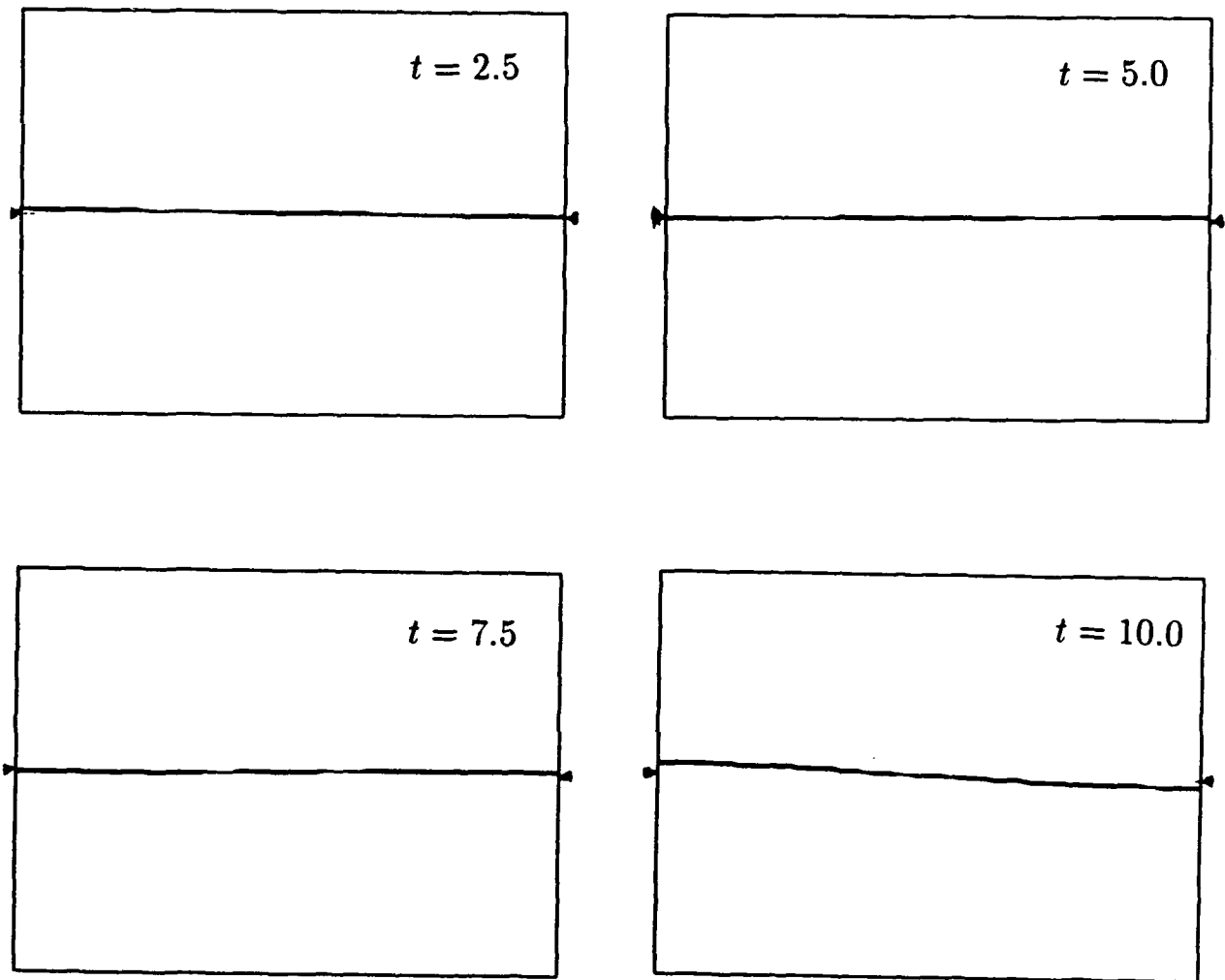


Figure 2.8: Density interface for selected times: oscillating tank test case.

OSCILLATING TANK TEST CASE

FREE SURFACE POSITIONS AT THE TANK WALLS

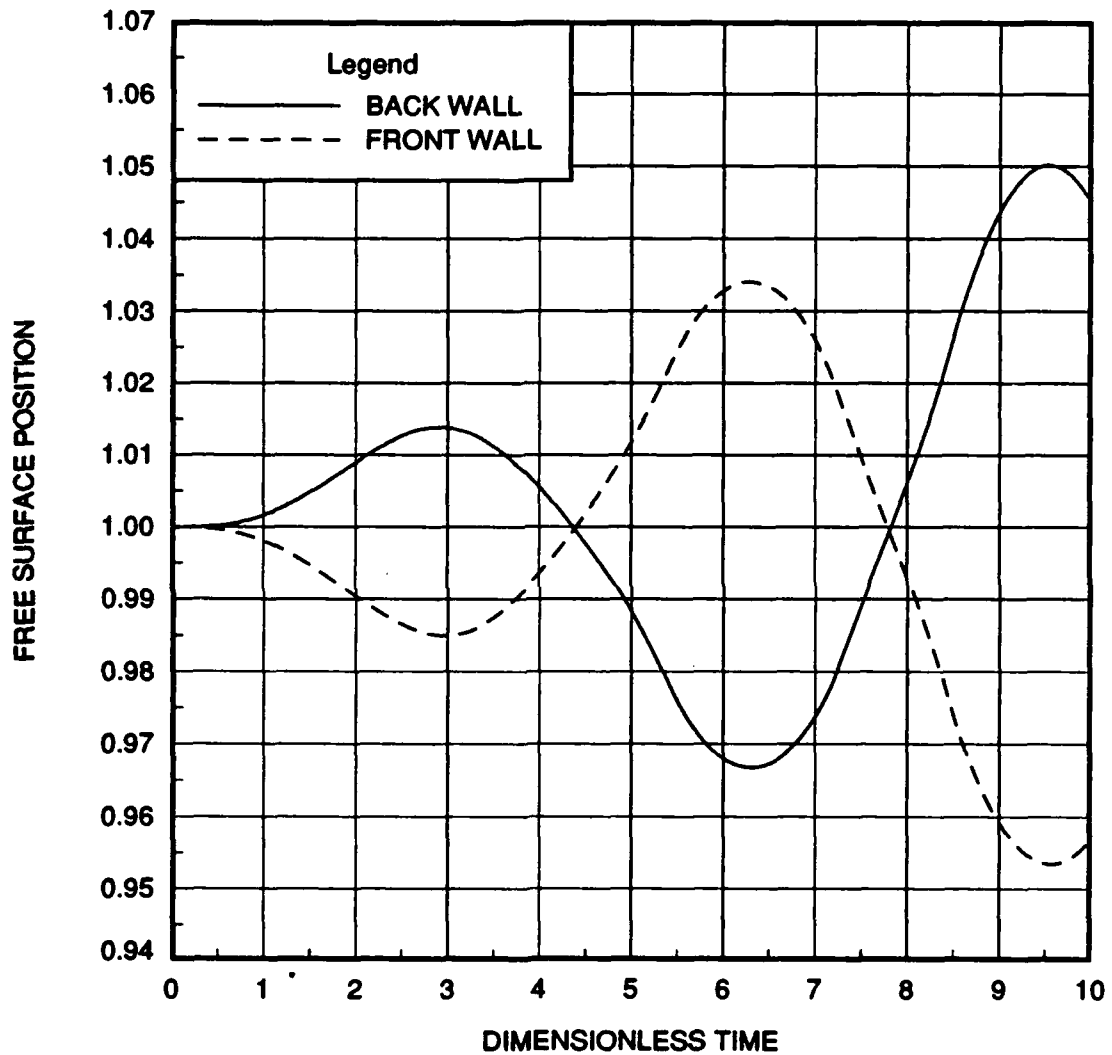


Figure 2.9: Free surface position versus time for front and back tank walls.

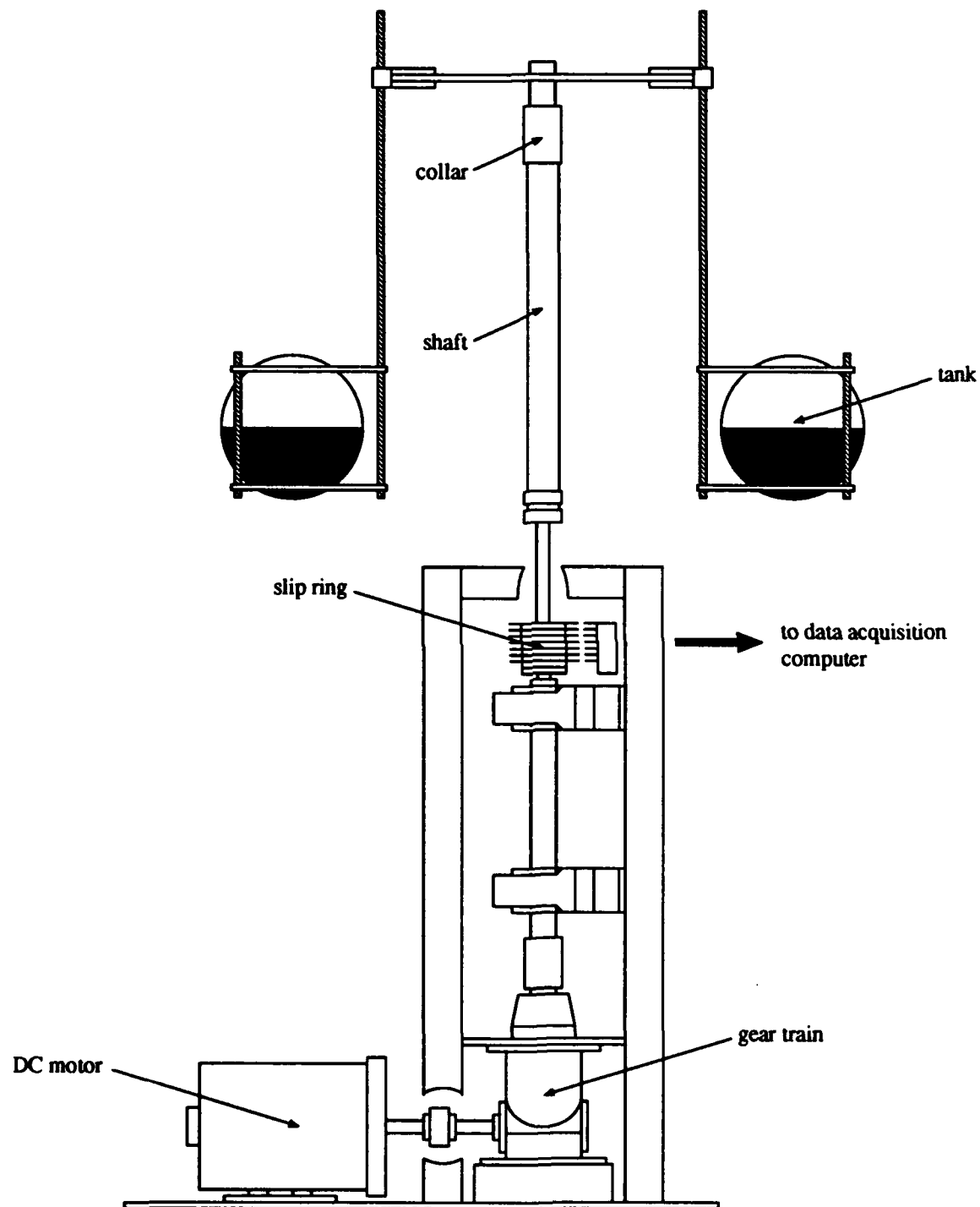


Figure 2.10: The satellite test rig.

tanks (50% filled with glycerine) were mounted using segments of 5/16-inch threaded rod extending downward from a horizontal crossbar attached to the upper body axis. The position of the center of the tanks under stationary and weightless conditions would be 10 inches from the vertical spin axis and 14 inches below the crossbar.

In order to allow a useful validation of the computer simulation code, the following quantities had to be measured for the spin-up test: angular velocity of the upper body, displacement of the tank position due to bending of the threaded rods, and fluid displacement in the tanks. Transducers mounted on the rig itself provided signals (through slip rings when necessary) to the data acquisition personal computer as described below. A list of specifications is given in Table 2.1.

A tachometer connected to the drive train of the rig provided a voltage nearly proportional to the speed of the rig. See the Calibration section for details on the calibration curve.

Strain gages were mounted on the inboard and outboard sides of both of the threaded rods on which one of the tanks was mounted. These four strain gages comprised a Wheatstone bridge which generated a signal proportional to the displacement of the center of the tank from the axis of the upper body. A conditioning circuit mounted on the upper body amplified the signal before it was sent through the slip rings to the terminal block on the data acquisition computer. This circuit is shown in Figure 2.3.1.

Three photopotentiometers were mounted on the tank in order to sense the fluid displacement of the free surface along vertical sections of the tank. Photopotentiometer 1, 2, and 3 measured fluid displacement along the "inboard," "outboard," and "lag" axis, respectively. These sensors were positioned so that their single-valued

Table 2.1: Description of Equipment

Component	Maker	Description
Data Acquisition Computer	IBM	PS/2 Model 50
Data Acquisition Board	National Instruments	MC-MIO16-9
Power Supply	Raytheon	QSA10-1.4 0-10VDC, 0.6A
Photopotentiometers		
Light Bulbs		SK46
Strain Gages		SR-4
Instrumentation Amplifier	Analog Devices	AD524BD 8913
DC Motor	General Electric	Model 5BPB56HAA100 90VDC, 1/4 hp 1725 RPM

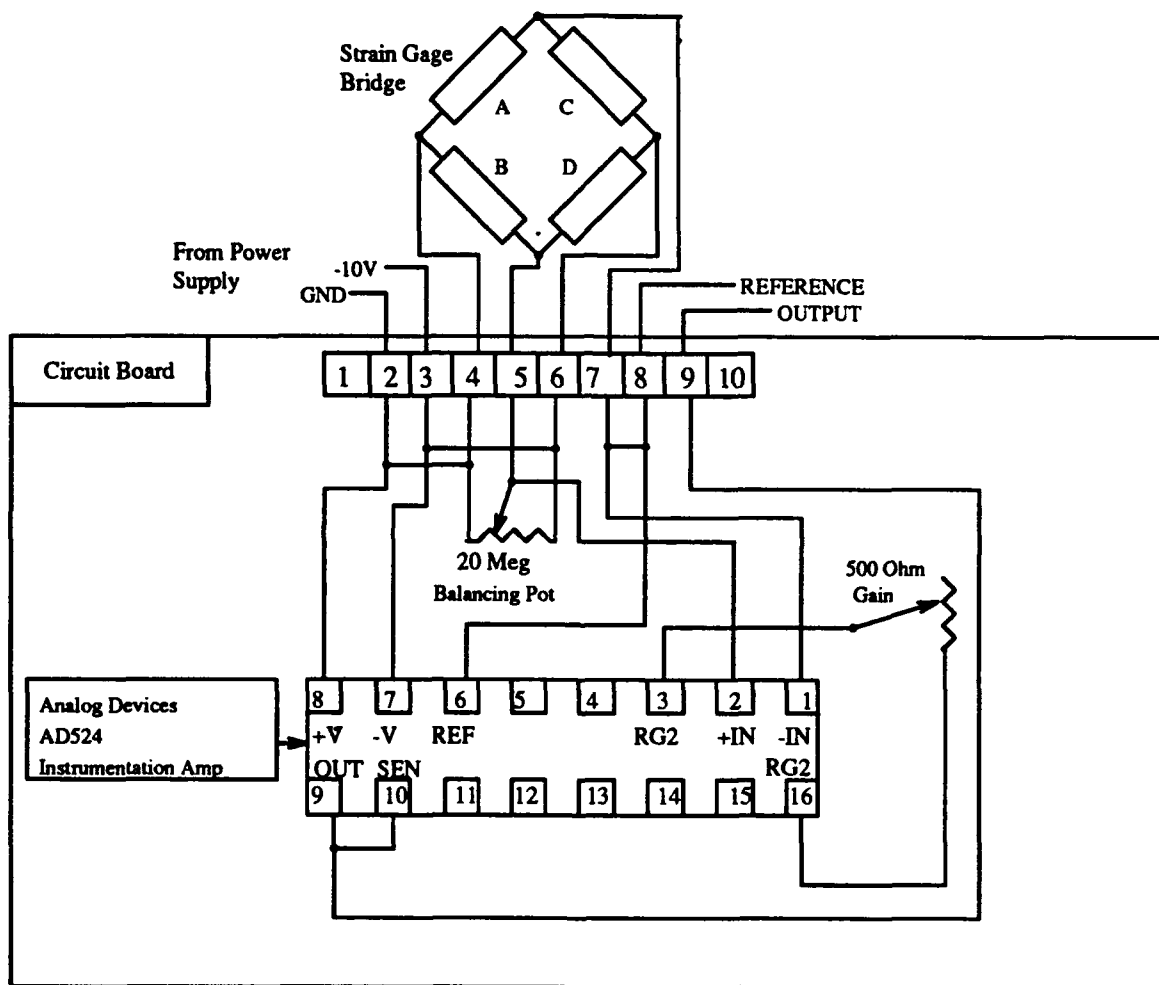


Figure 2.11: Strain Gage Conditioning Circuit

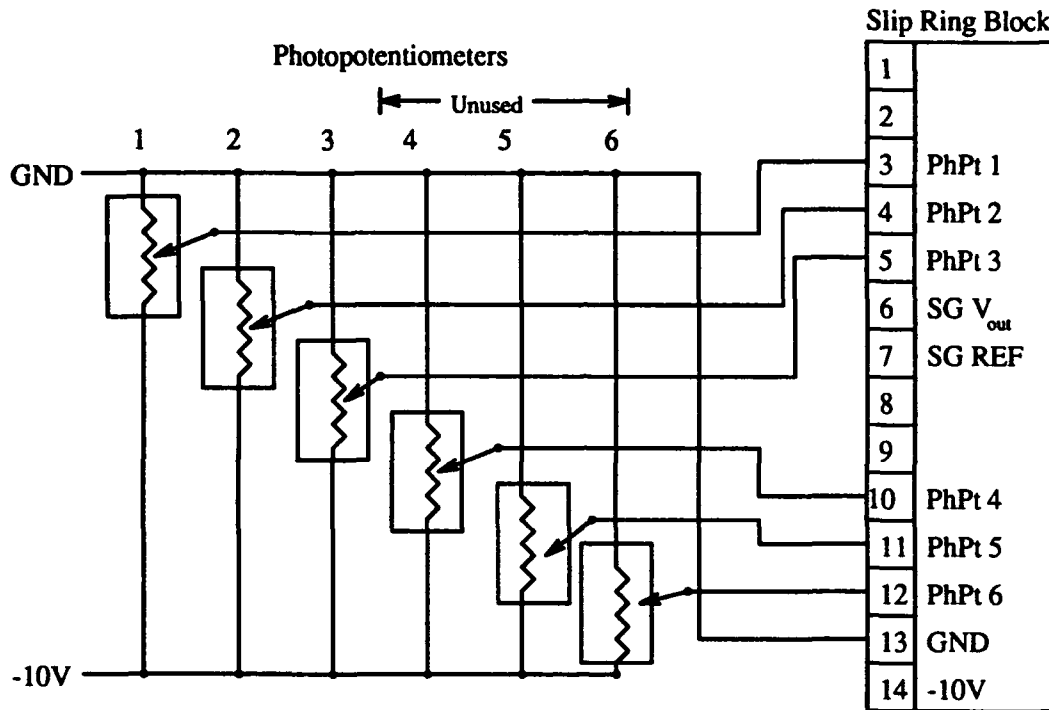


Figure 2.12: Photopotentiometer Circuit

range of measurement along these axes would include as much as possible of the fluid motion during spin-up. They acted as voltage dividers, sending on a portion of the 10-volt input signal in accordance with the amount of light which the moving fluid blocked. The resulting signal passed through the slip rings to the terminal block of the data acquisition computer. The circuit diagram is shown in Figure 2.12.

Each of the two tanks was equipped with an SK46 light bulb whose filament was positioned about 1-1/8 inch below the top of the tank. The two bulbs were wired in series across the 10-volt power supply, which also supplied power to the strain gage and photopotentiometer circuits.

Figure 2.13 shows the termination connections of the data acquisition computer used in the experiment. An IBM PS/2 equipped with a National Instruments Data

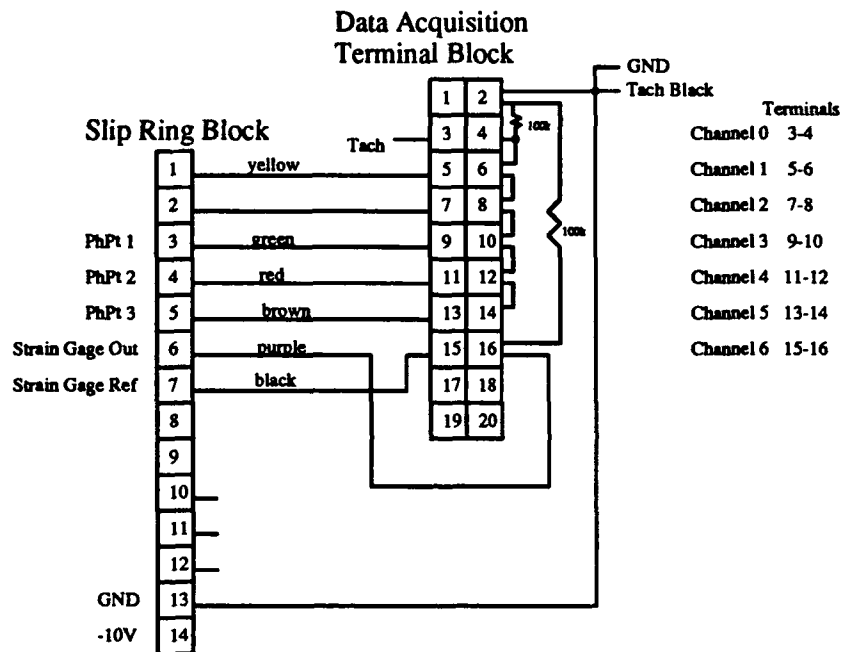


Figure 2.13: Data Acquisition Terminal Block Connections

Acquisition card was used. Specialized data acquisition software was written in Basic. The scan rate was 100/second, and for the spin-up runs, the strain gage and tachometer channels were given a gain of 10 in order to improve resolution.

2.3.2 Calibration

The tachometer, strain gages, and photopotentiometers were calibrated before the spin-up runs were performed. Photopotentiometers 1 and 2 were calibrated against pre-computed fluid displacements for steady-state spin velocities. In other words, for each steady-state spin rate, there is a stationary free-surface position, which was computed analytically. These values were compared to potentiometer voltage output at several steady-state spin rates (tanks constrained against radial displacement) in order to arrive at calibration curves for photopotentiometers 1 (in-

board) and 2 (outboard). (About 200 data points were taken at each spin rate.)

These curves were then fit with polynomials as shown in Figures 2.14 and 2.15. All photopotentiometer calibrations and spin-ups were performed with room lights off and tank-mounted light bulbs illuminated.

At the same time, the tachometer was also calibrated. Precise values of angular speed were obtained by adjusting the motor rheostat and counting revolutions. After the speed was adjusted to the desired value, the tachometer voltage readings along with those of Photopotentiometers 1 and 2 were taken by the computer.

Figure 2.16 shows the tachometer's voltage output, which is nearly linear with speed. The above procedure did not provide a large enough range for Photopotentiometer 3 (lag), since fluid displacement at this sensor is small for a steady-state speed. Therefore, this sensor was calibrated manually. The tank assembly was disconnected at the cross-bar and was tilted enough to achieve fluid surface displacement at 0.1 to 0.5-inch increments on a graduation strip along the photopotentiometer.

At each position, the data were recorded by hand. The resulting correlation of voltage output to free-surface position was fit with a polynomial, and is shown in Figure 2.17.

Finally, the strain gage circuit had to be calibrated. This was done by inserting various gage rods between the tanks in order to separate them by a known distance and sampling the resulting strain gage voltage output.

The gage rods were first fabricated to lengths of 11.50, 12.00, 12.50, and 13.00 ± 0.01 inches. Next, the strain gage bridge circuit was balanced by adjusting its balance potentiometer so that the voltage output was approximately zero when the 12.00-inch gage rod was inserted (this causes the tank to be in the zero-gravity equilibrium

position, centered 10 inches from the axis of rotation). Also, the gain potentiometer on the bridge circuit amplifier was set so that the voltage output would increase approximately one-tenth volt for each additional 0.5 inches of spread between the two tanks.

Once the strain gage bridge circuit had been adjusted, calibration could begin. Each gage rod was inserted between the bottom plates of the tank housings, one-half inch in from the corners of the plates, on the side of the axis where the terminal strip is located. For each rod, about 200 voltage samples were taken by the data acquisition computer, and the process was repeated twice. Figure 2.18 shows the resulting curve fit, which is quite linear.

2.3.3 Experiments

Three spin-ups were performed at each of the following target speeds: 30, 60, and 90 rpm (revolutions per minute). Each spin-up procedure consisted of starting the rig at a near-zero rotational speed and smoothly accelerating the rig to a set target rotational speed by manually turning the rheostat control of the DC motor. Since the duration of the acceleration was on the order of one second, significant sloshing was induced.

Data acquisition began just before spin-up in each case. One hundred samples per second were taken on each channel for a duration of 4 seconds. The resulting sample times and voltages were saved to a computer data file.

A FORTRAN program was written to put the raw data into meaningful form. After reading the raw data files, it used the polynomial curve fits from the calibration to translate the voltages into speed, ratio of free surface height to tank radius (h/r),

and tank displacement. For photopotentiometers 2 and 3, a subroutine was used to find the solution to the polynomial equations, since photopotentiometer voltage was plotted in terms of h/r . It then wrote the reduced data to a file.

2.3.4 Results

The results of all three of the 0-30 rpm spin-ups were very similar; the same was true for 0-45 rpm and 0-60 rpm. Therefore, the results of only the first run at each speed are presented here.

Figures 2.19, 2.20, and 2.21 show the angular speed, free-surface position, and tank deflection for these runs. Zeroes are shown on the plots of photopotentiometer 3 for times when its output went beyond the range of calibration. This type of clipping was also necessary for photopotentiometer 1 (inboard) in the time period just before $t = 1$ second because the output voltage dropped below the -7.05-volt calibration limit. In this range, the calibration was very sensitive.

The general behavior of the system was what one might expect: as the speed increased from a near standstill, the fluid sloshed toward the outer part of the tank, resulting in positive readings of h/r on the outboard side, and negative ones on the inboard. At the same time, the flexibility of the structure allowed the tank to flair out by about 3/4 inch in the 0-60 rpm case. It is interesting to note the approximately 2 to 3 hz oscillations superimposed on the fluid displacement and tank position curves in each case. This seems to indicate coupling between fluid slosh and tank position.

2.3.5 Numerical simulation

Two of the experimental runs described above were taken for comparison with results from computer simulations. As part of the research on liquid sloshing in spin-stabilized satellites, two codes have been developed: the first one, STRUCTURE, calculates the flexible system dynamics and the second, SLOSH3D, computes the sloshing motion of the fluid inside the tank.

These two codes have been integrated into one unit, where the two can exchange information about the tank-fluid system. At each time step of the calculations, the instantaneous positions, velocities, and accelerations (in the three coordinate directions) of the tank are passed on from STRUCTURE to SLOSH3D. Similarly, STRUCTURE gets the location of the mass center and the six components of moments of inertia of the liquid, as input at the beginning of every time step.

One of the primary inputs to the numerical computations is the rotational speed of the test rig as a function of time. The data obtained from the experiment were smoothed to remove measurement noise before being input to the numerical computations. This was done to minimize possible numerical instabilities due to the oscillatory data. Figure 2.22 a shows the data that was experimentally measured and the smoothed data that were input to the computations.

The computations were performed on a Cray Y-MP and took approximately 200 minutes of CPU time for each spin-up calculation. The calculations involved marching the solution in time for 3000 timesteps (each equal to 0.001 seconds) corresponding to a total time of 3.0 seconds of the actual spin-up experiment.

2.3.6 Discussion of results

Two computer runs were attempted: one for the final spin-up speed of 60 RPM and the other for 30 RPM. As the trend of the computed results was similar in both the cases, only one of them (corresponding to a final spin-up speed of 60 RPM) is discussed here.

Figure 2.22 shows the comparison of the computed and experimentally measured results for the 60 RPM case. Figure 2.22b shows the comparison of the free surface positions (inboard and outboard) between the experimental and computed results for the 60 RPM case. It can be seen that the transients compare reasonably well for the inboard end. The outboard data do not compare as well (this aspect is discussed later in more detail).

Figure 2.22c shows the comparison between the experimental and numerically computed radial positions of the tank center. It can be seen that the comparison is reasonably good.

The difference in the final outboard free-surface position between the experiment and the numerical computation is due to several factors, the more important of these being the experimental uncertainties in measuring the free-surface position, the uncertainty in the amount of liquid in the tank (computations assumed a fill ratio of 0.5), and computation of a tank angle that was too small due to the rigid cross-arm assumption. The numerical results also seem to be smoother as compared to the experimental data. This is attributed to the relatively coarse grid used in the computations ($41 \times 11 \times 11$).

The final radial position of the tank appears to have been predicted well by the code. The most significant source of discrepancy in the radial deflection values is

probably due to the assumption made in the STRUCTURE code of a perfectly rigid cross arm on the upper body of the test rig. In reality, a small deflection in this bar most likely results in a relatively large deflection in the tank position.

The rigid cross-arm assumption could also be responsible for the higher frequency of oscillation in the computed case, which can be seen in Fig. 2.22c. The transient oscillations in the first one second of the computed results is due to the initial condition used and the absence of viscous damping. The numerical computations assume that, at time = 0.0 seconds, the tank is at its vertical position without any static load and is suddenly subjected to the load due to the fluid mass at time greater than zero. This is thought to be the main cause of the oscillations seen in the computed results.

2.3.7 Concluding remarks

Given sufficient time and resources, the experimental and computational results for the spin-up case could be brought into even closer agreement. Improvements which could be implemented include: (1) photovoltaic fluid level sensors, which could be calibrated more reliably over a broader range, (2) inclusion of a flexible crossbar in the STRUCTURE code, and (3) a finer grid size for computing high-frequency fluid oscillations in the SLOSH3D code.

PHOTOPOTENTIOMETER 1 CALIBRATION AND CURVE FIT 12-4-92

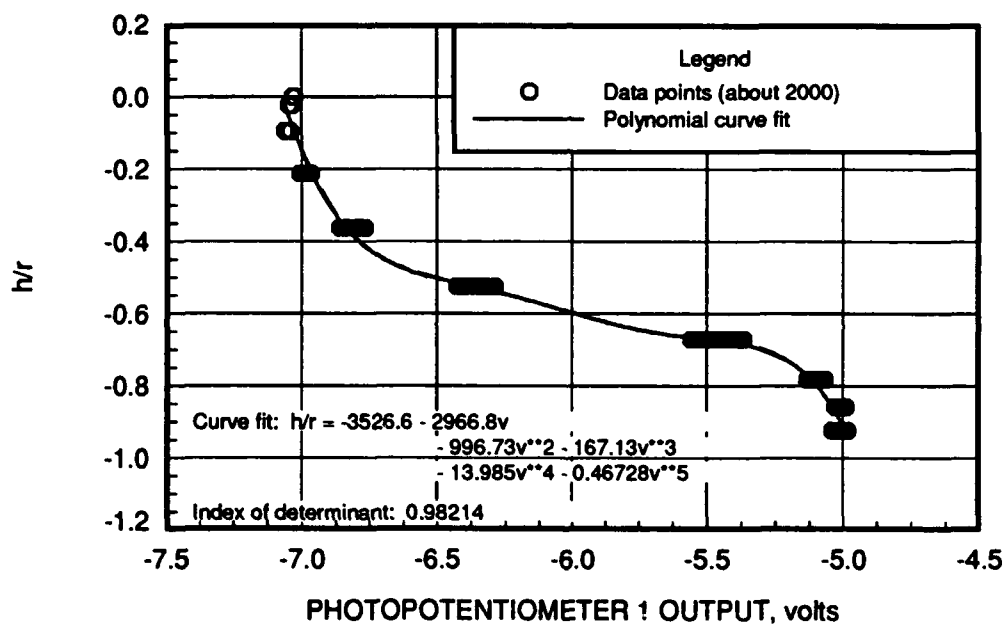


Figure 2.14: Photopotentiometer 1 Calibration

PHOTOPOTENTIOMETER 2 DATA AND CURVE FIT 12-4-92

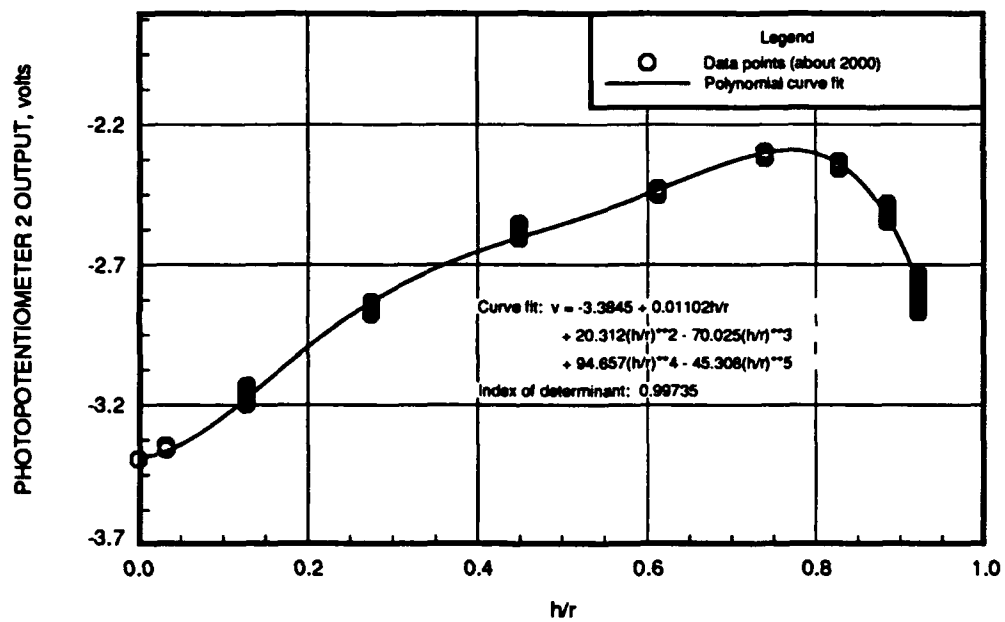


Figure 2.15: Photopotentiometer 2 Calibration

TACHOMETER CALIBRATION AND CURVE FIT 12-4-92

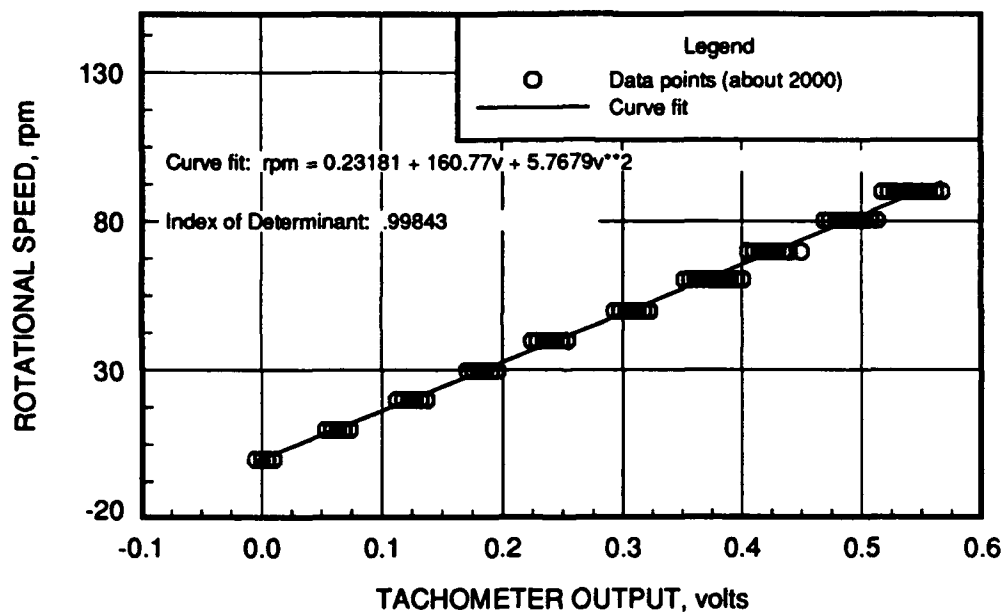


Figure 2.16: Tachometer Calibration

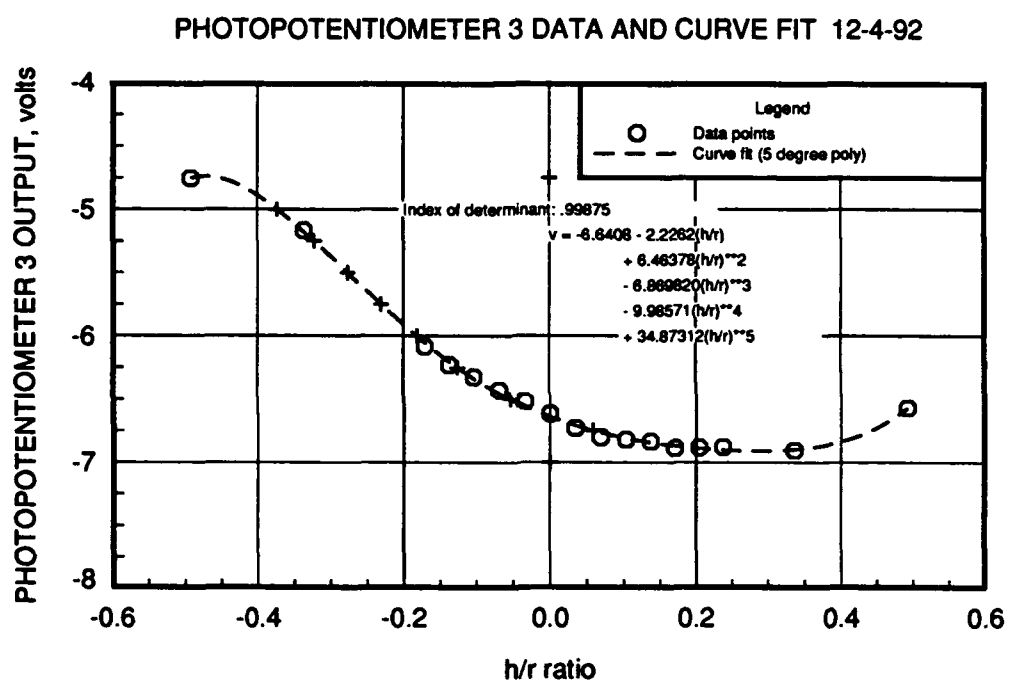


Figure 2.17: Photopotentiometer 3 Calibration

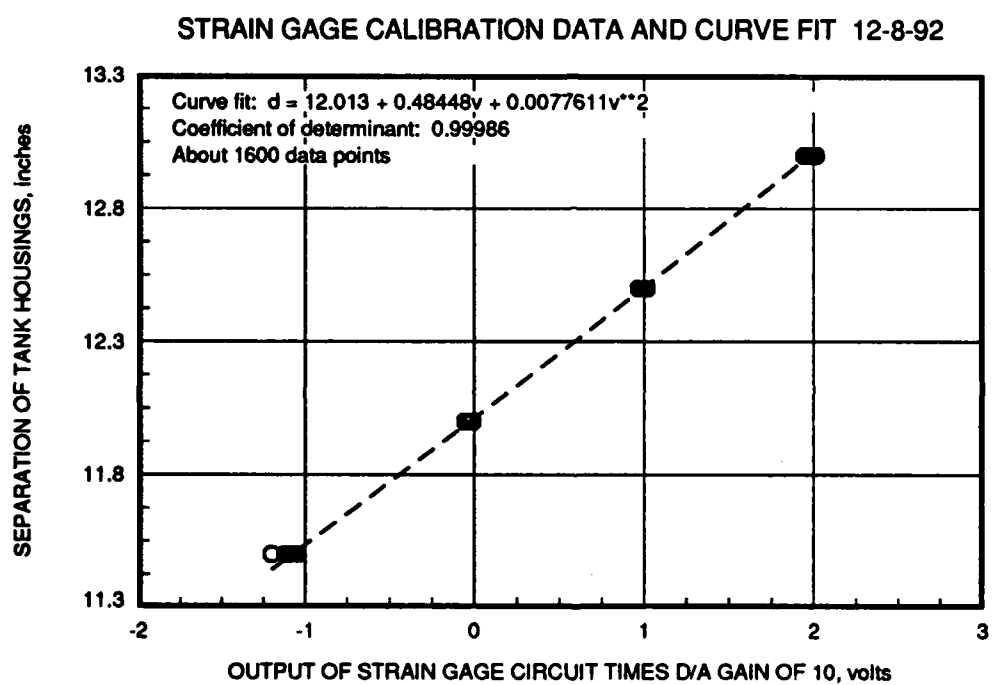


Figure 2.18: Strain Gage Calibration

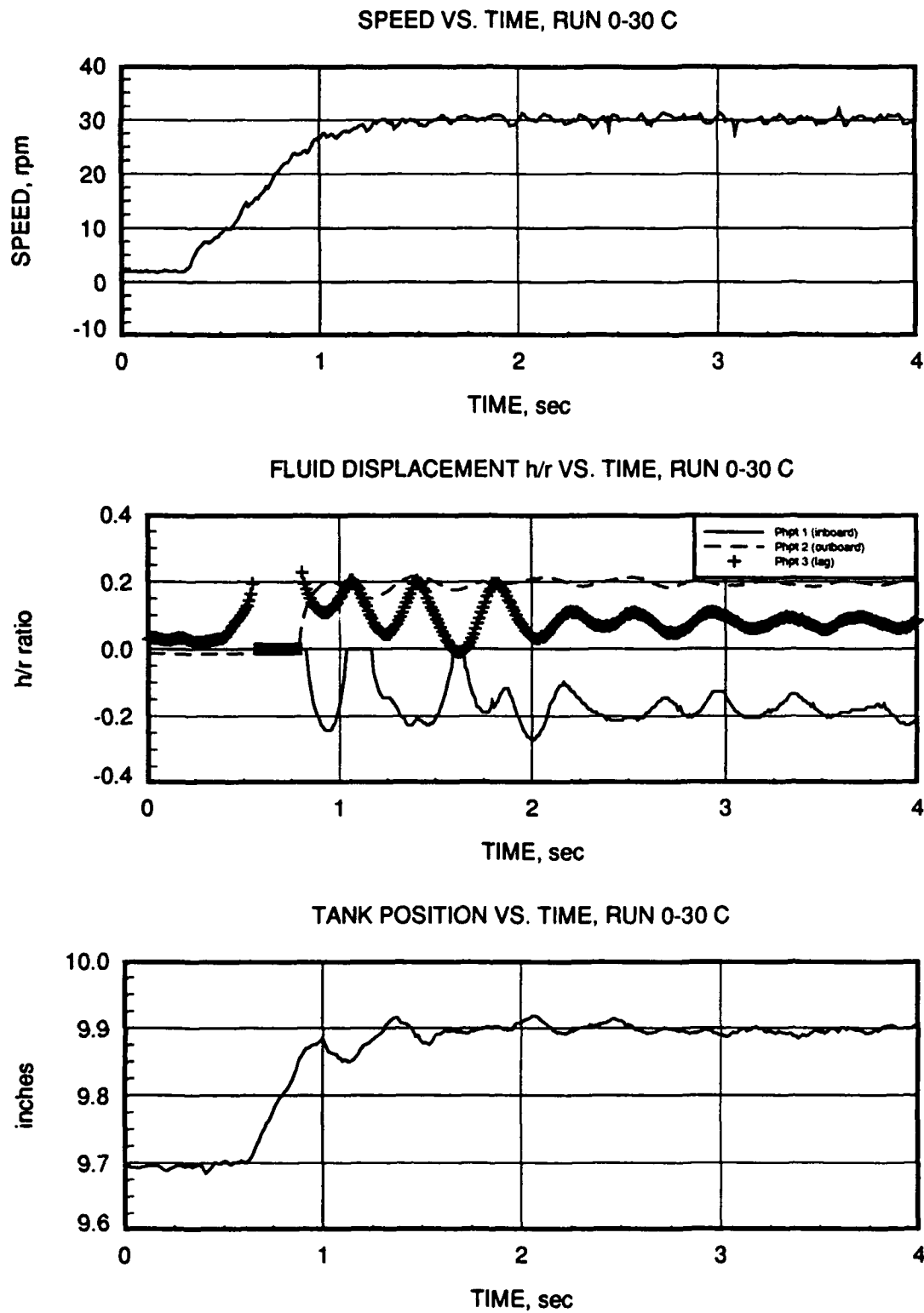


Figure 2.19: Results of Spin-up of 0 to 30 rpm: trial A.

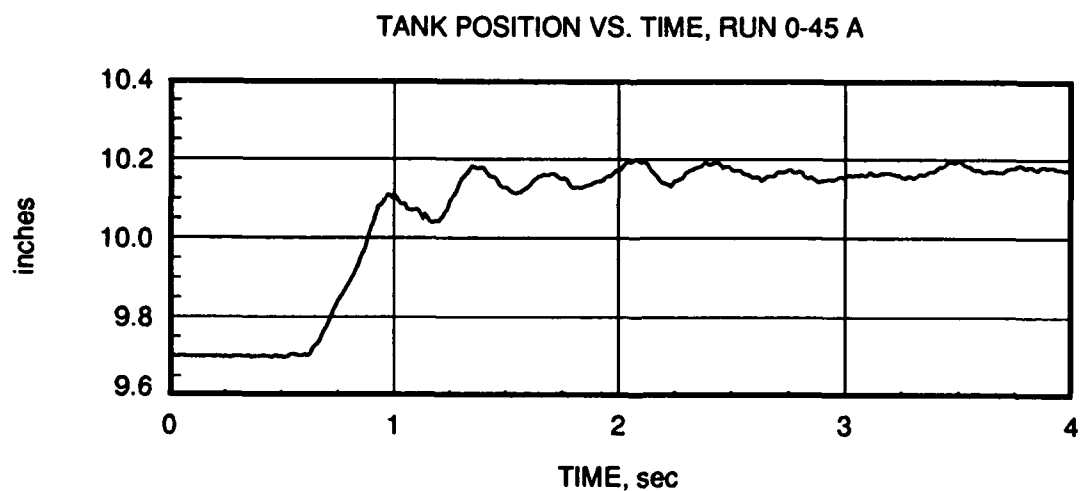
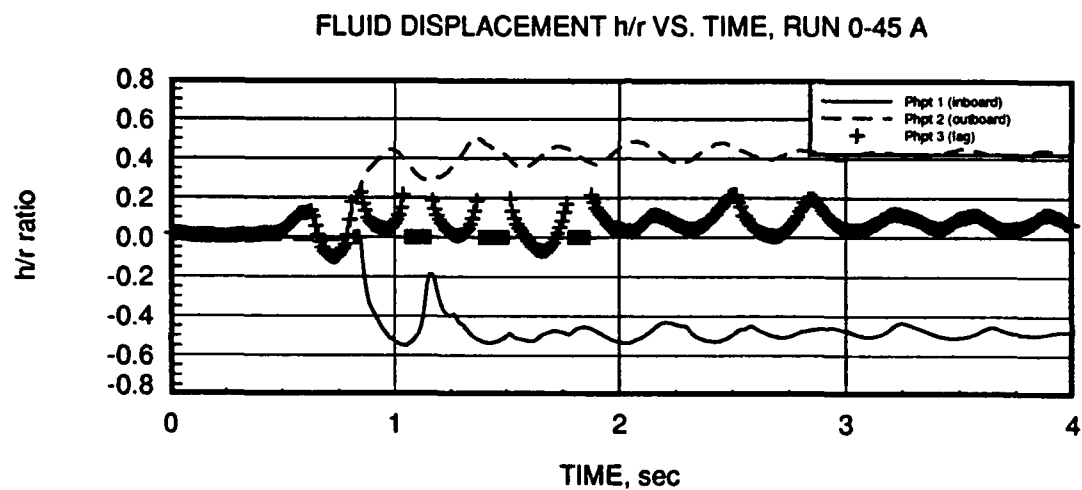
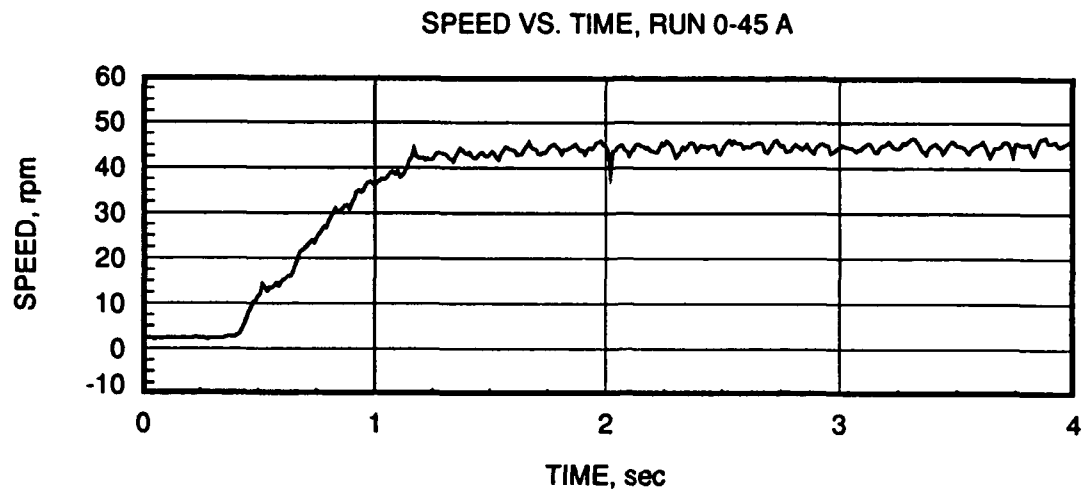


Figure 2.20: Results of Spin-up of 0 to 45 rpm, trial A

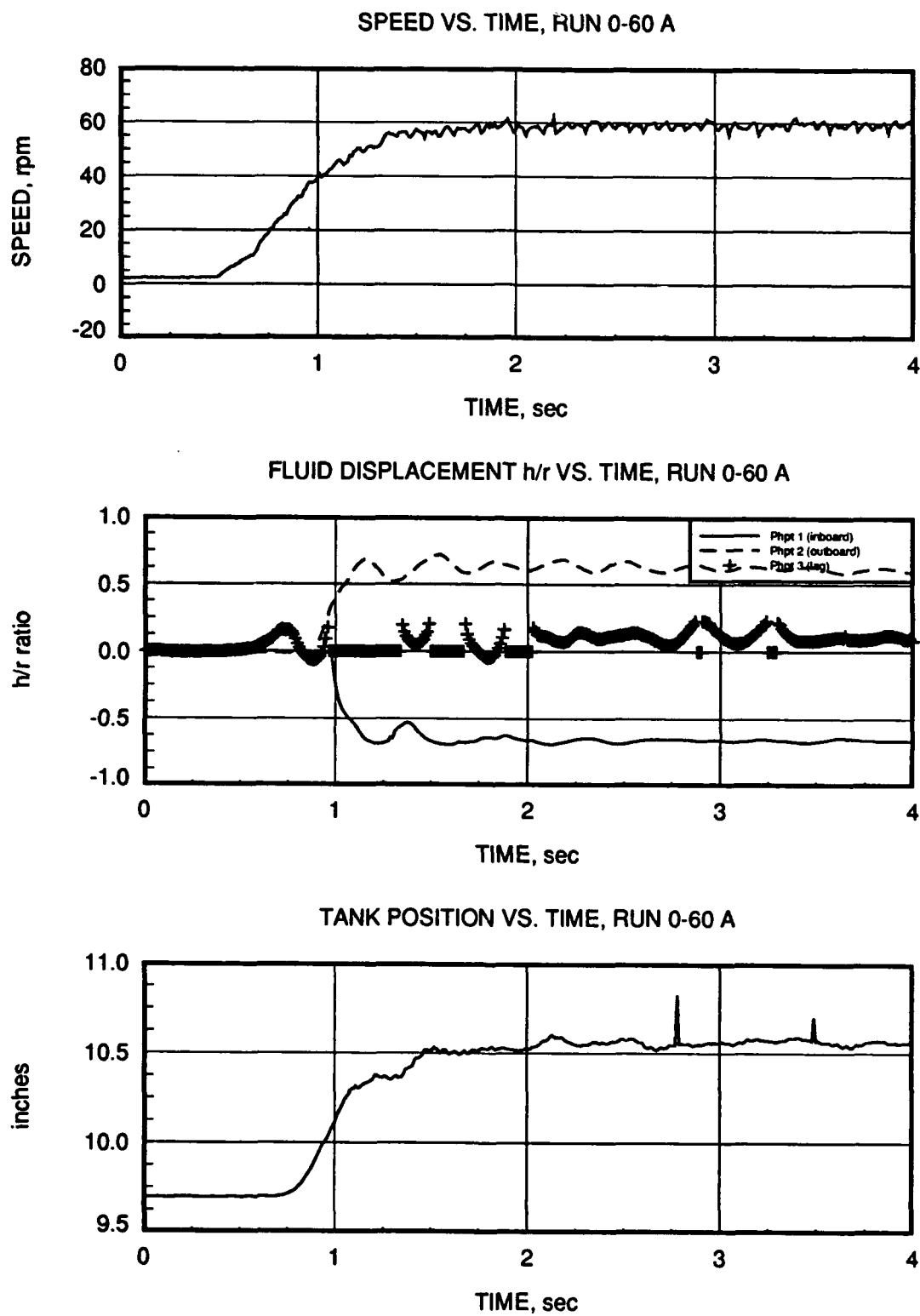


Figure 2.21: Results of Spin-up of 0 to 60 rpm, trial A

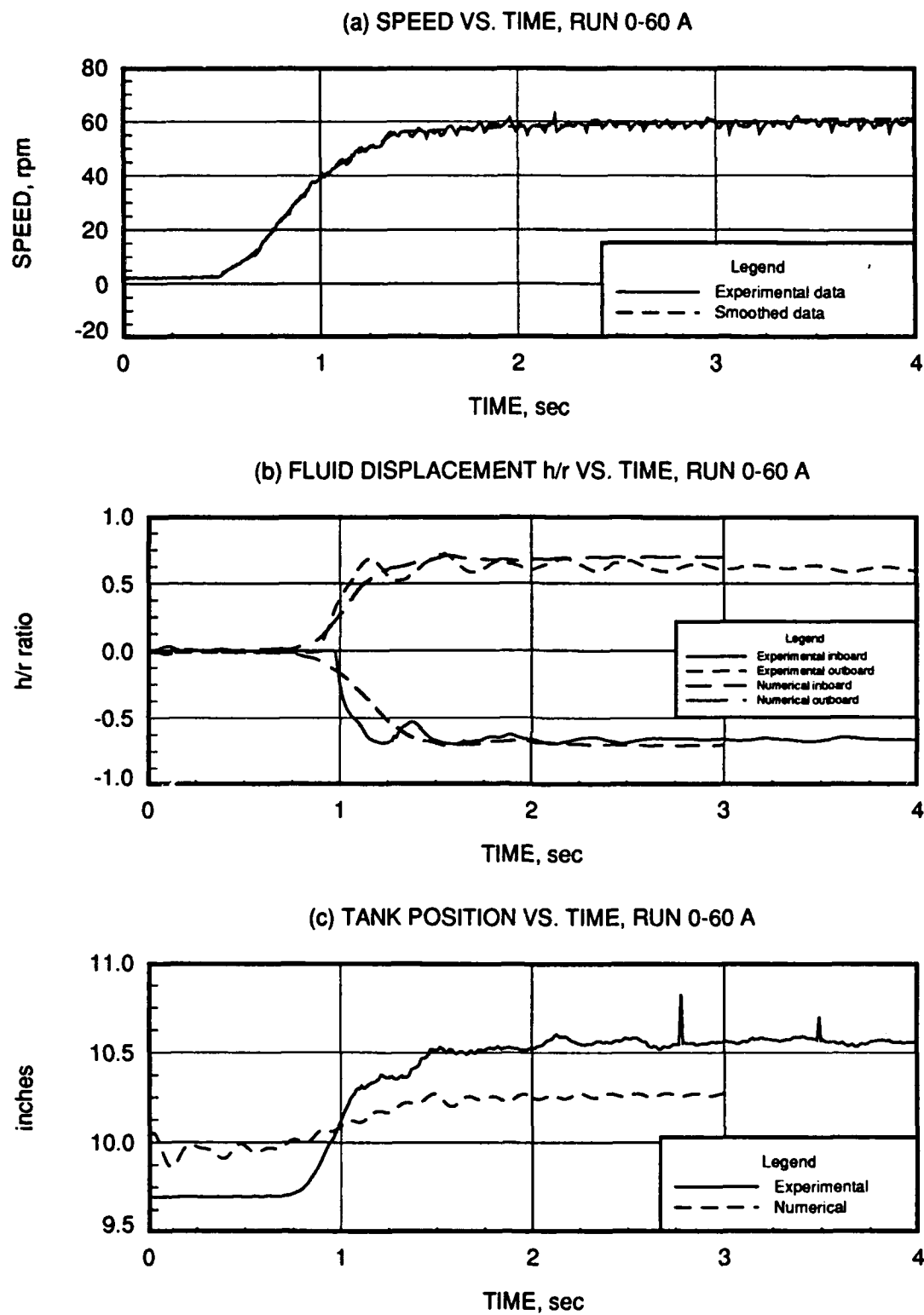


Figure 2.22: Comparison of numerical and experimental results of spin-up of 0 to 60 rpm: trial A.

BIBLIOGRAPHY

- [1] Anderson, D.A., J.C. Tannehill, and R.H. Pletcher (1984). *Computational Fluid Mechanics and Heat Transfer*, McGraw-Hill Book Co., New York.
- [2] Antontsev, S.N, Kazhikhov, A.V., and V.N. Monakhov (1990). *Boundary Value Problems in Mechanics of Nonhomogeneous Fluids*, North-Holland, Amsterdam.
- [3] Baumgarten, J.R., Flugrad, D.R., and J.M. Prusa (1989). "Investigation of Liquid Sloshing in Spin-Stabilized Satellites," ISU-ERI-Ames-90401, Iowa State University.
- [4] Baumgarten, J.R., Flugrad, D.R., and R.H. Pletcher (1990). "Investigation of Liquid Sloshing in Spin-Stabilized Satellites," ISU-ERI-Ames-90410, Iowa State University.
- [5] Baumgarten, J.R., Flugrad, D.R., and R.H. Pletcher (1991). "Investigation of Liquid Sloshing in Spin-Stabilized Satellites," ISU-ERI-Ames-92400, Iowa State University.
- [6] Chorin, A.J. (1967). "A Numerical Method for Solving Incompressible Viscous Flow Problems," *Journal of Computational Physics*, Vol. 2: 12 - 26.
- [7] Hirt, C.W., and B.D. Nichols (1981). "Volume of Fluid (VOF) Method for the Dynamics of Free Boundaries." *Journal of Computational Physics*, Vol. 39: 201-225.
- [8] Huerta, A., and W.K. Liu (1988). "Viscous Flow with Large Free Surface Motion," *Computer Methods in Applied Mechanics and Engineering*, Vol. 69: 277-324.
- [9] Jun, L. and D.B. Spalding (1988). "Numerical Simulation of Flows with Moving Interfaces." *PhysicoChemical Hydrodynamics*, Vol. 10, No. 5/6: 625-637.
- [10] Martin, J.C, and W.J. Moyce (1952). "An Experimental Study of the Collapse of Liquid Columns on a Rigid Horizontal Plane," *Phil. Trans. Royal Soc. London, Ser. A*, Vol. 244: 312-324.

- [11] Maxwell, T.T. and D.B. Spalding (1987). "Numerical Modelling of Free Surface Flows," in *Numerical Methods for Transient and Coupled Problems*, edited by R.W. Lewis, E. Hinton, and B.A. Schrefler, John Wiley & Sons, Ltd.
- [12] Simon, J. (1990). "Nonhomogeneous Viscous Incompressible Fluids: Existence of Velocity, Density, and Pressure" *SIAM J. Math. Anal.*, Vol. 21, No. 5: 1093-1117.
- [13] Stoker, J.J. (1957). *Water Waves*, Interscience Publishers Inc., New York.
- [14] Yoon, S., Kwak, D., and L. Chang (1989). "LU-SGS Implicit Algorithm for Three-Dimensional Incompressible Navier-Stokes Equations with a Source Term," AIAA Paper 89-1964-CP.

**APPENDIX A. Computer Simulation of a Test Rig to Model Sloshing
in Spin-Stabilized Satellites.**

Computer Simulation of a Test Rig to Model Sloshing in Spin-Stabilized Satellites

D. R. Flugrad
Iowa State University,
Ames, IA

L. A. Obermaier
Caterpillar Inc.,
Peoria, IL

Certain communications satellites carry liquid stores on board for station tending and attitude adjustment. However, sloshing of the liquid can cause an undesirable nutational motion of the spin-stabilized vehicle. In previous work a test rig was designed, built and instrumented to study the interaction between the rotating structure and liquid. To augment that experimental project, a computer model of the test rig has been developed to simulate the dynamic motion of the system for various parameter values. The sloshing liquid was replaced by a two degree-of-freedom pendulum in the mathematical model. Simulation results were compared with those from a general multibody dynamics program and with experimental measurements of the test rig motion to demonstrate the mathematical model's validity. Good agreement was achieved in both instances.

Introduction

Extensive research, both analytical and experimental, has been conducted on the stability of spacecraft having liquid propellant stores. A rigid body can be stabilized by spinning about an axis of either maximum or minimum moment of inertia. Common examples of spin stabilization about an axis of minimum moment of inertia include a spinning top or a football. However, systems containing a significant amount of liquid mass, such as the INTELSAT IV (Martin, 1971 and Slabinski, 1978) and the STAR 48 (Hill, 1985) communications satellites, as well as the XM761 artillery projectile (Miller, 1982), have experienced instability when spun about an axis of minimum moment of inertia. Sloshing of liquid payloads has been suspected of causing instability of the spin-stabilized bodies.

Viscous dissipation resulting from relative movement between a liquid and its container tends to reduce the kinetic energy of a system. The body, attempting to conserve angular momentum, is then forced to seek a lower energy state. For a given amount of angular momentum, spin about an axis of maximum moment of inertia represents the minimum energy state possible. If a body spun about its axis of minimum moment of inertia experiences energy dissipation, it will seek the lower energy state and will end up spinning about its axis of maximum moment of inertia if unrestrained. This is known as a flat spin.

Agrawal (1981) states that for a body with flexible elements, the ratio of the moment of inertia of the spin axis to that of the transverse axis must be greater than one for stability. Thus, to be stable, a body containing liquid must be spun about an axis of maximum moment of inertia.

Several launchings of the STAR 48 communications satellites

resulted in a coning motion of the spacecraft. Hill (1985) used an equivalent mechanical pendulum model, along with a mass representing the main body and rocket motor to approximate the STAR 48 system. He developed control laws using linearized equations of motion.

The INTELSAT IV communications satellite also experienced instability once launched. Slabinski (1978) conducted in-orbit testing of the satellite, as well as a theoretical analysis, to study the sloshing phenomenon inside the tanks containing liquid propellant. He developed relationships between driving frequencies and nutation frequencies. Martin (1971) experimented with tanks of liquid propellant on earth. Martin, through his experimental investigations, found that when a spinning tank is subjected to angular oscillations about an axis which is not parallel to an axis of symmetry of the tank, turbulent fluid motion is excited. However, when the tank is accelerated rectilinearly, the motion of its contents is relatively calm, like that of a rigid body. Because a sphere is axisymmetric, liquid in a sphere did not experience the turbulent motion that it did in differently shaped tanks. In the spherical tanks, the liquid behaved like a pendulous rigid body.

Many analytical attempts to quantify the movement of liquids in tanks have used a pendulum analogy. Such an analogy assumes that the liquid inside the tank moves as a spherical pendulum would under the same conditions. Sumner (1965) developed relations to describe a pendulum representing the liquid in spherical and oblate spheroidal nonrotating tanks as a function of tank geometry and fill fraction. The mass of the pendulum is not equal to the mass of the liquid in the tank. A nonsloshing mass is fixed at approximately the center of the tank. The sum of the nonslosh mass and the pendulum mass is equal to the total liquid mass. Sayar and Baumgarten (1982) included a rotational damper and a cubic spring in their pendulum analogy to improve Sumner's model in the nonlinear range.

Zedd and Dodge (1985) examined the energy dissipated by

Contributed by the Dynamic Systems and Control Division for publication in the JOURNAL OF DYNAMIC SYSTEMS, MEASUREMENT, AND CONTROL. Manuscript received by the Dynamic Systems and Control Division November 1989; revised manuscript received April 1992. Associate Technical Editor: N. S. Nairao.



Fig. 1 Schematic of mechanical system

liquids in rotating spherical tanks using a pendulum analogy. Their model included a pendulum, a rotor, and a viscous dashpot. Through this analogy, they developed equations for natural frequencies of the pendulum as functions of tank location, tank fill fraction, and the spin rate of the tank.

Cowles (1987) built a test rig to model a satellite containing liquid fuel stores. His model consisted of a motor driven shaft which supported a semi-rigid assembly. The assembly was connected to the vertical input shaft by a Hooke's type universal joint. The assembly held two tanks which were partially filled with water. By altering the location of the tanks and the dimensions of the assembly, Cowles was able to achieve a variety of test conditions, including spin about axes of maximum, intermediate, and minimum moments of inertia. When spun about an axis of maximum moment of inertia, the assembly was extremely stable, even when perturbed. The assembly, however, fell immediately into a flat spin when spun about an axis of intermediate moment of inertia. Though a configuration was designed and built for spin about an axis of minimum moment of inertia, tests were never completed because it was felt the assembly might be damaged in a collision with the supporting structure if it attempted to go into a flat spin.

Anderson (1988) redesigned the mechanical assembly built by Cowles. Anderson's assembly included a restricting collar so that even an unstable test assembly could not damage itself or the supporting structure. The redesign included instrumentation in order to acquire quantitative measurements of the motion of the assembly and the liquid contained in it. Just as predicted, Anderson found the case of spin about an axis of minimum moment of inertia to be unstable.

The work described in this study develops the equations of motion for the test rig designed and constructed by Cowles and Anderson. Equations of motion were derived using Lagrange's equations. State variables were chosen to best match the quantities measured by Anderson's instrumentation.

The liquid in each of the tanks was modeled as a two degree-of-freedom pendulum. This approach can only account for free surface liquid oscillations which will have natural frequencies greater than the coning frequency for the test rig. In order to account for lower liquid oscillation frequencies of the type associated with internal or inertial waves, a more complete model would have to be used. This would be important, for instance if one wanted to study oscillations strongly coupled to the coning motion.

The equations of motion developed for the pendulum analogy were numerically integrated. Results of the numerical simulation were compared with those from an existing rigid body dynamic analysis program to verify the validity of the nu-

merical simulation. Simulation results were also compared with Anderson's experimental results.

Development of Equations

A schematic drawing of the mechanical system modeled is shown in Fig. 1. The model contains four rigid bodies. A lower shaft which rotates in pillow block bearings supports the structure. The upper assembly is connected to the lower shaft by a Hooke's type universal joint. Two pendula, each with two degree-of-freedom motion representing the sloshing liquid, are symmetrically attached to the centers of the tanks. The pendula are assumed to be point masses suspended from the upper assembly by rigid, massless rods.

A note of clarification is perhaps necessary to define terminology of bodies in the system. The "test rig" is defined as the structure that encloses the liquid and its associated supports, as well as the contained fluid. This basically includes everything supported by the universal joint on the mechanical assembly. The "upper assembly" is associated with the mathematical model and does not have a direct physical representation. The upper assembly is defined as the test rig minus the enclosed liquid plus the nonslosh masses.

To develop the equations of motion for the system, a Lagrangian formulation was used. Through the use of coordinate transformations, position vectors were determined for each of the bodies. The position vectors were then differentiated with respect to time to determine velocities for the bodies. The kinetic and potential energies of the bodies were then developed. Once the equations of motion were determined according to Lagrange's equations, they were numerically integrated using a double precision version of DIFFEQ, a numerical integration program.

Coordinate Transformations and Body Positions. The positions of the bodies were determined through simple coordinate transformations consisting of rotations and translations of Cartesian coordinates. All coordinate systems used were defined to be right-handed.

The \hat{x}_1 - \hat{y}_1 - \hat{z}_1 coordinate system is stationary and is positioned at the center of the universal joint. The \hat{z}_1 axis is directed vertically upward. Positioning of the \hat{x}_1 and \hat{y}_1 axes is arbitrary.

Transformation to the \hat{x}_2 - \hat{y}_2 - \hat{z}_2 coordinate system is achieved by a right hand rotation about the \hat{z}_1 axis. The \hat{x}_2 - \hat{y}_2 - \hat{z}_2 coordinate system is attached to the lower shaft of the test rig and its origin is at the center of the universal joint. The \hat{x}_2 - \hat{y}_2 - \hat{z}_2 axes are fixed in such a way that when the \hat{z}_1 and \hat{z}_2 axes are aligned, the \hat{y}_2 components of the position vectors of the pendulum supports are zero. Generally, the matrix $[A_{12}]$ is defined such that

$$\begin{Bmatrix} \hat{x}_1 \\ \hat{y}_1 \\ \hat{z}_1 \\ 1 \end{Bmatrix} = [A_{12}] \begin{Bmatrix} \hat{x}_2 \\ \hat{y}_2 \\ \hat{z}_2 \\ 1 \end{Bmatrix} \quad (1)$$

The transformation matrix from the \hat{x}_2 - \hat{y}_2 - \hat{z}_2 coordinate system to the \hat{x}_3 - \hat{y}_3 - \hat{z}_3 coordinate system, $[A_{13}]$, is given in the Appendix.

The rotation of the upper assembly relative to the lower shaft is defined by the two rotation angles, λ . First, a rotation by an amount λ_1 about the \hat{y}_2 axis defines the transformation to the \hat{x}_3 - \hat{y}_3 - \hat{z}_3 coordinate system. Then the coordinate system is rotated through an angle λ_2 about the \hat{x}_3 axis to arrive at the \hat{x}_4 - \hat{y}_4 - \hat{z}_4 system.

The \hat{x}_4 - \hat{y}_4 - \hat{z}_4 coordinate system is fixed to the upper assembly in such a way that the \hat{y}_4 components of the position vectors from the universal joint to the pendulum supports is zero. The origins of the \hat{x}_3 - \hat{y}_3 - \hat{z}_3 and \hat{x}_4 - \hat{y}_4 - \hat{z}_4 systems are located at the center of the universal joint. The rotations between the 2, 3, and 4 coordinate systems are shown in Fig. 1.

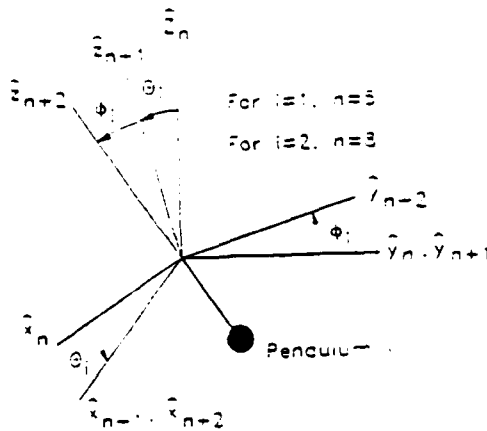


Fig. 2 Rotation coordinates for pendulums

Because the body is assumed to be axisymmetric, the position vector of the upper assembly is given by

$$r_{ua} = \rho \hat{z}_4 \quad (2)$$

where ρ is defined to be the height of the center of gravity of the upper assembly above the universal joint when λ_1 and λ_2 are equal to zero.

The pendula, which represent the water in the spherical tanks, are displaced from the universal joint. The physical constants r and (cg) are defined such that the position vector of the support of pendulum 1 is $r\hat{x}_4 - (cg)\hat{z}_4$. Consequently, the origin of the $\hat{x}_1\text{-}\hat{y}_1\text{-}\hat{z}_1$ system is defined to be at $r\hat{x}_4 - (cg)\hat{z}_4$. This is the location of the hinge point of pendulum 1, and also the location of one of the nonslough masses of the upper assembly. Similarly, the origin of the $\hat{x}_2\text{-}\hat{y}_2\text{-}\hat{z}_2$ system is located at $-r\hat{x}_4 - (cg)\hat{z}_4$, which is the location of the hinge point of the second pendulum, as well as the second nonslough mass. There are no relative rotations for the $\hat{x}_1\text{-}\hat{y}_1\text{-}\hat{z}_1$, $\hat{x}_2\text{-}\hat{y}_2\text{-}\hat{z}_2$, and $\hat{x}_3\text{-}\hat{y}_3\text{-}\hat{z}_3$ coordinate systems.

The radial rotation of the pendula are defined by the angles, θ . The angle θ_1 is defined by right hand rotation of the $\hat{x}_4\text{-}\hat{y}_4\text{-}\hat{z}_4$ system, about the \hat{y}_1 axis. In a parallel fashion, the angle θ_2 is defined by right-hand rotation of the $\hat{x}_4\text{-}\hat{y}_4\text{-}\hat{z}_4$ system about the \hat{y}_2 axis. Note that if both pendula are flared outward from the universal joint by an amount θ , then $\theta_1 = -\theta$ while $\theta_2 = -\theta$.

Circumferential (or tangential) rotations of the pendula are described by the ϕ angles. The $\hat{x}_1\text{-}\hat{y}_1\text{-}\hat{z}_1$ axes are rotated through the angle ϕ_1 about the \hat{x}_4 axis. The $\hat{x}_2\text{-}\hat{y}_2\text{-}\hat{z}_2$ coordinate system is fixed to pendulum 1. Similarly, the $\hat{x}_{10}\text{-}\hat{y}_{10}\text{-}\hat{z}_{10}$ axes, which are fixed to pendulum 2, are rotated through an angle ϕ_2 about the \hat{x}_9 axis. Rotations of the pendula relative to the upper assembly are represented in Fig. 2.

The local position vectors of the pendula, r_{p1} and r_{p2} are easily defined as

$$r_{p1} = -l\hat{z}_1 \quad (3)$$

and

$$r_{p2} = -l\hat{z}_{10} \quad (4)$$

where l is the length of the pendulum. This length is a function of tank size, tank shape, and fill height.

By direct substitution, the position vectors of the bodies can be expressed in terms of world coordinates. Thus,

$$\begin{Bmatrix} \hat{x}_1 \\ \hat{y}_1 \\ \hat{z}_1 \\ 1 \end{Bmatrix} = [A_{12}][A_{23}][A_{34}] \begin{Bmatrix} \hat{x}_4 \\ \hat{y}_4 \\ \hat{z}_4 \\ 1 \end{Bmatrix} \quad (5)$$

The overall transformation matrix, $[A_{14}]$, is simply the product

given by $[A_{12}][A_{23}][A_{34}]$. Since $r_{ua} = \rho\hat{z}_4$, it can be expressed as

$$\begin{aligned} r_{ua} = & \rho(\cos \psi \sin \lambda_1 \cos \lambda_2 + \sin \psi \sin \lambda_2)\hat{x}_1 \\ & + \rho(\sin \psi \sin \lambda_1 \cos \lambda_2 - \cos \psi \sin \lambda_2)\hat{y}_1 \\ & + \rho \cos \lambda_1 \cos \lambda_2 \hat{z}_1 \end{aligned} \quad (6)$$

In similar fashion,

$$\begin{Bmatrix} \hat{x}_1 \\ \hat{y}_1 \\ \hat{z}_1 \\ 1 \end{Bmatrix} = [A_{12}][A_{23}][A_{34}][A_{45}][A_{56}][A_{67}] \begin{Bmatrix} \hat{x}_7 \\ \hat{y}_7 \\ \hat{z}_7 \\ 1 \end{Bmatrix} \quad (7)$$

and

$$\begin{Bmatrix} \hat{x}_1 \\ \hat{y}_1 \\ \hat{z}_1 \\ 1 \end{Bmatrix} = [A_{12}][A_{23}][A_{34}][A_{45}][A_{49}][A_{9,10}] \begin{Bmatrix} \hat{x}_{10} \\ \hat{y}_{10} \\ \hat{z}_{10} \\ 1 \end{Bmatrix} \quad (8)$$

The position vectors r_{p1} and r_{p2} , expressed in terms of world coordinates, are presented in the Appendix.

Body Velocities and Energies. The translational velocities of the center of mass of the upper assembly and the two pendula can be determined by differentiating their position vectors with respect to time. Using the chain rule of calculus,

$$\mathbf{v} = \frac{d\mathbf{r}}{dt} = \sum_{i=1}^n \frac{\partial \mathbf{r}}{\partial q_i} \frac{dq_i}{dt} \quad (9)$$

Thus, differentiation of Eq. (6) produces

$$\begin{aligned} \mathbf{v}_{ua} = & \rho[\dot{\psi}(\cos \psi \sin \lambda_2 - \sin \psi \sin \lambda_1 \cos \lambda_2) \\ & - \dot{\lambda}_1 \cos \psi \cos \lambda_1 \cos \lambda_2 \\ & - \dot{\lambda}_2(-\cos \psi \sin \lambda_1 \sin \lambda_2 - \sin \psi \cos \lambda_2)]\hat{x}_1 \\ & - \rho[\dot{\psi}(\cos \psi \sin \lambda_1 \cos \lambda_2 - \sin \psi \sin \lambda_2) \\ & - \dot{\lambda}_1 \sin \psi \cos \lambda_1 \cos \lambda_2 \\ & - \dot{\lambda}_2(-\cos \psi \cos \lambda_2 - \sin \psi \sin \lambda_1 \sin \lambda_2)]\hat{y}_1 \\ & - \rho(\dot{\lambda}_1 \sin \lambda_1 \cos \lambda_2 - \dot{\lambda}_2 \cos \lambda_1 \sin \lambda_2)\hat{z}_1 \end{aligned} \quad (10)$$

Velocity vectors of the pendula are determined in an identical fashion. Due to their lengthiness, however, they are shown in the Appendix rather than here.

Using the addition theorem for angular velocities, the angular velocity of the upper assembly can be expressed as a sum of simple components as

$$\omega_{ua} = \dot{\psi}\hat{z}_1 + \dot{\lambda}_1\hat{y}_2 + \dot{\lambda}_2\hat{x}_3 \quad (11)$$

or expressed in terms of body fixed axes:

$$\begin{aligned} \omega_{ua} = & (-\dot{\psi} \sin \lambda_1 + \dot{\lambda}_2)\hat{x}_4 \\ & - (\dot{\psi} \cos \lambda_1 \sin \lambda_2 + \dot{\lambda}_1 \cos \lambda_2)\hat{y}_4 \\ & + (\dot{\psi} \cos \lambda_1 \cos \lambda_2 - \dot{\lambda}_1 \sin \lambda_2)\hat{z}_4 \end{aligned} \quad (12)$$

The inertia dyadic of the upper assembly, I_{ua} can be expressed as

$$\begin{aligned} I_{ua} = & I_{xx}\hat{x}_4\hat{x}_4 + I_{yy}\hat{y}_4\hat{y}_4 + I_{zz}\hat{z}_4\hat{z}_4 \\ & + I_{xy}(\hat{x}_4\hat{y}_4 + \hat{y}_4\hat{x}_4) + I_{yz}(\hat{y}_4\hat{z}_4 + \hat{z}_4\hat{y}_4) \end{aligned} \quad (13)$$

where I_{xi} is defined to be the inertia scalar of the upper assembly relative to its center of gravity for unit vectors \hat{x}_4 and \hat{y}_4 . Note that the body is assumed to have zero products of inertia about its center of gravity for the \hat{x}_4 and \hat{z}_4 axes.

The angular velocity of the lower shaft is simply

$$\omega_{ls} = \dot{\psi}\hat{z}_1 \quad (14)$$

Table 1 Test rig data for comparison between CAMS and SATELL. For these runs the transverse principal moments of inertia were both equal to I_r .

run	total mass	sphere diam	% fill	r	(cg)	spin speed	I_r	I_z
	slug	ft		ft	ft	rpm	slug ft ²	slug ft ²
1S	2.0	1	50	1	0	100	2.22	1.39
1C	2.0	1	50	1	0	100	2.22	1.39
3S	2.0	1	50	1	0	100	2.08	3.47
3C	2.0	1	50	1	0	100	2.08	3.47

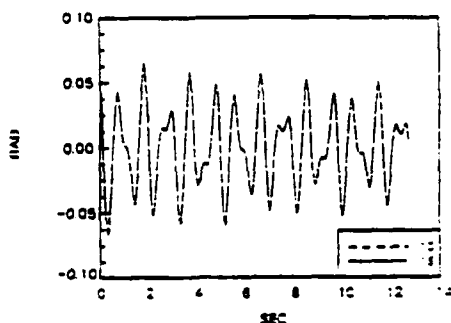


Fig. 3 Comparison of upper assembly rotation given by λ_1 for CAMS Case 1C and SATELL Case 1S

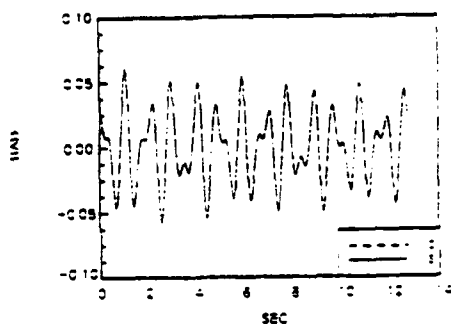


Fig. 4 Comparison of upper assembly rotation given by λ_2 for CAMS Case 1C and SATELL Case 1S

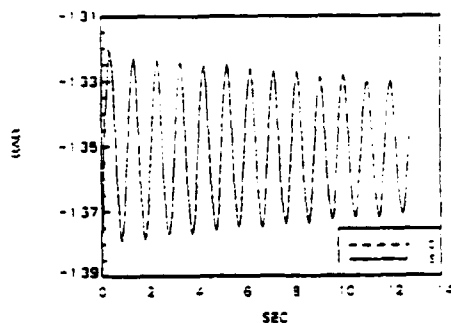


Fig. 5 Comparison of radial rotation of pendulum 1 given by θ_1 for CAMS Case 1C and SATELL Case 1S

The relevant term of the inertia dyadic for the lower shaft is the moment of inertia of the shaft about the \hat{z}_1 axis, I_{1s} . Because the pendula are assumed to be point masses, their inertia dyadics are zero.

The kinetic energy, T , of the system can now be calculated by summing the rotational and translational kinetic energies of all the bodies:

$$T = \frac{1}{2} m_s \dot{\mathbf{v}}_{p1} \cdot \dot{\mathbf{v}}_{p1} + \frac{1}{2} m_s \dot{\mathbf{v}}_{p2} \cdot \dot{\mathbf{v}}_{p2} + \frac{1}{2} m_{ue} \dot{\mathbf{v}}_{ue} \cdot \dot{\mathbf{v}}_{ue} - \frac{1}{2} \omega_{ue} \cdot \mathbf{I}_{ue} \omega_{ue} - \frac{1}{2} \omega_{1s} \cdot \mathbf{I}_{1s} \omega_{1s} \quad (15)$$

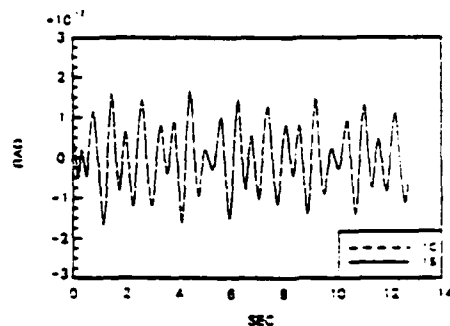


Fig. 6 Comparison of circumferential rotation of pendulum 1 given by ϕ_1 for CAMS Case 1C and SATELL Case 1S

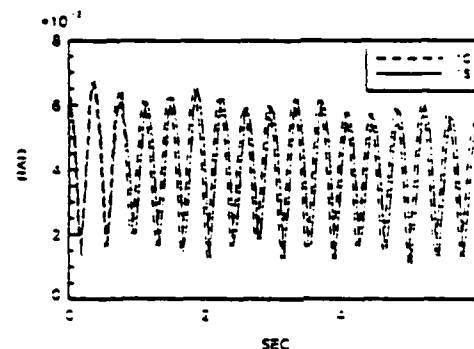


Fig. 7 Comparison of half cone angle, β , for CAMS Case 1C and SATELL Case 1S

where m_s is the mass of a pendulum and m_{ue} is the mass of the upper assembly.

The kinetic energy is expressed in matrix form as

$$T = \frac{1}{2} \{\dot{\mathbf{q}}\}^T [\mathbf{M}] \{\dot{\mathbf{q}}\} \quad (16)$$

where the matrix $[\mathbf{M}]$, shown in the Appendix, is symmetric. The vector $\{\mathbf{q}\}$ is defined as

$$\{\mathbf{q}\} = \begin{Bmatrix} \psi \\ \lambda_1 \\ \lambda_2 \\ \theta_1 \\ \phi_1 \\ \theta_2 \\ \phi_2 \end{Bmatrix} \quad (17)$$

The potential energy, V , of the system is determined from the elevation of each of the bodies. Thus,

$$V = m_{ue} g \rho \cos \lambda_1 \cos \lambda_2 + m_{pg} [l \sin \lambda_1 (\sin \theta_1 \cos \phi_1 + \sin \theta_2 \cos \phi_2) - l \cos \lambda_1 \cos \lambda_2 (\cos \theta_1 \cos \phi_1 + \cos \theta_2 \cos \phi_2) + l \cos \lambda_1 \sin \lambda_2 (\sin \phi_1 + \sin \phi_2) + 2(cg) \cos \lambda_1 \cos \lambda_2] \quad (18)$$

Lagrangian Formulation. The Lagrangian, L , for the system is defined simply as $L = T - V$. Equations of motion can be determined from Lagrange's equations of the second kind as

$$\frac{d}{dt} \left(\frac{\partial L}{\partial \dot{q}_r} \right) - \frac{\partial L}{\partial q_r} = F_{qr}, \quad r = 1, \dots, 7 \quad (19)$$

The generalized force, F_{qr} , due to viscous damping can be expressed as

$$F_{qr} = c_r \dot{q}_r, \quad r = 1, \dots, 7 \quad (20)$$

where c_r is the viscous damping coefficient expressed in dimensions of torque per unit angular velocity.

Table 2 Test rig data for comparison between experimental results and SATELL. For these runs the transverse principal moments of inertia, I_{11} and I_{22} , were slightly different.

run	total mass	height of c.g.	spin speed	I_z	I_{11}	I_{22}
	slug	ft	rpm	slug ft ²	slug ft ²	slug ft ²
1E	0.507	-0.080	-100	0.223	0.343	0.340
1SE	0.507	-0.080	-100	0.223	0.343	0.340
2E	0.431	-0.121	-70	0.324	0.280	0.289
2SE	0.431	-0.121	-70	0.324	0.280	0.289

Substituting $L = T - V$ into Eq. (19) and noting that V does not depend on \dot{q} we have

$$\frac{d}{dt} \left(\frac{\partial T}{\partial \dot{q}_r} \right) - \frac{\partial T}{\partial q_r} + \frac{\partial V}{\partial q_r} = F_{qr} \quad r = 1, \dots, 7 \quad (21)$$

Since $T = 0.5 \{\dot{q}\}^T [M] \{\dot{q}\}$ where $[M]$ does not depend on q , the first term on the left hand side of Eq. (21) is determined by

$$\frac{\partial T}{\partial \dot{q}_r} = [M] \{\dot{q}\} \quad (22)$$

and by the chain rule of calculus,

$$\frac{d}{dt} \left(\frac{\partial T}{\partial \dot{q}_r} \right) = [\dot{M}] \{\dot{q}\} + [M] \{\ddot{q}\} \quad (23)$$

For the second term on the left-hand side of Eq. (21),

$$\frac{\partial T}{\partial q_r} = \frac{1}{2} \sum_{j=1}^7 \frac{\partial M_{ij}}{\partial q_r} \dot{q}_i \dot{q}_j \quad (24)$$

So that the equations of motion become

$$\sum_{j=1}^7 (\dot{M}_{ij} \dot{q}_j + M_{ij} \ddot{q}_j) - \sum_{j=1}^7 \left(\frac{\partial M_{ij}}{\partial q_r} \dot{q}_i \dot{q}_j \right) + \frac{\partial V}{\partial q_r} = F_{qr} \quad r = 1, \dots, 7 \quad (25)$$

These equations are assembled into a matrix form,

$$[\dot{M}] \{\dot{q}\} + [M] \{\ddot{q}\} - [\text{DELM}]^T \{\dot{q}\} - \left\{ \frac{\partial V}{\partial q} \right\} = \{F_q\} \quad (26)$$

where $[\text{DELM}]$ is defined by

$$\text{DELM}_{ij} = \sum_{k=1}^7 \frac{\partial M_{ik}}{\partial q_j} \dot{q}_k \quad (27)$$

This system of equations was numerically integrated using a double precision version of DIFFEQ, a numerical integration program. The user of DIFFEQ must supply a subroutine which computes the derivatives of the state variables with respect to the independent variable, given the current values of the independent variable and the state variable.

Simulation Results

To ensure the accuracy of the equations of motion, simulation results were compared with those from a multibody dynamics program called CAMS. Results were also compared with experimental data.

CAMS (Control Analysis for Mechanical Systems), a three-dimensional multibody program, was used to verify the accuracy of the previously derived equations of motion. To run CAMS, a user creates a data file specifying the type of connection existing between bodies, as well as the inertial properties, initial positions, and initial orientations of all of the bodies in the system.

Because CAMS is more generic than the program tailored

specifically to solve the satellite problem, it was considerably more time consuming to generate an input data file for CAMS than for SATELL, the specific program written for this study. Several runs were completed using CAMS. However, only two representative runs are displayed here for brevity.

The physical values of the test rigs used for the analyses are given in Table 1. I_z is defined as the moment of inertia of the test rig about its spin axis. I_1 is defined as the moment of inertia of the test rig about a transverse axis through its center of gravity. For all runs in this section, the center of gravity of the test rig at its initial speed is located at the universal joint.

Figures 3-7 compare the output of CAMS and SATELL for a case in which half filled, one ft diameter spheres spin about an axis of maximum moment of inertia (specifically, $I_z/I_1 = 1.6$). Results for angles associated with pendulum 2 were very similar to those for pendulum 1, and thus are not displayed. Figure 7 shows the half cone angle versus time for each of the programs, where the half cone angle, β , is defined to be the angle between the \hat{z}_4 and \hat{z}_2 axes. Mathematically,

$$\beta = \cos^{-1}(\cos \lambda_1 \cos \lambda_2) \quad (28)$$

These two runs verify that the motion of the system is stable for spin about the axis of maximum moment of inertia. This can be seen, for example, in Figs. 3 and 4 where the magnitudes of the oscillating upper assembly rotation angles are decreasing with time. The effect of decreasing amplitude with time is even more pronounced for the radial rotation angles for the pendula as illustrated in Fig. 5. More important, however, is the exceptionally close agreement apparent between the CAMS and SATELL simulations. The output motions for the two runs displayed in Figs. 3-6 are so close, in fact, that they are indistinguishable. There is slight disagreement in the half cone angle curves depicted in Fig. 7, but even that difference is very small, with a phase difference of less than 0.01 s appearing early in the simulation.

Figures 8-11 compare the results of CAMS and SATELL for the case of spin about an axis of minimum moment of inertia. Both simulations indicate that the resulting motion is unstable as seen in Fig. 10 where the magnitude of the radial rotation angle for pendulum 2 is increasing with time. Figure 11 shows that the half cone angle also increases as the system seeks to reorient itself to spin about the axis of maximum moment of inertia. Once again, the two simulations agree so well that the pairs of curves plotted in Figs. 8-11 are identical except for a very slight difference that can be detected in the half cone angle of Fig. 11.

Comparison With Experimental Data. To determine the validity of the mathematical model, output from SATELL was compared with Anderson's (1988) experimental results.

In his experiments, Anderson used six-inch plastic spheres. Physical properties of two of the test rigs used in experiments are given in Table 2. In both cases, the spheres were half full. Two transverse moments of inertia are listed, with I_1 the moment of inertia of the test rig about the \hat{x}_4 axis and I_2 the moment of inertia of the test rig about the \hat{y}_4 axis.

Figures 12-15 show a comparison of experimental data and SATELL output for spin about an axis of minimum moment of inertia, runs 1E and 1SE. Only about ten seconds of experimental data could be acquired before the unstable upper assembly came to rest on a supporting collar.

Figures 12-15 clearly show that the system is unstable for spin about an axis of minimum moment of inertia with all the displayed variables increasing with time. Furthermore, as might be expected, the SATELL simulation results do not agree as well with experimental results as they did with the CAMS simulation.

However, the overall results are very similar in a number of important respects. For instance, Figs. 12 and 13 show that the oscillating magnitudes for the upper assembly rotation

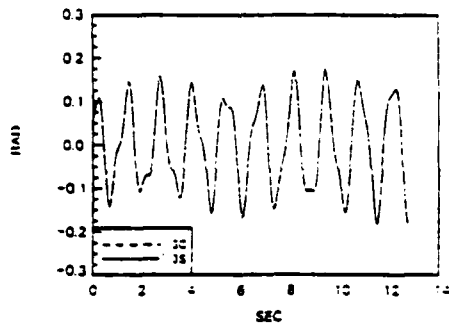


Fig. 8 Comparison of upper assembly rotation given by λ_1 for CAMS Case 3C and SATELL Case 3S

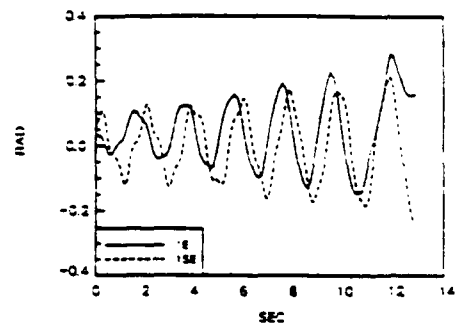


Fig. 12 Comparison of upper assembly rotation given by λ_1 for experimental Case 1E and SATELL Case 1SE

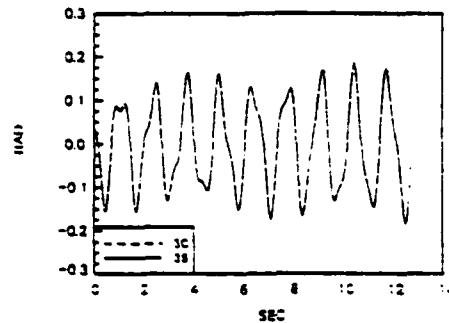


Fig. 9 Comparison of upper assembly rotation given by λ_2 for CAMS Case 3C and SATELL Case 3S

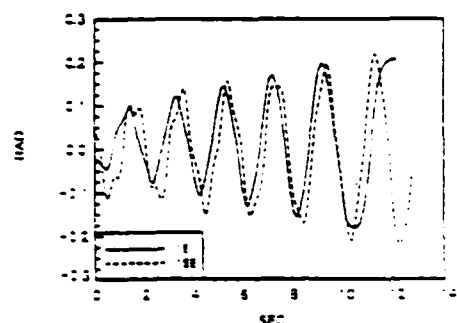


Fig. 13 Comparison of upper assembly rotation given by λ_2 for experimental Case 1E and SATELL Case 1SE

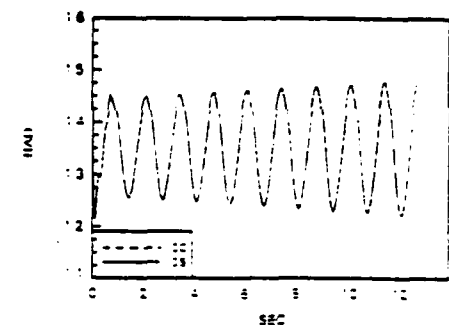


Fig. 10 Comparison of radial rotation of pendulum 2 given by θ_2 for CAMS Case 3C and SATELL Case 3S

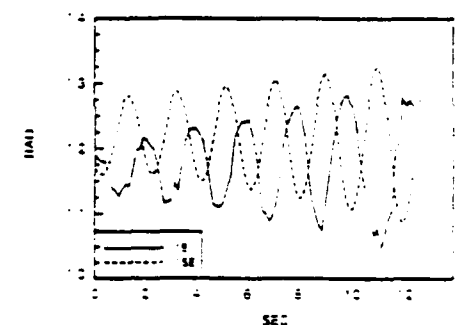


Fig. 14 Comparison of radial rotation of pendulum 2 given by θ_2 for experimental Case 1E and SATELL Case 1SE

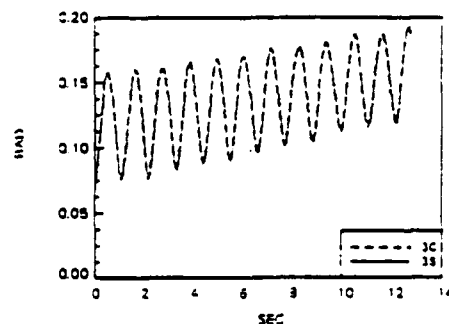


Fig. 11 Comparison of half cone angle, β , for CAMS Case 3C and SATELL Case 3S

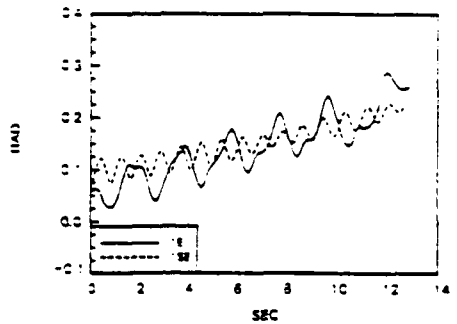


Fig. 15 Comparison of half cone angle, β , for experimental Case 1E and SATELL Case 1SE

angles are quite close as are the primary frequencies, even though the initial conditions for the simulation did not exactly match those for the experimental run.

Figure 14 displays rotation angles for pendulum 2 which do not agree as well as the upper assembly rotation angles of Figs. 12 and 13. Once again, though, the curve does show significant similarities. The overall oscillation magnitude and the fundamental frequency are roughly the same. The phase difference

of Fig. 14 can again be attributed at least partly to a difference in initial conditions.

The half cone angle depicted in Fig. 15 shows quite a bit of difference between the experimental results and the SATELL simulation. The oscillating magnitude of the experimental run appears to be about twice that of the SATELL simulation. Furthermore, the simulation displays a single higher frequency which is approximately twice that of the primary frequency

found in the experimental curve, although there does appear to be a secondary frequency of lower magnitude in the experimental results. The one significant similarity between the two curves, though, is the general increasing trend in the half cone angle associated with the overall unstable motion of the system.

Even though the comparison results between the SATELL simulation and the experimental runs are not as dramatic as the comparison between the two simulation packages, there is still a good deal of qualitative and a reasonable level of quantitative agreement. Since there were certainly small discrepancies in parameter values for such things as the masses and principal moments of inertia used in the SATELL simulations, it is perhaps surprising that the results agreed as closely as they did.

Conclusions

This work has developed the equations of motion for a test rig designed to model a spin-stabilized satellite. The applicability of the equations of motion to the motion of a satellite is based on two assumptions. The first is that the mechanical assembly is a valid model of a satellite, and the second is that the mathematical model is a valid model of the mechanical test rig.

The major accomplishments of the study have included:

- Development of the equations of motion of a spacecraft simulator using a Lagrangian formulation.
- Numerical integration of the developed equations of motion in order to simulate the motion of the test rig.
- Comparison with a multibody dynamics program to verify accuracy of the equations.
- Comparison with experimental results to determine the validity of the mathematical model.

Basic theories were confirmed. That is, that a body containing a sloshing fluid is stable when spun about an axis of maximum moment of inertia and unstable when spun about an axis of minimum moment of inertia.

Comparison of the results of SATELL with the results of CAMS showed good agreement. The results agreed very closely. The relative ease in calculating the input values for SATELL supports its use over that of CAMS for this particular application.

Agreement between experimental data and the output of SATELL was reasonable. The results showed similar frequencies and magnitudes. Difficulty in modeling the experimental setup arose in determining values for mass moments of inertia of the test rig. These values were calculated using formulas for mass moments of inertia of basic geometric shapes. Another difficulty was encountered in determining damping coefficients at the universal joint and pendulum supports.

Now that a computer program has been developed to simulate the dynamics of a spin-stabilized structure carrying liquid stores, many additional factors can be studied. For example, different size tanks and different inertias can be considered. The absence of gravity in outer space can also be simulated by simply setting the acceleration of gravity equal to zero. Furthermore, plans call for additional development of the computer program to handle cases where the liquid tanks are not perfectly symmetric and may not even hold the same quantity of liquid.

Acknowledgment

This study was accomplished with the support of the Air Force Office of Scientific Research under grant AFOSR-86-0080.

References

- Agrawal, B. N., 1981, "Stability of Spinning Spacecraft with Liquid-Filled Tanks," American Institute of Aeronautics and Astronautics, 19th Aerospace Sciences Meeting, St. Louis, MO.
- Anderson, M. D., 1988, "Instrumentation of a Spin-Stabilized Spacecraft Simulator with Liquid Fuel Stores," M.S. thesis, Iowa State University, Ames, IA.
- Cowles, D. S., 1987, "Design of a Spin-Stabilized Spacecraft Simulator with Liquid Fuel Stores," M.S. thesis, Iowa State University, Ames, IA.
- Hill, D. E., 1985, "Dynamics and Control of Spin-Stabilized Spacecraft with Sloshing Fluid Stores," Ph.D. dissertation, Iowa State University, Ames, IA.
- Martin, E. R., 1971, "Experimental Investigations on the Fuel Slosh of Dual-spin Spacecraft," *COMSAT Technical Review*, Vol. 1, No. 1, pp. 1-19.
- Miller, M. C., 1982, "Flight Instabilities of Spinning Projectiles Having Non-rigid Payloads," *Journal of Guidance and Control*, Vol. 5, No. 2, pp. 151-157.
- Sayar, B. A., and Baumgarten, J. R., 1982, "Linear and Nonlinear Analysis of Fluid Slosh Dampers," *ALAA Journal*, Vol. 20, No. 11, pp. 769-772.
- Slabinski, V. J., 1978, "INTELSAT IV In-orbit Liquid Slosh Tests and Problems in the Theoretical Analysis of the Data," *COMSAT Technical Review*, Vol. 8, No. 1, pp. 1-39.
- Sumner, I. E., 1965, "Experimentally Determined Pendulum Analogy of Liquid Sloshing in Spherical and Oblate-Spheroidal Tanks," Technical Note TN D-2737, National Aeronautics and Space Administration.
- Zedd, M. F., and Dodge, F. T., 1985, "Energy Dissipation of Liquids in Rotating Spherical Tanks Measured by a Forced Motion-Spin Table," NRL Report 8932, Naval Research Laboratory.

APPENDIX

$$[A_{12}] = \begin{bmatrix} \cos \psi & -\sin \psi & 0 & 0 \\ \sin \psi & \cos \psi & 0 & 0 \\ 0 & 0 & 1 & 0 \\ 0 & 0 & 0 & 1 \end{bmatrix}$$

$$[A_{23}] = \begin{bmatrix} \cos \lambda_1 & 0 & \sin \lambda_1 & 0 \\ 0 & 1 & 0 & 0 \\ -\sin \lambda_1 & 0 & \cos \lambda_1 & 0 \\ 0 & 0 & 0 & 1 \end{bmatrix}$$

$$[A_{34}] = \begin{bmatrix} 1 & 0 & 0 & 0 \\ 0 & \cos \lambda_2 & -\sin \lambda_2 & 0 \\ 0 & \sin \lambda_2 & \cos \lambda_2 & 0 \\ 0 & 0 & 0 & 1 \end{bmatrix}$$

$$[A_{45}] = \begin{bmatrix} 1 & 0 & 0 & r \\ 0 & 1 & 0 & 0 \\ 0 & 0 & 1 & (cg) \\ 0 & 0 & 0 & 1 \end{bmatrix}$$

$$[A_{48}] = \begin{bmatrix} 1 & 0 & 0 & -r \\ 0 & 1 & 0 & 0 \\ 0 & 0 & 1 & (cg) \\ 0 & 0 & 0 & 1 \end{bmatrix}$$

$$[A_{56}] = \begin{bmatrix} \cos \theta_1 & 0 & \sin \theta_1 & 0 \\ 0 & 1 & 0 & 0 \\ -\sin \theta_1 & 0 & \cos \theta_1 & 0 \\ 0 & 0 & 0 & 1 \end{bmatrix}$$

$$[A_{99}] = \begin{bmatrix} \cos \theta_2 & 0 & \sin \theta_2 & 0 \\ 0 & 1 & 0 & 0 \\ -\sin \theta_2 & 0 & \cos \theta_2 & 0 \\ 0 & 0 & 0 & 1 \end{bmatrix}$$

$$[A_{67}] = \begin{bmatrix} 1 & 0 & 0 & 0 \\ 0 & \cos \phi_1 & -\sin \phi_1 & 0 \\ 0 & \sin \phi_1 & \cos \phi_1 & 0 \\ 0 & 0 & 0 & 1 \end{bmatrix}$$

$$[A_{9,10}] = \begin{bmatrix} 1 & 0 & 0 & 0 \\ 0 & \cos \phi_2 & -\sin \phi_2 & 0 \\ 0 & \sin \phi_2 & \cos \phi_2 & 0 \\ 0 & 0 & 0 & 1 \end{bmatrix}$$

$$\begin{aligned} r_{p1} = & \{-l[\cos \psi(\cos \lambda_1 \sin \theta_1 \cos \phi_1 \\ & + \sin \lambda_1 \cos \lambda_2 \cos \theta_1 \cos \phi_1 - \sin \lambda_1 \sin \lambda_2 \sin \phi_1) \\ & + \sin \psi(\cos \lambda_2 \sin \phi_1 + \sin \lambda_2 \cos \theta_1 \cos \phi_1)] \\ & + r \cos \psi \cos \lambda_1 \\ & + (cg)(\cos \psi \sin \lambda_1 \cos \lambda_2 + \sin \psi \sin \lambda_2)]\dot{x}_1 \\ & \{-l[\sin \psi(\cos \lambda_1 \sin \theta_1 \cos \phi_1 \\ & + \sin \lambda_1 \cos \lambda_2 \cos \theta_1 \cos \phi_1 - \sin \lambda_1 \sin \lambda_2 \sin \phi_1) \\ & - \cos \psi(\cos \lambda_2 \sin \phi_1 + \sin \lambda_2 \cos \theta_1 \cos \phi_1)] \\ & + r \sin \psi \cos \lambda_1 \\ & + (cg)(\sin \psi \sin \lambda_1 \cos \lambda_2 - \cos \psi \sin \lambda_2)]\dot{y}_1 \\ & + [-l(-\sin \lambda_1 \sin \theta_1 \cos \phi_1 \\ & + \cos \lambda_1 \cos \lambda_2 \cos \theta_1 \cos \phi_1 - \cos \lambda_1 \sin \lambda_2 \sin \phi_1) \\ & - r \sin \lambda_1 + (cg)\cos \lambda_1 \cos \lambda_2]\dot{z}_1 \end{aligned}$$

$$\begin{aligned} r_{p2} = & \{-l[\cos \psi(\cos \lambda_1 \sin \theta_2 \cos \phi_2 \\ & + \sin \lambda_1 \cos \lambda_2 \cos \theta_2 \cos \phi_2 - \sin \lambda_1 \sin \lambda_2 \sin \phi_2) \\ & + \sin \psi(\cos \lambda_2 \sin \phi_2 + \sin \lambda_2 \cos \theta_2 \cos \phi_2)] \\ & - r \cos \psi \cos \lambda_1 \\ & + (cg)(\cos \psi \sin \lambda_1 \cos \lambda_2 - \sin \psi \sin \lambda_2)]\dot{x}_1 \\ & \{-l[\sin \psi(\cos \lambda_1 \sin \theta_2 \cos \phi_2 \\ & + \sin \lambda_1 \cos \lambda_2 \cos \theta_2 \cos \phi_2 - \sin \lambda_1 \sin \lambda_2 \sin \phi_2) \\ & - \cos \psi(\cos \lambda_2 \sin \phi_2 + \sin \lambda_2 \cos \theta_2 \cos \phi_2)] \\ & - r \sin \psi \cos \lambda_1 \\ & + (cg)(\sin \psi \sin \lambda_1 \cos \lambda_2 - \cos \psi \sin \lambda_2)]\dot{y}_1 \\ & + [-l(-\sin \lambda_1 \sin \theta_2 \cos \phi_2 \\ & + \cos \lambda_1 \cos \lambda_2 \cos \theta_2 \cos \phi_2 - \cos \lambda_1 \sin \lambda_2 \sin \phi_2) \\ & + r \sin \lambda_1 + (cg)\cos \lambda_1 \cos \lambda_2]\dot{z}_1 \end{aligned}$$

$$\begin{aligned} v_{p1} = & \{\dot{\psi}[\cos \psi(-l \cos \lambda_2 \sin \phi_1 - l \sin \lambda_2 \cos \theta_1 \cos \phi_1 \\ & - (cg)\sin \lambda_2) + \sin \psi(l \cos \lambda_1 \sin \theta_1 \cos \phi_1 \\ & + l \sin \lambda_1 \cos \lambda_2 \cos \theta_1 \cos \phi_1 - l \sin \lambda_1 \sin \lambda_2 \sin \phi_1 \\ & + r \cos \lambda_1 + (cg)\sin \lambda_1 \cos \lambda_2)] \\ & + \dot{\lambda}_1[\cos \psi(-l \cos \lambda_1 \cos \lambda_2 \cos \theta_1 \cos \phi_1 \\ & + l \cos \lambda_1 \sin \lambda_2 \sin \phi_1 \\ & + (cg)\cos \lambda_1 \cos \lambda_2 + l \sin \lambda_1 \sin \theta_1 \cos \phi_1 \\ & - r \sin \lambda_1 \sin \lambda_2)] + \dot{\lambda}_2[\cos \psi(l \sin \lambda_1 \cos \lambda_2 \sin \phi_1 \\ & + l \sin \lambda_1 \sin \lambda_2 \cos \theta_1 \cos \phi_1 - (cg)\sin \lambda_1 \sin \lambda_2) \\ & + \sin \psi(-l \cos \lambda_2 \cos \theta_1 \cos \phi_1 + (cg)\cos \lambda_2 \\ & + l \sin \lambda_2 \sin \phi_1)] + \dot{\theta}_1[\cos \psi(-l \cos \lambda_1 \cos \theta_1 \cos \phi_1 \\ & + l \sin \lambda_1 \cos \lambda_2 \sin \theta_1 \cos \phi_1) + l \sin \psi \sin \lambda_2 \sin \theta_1 \cos \phi_1 \\ & + \dot{\phi}_1[\cos \psi(l \sin \lambda_1 \sin \lambda_2 \cos \phi_1 + l \cos \lambda_1 \sin \theta_1 \sin \phi_1 \\ & + l \sin \lambda_1 \cos \lambda_2 \cos \theta_1 \sin \phi_1) + \sin \psi(-l \cos \lambda_2 \cos \phi_1 \end{aligned}$$

$$\begin{aligned} & + l \sin \lambda_2 \cos \theta_1 \sin \phi_1)]\dot{x}_1 + \{\dot{\psi}[\sin \psi(-l \cos \lambda_2 \sin \phi_1 \\ & - l \sin \lambda_2 \cos \theta_1 \cos \phi_1 + (cg)\sin \lambda_2) \\ & - \cos \psi(l \cos \lambda_1 \sin \theta_1 \cos \phi_1 \\ & + l \sin \lambda_1 \cos \lambda_2 \cos \theta_1 \cos \phi_1 - l \sin \lambda_1 \sin \lambda_2 \sin \phi_1 \\ & + r \cos \lambda_1 + (cg)\sin \lambda_1 \cos \lambda_2)] \\ & + \dot{\lambda}_1[\sin \psi(-l \cos \lambda_1 \cos \lambda_2 \cos \theta_1 \cos \phi_1 \\ & + l \cos \lambda_1 \sin \lambda_2 \sin \phi_1 \\ & + (cg)\cos \lambda_1 \cos \lambda_2 - l \sin \lambda_1 \sin \theta_1 \cos \phi_1 \\ & - r \sin \lambda_1 \sin \lambda_2)] + \dot{\lambda}_2[\sin \psi(l \sin \lambda_1 \cos \lambda_2 \sin \phi_1 \\ & + l \sin \lambda_1 \sin \lambda_2 \cos \theta_1 \cos \phi_1 - (cg)\sin \lambda_1 \sin \lambda_2) \\ & - \cos \psi(-l \cos \lambda_2 \cos \theta_1 \cos \phi_1 + (cg)\cos \lambda_2 \\ & + l \sin \lambda_2 \sin \phi_1)] + \dot{\theta}_1[\sin \psi(-l \cos \lambda_1 \cos \theta_1 \cos \phi_1 \\ & + l \sin \lambda_1 \cos \lambda_2 \sin \theta_1 \cos \phi_1) \\ & - l \cos \psi \sin \lambda_2 \sin \theta_1 \cos \phi_1] \\ & + \dot{\phi}_1[\sin \psi(l \sin \lambda_1 \sin \lambda_2 \cos \phi_1 + l \cos \lambda_1 \sin \theta_1 \sin \phi_1 \\ & + l \sin \lambda_1 \cos \lambda_2 \cos \theta_1 \sin \phi_1) - \cos \psi(-l \cos \lambda_2 \cos \phi_1 \\ & + l \sin \lambda_2 \cos \theta_1 \sin \phi_1)]\dot{y}_1 + [\dot{\lambda}_1(l \cos \lambda_1 \sin \theta_1 \cos \phi_1 \\ & - r \cos \lambda_1 - l \sin \lambda_1 \cos \lambda_2 \cos \theta_1 \cos \phi_1 \\ & - l \sin \lambda_1 \sin \lambda_2 \sin \phi_1 - (cg)\sin \lambda_1 \cos \lambda_2) \\ & + \dot{\lambda}_2(l \cos \lambda_1 \cos \lambda_2 \sin \phi_1 + l \cos \lambda_1 \sin \lambda_2 \cos \theta_1 \cos \phi_1 \\ & - (cg)\cos \lambda_1 \sin \lambda_2) - \dot{\theta}_1(l \sin \lambda_1 \cos \theta_1 \cos \phi_1 \\ & + l \cos \lambda_1 \cos \lambda_2 \sin \theta_1 \cos \phi_1) \\ & - \dot{\phi}_1(l \cos \lambda_1 \sin \lambda_2 \cos \phi_1 - l \sin \lambda_1 \sin \theta_1 \sin \phi_1 \\ & + l \cos \lambda_1 \cos \lambda_2 \cos \theta_1 \sin \phi_1)]\dot{z}_1 \end{aligned}$$

$$\begin{aligned} v_{p2} = & \{\dot{\psi}[\cos \psi(-l \cos \lambda_2 \sin \phi_2 - l \sin \lambda_2 \cos \theta_2 \cos \phi_2 \\ & - (cg)\sin \lambda_2) + \sin \psi(l \cos \lambda_1 \sin \theta_2 \cos \phi_2 \\ & + l \sin \lambda_1 \cos \lambda_2 \cos \theta_2 \cos \phi_2 - l \sin \lambda_1 \sin \lambda_2 \sin \phi_2 \\ & + r \cos \lambda_1 + (cg)\sin \lambda_1 \cos \lambda_2)] \\ & + \dot{\lambda}_1[\cos \psi(-l \cos \lambda_1 \cos \lambda_2 \cos \theta_2 \cos \phi_2 \\ & + l \cos \lambda_1 \sin \lambda_2 \sin \phi_2 \\ & + (cg)\cos \lambda_1 \cos \lambda_2 + l \sin \lambda_1 \sin \theta_2 \cos \phi_2 \\ & - r \sin \lambda_1 \sin \lambda_2)] + \dot{\lambda}_2[\cos \psi(l \sin \lambda_1 \cos \lambda_2 \sin \phi_2 \\ & + l \sin \lambda_1 \sin \lambda_2 \cos \theta_2 \cos \phi_2 \\ & - (cg)\sin \lambda_1 \sin \lambda_2) + \sin \psi(-l \cos \lambda_2 \cos \theta_2 \cos \phi_2 \\ & + (cg)\cos \lambda_2 + l \sin \lambda_2 \sin \phi_2)] \\ & + \dot{\theta}_2[\cos \psi(-l \cos \lambda_1 \cos \theta_2 \cos \phi_2 \\ & + l \sin \lambda_1 \cos \lambda_2 \sin \theta_2 \cos \phi_2) \\ & + l \sin \psi \sin \lambda_2 \sin \theta_2 \cos \phi_2] \\ & + \dot{\phi}_2[\cos \psi(l \sin \lambda_1 \sin \lambda_2 \cos \phi_2 + l \cos \lambda_1 \sin \theta_2 \sin \phi_2 \\ & + l \sin \lambda_1 \cos \lambda_2 \cos \theta_2 \sin \phi_2) \\ & + \sin \psi(-l \cos \lambda_2 \cos \phi_2 + l \sin \lambda_2 \cos \theta_2 \sin \phi_2)]\dot{x}_1 \\ & + \{\dot{\psi}[\sin \psi(-l \cos \lambda_2 \sin \phi_2 - l \sin \lambda_2 \cos \theta_2 \cos \phi_2 \\ & + (cg)\sin \lambda_2) - \cos \psi(l \cos \lambda_1 \sin \theta_2 \cos \phi_2 \end{aligned}$$

$$\begin{aligned}
& + l \sin \lambda_1 \cos \lambda_2 \cos \theta_2 \cos \phi_2 - l \sin \lambda_1 \sin \lambda_2 \sin \phi_2 \\
& + r \cos \lambda_1 + (cg) \sin \lambda_1 \cos \lambda_2] \\
& + \dot{\lambda}_1 [\sin \psi (-l \cos \lambda_1 \cos \lambda_2 \cos \theta_1 \cos \phi_2 \\
& + l \cos \lambda_1 \sin \lambda_2 \sin \phi_2 \\
& + (cg) \cos \lambda_1 \cos \lambda_2 + l \sin \lambda_1 \sin \theta_2 \cos \phi_2 \\
& - r \sin \lambda_1 \sin \lambda_2)] + \dot{\lambda}_2 [\sin \psi (l \sin \lambda_1 \cos \lambda_2 \sin \phi_2 \\
& + l \sin \lambda_1 \sin \lambda_2 \cos \theta_2 \cos \phi_2 - (cg) \sin \lambda_1 \sin \lambda_2) \\
& - \cos \psi (-l \cos \lambda_2 \cos \theta_2 \cos \phi_2 + (cg) \cos \lambda_2 \\
& + l \sin \lambda_2 \sin \phi_2)] + \dot{\theta}_2 [\sin \psi (-l \cos \lambda_1 \cos \theta_2 \cos \phi_2 \\
& + l \sin \lambda_1 \cos \lambda_2 \sin \theta_2 \cos \phi_2) \\
& - l \cos \psi \sin \lambda_2 \sin \theta_2 \cos \phi_2] \\
& + \dot{\phi}_2 [\sin \psi (l \sin \lambda_1 \sin \lambda_2 \cos \phi_2 + l \cos \lambda_1 \sin \theta_2 \sin \phi_2 \\
& + l \sin \lambda_1 \cos \lambda_2 \cos \theta_2 \sin \phi_2) \\
& - \cos \psi (-l \cos \lambda_2 \cos \phi_2 + l \sin \lambda_2 \cos \theta_2 \sin \phi_2)] \} \bar{p}_1 \\
& + [\dot{\lambda}_1 (l \cos \lambda_1 \sin \theta_2 \cos \phi_2 - r \cos \lambda_1 \\
& + l \sin \lambda_1 \cos \lambda_2 \cos \theta_2 \cos \phi_2 - l \sin \lambda_1 \sin \lambda_2 \sin \phi_2 \\
& - (cg) \sin \lambda_1 \cos \lambda_2) + \dot{\lambda}_2 (l \cos \lambda_1 \cos \lambda_2 \sin \phi_2 \\
& + l \cos \lambda_1 \sin \lambda_2 \cos \theta_2 \cos \phi_2 - (cg) \cos \lambda_1 \sin \lambda_2) \\
& + \dot{\theta}_2 (l \sin \lambda_1 \cos \theta_2 \cos \phi_2 + l \cos \lambda_1 \cos \lambda_2 \sin \theta_2 \cos \phi_2) \\
& + \dot{\phi}_2 (l \cos \lambda_1 \sin \lambda_2 \cos \phi_2 - l \sin \lambda_1 \sin \theta_2 \sin \phi_2 \\
& + l \cos \lambda_1 \cos \lambda_2 \cos \theta_2 \sin \phi_2)] \bar{z}_1
\end{aligned}$$

Because $[M]$ is symmetric, only the upper elements of the matrix are displayed here. The lower elements are determined by $M_{ij} = M_{ji}$.

$$\begin{aligned}
M_{11} = & m_s l^2 [(\cos^2 \lambda_2 + \sin^2 \lambda_1 \sin^2 \lambda_2)(\sin^2 \phi_1 - \sin^2 \phi_2) \\
& + \cos^2 \lambda_1 (\sin^2 \theta_1 \cos^2 \phi_1 + \sin^2 \theta_2 \cos^2 \phi_2) - (\sin^2 \lambda_2 \\
& + \sin^2 \lambda_1 \cos^2 \lambda_2)(\cos^2 \theta_1 \cos^2 \phi_1 - \cos^2 \theta_2 \cos^2 \phi_2) \\
& + 2 \cos^2 \lambda_1 \cos \lambda_2 \sin \lambda_2 (\cos \theta_1 \cos \phi_1 \sin \phi_1 \\
& + \cos \theta_2 \cos \phi_2 \sin \phi_2) \\
& + 2 \cos \lambda_1 \sin \lambda_1 \cos \lambda_2 (\cos \theta_1 \sin \theta_1 \cos^2 \phi_1 \\
& + \cos \theta_2 \sin \theta_2 \cos^2 \phi_2) \\
& - 2 \cos \lambda_1 \sin \lambda_1 \sin \lambda_2 (\cos \theta_1 \cos \phi_1 \sin \phi_1 \\
& + \cos \theta_2 \cos \phi_2 \sin \phi_2)] + 2m_s r^2 \cos^2 \lambda_1 \\
& + 2m_s (cg)^2 (\sin^2 \lambda_2 + \sin^2 \lambda_1 \cos^2 \lambda_2) \\
& + 2m_s l r [-\cos^2 \lambda_1 (\sin \theta_1 \cos \phi_1 - \sin \theta_2 \cos \phi_2) \\
& - \cos \lambda_1 \sin \lambda_1 \cos \lambda_2 (\cos \theta_1 \cos \phi_1 - \cos \theta_2 \cos \phi_2) \\
& + \lambda_1 \sin \lambda_1 \sin \lambda_2 (\sin \phi_1 - \sin \phi_2)] \\
& + 2m_s l (cg) [\cos^2 \lambda_1 \cos \lambda_2 \sin \lambda_2 (\sin \phi_1 + \sin \phi_2) \\
& - (\sin^2 \lambda_2 + \sin^2 \lambda_1 \cos^2 \lambda_2)(\cos \theta_1 \cos \phi_1 + \cos \theta_2 \cos \phi_2) \\
& - \cos \lambda_1 \sin \lambda_1 \cos \lambda_2 (\sin \theta_1 \cos \phi_1 \\
& + \sin \theta_2 \cos \phi_2)] + m_{ua} \rho^2 (\sin^2 \lambda_2 + \sin^2 \lambda_1 \sin^2 \lambda_2) \\
& + I_{xx} \sin^2 \lambda_1 + I_{yy} \cos^2 \lambda_1 \sin^2 \lambda_2 + I_{zz} \cos^2 \lambda_1 \cos^2 \lambda_2 \\
& - I_{xy} \cos \lambda_1 \sin \lambda_1 \sin \lambda_2 + I_{yz} \cos^2 \lambda_1 \cos \lambda_2 \sin \lambda_2 \\
M_{12} = & m_s l^2 [\cos \lambda_1 (\cos^2 \lambda_2 - \sin^2 \lambda_2)(\cos \theta_1 \cos \phi_1 \sin \phi_1
\end{aligned}$$

$$\begin{aligned}
& + \cos \theta_2 \cos \phi_2 \sin \phi_2) + \cos \lambda_1 \cos \lambda_2 \sin \lambda_2 \\
& \times (\cos^2 \theta_1 \cos^2 \phi_1 - \sin^2 \phi_1 + \cos^2 \theta_2 \cos^2 \phi_2 - \sin^2 \phi_2) \\
& - \sin \lambda_1 \sin \lambda_2 (\cos \theta_1 \sin \theta_1 \cos^2 \phi_1 \\
& + \cos \theta_2 \sin \theta_2 \cos^2 \phi_2) - \sin \lambda_1 \cos \lambda_2 \\
& \times (\sin \theta_1 \cos \phi_1 \sin \phi_1 + \sin \theta_2 \cos \phi_2 \sin \phi_2) \\
& + 2m_s (cg)^2 \cos \lambda_1 \cos \lambda_2 \sin \lambda_2 + m_s l r [\sin \lambda_1 \cos \lambda_2 \\
& \times (\sin \phi_1 - \sin \phi_2) + \sin \lambda_1 \sin \lambda_2 (\cos \theta_1 \cos \phi_1 \\
& - \cos \theta_2 \cos \phi_2)] + m_s l (cg) [-\cos \lambda_1 (\cos^2 \lambda_2 \\
& - \sin^2 \lambda_2)(\sin \phi_1 + \sin \phi_2) - 2 \cos \lambda_1 \cos \lambda_2 \sin \lambda_2 \\
& \times (\cos \theta_1 \cos \phi_1 + \cos \theta_2 \cos \phi_2) + \sin \lambda_1 \sin \lambda_2 \\
& \times (\sin \theta_1 \cos \phi_1 + \sin \theta_2 \cos \phi_2)] \\
& + m_{ua} \rho^2 \cos \lambda_1 \cos \lambda_2 \sin \lambda_2 + I_{yy} \cos \lambda_1 \cos \lambda_2 \sin \lambda_2 \\
& - I_{zz} \cos \lambda_1 \cos \lambda_2 \sin \lambda_2 - I_{xy} \cos \lambda_1 \sin \lambda_1 \sin \lambda_2 \\
& + I_{yz} \cos \lambda_1 (\cos^2 \lambda_2 - \sin^2 \lambda_2)
\end{aligned}$$

$$\begin{aligned}
M_{13} = & m_s l^2 [-\sin \lambda_1 (\sin^2 \phi_1 + \cos^2 \theta_1 \cos^2 \phi_1 + \sin^2 \phi_2 \\
& + \cos^2 \theta_2 \cos^2 \phi_2) - \cos \lambda_1 \cos \lambda_2 (\cos \theta_1 \sin \theta_1 \cos^2 \phi_1 \\
& + \cos \theta_2 \sin \theta_2 \cos^2 \phi_2) + \cos \lambda_1 \sin \lambda_2 \\
& \times (\sin \theta_1 \cos \phi_1 \sin \phi_1 + \sin \theta_2 \cos \phi_2 \sin \phi_2)] \\
& - 2m_s (cg)^2 \sin \lambda_1 + m_s l r [\cos \lambda_1 \cos \lambda_2 (\cos \theta_1 \cos \phi_1 \\
& - \cos \theta_2 \cos \phi_2) + \cos \lambda_1 \sin \lambda_2 (\sin \phi_1 - \sin \phi_2)] \\
& + m_s l (cg) [2 \sin \lambda_1 (\cos \theta_1 \cos \phi_1 + \cos \theta_2 \cos \phi_2) \\
& + \cos \lambda_1 \cos \lambda_2 (\sin \theta_1 \cos \phi_1 + \sin \theta_2 \cos \phi_2)] \\
& - m_{ua} \rho^2 \sin \lambda_1 - I_{xx} \sin \lambda_1 + I_{xy} \cos \lambda_1 \sin \lambda_2
\end{aligned}$$

$$\begin{aligned}
M_{14} = & m_s l^2 (\cos \lambda_1 \cos \lambda_2 \cos \theta_1 \cos \phi_1 \sin \phi_1 \\
& + \cos \lambda_1 \sin \lambda_2 \cos^2 \phi_1 - \sin \lambda_1 \sin \theta_1 \cos \phi_1 \sin \phi_1) \\
& - m_s l r \cos \lambda_1 \sin \lambda_2 \sin \theta_1 \cos \phi_1 \\
& - m_s l (cg) (-\cos \lambda_1 \sin \lambda_2 \cos \theta_1 \cos \phi_1)
\end{aligned}$$

$$\begin{aligned}
M_{15} = & -m_s l^2 (\cos \lambda_1 \cos \lambda_2 \sin \theta_1 + \sin \lambda_1 \cos \theta_1) \\
& + m_s l r (\cos \lambda_1 \cos \lambda_2 \cos \phi_1 - \cos \lambda_1 \sin \lambda_2 \cos \theta_1 \sin \phi_1) \\
& + m_s l (cg) (\sin \lambda_1 \cos \phi_1 - \cos \lambda_1 \sin \lambda_2 \sin \theta_1 \sin \phi_1)
\end{aligned}$$

$$\begin{aligned}
M_{16} = & m_s l^2 (\cos \lambda_1 \cos \lambda_2 \cos \theta_2 \cos \phi_2 \sin \phi_2 \\
& + \cos \lambda_1 \sin \lambda_2 \cos^2 \phi_2 - \sin \lambda_1 \sin \theta_2 \cos \phi_2 \sin \phi_2) \\
& + m_s l r \cos \lambda_1 \sin \lambda_2 \sin \theta_2 \cos \phi_2 \\
& - m_s l (cg) (-\cos \lambda_1 \sin \lambda_2 \cos \theta_2 \cos \phi_2)
\end{aligned}$$

$$\begin{aligned}
M_{17} = & -m_s l^2 (\cos \lambda_1 \cos \lambda_2 \sin \theta_2 + \sin \lambda_1 \cos \theta_2) \\
& + m_s l r (\cos \lambda_1 \cos \lambda_2 \cos \phi_2 - \cos \lambda_1 \sin \lambda_2 \cos \theta_2 \sin \phi_2) \\
& + m_s l (cg) (\sin \lambda_1 \cos \phi_2 + \cos \lambda_1 \sin \lambda_2 \sin \theta_2 \sin \phi_2)
\end{aligned}$$

$$\begin{aligned}
M_{22} = & m_s l^2 [\cos^2 \lambda_2 (\cos^2 \theta_1 \cos \phi_1 + \cos^2 \theta_2 \cos \phi_2) \\
& + \sin^2 \lambda_2 (\sin^2 \phi_1 + \sin^2 \phi_2) + (\sin^2 \theta_1 \cos^2 \phi_1 \\
& + \sin^2 \theta_2 \cos^2 \phi_2) - 2 \cos \lambda_2 \sin \lambda_2 (\cos \theta_1 \cos \phi_1 \sin \phi_1) \\
& + 2m_s r^2 + 2m_s (cg)^2 \cos^2 \lambda_2 - 2m_s l r (\sin \theta_1 \cos \phi_1 \\
& - \sin \theta_2 \cos \phi_2) + 2m_s l (cg) [-\cos^2 \lambda_2 (\cos \theta_1 \cos \phi_1 \\
& + \cos \theta_2 \cos \phi_2) + \cos \lambda_2 \sin \lambda_2 (\sin \phi_1 + \sin \phi_2)]
\end{aligned}$$

$$\begin{aligned}
& + m_{u0} \rho^2 \cos^2 \lambda_2 + I_{yy} \cos^2 \lambda_2 + I_{zz} \sin^2 \lambda_2 \\
& - I_{yz} \cos \lambda_2 \sin \lambda_2 \\
M_{23} = & m_s l^2 [\cos \lambda_2 (\sin \theta_1 \cos \phi_1 \sin \phi_1 + \sin \theta_2 \cos \phi_2 \sin \phi_2) \\
& + \sin \lambda_2 (\cos \theta_1 \sin \theta_1 \cos^2 \phi_1 + \cos \theta_2 \sin \theta_2 \cos^2 \phi_2)] \\
& - m_s l r [\cos \lambda_2 (\sin \phi_1 - \sin \phi_2) + \sin \lambda_2 (\cos \theta_1 \cos \phi_1 \\
& - \cos \theta_2 \cos \phi_2)] - m_s l (cg) \sin \lambda_2 (\sin \theta_1 \cos \phi_1 \\
& + \sin \theta_2 \cos \phi_2) + I_{xy} \cos \lambda_2 \\
M_{24} = & m_s l^2 (\cos \lambda_2 \cos^2 \phi_1 - \sin \lambda_2 \cos \theta_1 \cos \phi_1 \sin \phi_1) \\
& - m_s l r \cos \lambda_2 \sin \theta_1 \cos \phi_1 - m_s l (cg) \cos \lambda_2 \cos \theta_1 \cos \phi_1 \\
M_{25} = & m_s l^2 \sin \lambda_2 \sin \theta_1 + m_s l (cg) \cos \lambda_2 \sin \theta_1 \sin \phi_1 \\
& - m_s l r (\sin \lambda_2 \cos \phi_1 + \cos \lambda_2 \cos \theta_1 \sin \phi_1) \\
M_{26} = & m_s l^2 (\cos \lambda_2 \cos^2 \phi_2 - \sin \lambda_2 \cos \theta_2 \cos \phi_2 \sin \phi_2) \\
& + m_s l r \cos \lambda_2 \sin \theta_2 \cos \phi_2 - m_s l (cg) \cos \lambda_2 \cos \theta_2 \cos \phi_2 \\
M_{27} = & m_s l^2 \sin \lambda_2 \sin \theta_2 + m_s l (cg) \cos \lambda_2 \sin \theta_2 \sin \phi_2 \\
& - m_s l r (\sin \lambda_2 \cos \phi_2 + \cos \lambda_2 \cos \theta_2 \sin \phi_2) \\
M_{33} = & m_s l^2 [(\sin \phi_1 - \sin \phi_2) + (\cos^2 \theta_1 \cos^2 \phi_1 - \cos^2 \theta_2 \cos^2 \phi_2)] \\
& + 2m_s (cg)^2 - 2m_s l (cg) (\cos \theta_1 \cos \phi_1 + \cos \theta_2 \cos \phi_2) \\
& + m_{u0} \rho^2 + I_{xx} \\
M_{34} = & m_s l^2 \sin \theta_1 \cos \phi_1 \sin \phi_1 \\
M_{35} = & m_s l^2 \cos \theta_1 - m_s l (cg) \cos \phi_1 \\
M_{36} = & m_s l^2 \sin \theta_2 \cos \phi_2 \sin \phi_2 \\
M_{37} = & m_s l^2 \cos \theta_2 - m_s l (cg) \cos \phi_2 \\
M_{44} = & m_s l^2 \cos^2 \phi_1 \\
M_{45} = & 0. \\
M_{46} = & 0. \\
M_{47} = & 0. \\
M_{55} = & m_s l^2 \\
M_{56} = & 0. \\
M_{57} = & 0. \\
M_{66} = & m_s l^2 \cos^2 \phi_2 \\
M_{67} = & 0. \\
M_{77} = & m_s l^2
\end{aligned}$$

APPENDIX B. Motion Study of a Spin-Stabilized Satellite Test Rig.

MOTION STUDY OF A SPIN-STABILIZED SATELLITE TEST RIG

Troy E. Schick

Donald R. Flugrad, Jr.

Mechanical Engineering Department

Iowa State University

Ames, Iowa 50011

Abstract

This paper demonstrates a stability analysis of a spin-stabilized satellite test rig. Stability requirements are analytically derived by modeling the test rig as a system of rigid bodies. The stability requirements are numerically and experimentally verified. Experimental and numerical data is presented which shows instability for spin about the axis of maximum principal moment of inertia.

1 Introduction

In the late 1970s the Air Force launched several Star 48 communication satellites. Once in their geosynchronous earth orbit, these simple spin-stabilized satellites began to nutate and tumble. Hill [1] identified sloshing fluid stores as the likely source of the attitude control problems on these satellites. Sloshing fluid has also caused stability problems in other satellites, such as the Intelsat IV, a dual spin-stabilized satellite, which was investigated by Slabinski [2] and Martin [3].

To enable investigation of the sloshing fluid problem, Cowles [4] designed and constructed a test rig with two spherical fluid tanks symmetrically mounted in a rigid framework. The upper assembly was attached to a lower drive shaft with a Hooke's type universal joint. Figure 1 shows a schematic of the test rig that Cowles constructed. The test rig is driven by a 1/4 hp variable speed electric motor. A collar is used to restrain the universal joint while bringing the test rig up to speed. Once the test rig has reached the desired speed, the collar is lowered to allow free motion about the universal joint.

Anderson [5] instrumented Cowles' test rig. A tachometer was used to

enable measurement of the input spin rate. The pitch and yaw axis rotation angles of the upper assembly were measured with two rotating potentiometers that were mounted on the drive shaft below the universal joint. Finally, three photo potentiometers were mounted on each tank to track the location of the liquid free surface. The signals from these transducers were transmitted through a slip ring assembly mounted on the lower drive shaft. Anderson recorded data from the test rig which produced radial slosh frequencies and precession rates that agreed with actual in-orbit data for the Intelsat IV satellite reported by Slabinski.

Obermaier [6] wrote a simulation program, **SATELL**, which numerically integrates the equations of motion for the test rig described above. Obermaier modeled the sloshing fluid in the test rig's spherical tanks by pendulums as described by Sumner [7] and Sayer and Baumgarten [8]. The equations of motion for the test rig were derived using the Lagrangian formulation. Obermaier found excellent agreement between the results of her simulation program and the experimentally measured response of the test rig. This agreement makes **SATELL** very useful for testing different configurations of the test rig to identify the test setups which warrant experimental evaluation. Obermaier also identified frequencies from the simulation output that agreed

well with the predictions of Slabinski and the work of Zedd and Dodge [9].

In the first part of this study, stability requirements for the test rig modeled as a single rigid body and as a system of rigid bodies are presented. Agrawal [10] suggests that for stability a spin-stabilized satellite test rig must be spun about a principal axis with a moment of inertia that is greater than the transverse principal axes by a calculated margin. This margin was found by modeling the test rig as a system of rigid bodies and using the approach of McIntyre and Miyagi [11]. This approach considers the effects of products of inertia that result from certain sloshing modes of the fluid in the test rig tanks.

In the final part of this study, experimental and simulation runs are presented to verify the stability rules. The effects of gravity are also discussed for each case.

2 Stability Analysis of the Test Rig

According to well-established criteria developed in past experimental research by Cowles [4] and Anderson [5], a spin-stabilized satellite test rig must be spun about its axis of maximum principal moment of inertia to be stable.

Greenwood [12] analytically derived this rule is by assuming that a satellite behaves as a single torque-free rigid body, and by noting that kinetic energy is dissipated by the sloshing viscous fluid in the satellite fuel tanks while the total angular momentum remains constant. Since each axis of the test rig has a different moment of inertia, the kinetic energy level for spin about each axis is different for a given angular momentum. To conserve momentum the test rig will seek to spin about an axis associated with a minimum energy state as energy is dissipated by the sloshing liquid. For example, if the test rig is spinning about a given principal axis at a given kinetic energy level and a lower energy level exists for spin about a different principal axis, the test rig will try to rotate its spin axis to align with the axis of lower kinetic energy. The minimum kinetic energy is achieved for spin about the axis of maximum principal moment of inertia.

As stated earlier, the above stability rule assumes that the test rig behaves as a single torque-free rigid body. However, in work by Obermaier [6] the test rig was modeled successfully as a system of rigid bodies consisting of a center body with two attached pendulums as shown in Figure 2. The two pendulums model the fluid in the two test rig tanks as described by the work of Sumner [7]. Agrawal [10] has shown that for stability, spin-stabilized

satellites must be spun about a principal axis with a moment of inertia greater than the other principal axes by a calculated margin. Stability rules for the system of rigid bodies of Figure 2 are found using the approach of McIntyre and Miyagi [11]. This approach again assumes a torque-free condition and involves considering the test rig balance with respect to the oscillation modes of the pendulums. The stability rules for this system of rigid bodies verify Agrawal's conclusions that spinning the test rig or a satellite about its axis of maximum principal moment of inertia is not enough to insure stability.

McIntyre and Miyagi's approach begins with studying the four fundamental pendulum oscillation modes shown in Figure 3. These oscillation modes must be evaluated for nonzero products of inertia. Nonzero products of inertia can cause misalignment between the reference z-axis of the test rig and the axis of maximum principal moment of inertia or spin axis since the spin axis will be coincident with the principal axis. The test rig is considered to be out of balance when misalignment between the spin axis and the z-axis exists.

Pendulum oscillation Mode 1 from Figure 3 generates one nonzero product of inertia, I_{yz} . Agrawal [10] shows that the misalignment between the

spin axis and the z-axis resulting from this product of inertia is expressed as

$$\theta_x = \frac{I_{yz}}{I_z - I_y} \quad (1)$$

where θ_x is a rotation of the spin axis about the test rig's x-axis. It is also important to note that I_{yz} is the product of inertia of the test rig about its center of mass, and I_y and I_z are composite moments of inertia of the test rig (including pendulums) also about the center of mass.

Pendulum oscillation Mode 2 from Figure 3 also generates one nonzero product of inertia, I_{xy} . However, this product of inertia does not affect the test rig's balance.

Since the pendulum oscillation Mode 3 from Figure 3 yields no products of inertia, it also has no effect on the test rig's balance.

Pendulum oscillation Mode 4 from Figure 3 generates one nonzero product of inertia, I_{xz} . The misalignment between the spin axis and the z-axis caused by this product of inertia is expressed as

$$\theta_y = \frac{I_{xz}}{I_z - I_x} \quad (2)$$

where θ_y is a rotation of the spin axis about the test rig's y-axis. As before, I_{xz} is the product of inertia of the test rig about its center of mass, and I_x and

I_z are composite moments of inertia of the test rig (including pendulums) also about the center of mass.

Equations (1) and (2) show that Modes 1 and 4 are the only modes that offset the balance of the test rig. Continuing with McIntyre and Miyagi's approach, we must take precautions to prevent these modes from occurring.

First, the products of inertia for Equations (1) and (2) must be defined in terms of test rig dimensions. Then, stability rules must be developed with respect to the products and moments of inertia to prevent pendulum oscillations.

Figure 4 shows the rotation of the spin axis about the test rig's x-axis that results from pendulum oscillation Mode 1. Equation (1) defines the angle of rotation θ_x . The product of inertia, I_{yz} , for Equation (1) is defined in terms of test rig dimensions as

$$I_{yz} = 2M_s(CG)L \sin \beta \quad (3)$$

where M_s is the pendulum mass. Then, for small β

$$I_{yz} = 2M_s(CG)L\beta \quad (4)$$

Figure 4 also illustrates that the center of mass of the test rig is moved along the y-axis as a result of pendulum Mode 1 by the distance E_y . The center of

mass is located by

$$E_y M_{tot} = 2M_s L \sin \beta \quad (5)$$

where M_{tot} is the total mass of the test rig. Simplification for small β , produces

$$E_y = \frac{2M_s L \beta}{M_{tot}} \quad (6)$$

Figure 5 shows a view of the test rig's xy-plane containing the pendulums. The spin axis intercepts the y-axis on this plane at Y1 where

$$Y1 = E_y - (CG) \tan \theta_x \quad (7)$$

Simplification for small angles and substitution for θ_x and E_y from Equations (1) and (6) yields

$$Y1 = -2M_s L \beta \left(\frac{1}{M_{tot}} - \frac{(CG)^2}{I_z - I_y} \right) \quad (8)$$

Also shown in Figure 5 is the intercept of the extended pendulums with the y-axis which is given by

$$Y2 = R \tan \beta = R \beta \quad (9)$$

Now if Y1 is larger than Y2, β will increase in the xy plane as centrifugal forces align the pendulums perpendicular to the spin axis. Thus, for stability

Y2 must be larger than Y1. With the help of Equations (8) and (9) this results in the following expression

$$R\beta > -2M_s L \beta \left(\frac{1}{M_{tot}} - \frac{(CG)^2}{I_z - I_y} \right) \quad (10)$$

If β is cancelled and terms are rearranged, the stability rule becomes

$$I_z - I_y > \frac{(CG)^2}{\frac{R}{2M_s L} + \frac{1}{M_{tot}}} \quad (11)$$

Figure 6 shows the rotation about the test rig's y-axis that results from pendulum oscillation Mode 4. This rotation angle is defined by Equation (2). The product of inertia I_{xz} in Equation (2) is written in terms of test rig dimensions as

$$\begin{aligned} I_{xz} = & M_s(R + L \cos \alpha)((CG) + L \sin \alpha) - \\ & M_s(R + L \cos \alpha)((CG) - L \sin \alpha) \end{aligned} \quad (12)$$

Simplifying for small α and combining terms, one finds

$$I_{xz} = 2M_s L(R + L)\alpha \quad (13)$$

Now, if θ_y is larger than α , α will increase in the xz plane as centrifugal forces align the pendulums perpendicular to the spin axis. Thus for stability,

θ_y must be less than α . Equations (2) and (13) may be used to develop the following expression,

$$\frac{2M_y L(R + L)\alpha}{I_z - I_x} < \alpha \quad (14)$$

After cancellation of α and rearrangement of terms, the stability rule becomes

$$I_z - I_x > 2M_y L(R + L) \quad (15)$$

3 Verification of Stability Rules

The computer simulation program **SATELL**, and the experimental test rig were used to verify that Equations (11) and (15) govern the global stability of the test rig. As stated earlier, these stability rules were developed for a torque-free system of rigid bodies, but the test rig is of course subject to torques produced by gravity. For this reason, **SATELL** was also used to study the influence of gravity on the response of the test rig. A zero gravity environment was created by setting the acceleration due to gravity equal to zero when running **SATELL**. Since **SATELL** results and experimental data were used extensively, it is necessary to discuss the operational characteristics of both.

Obermaier [6] modeled the test rig with four bodies consisting of a rigid

upper assembly attached to a lower support shaft by a Hooke's type universal joint and two spherical pendulums which are symmetrically attached to the upper assembly. She compiled the equations of motion for this system of rigid bodies and developed a computer program named **SATELL** which is run with a double precision integration program named **DDIFFEQ**. Before **SATELL** can be run, initial conditions must be specified for the angles that define the positions of the rigid bodies, and all constants must be defined. There are four sets of Cartesian coordinates which are used to describe the orientations of the upper assembly.

The $\hat{x}_1 - \hat{y}_1 - \hat{z}_1$ coordinate system is stationary and is positioned at the center of the universal joint. The \hat{z}_1 axis is directed vertically upward. Positioning of the \hat{x}_1 and \hat{y}_1 axes is arbitrary.

Transformation to the $\hat{x}_2 - \hat{y}_2 - \hat{z}_2$ system is achieved by a right hand rotation by an amount ψ about the \hat{z}_1 axis. The $\hat{x}_2 - \hat{y}_2 - \hat{z}_2$ coordinate system is attached to the lower shaft of the test rig and its origin is at the center of the universal joint. The $\hat{x}_2 - \hat{y}_2 - \hat{z}_2$ axes are fixed in such a way that when the \hat{z}_1 and \hat{z}_2 are aligned, the \hat{y}_2 components of the position vectors of the pendulum supports are zero.

The rotation of the upper assembly relative to the lower shaft is defined

by the two rotation angles, λ . First, a rotation by an amount λ_1 about the \hat{y}_2 axis defines the transformation to the $\hat{x}_3 - \hat{y}_3 - \hat{z}_3$ coordinate system. Then, the coordinate system is rotated through an angle λ_2 about the \hat{x}_3 axis to arrive at the $\hat{x}_4 - \hat{y}_4 - \hat{z}_4$ system. The $\hat{x}_4 - \hat{y}_4 - \hat{z}_4$ system is attached to the upper assembly as shown on Figure 1. Figure 7 shows the rotations for the upper assembly on the universal joint about the lower support shaft. It should be noted that when running **SATELL**, λ_1 and λ_2 cannot be initially set to zero since this will cause singularities when integrating.

The remaining inputs for **SATELL** are L, R, CG, M_s , M_{ua} , \dot{I}_x , \dot{I}_y , \dot{I}_z , ρ , and spin rate. The inertia inputs to **SATELL** are for the rigid assembly including the nonslosh masses, not the steady state composite moments of inertia as defined previously. The constant ρ is defined to be the height of the center of gravity of the upper assembly above the universal joint when λ_1 and λ_2 are equal to zero. The constant M_{ua} is defined as the mass of the upper assembly of the test rig including the pendulum nonslosh masses. All other variables are as previously defined.

The test rig is equipped with nine transducers for making measurements. There are two rotating potentiometers, one on the \hat{x}_2 axis and the other on the \hat{y}_2 axis, that enable the measurement of variables that can be used to solve

for λ_1 and λ_2 . There are three photo potentiometers on each tank to measure the fluid free surface location. The final transducer is a tachometer that enables measurement of the spin rate. The signals from these transducers are transmitted through a slip ring assembly mounted on the lower drive shaft. An IBM model PS/2 equipped with a National Instruments data acquisition card was used to collect experimental data from the test rig. Eight channels of input were utilized to record data from the rotating potentiometers and the photo potentiometers. A voltmeter attached to the tachometer was used to set the spin rate.

The first step in the experimental procedure was to perform the transducer calibrations as described by Anderson [5] with the rig in the desired configuration. Next, the rig was brought up to speed with the collar up. The data acquisition program was then started and the collar was released. The experimental data recorded with the IBM was then down loaded onto a VAX 11/785 mainframe for plotting.

A limitation of the test rig that appears in the experimental data is that it can only rotate ± 2 radians (11.4 deg) about the \hat{x}_2 and \hat{y}_2 axes. Also, for safety, the test rig spin rates were kept below $14 \frac{\text{radians}}{\text{second}}$ (133.7 rpm).

The global stability of the test rig is governed by Equations (11) and

(15). Equation (11) must be satisfied to ensure stability about the x-axis or to restrain the horizontal pendulum oscillation Mode 1 of Figure 3. Equation (15) must be satisfied to ensure stability about the y-axis or to restrain the vertical pendulum oscillation Mode 4 of Figure 3.

This section deals with test rig configurations where the steady state composite center of mass is located at the universal joint. This requirement insures that gravity produces no net moments on the test rig. Also, this configuration is nearest to simulating an actual satellite in orbit. Using the dimensions for the two test rig configurations given in Table 1 in Equation (15), results in

$$I_z - I_x > 0.011 slug - ft^2 \quad (16)$$

Since both of the configurations in Table 1 satisfy Equation (11), Equation (16) governs the stability of these configurations. Run 1 of Table 1 does not satisfy Equation (16) and should result in an unstable response of λ_1 about the \hat{y}_2 axis caused by the vertical pendulum oscillation Mode 4 of Figure 3. Furthermore, inspection of the steady state inertias in Table 1 for Run 1 shows that the rig is spinning about the maximum principal axis. Figure

8 shows the experimental response of λ_1 and λ_2 for Run 1. As predicted, the response of λ_1 increases with time in an unstable manner. This experimentally verifies Agrawal's conclusion that spinning a satellite or a test rig about its axis of maximum principal moment of inertia is not enough to insure stability. Figure 8 shows the numerical response of λ_1 and λ_2 of Run 1 from **SATELL**. Root mean square difference calculations were performed on the numerical and experimental responses over the first second with .05 second increments. The results of these calculations were .048 radians rms difference for λ_1 and .024 radians rms difference for λ_2 . These small differences are explained by the difference in the initial conditions for λ_1 and λ_2 which were both set at .050 radians in **SATELL** and a nominal zero radians on the test rig. The nonzero initial conditions for the **SATELL** run were required to avoid singularities when integrating. Figure 8 also shows a simulated response for Run 1 from **SATELL** with zero gravity and the same initial conditions as above. This response also closely matches the experimental with .037 radians rms difference for λ_1 and .028 radians rms difference for λ_2 . When these differences are compared to those for the simulation with gravity, one finds that gravity does not affect the response of the test rig provided the center of mass is located at the universal joint.

Run 2 of Table 1 satisfies Equation (16) and should, therefore, be stable. Figure 9 shows the experimental and numerical responses for Run 2 which are stable for both λ_1 and λ_2 . The difference between the experimental and the numerical responses are .013 radians rms for λ_1 and .008 radians rms for λ_2 .

Figure 9 also shows the numerical simulation response for Run 2 with zero gravity. This response is stable and differs from the experimental by .015 radians rms on λ_1 and .008 radians rms on λ_2 .

Using the dimensions given for the two test rig configurations shown in Table 2, Equation (11) becomes

$$I_z - I_y > .003slug - ft^2 \quad (17)$$

Since both of the configurations in Table 3.2 satisfy Equation (15), Equation (17) governs the stability of these configurations. The two tanks on the test rig are located on the x-axis which makes duplicating the four configurations in Table 2 with the test rig impossible. For this reason only data from **SATELL** is presented.

Run 3 of Table 2 does not satisfy Equation (17) and should be unstable about the \hat{x}_2 axis as a result of the horizontal pendulum Mode 1 of Figure 3.

This statement is verified in Figure 10 which shows the simulated response of Run 3 for the test rig where λ_1 is steady and λ_2 is decreasing with time in an unstable fashion. Since the test rig is spinning about its axis of maximum principal moment of inertia for Run 3, as shown in Table 2, the unstable response agrees with Agrawal's stability criteria as previously mentioned. Figure 10 shows the zero gravity simulated response of λ_1 and λ_2 for Run 3 which matches the response with gravity. The similarity between these two responses implies that the test rig responds similar to an actual satellite when the composite center of mass is located at the universal joint.

Run 4 of Table 2 satisfies Equation (17) and should be stable. Figure 11 illustrates the stable simulated response of Run 4. Figure 11 also illustrates the simulated response of λ_1 and λ_2 for Run 4 with no gravity. Again, the zero gravity response is nearly identical to the response with gravity.

4 Conclusions

During this study, a great deal of emphasis was placed on understanding the motion of the test rig with respect to the sloshing modes of the fluid. As these relationships became clear, the stability requirements for the test rig

were developed. Simulation runs with **SATELL** and experimental runs with the test rig were made to verify the stability requirements and to confirm the understanding of the sloshing fluid oscillation modes.

The major accomplishments of this study include:

- Stability rules for the test rig were analytically developed and verified with **SATELL** and the experimental test rig.
- Numerical and experimental data were recorded for the test rig that demonstrated instability while spinning about the axis of maximum principal moment of inertia. This agrees with Agrawal's work.
- When the composite center of mass was located at the universal joint, the test rig responded as an actual satellite in orbit. This was verified by comparing experimental runs with simulation runs for zero gravity.
- When the moment of inertia for one of the transverse axes was too large for stability and the composite center of mass was at the universal joint, experimental and simulation data showed that the test rig attempted to reorient itself to spin about that transverse axis as predicted by single rigid body theory.

Future experimental research will be focused on the the effect that fluid viscosity has on the stability of the test rig. Also, elastic body effects will be included in a stability analysis of the test rig by a Lyapunov approach.

ACKNOWLEDGMENT

This study was accomplished with the support of the Air Force Office of Scientific Research under grant AFOSR-89-0403B.

References

- [1] Hill, Daniel E. "Dynamics and Control of Spin-stabilized Spacecraft with Sloshing Fluid Stores." Ph.D. dissertation, Iowa State University, Ames, Iowa, 1985.
- [2] Slabinski, V. J. "INTELSAT IV In-orbit Liquid Slosh Tests and Problems in the Theoretical Analysis of the Data." COMSAT Technical Review, 8, No. 1 (Spring 1978):1-39.
- [3] Martin, Ernesto R. "Experimental Investigations on the Fuel Slosh of Dual-spin Spacecraft." COMSAT Technical Review, 1, No. 1 (Fall 1971):1-19.
- [4] Cowles, Doug S. "Design of a Spin-Stabilized Spacecraft Simulator with Liquid Fuel Stores." M.S. thesis, Iowa State University, Ames, Iowa, 1987.
- [5] Anderson, Michael D. "Instrumentation of a Spin-Stabilized Spacecraft Simulator with Liquid Fuel Stores." M.S. thesis, Iowa State University, Ames, Iowa, 1988.

- [6] Obermaier, Lisa A. "Computer Simulation of a Spin-stabilized Spacecraft Simulator with Liquid Fuel Stores." M.S. thesis, Iowa State University, Ames, Iowa, 1988.
- [7] Sumner, Irving E. "Experimentally Determined Pendulum Analogy of Liquid Sloshing in Spherical and Oblate-Spheroidal Tanks." Technical Note TN D-2737. National Aeronautics and Space Administration, April 1965.
- [8] Sayer, Bashir A. and Baumgarten, J. R. "Linear and Nonlinear Analysis of Fluid Slosh Dampers." AIAA Journal, 20, No. 11 (November 1982): 769-772.
- [9] Zedd, Michael F. and Dodge, Franklin T. "Energy Dissipation of Liquids in Nutating Spherical Tanks Measured by a Forced Motion-Spin Table." NRL Report 8932. Washington D.C.: Naval Research Laboratory, October 1985.
- [10] Agrawal, Brij N. "Stability of Spinning Spacecraft with Liquid-Filled Tanks." American Institute of Aeronautics and Astronautics, 19th Aerospace Sciences Meeting, St. Louis, Missouri, January 1981.

- [11] McIntyre, J. E. and Miyagi, M. I. "A General Stability Principle for Spinning Flexible Bodies with Application to the Propellant Migration-Wobble Amplification Effect." Paper presented at the symposium on dynamics and controls of non-rigid spacecraft. Frascati, Italy, May 1976.
- [12] Greenwood, Donald T. "Principles of Dynamics." Englewood Cliffs, New Jersey: Prentice Hall, Inc., 1988.

Figure 1: Schematic of mechanical system

Figure 2: Model of test rig

Figure 3: Fundamental pendulum oscillation modes

Figure 4: Spin axis rotation caused by Mode 1

Figure 5: Pendulum oscillation plane for Mode 1

Figure 6: Spin axis rotation caused by Mode 4

Figure 7: Upper assembly rotations

Figure 8: λ_1 and λ_2 versus time for Run 1

Figure 9: λ_1 and λ_2 versus time for Run 2

Figure 10: λ_1 and λ_2 versus time for Run 3

Figure 11: λ_1 and λ_2 versus time for Run 4

Table 1: Test rig dimensions for Runs 1 and 2

	Run 1	Run 2
spin rate $\frac{rad}{sec}$	10.5	10.5
M , slug	0.0354	0.0354
L feet	0.1625	0.1625
R feet	0.833	0.833
CG feet	-0.7705	-0.6973
M_{ua} (dry) slug	0.7254	0.6924
I_x (upper assy.) slug ft ²	0.464	0.444
I_y (upper assy.) slug ft ²	0.253	0.233
I_z (upper assy.) slug ft ²	0.448	0.448
I_x (steady state) slug ft ²	0.516	0.487
I_y (steady state) slug ft ²	0.374	0.345
I_z (steady state) slug ft ²	0.518	0.517

Table 2: Test rig dimensions for Runs 3 and 4

	Run 3	Run 4
spin rate $\frac{rad}{sec}$	10.5	10.5
M , slug	0.0354	0.0354
L feet	0.1625	0.1625
R feet	0.833	0.833
CG feet	-0.4484	-0.4484
M_{ua} (dry) slug	0.5701	0.5701
I_x (upper assy.) slug ft ²	0.200	0.200
I_y (upper assy.) slug ft ²	0.300	0.290
I_z (upper assy.) slug ft ²	0.320	0.320
I_x (steady state) slug ft ²	0.219	0.219
I_y (steady state) slug ft ²	0.388	0.378
I_z (steady state) slug ft ²	0.389	0.389

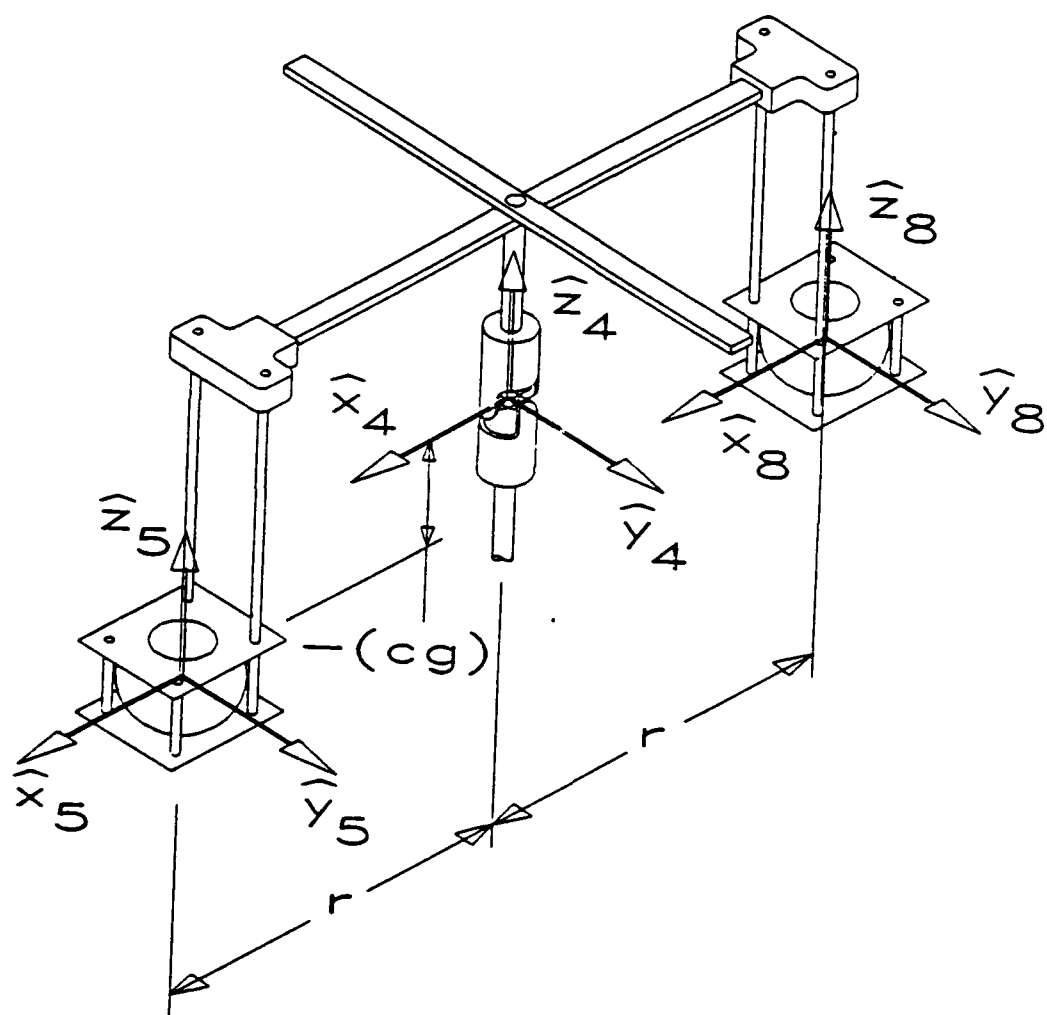


Fig. 1

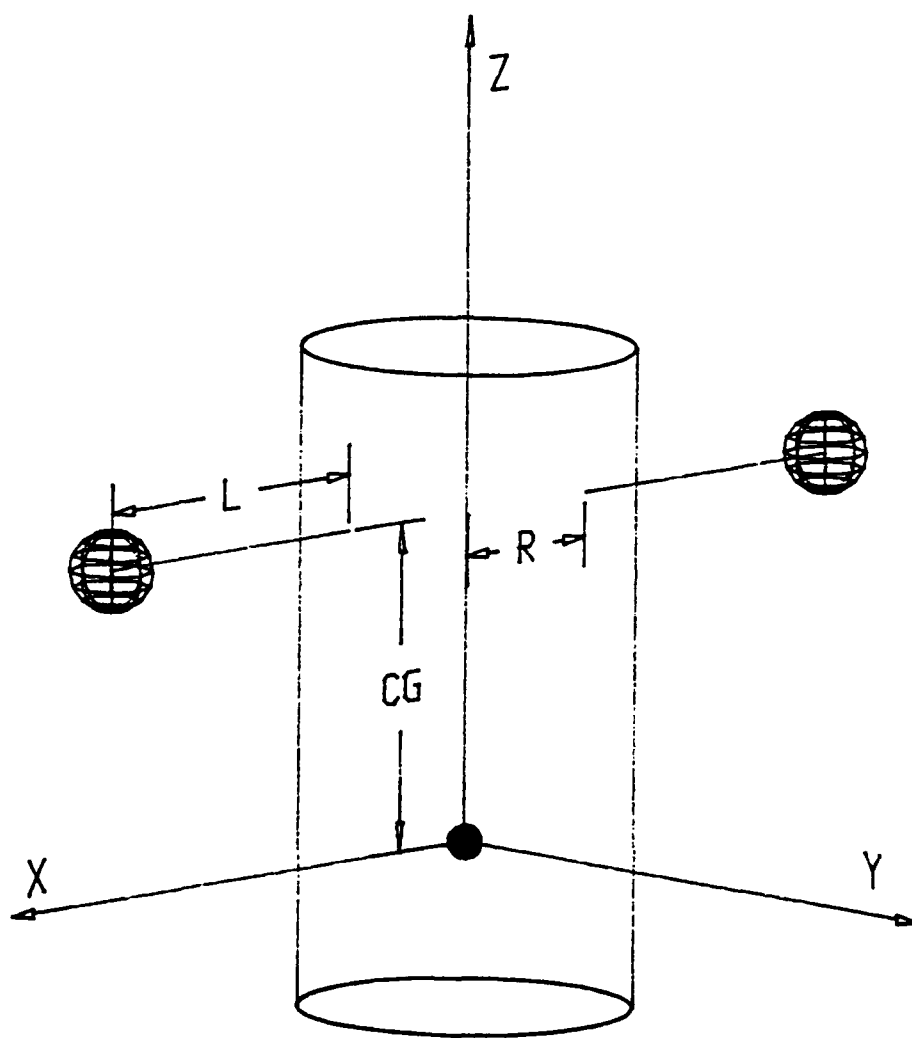


Fig. 2

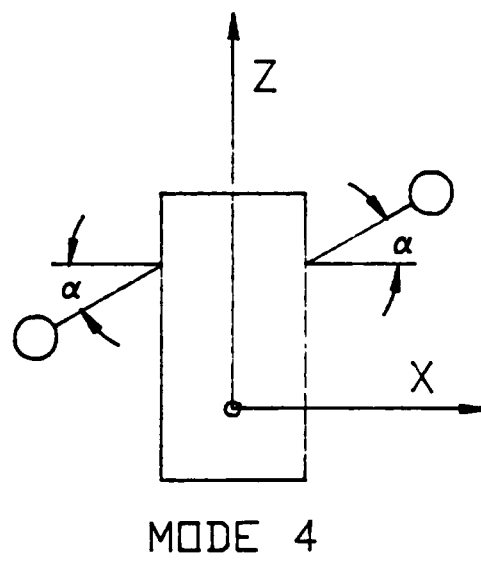
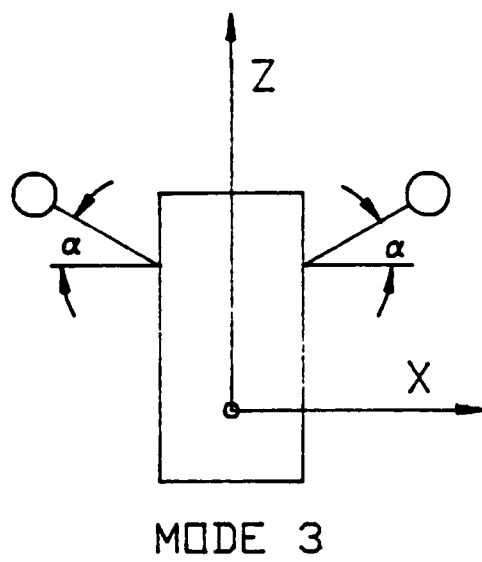
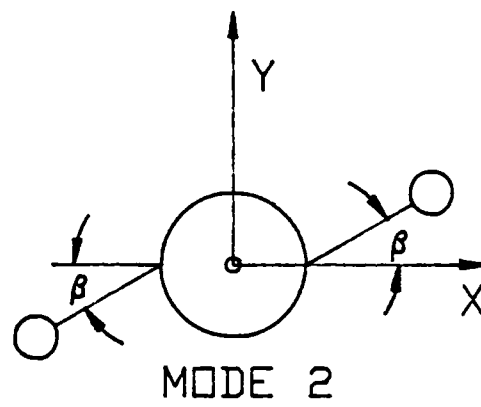
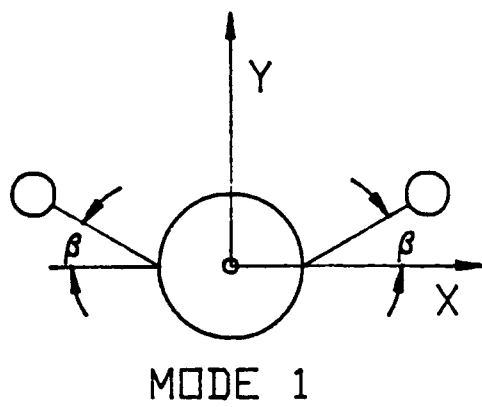


Fig. 3

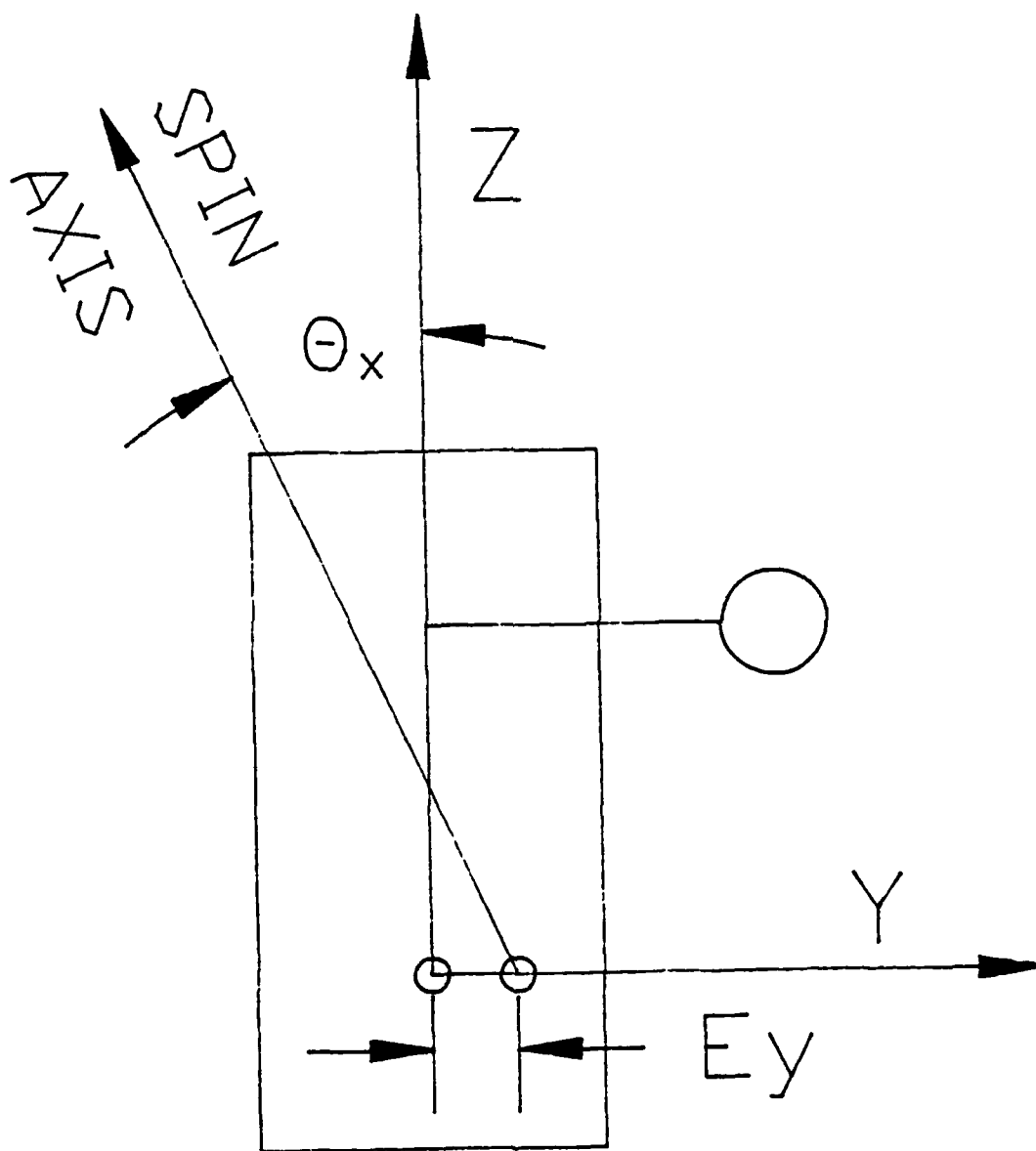


Fig. 4

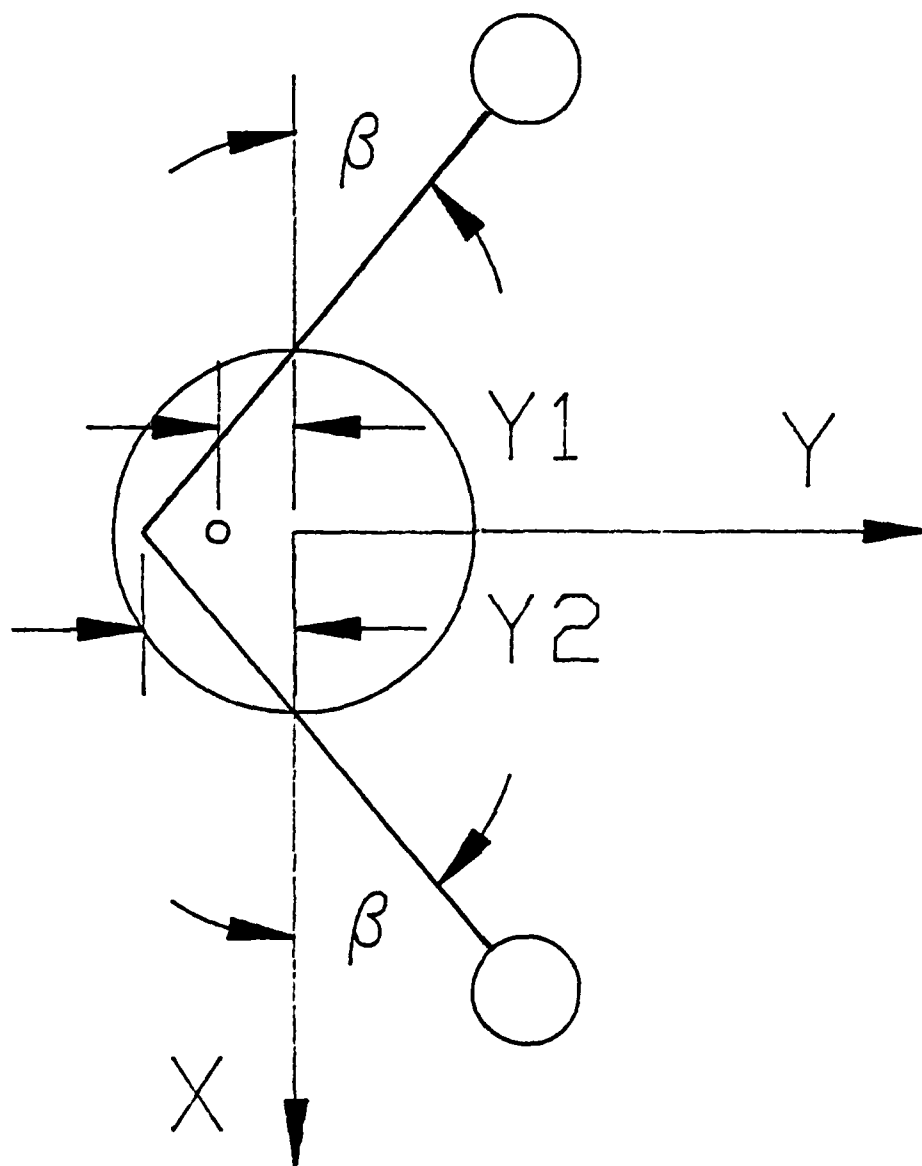


Fig. 5

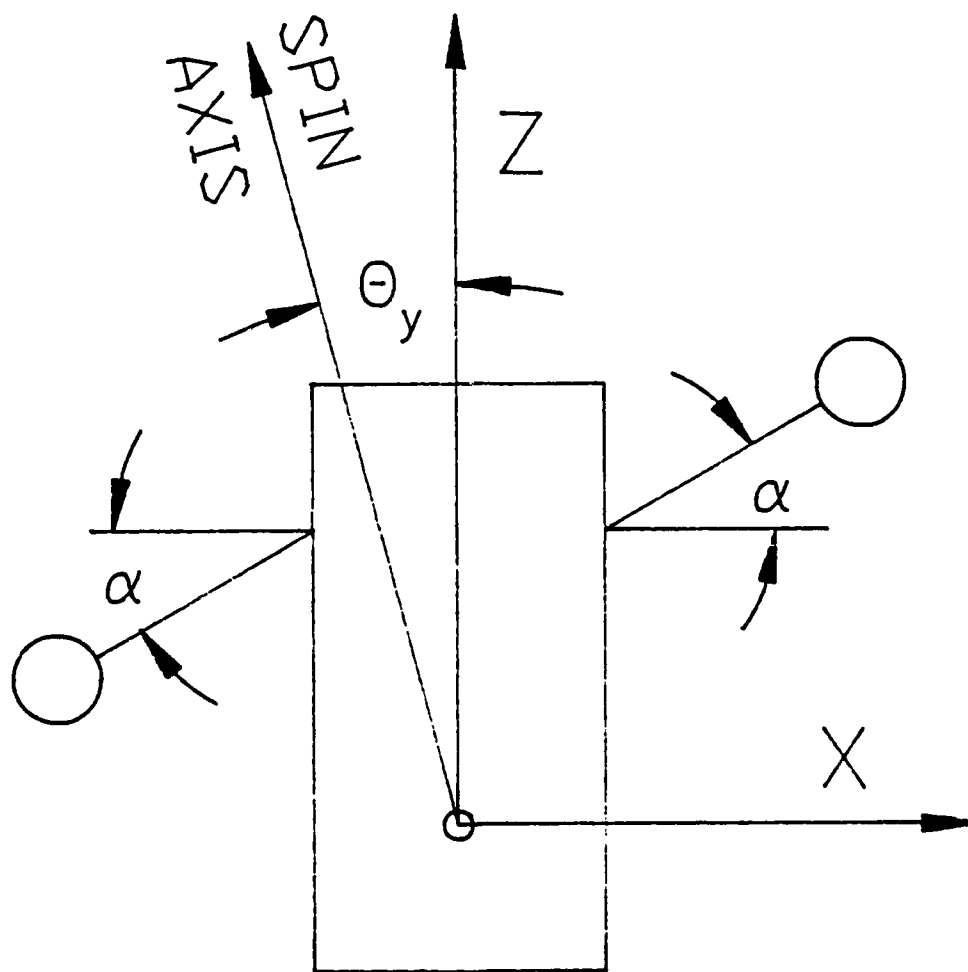


Fig. 6

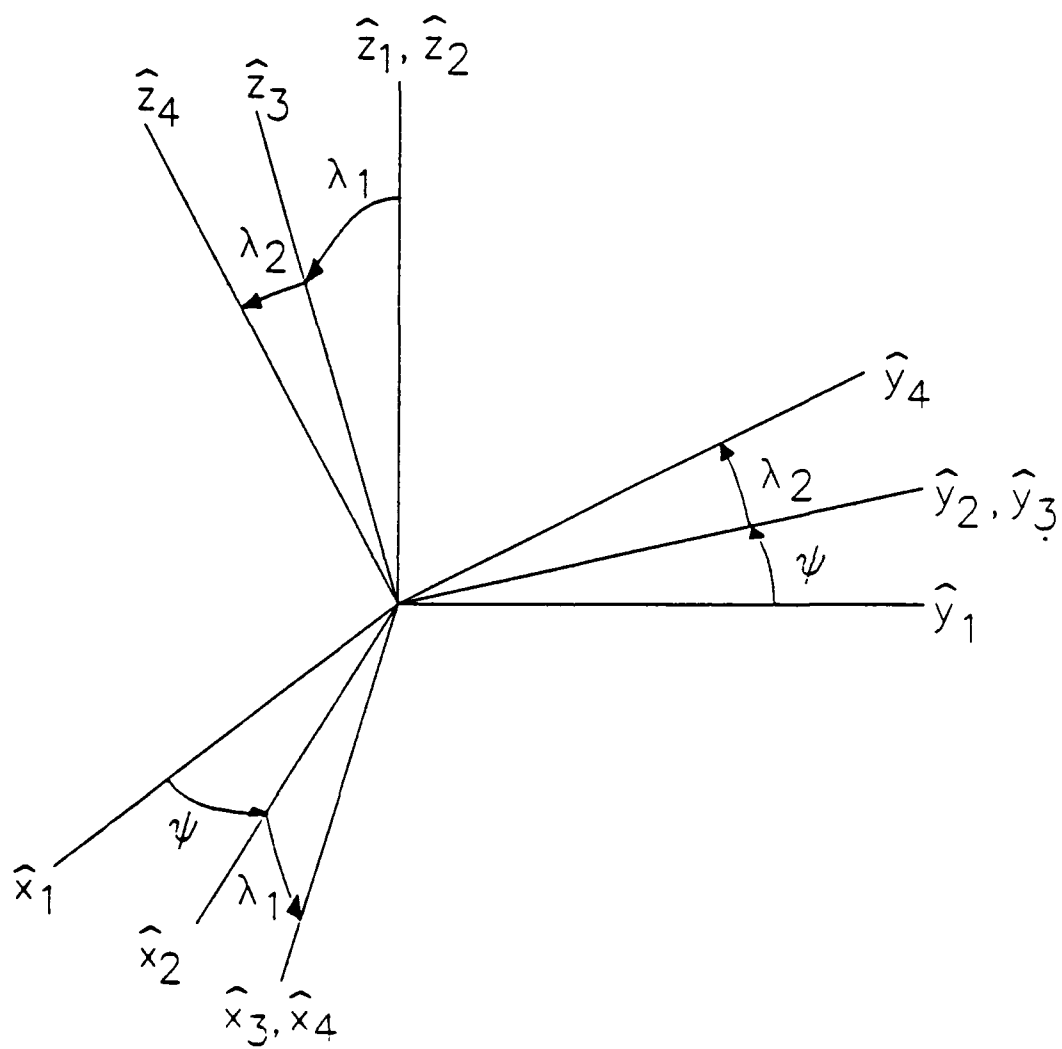


Fig. 7

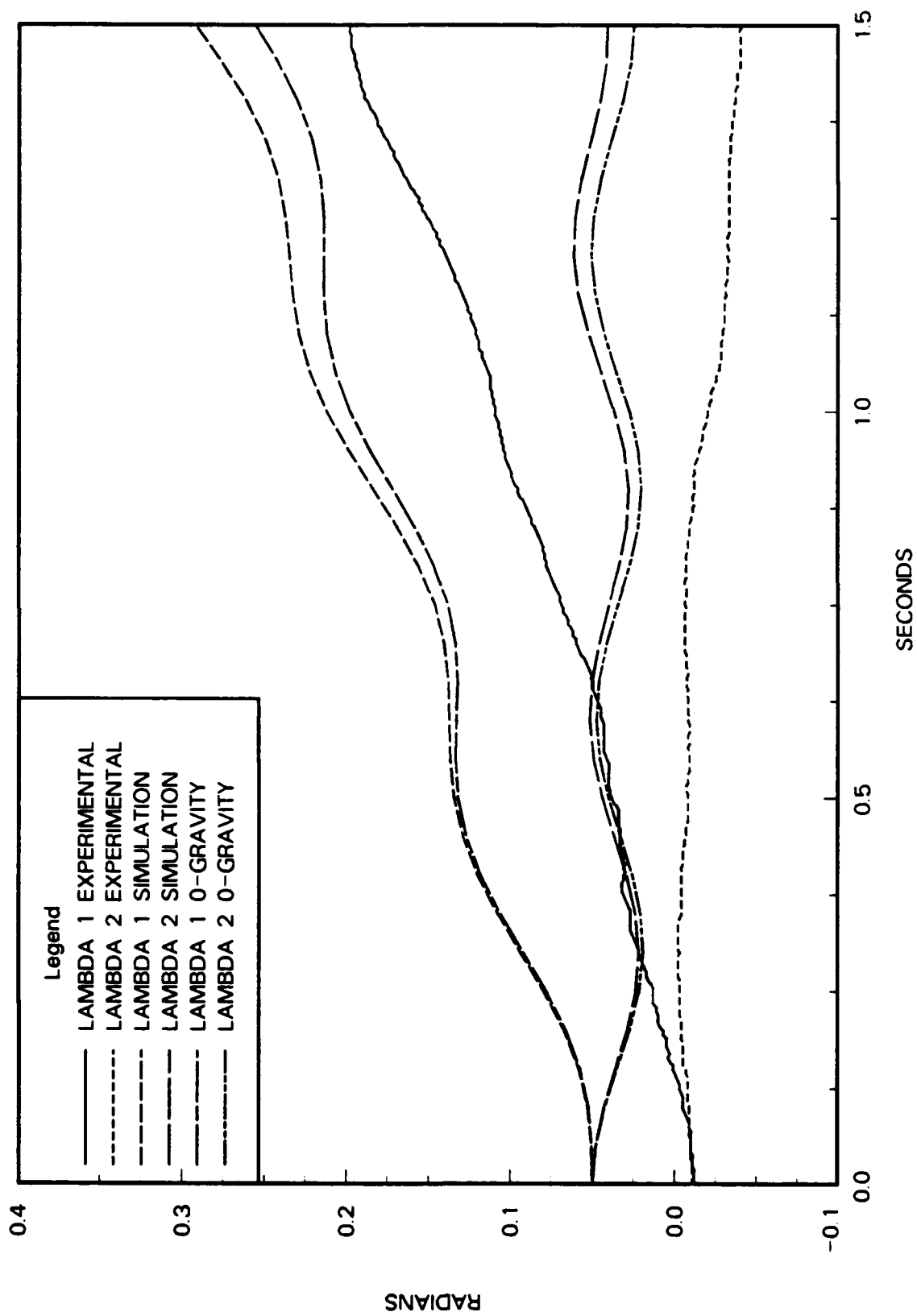


Fig. 8

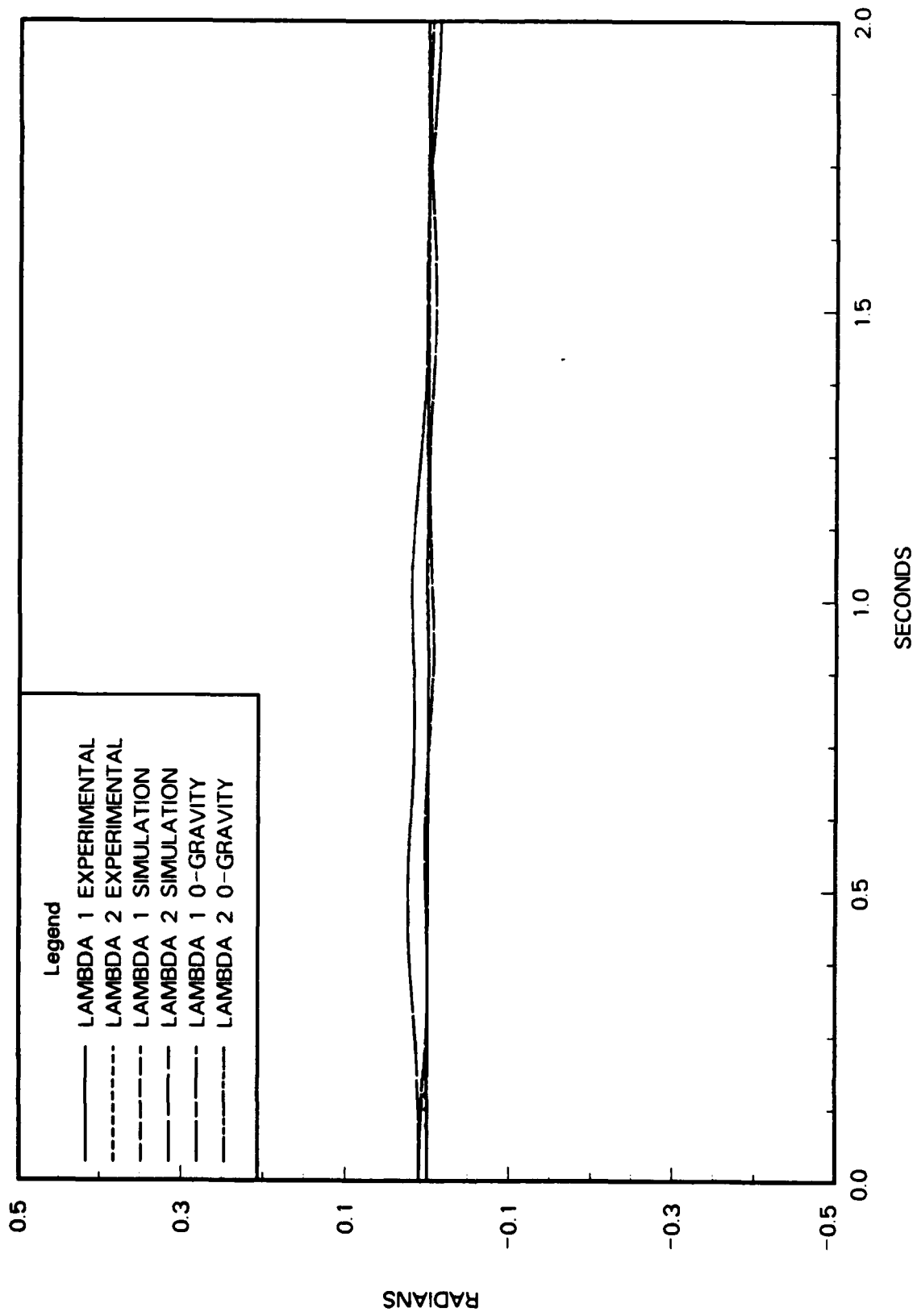


Fig. 9

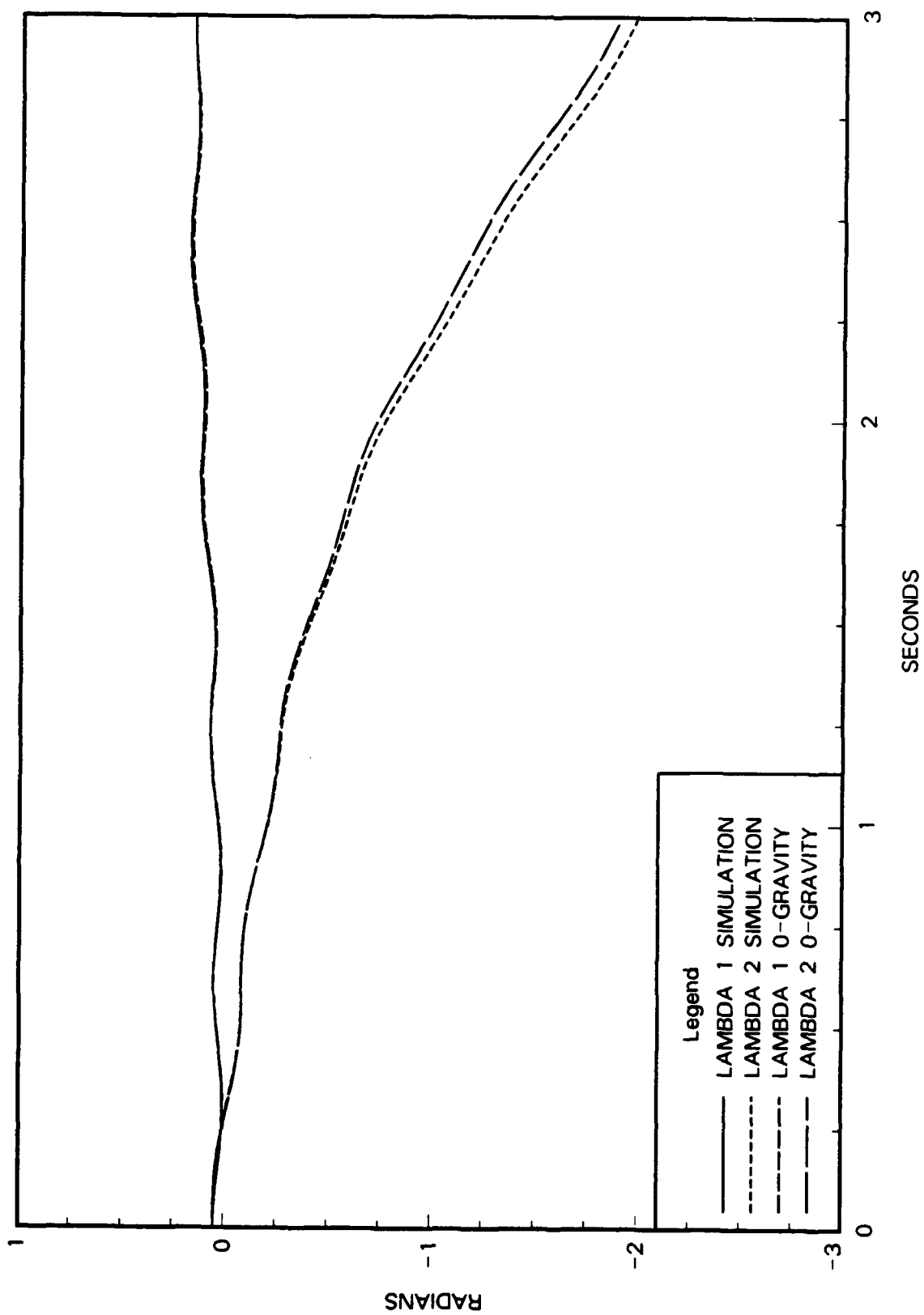


Fig. 10

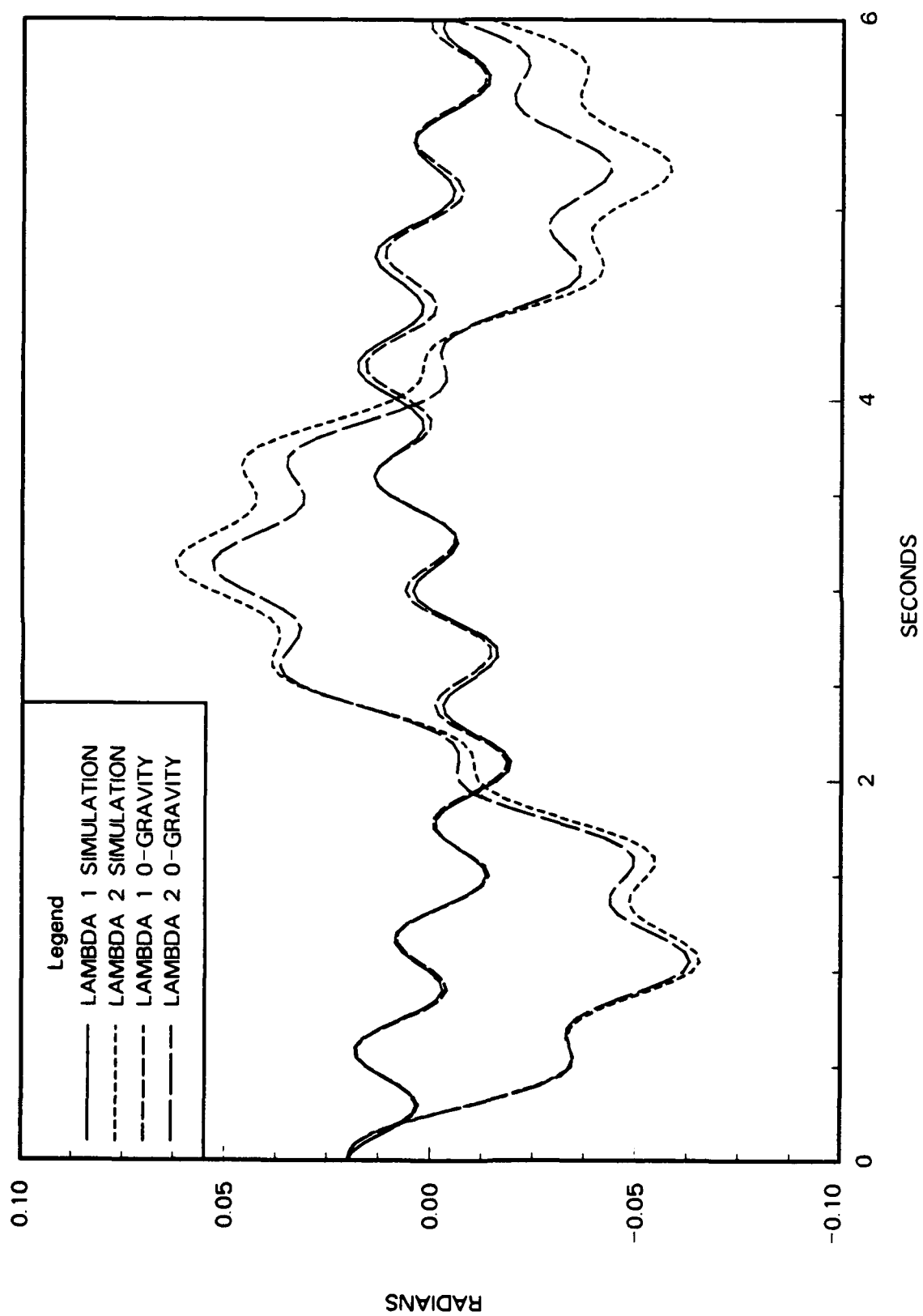


Fig. 11

**APPENDIX C. A Finite Element/Lagrangian Formulation Dynamic
Motion Prediction for a Flexible Satellite Simulator with Both Rigid and
Elastic Bodies**

A FINITE ELEMENT/LAGRANGIAN FORMULATION OF DYNAMIC MOTION PREDICTION FOR A FLEXIBLE SATELLITE SIMULATOR WITH BOTH RIGID AND ELASTIC BODIES

Jiechi Xu

Graduate Assistant

Joseph R. Baumgarten

Professor

Department of Mechanical Engineering
Iowa State University
Ames, IA 50011

ABSTRACT

In the present paper a systematic procedure has been conducted to derive dynamic equations by using Lagrange's formula for a multi-body system involving both rigid bodies and elastic members. Finite element analysis with a direct stiffness method has been employed to model the flexible subsystems. Nonlinear coupling terms between rigid body gross motion and elastic deflections are completely taken into account. Both the parameters of rigid body motion and the components of elastic displacements are considered as unknown degrees of freedom of the entire system. The assumption of specified gross motion is no longer necessary in the derivation and the resultant differential equations are highly nonlinear. Equations of motion for each individual subsystem are formulated associated with a moving frame instead of a traditional inertial coordinate system and are assembled by means of a compatibility matrix. The method is primarily developed for forward dynamics and it is also applicable in inverse dynamics.

INTRODUCTION

Flexible modeling has been an attractive but difficult topic for a long time. Severely restricted by the lag of computer speed in the early years and the complexity of mathematical formulation, traditional designs in robots, mechanisms, etc. have been limited in the realm of rigid body system. However, the increasing demands for higher operating speeds result in a situation that lightweight structures have to be used. An undesired by-product, the effect of flexibility, is now recognized as a critical issue. It becomes impossible to implement time-consuming numerical integration without solid support of sophisticated modern computers with high processing speed.

The past decade has seen significant advances in dynamic analysis for non-rigid body systems with elastic links. Extensive work has been conducted in dealing with flexible modeling. Most investigators employ a common approach that allows elastic deflections to be superimposed on gross (nominal) rigid body motion due to the nature of a specific problem. A drawback of that method is that the rigid body motion must be specified. It is, however, not always true that rigid body motion can be predefined, especially in some environments requiring that the motion of a system be predicted. Additionally there are those areas where the fluctuation between gross motion and elastic deflections are sensitive in analyzing system stability.

The purpose of this paper, therefore, is to develop a general modeling technique to conduct a systematic procedure for estab-

lishing dynamic equations of a flexible system by considering all the degrees of freedom of the system, rigid or elastic, as generalized coordinates. In addition, the procedure in formulation must be optimized and simplified so as to accommodate the needs in numerical analysis and computer programming.

PREVIOUS WORK

Flexible structure modeling, including the effects of elastic deflections and rotations, has been given considerable effort by engineers and researchers in the fields of robotics and mechanisms. A finite element method has been chosen over a modal expansion analysis to discretize the continuous systems due, in a large measure, to the fact that eigenvalues are not required to solve for the response of the system. An analytical formulation, based on energy methods, is usually applied associated with the finite element analysis (FEA) to develop dynamic equations of the system.

The first to exploit the advantages of the FEA with Lagrangian mechanics were Sunada and Dubowsky [1] [2]. Their model incorporated a Denavit-Hartenburg representation of the kinematic rigid body transformation excluding kinematic coupling. The degrees of freedom of the discretized system were reduced by means of Component Mode Synthesis (CMS). The equations of all links were assembled using a Compatibility Matrix routine. In their illustrative examples, a set of first order equations was solved numerically for a special case in which the mechanism's nominal speeds and accelerations are much smaller than the component elastic coordinate velocities and accelerations. In their later extended work, the assembly of dynamic equations was performed in symbolic form due to the special form of matrix terms. The final system equations were solved using a Newmark-Beta integration algorithm. Their approach is applicable for these problems where nominal rigid body motion is specified by kinematic constraints.

Early works by Naganathan and Soni [3] [4] [5] [6] [7] developed a fully nonlinear model employing a kinematic representation with rigid link based reference. The three-dimensional model was constructed by accounting for axial, torsional, and lateral deformations. Galerkin method was used with linear shape functions to represent the elasticity of the links. Link level matrices were transformed by time-varying compatibility matrices and cascaded into global matrices. Once again, the rigid body gross motion was specified at the revolute joints due to the nature of these problems. The element matrices then became constant at every time step in the numerical solutions.

In the work accomplished by Sadler and Yang [8] [9] [10], a total mechanism displacement was defined as a combination of the large rigid body gross motion and small elastic deformations.

Their method was applied both to planar multi-link mechanisms and to spatial robot manipulators. The effects of Rayleigh damping was introduced. In the mechanism applications, the authors claimed that their method can be employed both in the forward and inverse dynamics under conditions of either specified input forcing functions or motion of the crank in a four-bar linkage. A special treatment must be made to relate the link orientation angle to the total unknown displacement. This can be done for some mechanisms with one rigid body degree of freedom (DOF).

More recently, Nagarajan and Turcic [11] [12] developed a new approach to derive equations of motion for elastic mechanism systems. Both the rigid body and the elastic degrees of freedom were considered as generalized coordinates in their derivation. The equations were first formulated based on element level coordinate system in which elastic nodal displacements are measured. These equations were then transformed to a reference coordinate system to ensure compatibility of the displacement, velocity, and acceleration of the degrees of freedom that are common to two or more links during the assembly of the equations of motion. Due to generality in their work, the equations, both on element and system levels, are complicated and the transformation from element level to system level takes a great amount of effort which is necessary for their approach.

A literature survey of flexible models was completed by Cleghorn [13]. It was observed that the most effective model is one which incorporates Lagrange's equation with the finite element method. This produces a generalized element for easy application to flexible systems.

METHODOLOGY

In this section, a systematic procedure will be developed. Since the systems under consideration in this paper involve both rigid and elastic structures, derivations of motion equations will be all carried out. Lagrangian approach is selected to conduct system dynamics: finite element analysis with a direct stiffness method is to be employed to discretize elastic members and to determine their DOF and structural stiffness matrix in the potential energy term. For each individual body, Lagrangian equation can be expressed as

$$\frac{1}{dt} \left(\frac{\partial KE_i}{\partial \{\dot{q}_i\}^T} \right) - \frac{\partial KE_i}{\partial \{q_i\}^T} + \frac{\partial PE_i}{\partial \{q_i\}^T} = \{Q_i\} \quad (1)$$

where KE_i and PE_i are the i^{th} elastic member kinetic energy and potential energy respectively. $\{Q_i\}$ are those generalized forces not derivable from a potential function, and $\{q_i\}$ is a local vector of the generalized coordinates.

For a rigid substructure, the corresponding kinetic and potential energies are of the following forms.

$$\begin{aligned} KE_i &= \frac{1}{2} m_i \dot{V}_{ci} \cdot \dot{V}_{ci} + \frac{1}{2} \bar{I}_i \cdot \bar{\omega}_i \cdot \bar{\omega}_i \\ PE_i &= \text{gravitational potential energy} \end{aligned} \quad (2)$$

where m_i is the body mass, \dot{V}_{ci} is a velocity vector at the mass center, $\bar{\omega}_i$ is an angular velocity vector, and \bar{I}_i is an inertial dyadic about the mass center. The potential energy term is due to conservative force fields and only gravity is involved usually.

For an elastic substructure, both the kinetic and potential energy terms are different from those of a rigid substructure. They can be written as

$$\begin{aligned} KE_i &= \frac{1}{2} \sum_{g=1}^{N_i} \int_0^{l_i} \rho_i A_i \dot{V}_{ig} \cdot \dot{V}_{ig} ds \\ PE_i &= \frac{1}{2} \{q_i\}^T [k_{ii}] \{q_i\} + \text{gravitational potential energy} \end{aligned} \quad (3)$$

where g stands for grids or nodes, N_i is the total number of the elements, l_i is the length of each element, ρ_i and A_i are the mass

density and cross section area of each element respectively, and \dot{V}_{ig} is a generic velocity vector in element g . As shown above, potential energy consists of two terms. The first one is due to the structure elastic deflection and is named the elastic strain energy. The second one is due to the structure elevation in the field of gravity both in a macro rigid body motion and in a micro elastic vibration. After differentiating both the kinetic and potential energy terms and substituting them into Eq. 1, one can obtain the following matrix dynamic equations in the form of second order nonlinear ordinary differential equations with time-varying coefficient matrices for each separate substructure.

$$\begin{aligned} [m_i(q_i)] \{\ddot{q}_i\} + ([c_{ci}(q_i, \dot{q}_i)] + [c_{vi}]) \{\dot{q}_i\} + [k_i(q_i)] \{q_i\} \\ = \{f_i(q_i)\} \quad (i = 0, \dots, N) \end{aligned} \quad (4)$$

where, N is the total number of the subsystems, $[m_i]$ is a mass matrix, $[c_{ci}]$ is a damping matrix due to the Coriolis and centrifugal accelerations, $[c_{vi}]$ is a viscous damping matrix which is not derivable analytically, $[k_i]$ is a stiffness matrix including the conventional structure stiffness, and $\{f_i\}$ is a force vector involving the external active nonconservative forces.

With a set of dynamic equations for each substructure in the form of Eq. 4, one must assemble them together to form a set of equations at a global level for the entire system. One must also define a global vector of the generalized coordinates $\{q\}$ which is chosen from each local vector of the generalized coordinates $\{q_i\}$ such that every coordinate in $\{q\}$ must be independent of each other (though some coordinates in the different vectors $\{q_i\}$ may be overlapped). A relationship between the global vector and each local vector of the generalized coordinates can then be determined from

$$\{q_i\} = [\Phi_i] \{q\} \quad (5)$$

where $[\Phi_i]$ is a compatibility matrix in which each element is, in general, a function of time. By means of virtual work principle, the system equations at global level can finally be set up as

$$[M] \{\ddot{q}\} + ([C_c] + [C_v]) \{\dot{q}\} + [K] \{q\} = \{F\} \quad (6)$$

FINITE ELEMENT ANALYSIS (FEA)

Each elastic substructure will be modeled by using a predefined beam element. In order to reduce the element degrees of freedom without major loss in beam flexibility, two transverse deflections and two rotations are allowed for each node which has in general six elastic degrees of freedom. In addition, the following conditions are assumed.

- Elementary beam theory applies and elastic flexure obeys Hook's Law.
- Each beam undergoes two different bendings in two planes and is considered rigid longitudinally.
- Two orthogonal deflections are not related to each other and are therefore uncoupled.

Following a conventional direct stiffness method [14], a displacement function with the form of a polynomial function is pre-assumed first with knowledge of the external loadings. The boundary conditions are then applied followed by the direct application of the strain/stress relationships with the sign conventions of the bending moments and shear forces.

Displacement Function

From the classic elasticity theory [15], a function of static transverse deflection for a cantilever beam can be determined depending on external loading acting on the beam. With no distributed loading, the highest order of the polynomial function is of order three. Then,

$$y = a_0 + a_1 x + a_2 x^2 + a_3 x^3 \quad (7)$$

where a_i ($i = 0, 1, 2, 3$) are the constant coefficients, x and y are the corresponding elastic substructure axial and lateral coordinates. The above equation will be employed as a displacement function for each beam element.

Boundary Conditions

Four boundary conditions for each element are proposed as follows:

$$\begin{aligned} s = 0 & \text{ deflection} = d_1 \text{ and slope} = \phi_1 \\ s = l & \text{ deflection} = d_2 \text{ and slope} = \phi_2 \end{aligned}$$

where s is an element coordinate aligned with center line of an undeformed beam, d_1 and ϕ_1 ($i = 1, 2$) are the transverse displacements and rotations at the corresponding nodes, respectively, and l is the length of the element. Applying above four boundary conditions to Eq. 7, it can be demonstrated that the final displacement functions in matrix form are of the following expressions.

$$\begin{aligned} u(s) &= \{d\}^T [Y] \{s\} \\ &= \{s\}^T [Y]^T \{d\} \\ v(s) &= \{d\}^T [Z] \{s\} \\ &= \{s\}^T [Z]^T \{d\} \end{aligned}$$

and

$$\begin{aligned} \{s\} &= \{1 \ s \ s^2 \ s^3\}^T \\ \{d\} &= \{d_{1y} \ \phi_{1z} \ d_{1z} \ \phi_{1y} \ d_{2y} \ \phi_{2z} \ d_{2z} \ \phi_{2y}\}^T \end{aligned} \quad (8)$$

where $\{d\}$ are the generalized coordinates for each beam element, $\{s\}$ is a generalized function vector, $[Y]$ and $[Z]$ are constant matrices (see Appendix A), and $\{s\}^T [Y]^T$ and $\{s\}^T [Z]^T$ are conventional shape functions for each planar bending.

Structure Stiffness Matrix

For small elastic deflection, the bending moments and shear forces, in the case of plane x - y for instance, are found to be

$$\begin{aligned} m(s) &= EI_z \frac{\partial^2 v}{\partial s^2} \\ V(s) &= EI_z \frac{\partial^3 v}{\partial s^3} \end{aligned} \quad (9)$$

where E is Young's modulus and I_z is the principal moment of inertia about the z axis. According to Eq. 8, an element nodal force vector is correspondingly defined as

$$\{f\} = \{f_{1y} \ m_{1z} \ f_{1z} \ m_{1y} \ f_{2y} \ m_{2z} \ f_{2z} \ m_{2y}\}^T \quad (10)$$

Applying four force boundary conditions for each node in Eq. 9 followed by comparing the following form

$$\{f\} = [k_s] \{d\}, \quad (11)$$

a final expression of the structure stiffness matrix can be obtained and formulated as

$$[k_s] = \frac{EI}{l^3} (C_x [\beta_1]^T [k_1] [\beta_1] + C_y [\beta_2]^T [k_2] [\beta_2]) \quad (12)$$

where $[k_s]$ is a symmetric matrix, l is the length of an element, I is an average value of I_y and I_z , C_y and C_z are two constant ratios of I_y and I_z to l respectively, $[\beta_1]$ and $[\beta_2]$ (see Appendix A) are two constant matrices with either unity elements or zero elements, and $[k_1]$ and $[k_2]$ are the bending stiffness matrices for the corresponding planes.

DERIVATION OF DYNAMIC EQUATIONS AT LOCAL LEVEL

As illustrated in Fig. 1, the coordinate system $(\hat{i}_0, \hat{j}_0, \hat{k}_0)$ is a floating (moving) frame attached to the moving system, and set $(\hat{i}_1, \hat{j}_1, \hat{k}_1)$ is a reference frame for an arbitrary beam i . \hat{R}_i is a rigid body position vector, which describes the rigid body motion of the system. \hat{p}_{ig} is a local position vector measured in the reference frame for an arbitrary point P' in element g after deflection, which is considered as a position vector due to elastic deformation. \bar{r}_{ig} is an absolute position vector of the point P'

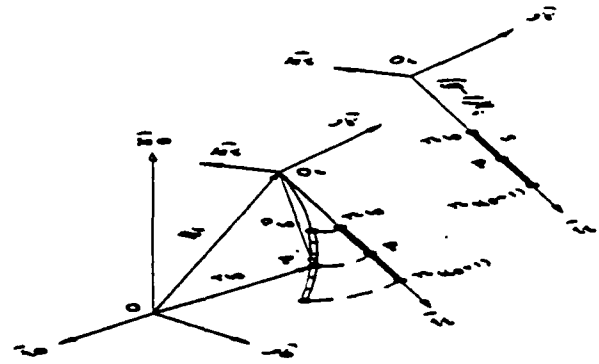


Figure 1: Elastic Deflection of A Generic Flexible Beam

relative to the moving frame $(\hat{i}_0, \hat{j}_0, \hat{k}_0)$, which combines the rigid body motion and elastic vibration.

Position and Velocity Vectors

A position vector describing point P' can be found as

$$\begin{aligned} \bar{r}_{ig} &= \hat{R}_i + \hat{p}_{ig} \\ &= \{\hat{e}_0\}^T (\{R_i\} + [T_{0i}] \{\rho_{ig}\}) \end{aligned} \quad (13)$$

where $\{\hat{e}_0\} = \{\hat{i}_0 \ \hat{j}_0 \ \hat{k}_0\}^T$, a unit direction vector, $\{R_i\}$ and $\{\rho_{ig}\}$ are the rigid and elastic position vectors, and $[T_{0i}]$ is a transformation matrix between two frames mentioned above. A corresponding matrix equation formulated in the moving frame takes the following form.

$$\{r_{ig}\} = \{R_i\} + [T_{0i}] \{\rho_{ig}\} \quad (14)$$

Differentiating the above equation gives a velocity equation which can be written as

$$\begin{aligned} \{\dot{r}_{ig}\} &= [\hat{\Omega}] (\{R_i\} + [T_{0i}] \{\rho_{ig}\}) + \{R_i\} \\ &\quad + [T_{0i}] \{\dot{\rho}_{ig}\} + [\dot{T}_{0i}] \{\rho_{ig}\} \end{aligned} \quad (15)$$

where $\{\dot{r}_{ig}\}$ denotes $d\{r_{ig}\}/dt$, $\{\dot{R}_i\}$, $\{\dot{\rho}_{ig}\}$, and $[\dot{T}_{0i}]$ are the time rates of the corresponding vectors and the transformation matrix, and $[\hat{\Omega}]$ (see Appendix B) is a skew matrix derived from a rigid body system angular velocity $\{\Omega\}$ which can be expressed as

$$\{\Omega\} = [N] \{\dot{\lambda}\} \quad (16)$$

where $\{\dot{\lambda}\}$ are the time rates of the rigid body generalized coordinates, and $[N]$ is a time-varying coefficient matrix which can be partitioned¹ as $[\underline{N}_1 \ \underline{N}_2 \ \underline{N}_3]^T$.

For a case with no relative motion between the moving and reference frames, Eq. 15 can be written in the following form in detail after substituting Eqs. 16 and 8 into Eq. 15 followed by rearrangement and a new definition for the i^{th} beam generalized coordinates $\{q_i\}$ composed of both rigid body generalized coordinates $\{\lambda\}$ and elastic generalized coordinates $\{d_1\}, \{d_2\}, \dots, \{d_m\}$ (see Eq. 8).

$$\begin{aligned} \{\dot{r}_{ig}\} &= \begin{bmatrix} (R_{i3} + T_{31}\rho_{ig})\underline{N}_3 - \\ (R_{i1} + T_{11}\rho_{ig})\underline{N}_2 - \\ (R_{i2} + T_{21}\rho_{ig})\underline{N}_1 - \\ (R_{i2} + T_{21}\rho_{ig})\underline{N}_3 \\ (R_{i3} + T_{31}\rho_{ig})\underline{N}_1 \\ (R_{i1} + T_{11}\rho_{ig})\underline{N}_2 \end{bmatrix} [\Theta_{i,\lambda}] \{\dot{q}_i\} + \\ &\quad \begin{bmatrix} \underline{z}^T (Y^T T_{12} + Z^T T_{13}) \\ \underline{z}^T (Y^T T_{22} + Z^T T_{23}) \\ \underline{z}^T (Y^T T_{32} + Z^T T_{33}) \end{bmatrix} [\Theta_{i,d}] \{\dot{q}_i\} + \end{aligned}$$

¹ A matrix is also denoted by a letter with underline, i.e., \underline{N} .

$$\begin{bmatrix} \frac{1}{2} \frac{\partial}{\partial \dot{q}_1} \{ (T_{11} \dot{Y}_1 + T_{12} \dot{Z}_1) \dot{Y}_2 - \\ \frac{1}{2} \frac{\partial}{\partial \dot{q}_2} \{ (T_{12} \dot{Y}_1 + T_{11} \dot{Z}_1) \dot{Y}_2 - \\ \frac{1}{2} \frac{\partial}{\partial \dot{q}_3} \{ (T_{21} \dot{Y}_1 + T_{22} \dot{Z}_1) \dot{Y}_2 - \\ (T_{22} \dot{Y}_1 + T_{21} \dot{Z}_1) \dot{Y}_2 \} \} \\ \frac{1}{2} \frac{\partial}{\partial \dot{q}_4} \{ (T_{21} \dot{Y}_1 + T_{22} \dot{Z}_1) \dot{Y}_2 - \\ (T_{22} \dot{Y}_1 + T_{21} \dot{Z}_1) \dot{Y}_2 \} \} \\ \frac{1}{2} \frac{\partial}{\partial \dot{q}_5} \{ (T_{21} \dot{Y}_1 + T_{22} \dot{Z}_1) \dot{Y}_2 - \\ (T_{22} \dot{Y}_1 + T_{21} \dot{Z}_1) \dot{Y}_2 \} \} \end{bmatrix} \{ \Theta_{1,1} \} \{ \dot{q}_i \} \quad (17)$$

where R_{ij} ($j = 1, 2$) are the components of the rigid body position vector $\{R_i\}$, $\rho_{gs} = (j-1)l_s + s$, T_{ij} are the elements in the 3×3 transformation matrix $[T_{0i}]$, and

$$\begin{aligned} \{ \dot{q}_i \}^T &= \{ \dot{Y}_1^T \quad \dot{Y}_2^T \quad \dots \quad \dot{Y}_m^T \quad \dot{Z}_1^T \quad \dots \quad \dot{Z}_m^T \} \\ \{ \Theta_{1,1} \} &= \{ I_{11} \quad 0 \} \\ \{ \Theta_{1,gd} \} &= \{ 0 \quad I_{11} \quad 0 \} \\ \{ \Lambda \} &= \{ \Theta_{1,1} \} \{ \dot{q}_i \} \\ \{ \dot{q}_i \} &= \{ \Theta_{1,gd} \} \{ \dot{q}_i \} \end{aligned} \quad (18)$$

where $\{ \Theta_{1,1} \}$ and $\{ \Theta_{1,gd} \}$ are types of compatibility matrices, $\{ \dot{q}_i \}$ are the generalized coordinates, $[I_1]$ and $[I_d]$ are the 3×3 and 3×3 unit matrices respectively, and 0 's are the zero matrices.

Elastic Beam Kinetic Energy

It can be demonstrated that premultiplying the velocity vector (see Eq. 17) by its transpose vector will result in a velocity square term as shown below.

$$\begin{aligned} \dot{q}_i^2 &= \{ \dot{q}_i \}^T \left(\{ \Theta_{1,1} \}^T [V]^T \begin{bmatrix} \dot{R}_1^2 + \dot{R}_2^2 & -\dot{R}_1 \dot{R}_2 \\ -\dot{R}_1 \dot{R}_2 & -\dot{R}_2 \dot{R}_1 \end{bmatrix} \right. \\ &\quad \left. \begin{array}{l} \text{Symmetry} \\ \dot{R}_1^2 + \dot{R}_2^2 \end{array} \right) [V][\Theta_{1,1}] + \\ &\quad \{ \Theta_{1,gd} \}^T (\dot{B}_{11} + \dot{B}_{22} + \dot{B}_{33}) \{ \Theta_{1,gd} \} + \\ &\quad \{ \Theta_{1,1} \}^T [V]^T \begin{bmatrix} \frac{1}{2} \frac{\partial}{\partial \dot{q}_1} \{ (\dot{B}_{22} + \dot{B}_{33}) \} \frac{\partial}{\partial \dot{q}_1} \dot{q}_1 \\ -\frac{1}{2} \frac{\partial}{\partial \dot{q}_2} \{ (\dot{B}_{22} + \dot{B}_{33}) \} \frac{\partial}{\partial \dot{q}_1} \dot{q}_1 \\ -\frac{1}{2} \frac{\partial}{\partial \dot{q}_3} \{ (\dot{B}_{22} + \dot{B}_{33}) \} \frac{\partial}{\partial \dot{q}_1} \dot{q}_1 \\ \vdots \\ -\frac{1}{2} \frac{\partial}{\partial \dot{q}_m} \{ (\dot{B}_{22} + \dot{B}_{33}) \} \frac{\partial}{\partial \dot{q}_1} \dot{q}_1 \\ \vdots \\ \frac{1}{2} \frac{\partial}{\partial \dot{q}_1} \{ (\dot{B}_{22} + \dot{B}_{33}) \} \frac{\partial}{\partial \dot{q}_2} \dot{q}_2 \\ \vdots \\ -\frac{1}{2} \frac{\partial}{\partial \dot{q}_2} \{ (\dot{B}_{22} + \dot{B}_{33}) \} \frac{\partial}{\partial \dot{q}_2} \dot{q}_2 \\ \vdots \\ \frac{1}{2} \frac{\partial}{\partial \dot{q}_1} \{ (\dot{B}_{22} + \dot{B}_{33}) \} \frac{\partial}{\partial \dot{q}_3} \dot{q}_3 \\ \vdots \\ -\frac{1}{2} \frac{\partial}{\partial \dot{q}_3} \{ (\dot{B}_{22} + \dot{B}_{33}) \} \frac{\partial}{\partial \dot{q}_3} \dot{q}_3 \\ \vdots \\ \frac{1}{2} \frac{\partial}{\partial \dot{q}_1} \{ (\dot{B}_{22} + \dot{B}_{33}) \} \frac{\partial}{\partial \dot{q}_m} \dot{q}_m \\ \vdots \\ -\frac{1}{2} \frac{\partial}{\partial \dot{q}_m} \{ (\dot{B}_{22} + \dot{B}_{33}) \} \frac{\partial}{\partial \dot{q}_m} \dot{q}_m \end{bmatrix} [V][\Theta_{1,1}] + \\ &\quad \{ \Theta_{1,1} \}^T [V]^T \begin{bmatrix} \dot{D}_{23} - \dot{D}_{32} \\ \dot{D}_{31} - \dot{D}_{13} \\ \dot{D}_{12} - \dot{D}_{21} \end{bmatrix} \{ \Theta_{1,gd} \} + \\ &\quad \{ \Theta_{1,gd} \}^T \begin{bmatrix} \dot{D}_{23} - \dot{D}_{32} & \dot{D}_{31} - \dot{D}_{13} & \dot{D}_{12} - \dot{D}_{21} \end{bmatrix} \cdot \\ &\quad [V][\Theta_{1,1}] + \{ \Theta_{1,1} \}^T [V]^T \begin{bmatrix} 2(\dot{D}_{23} + \dot{D}_{32}) \frac{\partial}{\partial \dot{q}_1} \dot{q}_1 \\ -(\dot{D}_{12} + \dot{D}_{21}) \frac{\partial}{\partial \dot{q}_2} \dot{q}_2 \\ -(\dot{D}_{13} + \dot{D}_{31}) \frac{\partial}{\partial \dot{q}_3} \dot{q}_3 \end{bmatrix} \\ &\quad \left. \begin{array}{l} \vdots \\ 2(\dot{D}_{11} + \dot{D}_{33}) \frac{\partial}{\partial \dot{q}_1} \dot{q}_1 \\ \vdots \\ -(\dot{D}_{23} + \dot{D}_{32}) \frac{\partial}{\partial \dot{q}_2} \dot{q}_2 \\ \vdots \\ 2(\dot{D}_{11} + \dot{D}_{22}) \frac{\partial}{\partial \dot{q}_3} \dot{q}_3 \end{array} \right] [V][\Theta_{1,1}] + \\ &\quad \{ \Theta_{1,1} \}^T [V]^T \begin{bmatrix} \frac{1}{2} \frac{\partial}{\partial \dot{q}_1} \{ (\dot{B}_{22} - \dot{B}_{33}) \} \frac{\partial}{\partial \dot{q}_1} \dot{q}_1 \\ \frac{1}{2} \frac{\partial}{\partial \dot{q}_2} \{ (\dot{B}_{22} - \dot{B}_{33}) \} \frac{\partial}{\partial \dot{q}_1} \dot{q}_1 \\ \frac{1}{2} \frac{\partial}{\partial \dot{q}_3} \{ (\dot{B}_{22} - \dot{B}_{33}) \} \frac{\partial}{\partial \dot{q}_1} \dot{q}_1 \\ \vdots \\ \frac{1}{2} \frac{\partial}{\partial \dot{q}_1} \{ (\dot{B}_{22} - \dot{B}_{33}) \} \frac{\partial}{\partial \dot{q}_2} \dot{q}_2 \\ \vdots \\ \frac{1}{2} \frac{\partial}{\partial \dot{q}_2} \{ (\dot{B}_{22} - \dot{B}_{33}) \} \frac{\partial}{\partial \dot{q}_2} \dot{q}_2 \\ \vdots \\ \frac{1}{2} \frac{\partial}{\partial \dot{q}_1} \{ (\dot{B}_{22} - \dot{B}_{33}) \} \frac{\partial}{\partial \dot{q}_3} \dot{q}_3 \\ \vdots \\ \frac{1}{2} \frac{\partial}{\partial \dot{q}_3} \{ (\dot{B}_{22} - \dot{B}_{33}) \} \frac{\partial}{\partial \dot{q}_3} \dot{q}_3 \\ \vdots \\ \frac{1}{2} \frac{\partial}{\partial \dot{q}_1} \{ (\dot{B}_{22} - \dot{B}_{33}) \} \frac{\partial}{\partial \dot{q}_m} \dot{q}_m \\ \vdots \\ \frac{1}{2} \frac{\partial}{\partial \dot{q}_m} \{ (\dot{B}_{22} - \dot{B}_{33}) \} \frac{\partial}{\partial \dot{q}_m} \dot{q}_m \end{bmatrix} \{ \Theta_{1,1} \} + \end{aligned}$$

$$\{ \Theta_{1,gd} \}^T \left((\dot{B}_{12} - \dot{B}_{21}) \frac{\partial}{\partial \dot{q}_1} \dot{q}_1 (\dot{B}_{13} - \dot{B}_{31}) \frac{\partial}{\partial \dot{q}_1} \dot{q}_1 \right. \\ \left. (\dot{B}_{21} - \dot{B}_{12}) \frac{\partial}{\partial \dot{q}_2} \dot{q}_2 \right) [V][\Theta_{1,1}] \{ \dot{q}_i \} \quad (19)$$

where $\{ \Theta_{1,1} \}$, $\{ \Theta_{1,gd} \}$, $\{ \dot{B}_{ij} \}$ ($i, j = 1, 2, 3$), and $\{ \dot{D}_{ij} \}$ ($i, j = 1, 2, 3$) are all constant matrices (see Appendix A). Substituting the above equation into Eq. 3 followed by rearrangement yields a compact equation of the kinetic energy for an elastic beam.

$$KE = \frac{1}{2} \{ \dot{q}_i \}^T [m_i] \{ \dot{q}_i \} \quad (20)$$

where $[m_i]$ is a symmetric mass matrix having the following form.

$$\begin{aligned} [m_i] &= [m_{ic}] + \{ \Theta_{1,1} \}^T [V]^T \cdot \\ &\quad \left([G_{11}] + \left[\frac{1}{2} \frac{\partial}{\partial \dot{q}_1} \{ (\dot{B}_{22} - \dot{B}_{33}) \} \frac{\partial}{\partial \dot{q}_1} \dot{q}_1 \right. \right. \\ &\quad \left. \left. [G_{12}] + \left[\frac{1}{2} \frac{\partial}{\partial \dot{q}_2} \{ (\dot{B}_{22} - \dot{B}_{33}) \} \frac{\partial}{\partial \dot{q}_1} \dot{q}_1 \right. \right. \right. \\ &\quad \left. \left. \left. [G_{12}]^T + \left[\frac{1}{2} \frac{\partial}{\partial \dot{q}_1} \{ (\dot{B}_{22} - \dot{B}_{33}) \} \frac{\partial}{\partial \dot{q}_2} \dot{q}_2 \right. \right. \right. \right. \end{aligned} \quad (21)$$

where $[m_{ic}]$ and $[G_{11}]$ are the constant symmetric square matrices (see Appendix A), $\{ \dot{B}_{22} \}$ and $\{ \dot{B}_{33} \}$ ($i, j = 1, 2, 3$) are the constant nonsymmetric square matrices, $\{ \dot{D}_{32} \}$ ($i, j = 1, 2, 3$) are the constant vectors, and $[G_{12}]$ is a constant rectangular matrix.

Elastic Beam Potential Energy

The total potential energy is a summation of the body force potential energy and the elastic strain energy. The former is the negative work done by gravity. The latter can be written as

$$U_{e1} = \frac{1}{2} \sum_{g=1}^{N_1} \{ \dot{q}_i \}^T \{ [k_{1,g}] \{ \dot{q}_i \} \} \quad (22)$$

where $[k_{1,g}]$ is a structural stiffness matrix, developed in the previous section, for g^{th} element of beam 1. According to Eqs. 12 and 14, it can be shown that the total potential energy takes the following form as

$$PE = \frac{1}{2} \{ \dot{q}_i \}^T [k_{11}] \{ \dot{q}_i \} + V_i + \{ h_i \}^T \{ \dot{q}_i \} \quad (23)$$

where the term V_i and vector $\{ h_i \}$ are the functions of the generalized coordinates $\{ \dot{q}_i \}$. The first term represents the elastic strain energy. The last two terms, on the other hand, combine the body force potential energy in which the term V_i is due to the rigid body motion while the term $\{ h_i \}^T \{ \dot{q}_i \}$ is due to the elastic deflections.

Local Level Dynamic Equations

Substituting Eqs. 20 and 22 into Lagrangian formula, Eq. 1, will yield a set of dynamic equations in matrix form for the i^{th} elastic beam.

$$[m_i] \{ \ddot{q}_i \} + [c_i] \{ \dot{q}_i \} + [k_i] \{ q_i \} = \{ f_i \} \quad (24)$$

where $[m_i]$ is a mass matrix, $[c_i]$ is a damping matrix which results from Coriolis and centrifugal accelerations, $[k_i]$ is a stiffness matrix accounting for both the structural stiffness due to elastic deflections and the coupling term between rigid body motion and elastic deformation, and $\{ f_i \}$ is a generalized force vector. In general, the mass and stiffness matrices and the force vector are the functions of generalized coordinates $\{ q_i \}$ while the damping matrix is a function of both $\{ q_i \}$ and $\{ \dot{q}_i \}$. Furthermore, these coefficient matrices and force vectors can be written as

$$\begin{aligned} [c_i] &= [m_i] - \frac{1}{2} \frac{\partial ([m_i]^T \{ \dot{q}_i \})}{\partial \{ \dot{q}_i \}^T} \\ [k_i] &= [k_{11}] + [J_i] \\ \{ f_i \} &= \{ f_{a1} \} + \{ f_{c1} \} - \{ f_{11} \} - \{ f_{12} \} \end{aligned} \quad (25)$$

where $\{\dot{m}_i\}$ is the time rate of the mass matrix $\{m_i\}$, $\{f_{ci}\}$ is a force vector due to the external loadings, $\{f_{ci}\}$ is a connecting force vector (which would vanish automatically in the matrix assembly from the local level to the global level with the condition of the selection of the independent global generalized coordinates), and the matrix $\{J_i\}$ and the vectors $\{f_{i1}\}$ and $\{f_{i2}\}$ are all derived from the potential energy term as shown in Appendix A. The damping matrix $\{c_i\}$ consists of a Coriolis term and a centrifugal term. The former is a symmetric matrix. The latter is a nonsymmetric matrix and is derived in Appendix C.

Derivation of motion equations for rigid members in a system can also be done by following the procedures demonstrated in the previous sections. First, one should identify a position vector, like the one shown in Eq. 14, which will account for elastic displacements of the flexible substructures preceding the rigid body. Second, a velocity square term resulted from differentiating the position vector could be found. Third, it is necessary to obtain an inertial dyadic of the rigid body about its mass center and an angular velocity vector including the rigid body angular velocity and the elastic rotation rates influenced by deflections. The final step is to find rigid body kinetic and potential energies as shown in Eq. 2 followed by substituting the results into Lagrange's equation.

GLOBAL LEVEL DYNAMIC EQUATIONS

In the previous sections, it has been demonstrated that each of the subsystem has a different set of dynamic equations expressed at the local level. Assembling these subsystem equations at the global level will constitute the system dynamic equations. An assembly routine must be found so as that the coefficient matrices and the generalized force vectors for each substructure are compatible. Geometric constraints between the subsystems must be applied. One must also define a set of global generalized coordinates which are independent of each other.

Compatibility Matrix

A matrix which linearly relates the local coordinates with the global coordinates is called the compatibility matrix. For a system with an independent set of global generalized coordinates $\{q\}$ with n components, these local coordinates $\{q_i\}$ with m elements for the i^{th} subsystem can be expressed as

$$\{q_i\} = [\Phi_i]\{q\} \quad (26)$$

where the compatibility matrix $[\Phi_i]$ is an $m \times n$ matrix and is in general a time-varying function of the rigid body generalized coordinates.

Assembly of Subsystem Equations

Differentiating Eq. 26 with respect to time and applying the results into subsystem equation, Eq. 24, will result in the following system dynamic equations.

$$[M]\{\ddot{q}\} + [C]\{\dot{q}\} + [K]\{q\} = \{F\} \quad (27)$$

where the global mass, damping, and stiffness matrices and the global generalized force vector are formulated as follows:

$$[M] = \sum_{i=1}^N [\Phi_i]^T [m_i] [\Phi_i]$$

$$[C] = \sum_{i=1}^N ([\Phi_i]^T [c_i] [\Phi_i] + 2[\Phi_i]^T [m_i] [\dot{\Phi}_i])$$

$$[K] = \sum_{i=1}^N ([\Phi_i]^T [k_i] [\Phi_i] + [\Phi_i]^T [c_i] [\dot{\Phi}_i] + [\Phi_i]^T [m_i] [\ddot{\Phi}_i])$$

$$\{F\} = \sum_{i=1}^N [\Phi_i]^T \{f_i\} \quad (28)$$

where N is the total number of the subsystems. Structural and/or fluid viscous damping matrices can be added in each $\{c_i\}$ matrix, and the connecting force terms in each $\{f_i\}$ vector will vanish automatically during the process of matrix assembly.

CONCLUSIONS

A systematic mathematical model predicting the dynamic motion for a multi-body system including both rigid and elastic substructures has been fully developed in this paper. A conventional finite element analysis with a direct stiffness method is used to discretize the elastic continuous subsystems. A third order polynomial function is adopted in the shape function in order to exclude the effects of longitudinal displacement and beam twisting which are usually of higher order magnitudes compared with other deformations in the most flexible systems. The Lagrangian equation is employed, with both the rigid body degrees of freedom and the elastic degrees of freedom treated as generalized coordinates of the entire system. The elastic deformations of each element are measured at a substructure level, which is based on a corresponding undeformed body, so that they are compatible at the local level. Kinetic energy and potential energy are formulated for both the elastic and rigid members. Nonlinear coupling terms due to Coriolis motion are completely derived and are explicitly expressed in a matrix form.

The final set of system dynamic equations of motion is expressed in a closed form showing high nonlinearity with time-varying coefficient matrices and generalized force terms. Numerical technique which can solve the equations with mixed rigid and elastic variables is under investigation. The procedure developed in this paper is applicable to the flexible system with planar motion, as well as spatial motion.

ACKNOWLEDGEMENT

The authors would like to acknowledge the financial support of the Air Force Office of Scientific Research under Grant No. AFOSR-89-0403.

References

- [1] Sunada, W.H. and Dubowsky, S., 1981, "The Application of Finite Element Methods to the Dynamic Analysis of Flexible Spatial and Co-Planar Linkage Systems," *ASME Journal of Mechanical Design*, Vol. 103, pp. 643-651.
- [2] Sunada, W.H. and Dubowsky, S., 1983, "On the Dynamic Analysis and Behavior of Industrial Robotic Manipulators with Elastic Members," *ASME Journal of Mechanisms, Transmissions, and Automation in Design*, Vol. 105, pp. 42-51.
- [3] Naganathan, G. and Soni, A.H., 1986, "Non-Linear Flexibility Studies for Spatial Manipulators," *IEEE International Conference on Decision and Control*, Vol. 1, pp. 373-378.
- [4] Naganathan, G. and Soni, A.H., 1987, "Coupling Effects of Kinematics and Flexibility in Manipulators," *The International Journal of Robotics Research*, Vol. 6, No. 1, pp. 75-84.
- [5] Naganathan, G. and Soni, A.H., 1987, "An Analytical and Experimental Investigation of Flexible Manipulator Performance," *IEEE International Conference on Robotics and Automation*, Vol. 1, pp. 767-773.
- [6] Naganathan, G. and Soni, A.H., 1988, "Nonlinear Modeling of Kinematic and Flexibility Effects in Manipulator Design," *ASME Journal of Mechanisms, Transmissions, and Automation Design*, Vol. 110, pp. 243-254.

- [7] Naganathan, G. and Soni, A.H., "Dynamic Response of a Manipulator," 5th Applied Mechanisms Conference Proceedings, Kansas City, Missouri, Vol. 2, Session XII.A, pp. III.1-6.
- [8] Sadler, J.P., Yang, Z., and Rouch, K.E., 1988, "The Use of ANSYS for the Analysis of Flexible Four-Bar Linkages," *Trends and Developments in Mechanisms, Machines, and Robots-1988*, ASMEDE-Vol. 15-2, pp. 441-447.
- [9] Yang, Z. and Sadler, J.P., 1990, "Large Displacement Finite Element Analysis of Flexible Linkages," *ASME Journal of Mechanical Design*, Vol. 112, pp. 175-182.
- [10] Yang, Z. and Sadler, J.P., 1990, "Finite Element Modeling of Spatial Robot Manipulators," *ASME 21st Mechanisms, Machines, and Robots Conference*, September, 1990, Chicago, IL.
- [11] Nagarajan, S. and Turcic, D.A., 1990, "Lagrangian Formulation of the Equations of Motion for Elastic Mechanisms With Mutual Dependence Between Rigid Body and Elastic Motions. Part I: Element Level Equations," *Journal of Dynamic Systems, Measurement, and Control*, Vol. 112, pp. 203-214.
- [12] Nagarajan, S. and Turcic, D.A., 1990, "Lagrangian Formulation of the Equations of Motion for Elastic Mechanisms With Mutual Dependence Between Rigid Body and Elastic Motions. Part II: System Equations," *Journal of Dynamic Systems, Measurement, and Control*, Vol. 112, pp. 215-224.
- [13] Gaultier, P.E. and Cleghorn, W.L., 1989, "Modeling of Flexible Manipulator Dynamics: A Literature Survey," *The 1st National Conference on Applied Mechanisms and Robotics*, Cincinnati, Ohio, 89AMR-2C-3, pp. 1-10.
- [14] Logan, D.L., 1986, *A First Course in The Finite Element Analysis*, PWS Publishers.
- [15] Timoshenko, S. and Gere, J., 1972, *Mechanics of Materials*, Van Nostrand Reinhold Company.

APPENDICES

A: Coefficient Matrices

$$[Y] = \begin{bmatrix} \frac{1}{L} & \frac{D_1}{L} \\ \frac{0}{L} & \frac{0}{L} \\ \frac{0}{L} & \frac{D_2}{L} \\ \frac{0}{L} & \frac{0}{L} \end{bmatrix} \quad [Z] = \begin{bmatrix} \frac{0}{L} & \frac{0}{L} \\ \frac{1}{L} & \frac{D_3}{L} \\ \frac{0}{L} & \frac{0}{L} \\ \frac{0}{L} & \frac{D_4}{L} \end{bmatrix} \quad [T] = \begin{bmatrix} 1 & 0 \\ 0 & -1 \end{bmatrix}$$

$$[D_1] = \begin{bmatrix} -\frac{1}{L^2} & \frac{1}{L^2} \\ -\frac{1}{L^2} & \frac{1}{L^2} \end{bmatrix} \quad [D_2] = \begin{bmatrix} \frac{1}{L^2} & -\frac{1}{L^2} \\ -\frac{1}{L^2} & \frac{1}{L^2} \end{bmatrix}$$

$$[D_3] = \begin{bmatrix} \frac{1}{L^2} & -\frac{1}{L^2} \\ \frac{1}{L^2} & -\frac{1}{L^2} \end{bmatrix} \quad [k_1] = \begin{bmatrix} 12 & 6l & -12 & 6l \\ 6l & 4l^2 & -6l & 2l^2 \\ -12 & -6l & 12 & -6l \\ 6l & 2l^2 & -6l & 4l^2 \end{bmatrix} \quad \text{Sym}$$

$$[D_4] = \begin{bmatrix} -\frac{1}{L^2} & \frac{1}{L^2} \\ \frac{1}{L^2} & -\frac{1}{L^2} \end{bmatrix} \quad [k_2] = \begin{bmatrix} 12 & 6l & -12 & 6l \\ -6l & 4l^2 & 6l & -2l^2 \\ -12 & 6l & 12 & -6l \\ -6l & -2l^2 & 6l & 4l^2 \end{bmatrix} \quad \text{Sym}$$

$$[\beta_1] = \begin{bmatrix} \frac{1}{L} & \frac{0}{L} & \frac{0}{L} & \frac{0}{L} \\ \frac{0}{L} & \frac{0}{L} & \frac{1}{L} & \frac{0}{L} \end{bmatrix} \quad [\beta_2] = \begin{bmatrix} \frac{0}{L} & \frac{1}{L} & \frac{0}{L} & \frac{0}{L} \\ \frac{0}{L} & \frac{0}{L} & \frac{0}{L} & \frac{1}{L} \end{bmatrix}$$

where $[I]$ is a 2×2 unit matrix and $[0]$ is a 2×2 zero matrix.

$$\{\dot{R}\} = \begin{Bmatrix} \dot{R}_1 \\ \dot{R}_2 \\ \dot{R}_3 \end{Bmatrix} = \begin{Bmatrix} R_{11} + T_{11}\rho_{1gs} \\ R_{12} + T_{21}\rho_{1gs} \\ R_{13} + T_{31}\rho_{1gs} \end{Bmatrix}$$

$$\{\dot{z}\} = \begin{Bmatrix} T_{12}Y + T_{13}Z \\ T_{22}Y + T_{23}Z \\ T_{32}Y + T_{33}Z \end{Bmatrix}$$

$$\{\dot{\theta}\} = \begin{Bmatrix} \dot{\theta}_{11} & \dot{\theta}_{12} & \dot{\theta}_{13} \\ \dot{\theta}_{21} & \dot{\theta}_{22} & \dot{\theta}_{23} \\ \dot{\theta}_{31} & \dot{\theta}_{32} & \dot{\theta}_{33} \end{Bmatrix} = \{\dot{z}\}\{s\}\{s\}^T\{\dot{z}\}^T$$

$$\{\dot{D}\} = \begin{Bmatrix} \dot{D}_{11} & \dot{D}_{12} & \dot{D}_{13} \\ \dot{D}_{21} & \dot{D}_{22} & \dot{D}_{23} \\ \dot{D}_{31} & \dot{D}_{32} & \dot{D}_{33} \end{Bmatrix} = \{\dot{R}\}\{s\}^T\{\dot{z}\}^T$$

where $T_{ij}(i, j = 1, 2, 3)$ are the elements of matrix $[T_{ij}]$.

$$[m_{ie}] = \rho_i A_i \sum_{g=1}^{N_i} \int_0^{l_i} [\Theta_{igd}]^T ([\dot{B}_{11}] + [\dot{B}_{22}] + [\dot{B}_{33}]) [\Theta_{igd}] ds$$

$$[G_{11}] = \rho_i A_i \sum_{g=1}^{N_i} \int_0^{l_i} \begin{bmatrix} \dot{R}_1^2 + \dot{R}_2^2 & -\dot{R}_1\dot{R}_2 & -\dot{R}_1\dot{R}_3 & \text{sym.} \\ -\dot{R}_1\dot{R}_2 & \dot{R}_1^2 + \dot{R}_2^2 & -\dot{R}_2\dot{R}_3 & \dot{R}_1^2 + \dot{R}_2^2 \\ -\dot{R}_1\dot{R}_3 & -\dot{R}_2\dot{R}_3 & \dot{R}_1^2 + \dot{R}_2^2 & \end{bmatrix} ds$$

$$[G_{12}] = \rho_i A_i \sum_{g=1}^{N_i} \int_0^{l_i} \begin{bmatrix} \dot{D}_{23} - \dot{D}_{32} \\ \dot{D}_{31} - \dot{D}_{13} \\ \dot{D}_{12} - \dot{D}_{21} \end{bmatrix} [\Theta_{igd}] ds$$

$$[E] = \rho_i A_i \sum_{g=1}^{N_i} \int_0^{l_i} \begin{bmatrix} \Theta_{igd}^T (\dot{B}_{32} - \dot{B}_{23}) \Theta_{igd} \\ \Theta_{igd}^T (\dot{B}_{13} - \dot{B}_{31}) \Theta_{igd} \\ \Theta_{igd}^T (\dot{B}_{21} - \dot{B}_{12}) \Theta_{igd} \end{bmatrix} ds$$

$$[B] = \rho_i A_i \sum_{g=1}^{N_i} \int_0^{l_i} \begin{bmatrix} \Theta_{igd}^T (\dot{B}_{22} + \dot{B}_{33}) \Theta_{igd} \\ -\Theta_{igd}^T \dot{B}_{21} \Theta_{igd} \\ -\Theta_{igd}^T \dot{B}_{31} \Theta_{igd} \\ -\Theta_{igd}^T \dot{B}_{12} \Theta_{igd} \\ \Theta_{igd}^T (\dot{B}_{11} + \dot{B}_{22}) \Theta_{igd} \\ -\Theta_{igd}^T \dot{B}_{13} \Theta_{igd} \\ -\Theta_{igd}^T \dot{B}_{23} \Theta_{igd} \\ \Theta_{igd}^T (\dot{B}_{11} + \dot{B}_{22}) \Theta_{igd} \end{bmatrix} ds$$

$$[D] = \rho_i A_i \sum_{g=1}^{N_i} \int_0^{l_i} \begin{bmatrix} 2(\dot{D}_{22} + \dot{D}_{33}) \Theta_{igd} \\ -(\dot{D}_{12} + \dot{D}_{21}) \Theta_{igd} \\ -(\dot{D}_{13} + \dot{D}_{31}) \Theta_{igd} \\ \text{symmetry} \\ 2(\dot{D}_{11} + \dot{D}_{33}) \Theta_{igd} \\ -(\dot{D}_{23} + \dot{D}_{32}) \Theta_{igd} \\ 2(\dot{D}_{11} + \dot{D}_{22}) \Theta_{igd} \end{bmatrix} ds$$

and

$$[k_{11}] = \sum_{g=1}^{N_i} [\Theta_{igd}]^T [k_{11g}] [\Theta_{igd}]$$

$$[J_i] = m_i G \frac{\partial \{\dot{T}\}}{\partial \{q_i\}^T} [T_{0i}] \int_0^{l_i} \frac{1}{L_i} \left[\frac{z^T Y^T}{Z^T} \right] ds \sum_{g=1}^{N_i} [\Theta_{igd}]$$

$$\{f_{11}\} = m_i G \frac{\partial \{\dot{T}\}}{\partial \{q_i\}^T} (\{R\} + [T_{0i}] \left\{ \frac{1}{2} L_i, 0, 0 \right\}^T)$$

$$\{f_{12}\} = m_i G \left([T_{0i}] \int_0^{l_i} \frac{1}{L_i} \left[\frac{z^T Y^T}{Z^T} \right] ds \sum_{g=1}^{N_i} [\Theta_{igd}] \right) \{\dot{T}\}$$

$$\{\dot{T}\} = (\{0, 0, 1\} [T_{0i}])^T$$

where ρ_i is the mass density, A_i is the cross section area of beam i , m_i is the total beam mass, L_i is the total length of the beam. G is gravity, $[T_{0i}]$ is a rotational transformation matrix from the inertial frame ($\hat{e}_1, \hat{e}_2, \hat{e}_3$) to the moving frame ($\hat{i}_0, \hat{j}_0, \hat{k}_0$), and $[k_{11g}]$ is a structure stiffness matrix of the g^{th} element in beam i .

B: Skew Matrix and Matrix Properties

For a given vector, $\vec{\Omega}$, a corresponding skew matrix $[\hat{\Omega}]$ is defined as

$$[\hat{\Omega}] = \begin{bmatrix} 0 & -\Omega_1 & \Omega_2 \\ \Omega_1 & 0 & -\Omega_3 \\ -\Omega_2 & \Omega_3 & 0 \end{bmatrix}$$

where $\Omega_i (i = 1, 2, 3)$ are the components of the vector $\vec{\Omega}$.

If $\{q\}$ is a vector with n -dimension, and a scalar ϕ and a vector $\{z\}$ with m -dimension are the functions of $\{q\}$, the following matrix derivatives are then defined, as

$$\frac{\partial \phi}{\partial \{q\}^T} = \left\{ \frac{\partial \phi}{\partial q_i} \right\} (i = 1, \dots, n)$$

$$\frac{\partial \{z\}}{\partial \{q\}^T} = \left[\frac{\partial z_i}{\partial q_j} \right] (i = 1, \dots, m; j = 1, \dots, n)$$

where $\{\partial \phi / \partial q_i\}$ is an n -dimensional vector, and $[\partial z_i / \partial q_j]$ is an $n \times m$ matrix where i determines a row and j determines a column for the matrix. The following properties of the matrix partial derivatives are derived.

$$\frac{\partial}{\partial \{q\}^T} (\{z\}^T \{b\}) = \frac{\partial \{z\}}{\partial \{q\}^T} \{b\} + \frac{\partial \{b\}}{\partial \{q\}^T} \{z\}$$

$$\frac{\partial}{\partial \{q\}^T} ([C] \{q\}) = [C]^T$$

$$\frac{\partial}{\partial \{q\}^T} (\{q\}^T [C] \{q\}) = ([C] + [C]^T) \{q\}$$

$$\frac{\partial}{\partial \{q\}^T} (\phi_1 \phi_2) = \frac{\partial \phi_1}{\partial \{q\}^T} \phi_2 + \frac{\partial \phi_2}{\partial \{q\}^T} \phi_1$$

$$\frac{\partial}{\partial \{q\}^T} ([B] \{a\}) = \frac{\partial \{a\}}{\partial \{q\}^T} [B]^T +$$

$$+ \left[\frac{\partial \{b_1\}}{\partial \{q\}^T} \{a\} \dots \frac{\partial \{b_n\}}{\partial \{q\}^T} \{a\} \right]^T$$

$$\text{where } [B] = \begin{bmatrix} \{b_1\} & \dots & \{b_n\} \end{bmatrix}^T$$

where $\{z\}$, $\{b\}$, ϕ_1 , ϕ_2 , and $[B]$ are all the functions of $\{q\}$, $[C]$ is a constant matrix, and $\{b_i\} (i = 1, \dots, n)$ are the submatrices in $[B]$.

C: Derivation of $\frac{1}{2} \partial ([m_{ic}]^T \{\dot{q}_i\}) / \partial \{q_i\}^T$

Kinetic energy for the i^{th} beam is

$$K E_i = \frac{1}{2} \{\dot{q}_i\}^T [m_{ic}] \{\dot{q}_i\}$$

$$= K E_{ic} + K E_{i1} + 2 K E_{i2} \quad (29)$$

where

$$K E_{ic} = \frac{1}{2} \{\dot{q}_i\}^T [m_{ic}] \{\dot{q}_i\} \quad (30)$$

$$K E_{i1} = \frac{1}{2} \{\dot{q}_i\}^T [\Theta_{i\lambda}]^T [N]^T ([G_{i1}] + [s] + [T]) [N] [\Theta_{i\lambda}] \{\dot{q}_i\} \quad (31)$$

$$K E_{i2} = \frac{1}{2} \{\dot{q}_i\}^T [\Theta_{i\lambda}]^T [N]^T ([G_{i2}] + [X]) \{\dot{q}_i\} \quad (32)$$

where

$$[s] = \begin{bmatrix} \underline{q}^T \underline{B}_{s0} \underline{q} \end{bmatrix}$$

$$[T] = \begin{bmatrix} \underline{Q}_{s0} \underline{q} \end{bmatrix}$$

$$[X] = \begin{bmatrix} \underline{q}^T \underline{E}_0^T \end{bmatrix}$$

Partial differentiating Eq. 29 with respect to vector $\{q_i\}$ gives

$$\frac{\partial K E_i}{\partial \{q_i\}^T} = \frac{1}{2} \frac{\partial ([m_{ic}]^T \{\dot{q}_i\})}{\partial \{q_i\}^T} \{\dot{q}_i\}$$

$$= \frac{\partial K E_{ic}}{\partial \{q_i\}^T} + \frac{\partial K E_{i1}}{\partial \{q_i\}^T} + 2 \frac{\partial K E_{i2}}{\partial \{q_i\}^T} \quad (33)$$

where the first term vanishes because $[m_{ic}]$ is a constant matrix. The second term in the above equation can be written as

$$\frac{\partial K E_{i1}}{\partial \{q_i\}^T} = \frac{1}{2} \frac{\partial ([N] [\Theta_{i\lambda}] \{\dot{q}_i\})}{\partial \{q_i\}^T} ([G_{i1}] + [s] + [T])$$

$$[N] [\Theta_{i\lambda}] \{\dot{q}_i\} +$$

$$\frac{1}{2} \frac{\partial}{\partial \{q_i\}^T} ([G_{i1}] + [s] + [T])$$

$$[N] [\Theta_{i\lambda}] \{\dot{q}_i\} \quad (34)$$

where

$$\frac{\partial ([N] [\Theta_{i\lambda}] \{\dot{q}_i\})}{\partial \{q_i\}^T} = \frac{\partial}{\partial \{q_i\}^T} \left(\begin{bmatrix} \underline{N}_1 \\ \underline{N}_2 \\ \underline{N}_3 \end{bmatrix} [\Theta_{i\lambda}] \{\dot{q}_i\} \right)$$

$$= \left[\frac{\partial \underline{N}_1^T}{\partial \{q_i\}^T} \underline{\Theta}_{i\lambda} \underline{q}_1, \frac{\partial \underline{N}_2^T}{\partial \{q_i\}^T} \underline{\Theta}_{i\lambda} \underline{q}_2, \frac{\partial \underline{N}_3^T}{\partial \{q_i\}^T} \underline{\Theta}_{i\lambda} \underline{q}_3 \right] \quad (35)$$

and

$$\frac{\partial}{\partial \{q_i\}^T} ([G_{i1}] + [s] + [T]) [N] [\Theta_{i\lambda}] \{\dot{q}_i\} =$$

$$\frac{\partial ([N] [\Theta_{i\lambda}] \{\dot{q}_i\})}{\partial \{q_i\}^T} ([G_{i1}]^T + [s]^T + [T]^T) +$$

$$\left[\frac{\partial (\underline{z}_1 + \underline{I}_1)}{\partial \{q_i\}^T} \underline{N} \underline{\Theta}_{i\lambda} \underline{q}_1, \frac{\partial (\underline{z}_2 + \underline{I}_2)}{\partial \{q_i\}^T} \underline{N} \underline{\Theta}_{i\lambda} \underline{q}_2, \right.$$

$$\left. \frac{\partial (\underline{z}_3 + \underline{I}_3)}{\partial \{q_i\}^T} \underline{N} \underline{\Theta}_{i\lambda} \underline{q}_3 \right] \quad (36)$$

where

$$[s] = \begin{bmatrix} \underline{z}_1 & \underline{z}_2 & \underline{z}_3 \end{bmatrix}$$

$$[T] = \begin{bmatrix} \underline{I}_1 & \underline{I}_2 & \underline{I}_3 \end{bmatrix}$$

Substituting Eq. 35 and Eq. 36 into Eq. 34 gives

$$\frac{\partial K E_{i1}}{\partial \{q_i\}^T} = \left[\frac{\partial \underline{N}_1^T}{\partial \{q_i\}^T} \underline{\Theta}_{i\lambda} \underline{q}_1, \frac{\partial \underline{N}_2^T}{\partial \{q_i\}^T} \underline{\Theta}_{i\lambda} \underline{q}_2, \frac{\partial \underline{N}_3^T}{\partial \{q_i\}^T} \underline{\Theta}_{i\lambda} \underline{q}_3 \right] ([G_{i1}] + [s] + [T])$$

$$[N] [\Theta_{i\lambda}] \{\dot{q}_i\} + \frac{1}{2} \left[\frac{\partial (\underline{z}_1 + \underline{I}_1)}{\partial \{q_i\}^T} \underline{N} \underline{\Theta}_{i\lambda} \underline{q}_1, \right.$$

$$\left. \frac{\partial (\underline{z}_2 + \underline{I}_2)}{\partial \{q_i\}^T} \underline{N} \underline{\Theta}_{i\lambda} \underline{q}_2, \frac{\partial (\underline{z}_3 + \underline{I}_3)}{\partial \{q_i\}^T} \underline{N} \underline{\Theta}_{i\lambda} \underline{q}_3 \right]$$

$$[N] [\Theta_{i\lambda}] \{\dot{q}_i\}$$

$$= (1) + (2) \quad (37)$$

where (1) and (2) are used for identification. The second term in the above equation can be rewritten in a pattern as shown below.

$$(2) = \frac{1}{2} \sum_{j=1}^3 \frac{\partial (\{s_j\} + \{T_j\})}{\partial \{q_i\}^T} [N] [\Theta_{i\lambda}] \{\dot{q}_i\} \{N_j\} [\Theta_{i\lambda}] \{\dot{q}_i\} \quad (38)$$

where

$$\{s_j\} + \{T_j\} =$$

$$\left\{ \begin{bmatrix} \underline{q}_1^T \underline{B}_{s1} \underline{q}_1 + \underline{Q}_{s1} \underline{q}_1 \\ \underline{q}_2^T \underline{B}_{s2} \underline{q}_2 + \underline{Q}_{s2} \underline{q}_2 \\ \underline{q}_3^T \underline{B}_{s3} \underline{q}_3 + \underline{Q}_{s3} \underline{q}_3 \end{bmatrix} \right\} = \left\{ \begin{bmatrix} C_1 \\ C_2 \\ C_3 \end{bmatrix} \right\} = \{C\}$$

Thus,

$$\frac{\partial (\{s_j\} + \{T_j\})}{\partial \{q_i\}^T} = \left[\frac{\partial C_1}{\partial \{q_i\}^T}, \frac{\partial C_2}{\partial \{q_i\}^T}, \frac{\partial C_3}{\partial \{q_i\}^T} \right] \quad (39)$$

Substituting Eq. 39 into Eq. 38 gives

$$(2) = \frac{1}{2} \sum_{j=1}^3 \sum_{\alpha=1}^3 \frac{\partial C_{j\alpha}}{\partial \{q_i\}^T} \{N_j\} [\Theta_{i\alpha}] \{q_i\} \{N_j\} [\Theta_{i\alpha}] \{q_i\} \quad (40)$$

where

$$\begin{aligned} \frac{\partial C_{j\alpha}}{\partial \{q_i\}^T} &= \frac{1}{2} \{q_i\}^T \{B_{j\alpha}\} \{q_i\} + \{D_{j\alpha}\} \{q_i\} \\ &= ([B_{j\alpha}] + [B_{j\alpha}]^T) \{q_i\} + \{D_{j\alpha}\}^T \quad (\alpha = 1, 2, 3) \quad (41) \end{aligned}$$

Substituting Eq. 41 and Eq. 40 into Eq. 37 gives

$$\begin{aligned} \frac{\partial K E_{11}}{\partial \{q_i\}^T} &= \\ &\left[\frac{\partial Y_1^T}{\partial \{q_i\}^T} \Theta_{i1} \underline{\hat{q}}_1, \frac{\partial Y_2^T}{\partial \{q_i\}^T} \Theta_{i2} \underline{\hat{q}}_2, \frac{\partial Y_3^T}{\partial \{q_i\}^T} \Theta_{i3} \underline{\hat{q}}_3 \right] \\ &([G_{11}] + [g] + [T]) [N] [\Theta_{i1}] \{q_i\} + \\ &\frac{1}{2} \sum_{j=1}^3 \sum_{\alpha=1}^3 \{ ([B_{j\alpha}] + [B_{j\alpha}]^T) \{q_i\} + \{D_{j\alpha}\}^T \} \\ &\{q_i\}^T [\Theta_{i\alpha}]^T \{N_j\}^T \{N_j\} [\Theta_{i\alpha}] \{q_i\} \quad (42) \end{aligned}$$

The last term in Eq. 33 is

$$\begin{aligned} 2 \frac{\partial K E_{12}}{\partial \{q_i\}^T} &= \\ &\frac{\partial ([N] [\Theta_{i1}] \{q_i\})}{\partial \{q_i\}^T} ([G_{12}] + [X]) \{q_i\} + \\ &\frac{\partial}{\partial \{q_i\}^T} ([G_{12}] + [X]) \{q_i\} [N] [\Theta_{i1}] \{q_i\} \\ &= \frac{\partial ([N] [\Theta_{i1}] \{q_i\})}{\partial \{q_i\}^T} ([G_{12}] + [X]) \{q_i\} + \\ &\left[\frac{\partial X_1}{\partial \{q_i\}^T} \underline{\hat{q}}_1, \frac{\partial X_2}{\partial \{q_i\}^T} \underline{\hat{q}}_2, \frac{\partial X_3}{\partial \{q_i\}^T} \underline{\hat{q}}_3 \right] [N] [\Theta_{i1}] \{q_i\} \quad (43) \end{aligned}$$

where

$$[X] = [X_1 \ X_2 \ X_3]^T \text{ and } \{X_\alpha\} = \{E_\alpha\} \{q_i\}. \quad (44)$$

Substituting Eq. 44 into Eq. 43 gives

$$\begin{aligned} 2 \frac{\partial K E_{12}}{\partial \{q_i\}^T} &= \\ &\frac{\partial ([N] [\Theta_{i1}] \{q_i\})}{\partial \{q_i\}^T} ([G_{12}] + [X]) \{q_i\} + \\ &[E_1^T \underline{\hat{q}}_1 \ E_2^T \underline{\hat{q}}_2 \ E_3^T \underline{\hat{q}}_3] [N] [\Theta_{i1}] \{q_i\} \quad (45) \end{aligned}$$

Substituting Eq. 42 and Eq. 45 into Eq. 33 yields the final result, as

$$\begin{aligned} \frac{1}{2} \frac{\partial ([m_i]^T \{q_i\})}{\partial \{q_i\}^T} &= \\ &\left[\frac{\partial N_1^T}{\partial \{q_i\}^T} \Theta_{i1} \underline{\hat{q}}_1, \frac{\partial N_2^T}{\partial \{q_i\}^T} \Theta_{i2} \underline{\hat{q}}_2, \frac{\partial N_3^T}{\partial \{q_i\}^T} \Theta_{i3} \underline{\hat{q}}_3 \right] \\ &\{ ([G_{11}] + [q_1^T E_{3\alpha} \underline{\hat{q}}_3] + [D_{3\alpha} \underline{\hat{q}}_3]) \\ &[N] [\Theta_{i1}] + ([G_{12}] + [q_1^T E_1^T]) \} + \\ &[E_1^T \underline{\hat{q}}_1 \ E_2^T \underline{\hat{q}}_2 \ E_3^T \underline{\hat{q}}_3] [N] [\Theta_{i1}] + \\ &\frac{1}{2} \sum_{j=1}^3 \sum_{\alpha=1}^3 \{ ([B_{j\alpha}] + [B_{j\alpha}]^T) \{q_i\} + \{D_{j\alpha}\}^T \} \\ &\{q_i\}^T [\Theta_{i\alpha}]^T \{N_j\}^T \{N_j\} [\Theta_{i\alpha}] \quad (46) \end{aligned}$$

**APPENDIX D. Modeling of Multibody Flexible Articulated Structures
with Mutually Coupled Motions: Part I - General Theory.**

MODELING OF MULTIBODY FLEXIBLE ARTICULATED STRUCTURES WITH MUTUALLY COUPLED MOTIONS: PART I — GENERAL THEORY

Jiechi Xu and Joseph R. Baumgarten
Department of Mechanical Engineering
Iowa State University
Ames, Iowa

ABSTRACT

In the present paper a general systematic modeling procedure has been conducted in deriving dynamic equations of motion using Lagrange's approach for a spatial multibody structural system involving rigid bodies and elastic members. Both the rigid body degrees of freedom and the elastic degrees of freedom are considered as unknown generalized coordinates of the entire system in order to reflect the nature of mutually coupled rigid body and elastic motions. The assumption of specified rigid body gross motion is no longer necessary in the equation derivation and the resulting differential equations are highly nonlinear. Finite element analysis (FEA) with direct stiffness method has been employed to model the flexible substructures. Nonlinear coupling terms between the rigid body and elastic motions are fully derived and are explicitly expressed in matrix form. The equations of motion of each individual subsystem are formulated based on a moving frame instead of a traditional inertial frame. These local level equations of motion are assembled to obtain the system equations with the implementation of geometric boundary conditions by means of a compatibility matrix.

INTRODUCTION

Flexible dynamic modeling has been an attractive but difficult topic for a long time. Severely restricted by the lag of computer processing speed in the early years and the complexity of mathematical formulation, traditional designs in robots, mechanisms, and other relatively flexible structures have been limited to the realm of rigid body dynamics. However, increasing demands for higher operating speeds and better performance result in a situation that the light weight structures are objectively desired. A by-product of the flexibility effect is now recognized as a critical issue. It becomes impossible to implement time-consuming numerical integration without solid support of sophisticated modern computers with high processing speed capability.

The past decade has seen significant advances in dynamic analysis for flexible multibody systems. Extensive work, analytically and experimentally, has been conducted in dealing with flexible modeling. Most investigators however employ a common approach in which the elastic deformations are superimposed on the rigid body gross motion due to the nature of their specific problems. The application of that method is severely limited due to the fact of requirement of predefined rigid body motion. It is therefore very desirable to investigate a new approach in which all the degrees of freedom (DOF) of a system, elastic as well as rigid, are treated as unknown general-

ized coordinates. This enables analysis of situations where the rigid body motion needs to be predicted and the relationship between two motions effects the system stability.

The purpose of this paper is to develop a general modeling technique to conduct such a systematic procedure for establishing dynamic motion equations of a flexible system with mutually dependent rigid body and elastic motions. In addition, the formulation procedure is to be optimized and simplified so as to accommodate the needs of numerical analysis and computer programming.

PREVIOUS WORK REVIEW

The first to exploit the advantages of the FEA with Lagrangian mechanics were Sunada and Dubowsky [1,2]. Their model incorporated a Denavit-Hartenburg representation of the kinematic rigid body transformation excluding kinematic coupling. The degrees of freedom of the discretized system were reduced by means of Component Mode Synthesis (CMS). The equations of motion of all links were assembled using a Compatibility Matrix routine. In their illustrative examples, a set of first order equations was solved numerically for a special case in which the mechanism's nominal speeds and accelerations are much smaller than the component elastic coordinate velocities and accelerations. In their later extended work, the assembly of dynamic equations was performed in symbolic form due to the special form of matrix terms. The final system equations were solved using a Newmark-Beta integration algorithm. Their approach is applicable for these problems where nominal rigid body motion is specified by kinematic constraints.

Early works by Naganathan and Soni [3,4] [5] [6] [7] developed a fully nonlinear model employing a kinematic representation with rigid link based reference. The three-dimensional model was constructed by accounting for axial, torsional, and lateral deformations. Galerkin method was used with linear shape functions to represent the elasticity of the links. Link level matrices were transformed by time-varying compatibility matrices and cascaded into global matrices. The rigid body gross motion was specified at the revolute joints, and, subsequently, the element matrices became constant at each time step in the numerical integration.

Presented by Simo and Vu-Quoc [8] [9], a different problem arose in simulating dynamic response of a flexible plane beam subject to large overall motions. Two orthogonal coordinates, measured in an inertial frame, were defined to account for the large overall rigid body motion and small elastic deformation. Hamilton's dynamics associated with Galerkin spatial discretization were employed in the formula-

tion, in which the use of finite strain rod theories capable of treating finite rotations was essential. The inherent nonlinear character of the problem was transferred to the stiffness part of the equations of motion, which resulted in the possible numerical implementation by means of any commercial finite element codes being able to analyze nonlinear structural dynamics.

In the work accomplished by Sadler and Yang[10][11][12], a total mechanism displacement was defined to reflect the large rigid body gross motion and small elastic deformations in the dynamic modeling. Example problems were demonstrated in two different categories: planar multi-link mechanisms and spatial robot manipulators. The effects of Rayleigh damping was introduced. In the mechanism applications, the authors claimed that the method could be employed in the forward, as well as the inverse dynamic analyses if either the input forcing functions or the crank motion are specified. The link orientation angle must be related to the total unknown displacement in the formulation, which is possible for the mechanisms with one rigid body degree of freedom.

More recently, Nagarajan and Turcic[13][14] developed a new approach to derive equations of motion for elastic mechanism systems. Both the rigid body and the elastic degrees of freedom were considered as generalized coordinates in the derivation. The equations were first formulated based on element level coordinate system in which elastic nodal displacements are measured. The equations were then transformed to a reference coordinate system to ensure compatibility of the displacement, velocity, and acceleration of the degrees of freedom that are common to two or more links during the assembly of the equations of motion. Attempted to be general in their work, the equations, at element and system levels, are complicated and the transformation from element level to system level takes a great amount of effort while it is essential for the approach.

A literature survey of flexible models was completed by Cleghorn [15]. It was observed that the most effective model is one which incorporates Lagrange's equation with the finite element method. This produces a generalized element for easy application to flexible systems.

CURRENT APPROACH

In the current paper, a method combining Lagrangian dynamics with finite element analysis is developed in the modeling of dynamic response of multibody flexible structures. Lagrange's approach is selected to conduct system dynamic equations: finite element analysis with direct stiffness method is employed to discretize the elastic members in the system and to determine elastic degrees of freedom and the structural stiffness matrix which is required in finding elastic strain energy. Each flexible beam is assumed as a slender beam which is therefore to be modeled by beam element. The generalized coordinates of an entire system reflect both the parameters from the rigid body gross motion and the components of elastic displacements. The nonlinear coupling terms in all the coefficient matrices and the generalized force vectors are completely defined and formulated mathematically in detail. For an individual body, Lagrangian equation in matrix form can be expressed as

$$\frac{d}{dt} \left(\frac{\partial KE_i}{\partial \dot{q}_i} \right) - \frac{\partial KE_i}{\partial q_i} - \frac{\partial PE_i}{\partial q_i} = Q_i \quad (1)$$

where KE_i and PE_i are the kinetic and potential energies of the body, Q_i are the nonconservative forces, and q_i are the local generalized coordinates which reflect the degrees of freedom of the body. A general expression of kinetic energy of an elastic beam modeled by finite element can be written as

$$KE_i = \frac{1}{2} \sum_{g=1}^{N_i} \int_0^{l_i} \rho_i A_i \dot{\bar{V}}_{ig} \cdot \dot{\bar{V}}_{ig} ds \quad (2)$$

where N_i is the total number of the finite elements, l_i is the length of the g^{th} element which is usually the same for all the beam elements, ρ_i and A_i are the mass density and cross sectional area of the beam, and \bar{V}_{ig} is a generic velocity vector in element g . The above equation clearly shows that the velocity squared term plays a major role in kinetic energy. On the other hand, potential energy, consisting of body force potential energy as well as the structural strain energy, can be written as

$$PE_i = \frac{1}{2} \mathbf{q}_i^T \mathbf{K}_i \mathbf{q}_i + V_i(G) \quad (3)$$

where the first term is the elastic strain energy and the second term is a potential function which accounts for the beam elevation in the gravity field in the scopes of both the macro rigid body motion and the micro elastic vibration. After differentiating the kinetic and potential energy terms and substituting the results into Eq. 1, one can obtain the equations of motion in matrix form in the following.

$$\mathbf{m}_i(\mathbf{q}_i) \ddot{\mathbf{q}}_i - \mathbf{c}_i(\mathbf{q}_i, \dot{\mathbf{q}}_i) \dot{\mathbf{q}}_i - \mathbf{k}_i(\mathbf{q}_i) \mathbf{q}_i = \mathbf{f}_i(\mathbf{q}_i) \quad (4)$$

where the mass matrix \mathbf{m}_i is in general a function of the generalized coordinates \mathbf{q}_i , the damping matrix \mathbf{c}_i , resulting from the Coriolis and centrifugal accelerations, is a function of the generalized coordinates and velocities, the stiffness matrix \mathbf{k}_i , including the conventional structural stiffness, is a function of \mathbf{q}_i only, and the generalized force vector \mathbf{f}_i , involving the external nonconservative forces acting on the beam, is also a function of \mathbf{q}_i only.

A set of global generalized coordinates \mathbf{q} is defined first. These coordinates are chosen from the local generalized coordinates \mathbf{q}_i such that every coordinate in \mathbf{q} must be independent of each other. The relationship between the global and the local generalized coordinates is then determined by the following equation.

$$\mathbf{q}_i = \Phi_i \mathbf{q} \quad (5)$$

where Φ_i is a compatibility matrix which is in general a function of time. Differentiating the above equation with respect to time followed by the substitutions and the pre-multiplication of Φ_i in Eq. 4, one can finally obtain the system equations in the following form, as

$$\mathbf{M} \ddot{\mathbf{q}} - \mathbf{C} \dot{\mathbf{q}} - \mathbf{K} \mathbf{q} = \mathbf{F} \quad (6)$$

In the following sections, more detailed procedures and formulations are developed step by step. A demonstrative example is illustrated in Part II in which the simulation results are verified by the experimental data.

FINITE ELEMENT ANALYSIS

Each elastic beam is to be modeled by using several conventional predefined beam elements. The maximum degrees of freedom for each node in an element are six. They include two orthogonal transverse deflections and two corresponding rotations, one longitudinal displacement, and one twisting about the element axis. In order to achieve relatively simple modeling, only the transverse deflections and rotations are allowed at each node. The contributions of the other two displacements are neglected in most cases (it is referred to [16][17] for a complete modeling). The following conditions are therefore assumed for each element.

- Elementary beam theory applies and elastic flexure obeys Hooke's law.
- Each beam undergoes two uncoupled orthogonal deflections and rotations.
- Longitudinal displacement and axial twisting are neglected.

Following a conventional direct stiffness method[18], a polynomial displacement function is preassumed with knowledge of the external

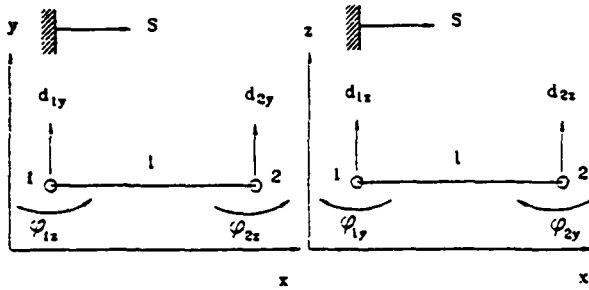


Figure 1: Sign conventions of nodal displacements

loadings. The boundary conditions are applied followed by direct application of the strain/stress relationships with sign conventions of the bending moments and shear forces. A structural stiffness matrix is obtained by comparing the relationship between the nodal forces and the nodal displacements.

Displacement Function

It is indicated from the classic elasticity theory¹⁹ that a polynomial function of the static transverse deflection for a cantilever beam can be determined, depending on the type of external loadings acting on the beam. With no distributed loading, the highest order of the polynomial function is of order three, that is

$$y = a_0 - a_1x - a_2x^2 - a_3x^3 \quad (7)$$

where x denotes axial coordinate of the beam, y is the corresponding transverse deflection, and a_i ($i = 0, 1, 2, 3$) are the constant coefficients. The above formula is then employed as a displacement function for each beam element.

Geometric Boundary Conditions

As illustrated in Fig. 1, four geometric boundary conditions are proposed for each element as follows:

$$\begin{aligned} s = 0 & \text{ deflection} = d_1; \text{ and slope} = \phi_1 \\ s = l & \text{ deflection} = d_2; \text{ and slope} = \phi_2 \end{aligned}$$

where s is the local axial coordinate in an undeformed element segment, d_i and ϕ_i ($i = 1, 2$) are the transverse deflections and slopes at the corresponding nodes, respectively, and l is the length of the element. By applying above four geometric boundary conditions to Eq. 7, it can be demonstrated that the final displacement functions, in matrix form, in each orthogonal plane are of the following forms.

$$v(s) = d^T Y s = s^T Y^T d \quad (8)$$

$$w(s) = d^T Z s = s^T Z^T d \quad (9)$$

where Y and Z are the constant matrices (see Appendix), $v(s)$ and $w(s)$ are the displacement functions in the $X-Y$ and $X-Z$ planes, respectively, and d and s are the generalized nodal coordinates of the element under consideration and a generalized function vector, respectively, which are defined as

$$\begin{aligned} d &= \{d_1, \phi_1, d_2, \phi_2, d_1, \phi_1, d_2, \phi_2\}^T \\ s &= \{1, s, s^2, s^3\}^T \end{aligned} \quad (10)$$

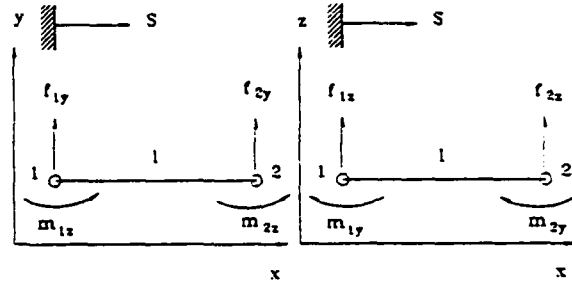


Figure 2: Sign conventions of nodal forces

where d_{iy} and ϕ_{iz} ($i = 1, 2$) are the deflections and slopes in the $X-Y$ plane while d_{iz} and ϕ_{iy} ($i = 1, 2$) are the deflections and slopes in the $X-Z$ plane. It is noted that $s^T Y^T$ and $s^T Z^T$ in Eqs. 8, 9, are the conventional shape functions of each orthogonal bending.

Structural Stiffness Matrix

For small elastic deflection, the formulas of the bending moments and shear forces are found to be

$$M(s) = EI_s \frac{\partial^2 u(s)}{\partial s^2}; \quad V(s) = EI_s \frac{\partial^3 u(s)}{\partial s^3} \quad (11)$$

where E is Young's modulus, I_s is the principle moment of inertia, and $u(s)$ is a transverse deflection function (either $v(s)$ or $w(s)$). According to Eq. 10, a corresponding vector of generalized nodal forces is defined as

$$f = \{f_{1y}, m_{1z}, f_{2y}, m_{2z}, f_{1z}, m_{1y}, f_{2z}, m_{2y}\}^T \quad (12)$$

where f_i ($i = 1, 2$) are the nodal forces and moments as shown in Fig. 2. Referring to geometric boundary conditions, four force boundary conditions are accordingly determined as

$$\begin{aligned} s = 0 & \text{ bending moment} = m_1; \quad \text{shear force} = f_1 \\ s = l & \text{ bending moment} = m_2; \quad \text{shear force} = f_2 \end{aligned}$$

Applying these four force boundary conditions for each orthogonal bending to Eq. 7 and arranging the results in the following standard form as

$$f = k, d. \quad (13)$$

one can find that the structural stiffness matrix takes the following expression, as

$$k_s = \frac{EI}{l^3} (C_1 \beta_1^T k_1 \beta_1 - C_2 \beta_2^T k_2 \beta_2) \quad (14)$$

where k_s is a symmetric stiffness matrix, l is the length of the element, I is the arithmetic average of I_y and I_z , C_1 and C_2 are the constant ratios of I_y and I_z to I , respectively, β_1 and β_2 are the constant matrices, and k_1 and k_2 are two stiffness matrices (see Appendix). The structural stiffness matrix is to be used in formulating the structural strain energy which is part of the potential energy of a moving elastic beam.

LOCAL LEVEL MOTION EQUATIONS

In the present paper emphasis is placed on studying dynamic re-

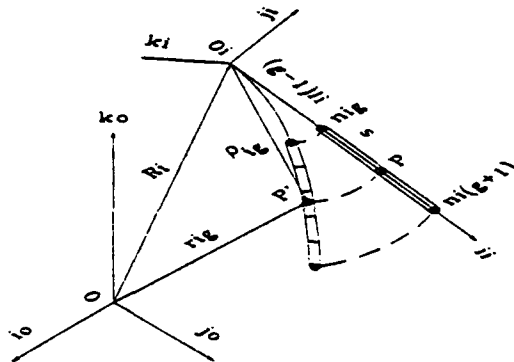


Figure 3: Deflection of a generic flexible beam

sponse of spherical unconstrained structural systems. Fig. 3 shows a generic finite element in an arbitrary elastic beam in such a structural system. Two sets of Cartesian coordinates are set up in assisting the representations of the rigid body motion and elastic deformation. Set (i_0, j_0, k_0) constitutes a floating (moving) frame of which the origin O is located at a spherical universal joint with three rotations. Set (i_1, j_1, k_1) , which accommodates the arbitrary elastic beam, is a reference frame which is relative to the moving frame. Vector \bar{R}_1 is a position vector which indicates the position of the origin of the reference frame under consideration relative to the moving frame. This vector is considered as a rigid body position vector which describes the rigid body motion of the elastic beam. Vector $\bar{\rho}_{1g}$ is a local position vector measured in the reference frame for an arbitrary point P' in element g after its deformation. This $\bar{\rho}_{1g}$ vector features both the rigid body motion of point P' relative to the moving frame and the elastic motion relative to the reference frame. Vector \bar{r}_{1g} , measured in the moving frame, is an absolute position vector which combines the rigid body and elastic motions of point P' .

Position and Velocity Vectors

Referring to Fig. 3 again, the absolute position vector of point P' can be found as

$$\bar{r}_{1g} = \bar{R}_1 + \bar{\rho}_{1g} = \bar{e}_0^T (\bar{R}_1 + T_{\alpha} \bar{\rho}_{1g}) \quad (15)$$

where $\bar{e}_0 = \{i_0, j_0, k_0\}^T$, a unit direction vector of the moving frame. \bar{R}_1 and $\bar{\rho}_{1g}$ are the reference and local position vectors in matrix form, and T_{α} is a 3×3 transformation matrix from the moving frame to the reference frame, i.e., $\bar{e}_0 = T_{\alpha} \bar{e}_1$, where \bar{e}_1 is a unit direction vector of the reference frame. A corresponding position equation in matrix form formulated in the moving frame $\{i_0, j_0, k_0\}$ takes the following form as

$$r_{1g} = R_1 + T_{\alpha} \rho_{1g} \quad (16)$$

All the vectors in the following sections will also be expressed relative to the same moving frame except where mentioned. Differentiating Eq. 16 with respect to time gives a velocity formula which can be written as

$$\dot{r}_{1g} = \dot{\Omega} (R_1 + T_{\alpha} \rho_{1g}) + \dot{R}_1 + \dot{T}_{\alpha} \rho_{1g} + T_{\alpha} \dot{\rho}_{1g} \quad (17)$$

where \dot{r}_{1g} denotes dr_{1g}/dt , \dot{R}_1 , $\dot{\rho}_{1g}$, and \dot{T}_{α} are the time rates of the corresponding vectors and the transformation matrix, and $\dot{\Omega}$ is

a skew-symmetric matrix (see Appendix) derived from a rigid body system angular velocity Ω which can be expressed as

$$\Omega^T = \dot{\lambda}^T N^T = \dot{\lambda}^T [N_1 \ N_2 \ N_3] \quad (18)$$

where $\dot{\lambda}$ is a generalized angular velocity vector containing the time rates of three rotating angles about the spherical universal joint, and N is a 3×3 time-varying coefficient matrix which can be partitioned as $[N_1 N_2 N_3]^T$. The rigid body system angular velocity Ω governs the angular motion of the moving frame \bar{e}_0 which is relative to an inertial frame \bar{e}_1 . Position vectors R_1 and ρ_{1g} can be further written as

$$R_1^T = \{R_{11} \ R_{12} \ R_{13}\}^T \quad (19)$$

$$\rho_{1g} = \begin{Bmatrix} \rho_{1g1} \\ \rho_{1g2} \\ \rho_{1g3} \end{Bmatrix} = \begin{Bmatrix} (g-1)l_1 - s \\ v_{1g} \\ w_{1g} \end{Bmatrix} \quad (20)$$

where R_{1j} ($j = 1, 2, 3$) are three rigid body components of vector R_1 , ρ_{1gj} is a rigid body component of vector ρ_{1g} , and v_{1g} and w_{1g} are two elastic components reflecting two orthogonal deflections as shown in Eqs. 8.9. Therefore the time rates of the corresponding position vectors are found to be

$$\dot{R}_1 = 0 \quad (21)$$

$$\dot{\rho}_{1g}^T = \{0 \ \dot{v}_{1g} \ \dot{w}_{1g}\} \quad (22)$$

For the cases with no revolute joint between elastic beams, the last term in Eq. 17 can be dropped out. A set of generalized coordinates for the i^{th} elastic beam can be defined in terms of three rotation angles and generalized nodal displacements in each element. Thus,

$$q_i^T = \{\lambda^T d_{11y} \phi_{11z} d_{11z} \phi_{11y} d_{12y} \phi_{12z} d_{12z} \phi_{12y} \dots d_{1Ny} \phi_{1Nz} d_{1Nz} \phi_{1Ny}\} \\ = \{\lambda^T d_{11}^T d_{12}^T \dots d_{1N}^T\} \quad (23)$$

where each d_{1g} ($g = 1, 2, \dots, N_1$) contains eight components as defined in Eq. 10, and N_1 is the total number of elements in the i^{th} elastic beam. The relationships between vectors λ , d_{1g} and q_i are then established, as

$$\lambda = \Theta_{1\lambda} q_i \quad (24)$$

$$d_{1g} = \Theta_{1gd} q_i \quad (25)$$

where $\Theta_{1\lambda}$ and Θ_{1gd} are types of linear compatibility matrices. A more compatible expression of the velocity vector can be written as a function of the time rate of the generalized coordinates \dot{q} by substituting Eqs. 8-10 and 18-25 into Eq. 17. Followed by necessary rearrangement, there results

$$\dot{r}_{1g} = \begin{bmatrix} (R_{13} - T_{31} \rho_{1g1}) N_2 - (R_{12} - T_{21} \rho_{1g1}) N_3 \\ (R_{11} - T_{11} \rho_{1g1}) N_3 - (R_{13} - T_{31} \rho_{1g1}) N_1 \\ (R_{12} - T_{21} \rho_{1g1}) N_1 - (R_{11} - T_{11} \rho_{1g1}) N_2 \end{bmatrix} \Theta_{1\lambda} \dot{q}_i \\ - \begin{bmatrix} s^T (Y_1^T T_{13} + Z_1^T T_{13}) \\ s^T (Y_1^T T_{23} + Z_1^T T_{23}) \\ s^T (Y_1^T T_{33} + Z_1^T T_{33}) \end{bmatrix} \Theta_{1gd} \dot{q}_i - \\ \begin{bmatrix} q_i^T \Theta_{1gd}^T ((T_{33} Y_1 + T_{33} Z_1) s N_2 - \\ q_i^T \Theta_{1gd}^T ((T_{13} Y_1 + T_{13} Z_1) s N_2 - \\ q_i^T \Theta_{1gd}^T ((T_{23} Y_1 + T_{23} Z_1) s N_1 - \\ -(T_{23} Y_1 + T_{23} Z_1) s N_3) \\ -(T_{33} Y_1 + T_{33} Z_1) s N_1) \\ -(T_{13} Y_1 + T_{13} Z_1) s N_2) \end{bmatrix} \Theta_{1\lambda} \dot{q}_i \quad (26)$$

where $T_{\alpha j}$ ($\alpha, j = 1, 2, 3$) are the elements of the transformation matrix T_{α} .

Velocity Square Term

The purpose of formulating the velocity square term is to find the beam kinetic energy which is defined as

$$KE = \frac{1}{2} \sum_{g=1}^N \int_0^{l_g} \dot{\mathbf{V}}_{1g} \cdot \dot{\mathbf{V}}_{1g} dm_{1g} \quad (27)$$

where N is the total number of elements, l_g is the length of the g^{th} element in the i^{th} beam, $\dot{\mathbf{V}}_{1g}$ is a velocity vector of an arbitrary point in the element. Substituting $\rho_i A_i ds$ for dm_{1g} and $\dot{\mathbf{r}}_{1g} \hat{\mathbf{e}}_3$ or $\dot{\mathbf{e}}_3^T \dot{\mathbf{r}}_{1g}$ for $\dot{\mathbf{V}}_{1g}$, the above kinetic energy equation becomes

$$KE = \frac{1}{2} \rho_i A_i \sum_{g=1}^N \int_0^{l_g} \dot{\mathbf{r}}_{1g}^T \dot{\mathbf{r}}_{1g} ds \quad (28)$$

where ρ_i and A_i are the mass density and cross sectional area of the beam, respectively. Eq. 28 indicates that finding the velocity square term is prior to finding the kinetic energy. As shown in Eqs. 10 and 20, the velocity vector in Eq. 28 is also a function of the local axial coordinate s . This indicates that it is a challenging task to formulate the velocity square term properly such that the integration in Eq. 28 can be carried out analytically. For simplicity, Eq. 28 is reformulated in a symbolic fashion by the following form, as

$$\dot{\mathbf{r}}_{1g} = [1] \odot_{1,1} \dot{\mathbf{q}}_i - [2] \odot_{1,2} \dot{\mathbf{q}}_i - [3] \odot_{1,3} \dot{\mathbf{q}}_i \quad (29)$$

where matrices $[1]$, $[2]$, and $[3]$ represent the corresponding matrices in Eq. 26 in the same order. Premultiplying the velocity vector by its transpose vector will result in the velocity square term as

$$\begin{aligned} \dot{\mathbf{r}}_{1g}^T \dot{\mathbf{r}}_{1g} = & \dot{\mathbf{q}}_i^T (\odot_{1,1}^T [1]^T [1] - [3]^T [3] - [1]^T [3] - [3]^T [1] \odot_{1,1}) \\ & - \odot_{1,2}^T [2]^T [2] \odot_{1,2} - \odot_{1,1}^T ([1]^T - [3]^T) [2] \odot_{1,2} \\ & - \odot_{1,2}^T [2]^T ([1] - [3]) \odot_{1,1} \dot{\mathbf{q}}_i \end{aligned} \quad (30)$$

By defining the following terms

$$\begin{aligned} \mathbf{a} = \begin{bmatrix} a_1 \\ a_2 \\ a_3 \end{bmatrix} &= \begin{bmatrix} T_{12} Y_i - T_{13} Z_i \\ T_{22} Y_i - T_{23} Z_i \\ T_{32} Y_i - T_{33} Z_i \end{bmatrix} \\ \mathbf{d} = \begin{bmatrix} d_1 \\ d_2 \\ d_3 \end{bmatrix} &= \begin{bmatrix} s^2 a_1^2 \\ s^2 a_2^2 \\ s^2 a_3^2 \end{bmatrix} \\ \mathbf{R} = \begin{bmatrix} R_1 \\ R_2 \\ R_3 \end{bmatrix} &= \begin{bmatrix} R_{11} - T_{11} \rho_i A_i \\ R_{21} - T_{21} \rho_i A_i \\ R_{31} - T_{31} \rho_i A_i \end{bmatrix} \end{aligned}$$

it can be demonstrated that the symbolic matrices $[i]$ ($i = 1, 2, 3$) in Eq. 29 become

$$[1] = \dot{\mathbf{R}}^T \mathbf{N}; [2] = \mathbf{d}; [3] = -[\dot{\mathbf{d}}] \otimes \Gamma(\odot_{1,2} \mathbf{q}_i) \mathbf{N}$$

where $[\dot{\mathbf{d}}]$ is a skew-symmetric matrix associated with the matrix \mathbf{d} (see Appendix), and Γ and \otimes are matrix operators defined in Appendix . Thus,

$$\begin{aligned} [1]^T [1] &= \mathbf{N}^T \dot{\mathbf{R}} \dot{\mathbf{R}}^T \mathbf{N}; [2]^T [2] = \mathbf{d}^T \mathbf{d} \\ [3]^T [3] &= \mathbf{N}^T \Gamma(\mathbf{q}_i^T \odot_{1,2}^T) \otimes ([\dot{\mathbf{d}}]^T [\dot{\mathbf{d}}]) \otimes \Gamma(\odot_{1,2} \mathbf{q}_i) \mathbf{N} \\ [1]^T [2] &= \mathbf{N}^T \dot{\mathbf{R}}^T [\dot{\mathbf{d}}] \otimes \Gamma(\odot_{1,2} \mathbf{q}_i) \mathbf{N} \\ [1]^T [3] &= \mathbf{N}^T \dot{\mathbf{R}} \mathbf{d}; [2]^T [3] = \mathbf{d}^T [\dot{\mathbf{d}}] \otimes \Gamma(\odot_{1,2} \mathbf{q}_i) \mathbf{N} \end{aligned}$$

By substituting above expressions into Eq. 30, the velocity square term becomes

$$\dot{\mathbf{r}}_{1g}^T \dot{\mathbf{r}}_{1g} =$$

$$\begin{aligned} & \dot{\mathbf{q}}_i^T (\odot_{1,1}^T \mathbf{N}^T (\Gamma(\mathbf{q}_i^T \odot_{1,2}^T) \otimes [\dot{\mathbf{d}}]^T [\dot{\mathbf{d}}]) \otimes \Gamma(\odot_{1,2} \mathbf{q}_i) \\ & - \dot{\mathbf{R}} \dot{\mathbf{R}}^T - [\dot{\mathbf{R}}^T \dot{\mathbf{d}} - \dot{\mathbf{d}} \dot{\mathbf{R}}^T] \otimes \Gamma(\odot_{1,2} \mathbf{q}_i) \mathbf{N} \odot_{1,1} \\ & + \odot_{1,2}^T \mathbf{N}^T (\dot{\mathbf{R}} \mathbf{d} - \Gamma^T(\odot_{1,2} \mathbf{q}_i) \otimes [\dot{\mathbf{d}}]^T \mathbf{d}) \odot_{1,2} \\ & - \odot_{1,2}^T \mathbf{d} (\dot{\mathbf{R}}^T \dot{\mathbf{R}} + \mathbf{d}^T [\dot{\mathbf{d}}] \otimes \Gamma(\odot_{1,2} \mathbf{q}_i) \mathbf{N} \odot_{1,1} \\ & - \odot_{1,2}^T \mathbf{d}^T \odot_{1,2} \mathbf{d}) \dot{\mathbf{q}}_i \end{aligned} \quad (31)$$

Kinetic Energy

Substituting Eq. 31 into Eq. 28 yields a more compact form of the kinetic energy as

$$KE = \frac{1}{2} \dot{\mathbf{q}}_i^T \mathbf{m}_i \dot{\mathbf{q}}_i \quad (32)$$

where \mathbf{m}_i is a symmetric mass matrix which is formulated as

$$\begin{aligned} \mathbf{m}_i = & \mathbf{m}_{i0} + \odot_{1,1}^T \mathbf{N}^T (\mathbf{G}_{11} + \mathbf{H}_{11} + \mathbf{H}_{12}) \mathbf{N} \odot_{1,1} \\ & - \odot_{1,2}^T \mathbf{N}^T (\mathbf{G}_{12} + \mathbf{H}_{12}) \odot_{1,2} \\ & - \odot_{1,2}^T (\mathbf{G}_{22} + \mathbf{H}_{22}) \mathbf{N} \odot_{1,1} \end{aligned} \quad (33)$$

where

$$\begin{aligned} \mathbf{m}_{i0} &= \rho_i A_i \sum_{g=1}^N \odot_{1,2}^T \int_0^{l_g} \mathbf{d}^T \mathbf{d} ds \odot_{1,2} \\ \mathbf{G}_{11} &= \rho_i A_i \sum_{g=1}^N \int_0^{l_g} \dot{\mathbf{R}} \dot{\mathbf{R}}^T ds \\ \mathbf{G}_{12} &= \rho_i A_i \sum_{g=1}^N \int_0^{l_g} \dot{\mathbf{R}} \mathbf{d} ds \\ \mathbf{H}_{11} &= \rho_i A_i \sum_{g=1}^N \Gamma^T(\odot_{1,2} \mathbf{q}_i) \otimes \int_0^{l_g} [\dot{\mathbf{d}}]^T [\dot{\mathbf{d}}] ds \\ & \otimes \Gamma(\odot_{1,2} \mathbf{q}_i) \\ \mathbf{H}_{12} &= \rho_i A_i \sum_{g=1}^N \int_0^{l_g} [\dot{\mathbf{R}}^T \dot{\mathbf{d}} - \dot{\mathbf{d}} \dot{\mathbf{R}}^T] ds \otimes \Gamma(\odot_{1,2} \mathbf{q}_i) \\ \mathbf{H}_{22} &= \rho_i A_i \sum_{g=1}^N \Gamma^T(\odot_{1,2} \mathbf{q}_i) \otimes \int_0^{l_g} [\dot{\mathbf{d}}]^T \mathbf{d} ds \end{aligned} \quad (34)$$

where \mathbf{m}_{i0} and \mathbf{G}_{11} are the constant symmetric matrices, \mathbf{G}_{12} is a constant rectangular matrix, \mathbf{H}_{11} and \mathbf{H}_{12} are the time-varying symmetric matrices, and \mathbf{H}_{22} is a time-varying rectangular matrix.

Potential Energy

The total potential energy of an elastic beam is the summation of the body force potential energy and the elastic strain energy. The former is defined as the negative work done by gravity, i.e.

$$U_b = \sum_{g=1}^N U_{bg} = \sum_{g=1}^N \int_V -dm_i \bar{\mathbf{G}} \cdot \bar{\mathbf{r}}_{1g} \quad (35)$$

where $dm_i = \rho_i A_i ds$, $\bar{\mathbf{G}} = -G \hat{\mathbf{e}}_3$ in which $\hat{\mathbf{e}}_3$ is the vertical coordinate of the inertial frame ($\hat{\mathbf{e}}_1, \hat{\mathbf{e}}_2, \hat{\mathbf{e}}_3$), and $\bar{\mathbf{r}}_{1g}$ is a position vector as defined in the previous sections. Substituting Eqs. 7, 9, 15, 20, and 25 into Eq. 35 will result in a compact form of the body force potential energy in matrix form as

$$U_b = V_i + \mathbf{f}_i^T \mathbf{q}_i \quad (36)$$

where V_i is a potential function which represents the rigid body potential energy and \mathbf{f}_i^T is a force vector due to the elastic deflection. These two terms can be further formulated as

$$V_i = m_i G b^T \mathbf{T}_{10} (\mathbf{R}_i - \frac{L_i}{2} \mathbf{T}_{20} \mathbf{a})$$

$$\xi^T = \frac{m_i L_i}{L_i} b^T T_{i0} T_{i0} \int_0^{L_i} \begin{bmatrix} 0 \\ s^T Y_i^T \\ s^T Z_i^T \end{bmatrix} ds \sum_{g=1}^{N_i} \Theta_{i,g}$$

where m_i is the mass of the beam, L_i is the length of the beam, T_{i0} is a time-varying transformation matrix between the inertial frame and the moving frame, $a^T = \{1 \ 0 \ 0\}$, and $b^T = \{0 \ 0 \ 1\}$. The elastic strain energy is defined as

$$U_{e,i} = \sum_{g=1}^{N_i} U_{e,i,g} = \frac{1}{2} \sum_{g=1}^{N_i} q_i^T (\Theta_{i,g}^T k_{i,g} \Theta_{i,g}) q_i \quad (37)$$

where $k_{i,g}$ is a structural stiffness matrix of the g^{th} element in the i^{th} elastic beam, as shown in Eq. 14. Therefore, the total potential energy can be found as

$$PE_i = \frac{1}{2} q_i^T k_{i,i} q_i - V_i - f_i^T q_i \quad (38)$$

where $k_{i,i} = \sum_{g=1}^{N_i} \Theta_{i,g}^T k_{i,g} \Theta_{i,g}$, a symmetric constant matrix.

Motion Equations

By substituting the formulas of kinetic and potential energies in Eqs. 32 and 38 into the Lagrange's equation, Eq. 1, the equations of motion of an arbitrary free elastic beam at the local level can be written as

$$\begin{aligned} m_i \ddot{q}_i - \left(\dot{m}_i - \frac{1}{2} \frac{\partial(m_i \dot{q}_i)}{\partial \dot{q}_i} \right) \dot{q}_i - \\ \left(k_{i,i} - \frac{\partial f_i}{\partial \dot{q}_i} \right) q_i = Q_i - f_i - \frac{\partial V_i}{\partial \dot{q}_i} \end{aligned} \quad (39)$$

The above equations clearly show the nonlinearity involved in the time-varying coefficient matrices. Referring to Appendix , some of the matrix partial differentiations can be derived immediately in the follows:

$$\begin{aligned} \frac{\partial f_i}{\partial \dot{q}_i} &= \frac{m_i G}{L_i} \frac{\partial(T_{i0}^T b)}{\partial \dot{q}_i} T_{i0} \int_0^{L_i} \begin{bmatrix} 0 \\ s^T Y_i^T \\ s^T Z_i^T \end{bmatrix} ds \\ &\quad \sum_{g=1}^{N_i} \Theta_{i,g} \end{aligned} \quad (40)$$

$$\frac{\partial V_i}{\partial \dot{q}_i} = m_i G \frac{\partial(T_{i0}^T b)}{\partial \dot{q}_i} (R_i - \frac{L_i}{2} T_{i0} a) \quad (41)$$

The partial differentiations on the right hand sides of the above equations can be carried out analytically by substituting the specific transformation matrix for T_{i0} .

Derivation of $\frac{1}{2} \partial(m_i \dot{q}_i) / \partial \dot{q}_i$

Referring to Eq. 32, the formula of kinetic energy of the i^{th} beam is rearranged in the following, as

$$KE_i = \frac{1}{2} \dot{q}_i^T m_i \dot{q}_i = KE_{i,e} + KE_{i,1} + 2KE_{i,2} \quad (42)$$

where

$$KE_{i,e} = \frac{1}{2} \dot{q}_i^T m_{i,e} \dot{q}_i \quad (43)$$

$$KE_{i,1} = \frac{1}{2} \dot{q}_i^T \Theta_{i,1}^T N^T (G_{i,1} - H_{i,1} - H_{i,2}) N \Theta_{i,1} \dot{q}_i$$

$$KE_{i,2} = \frac{1}{2} \dot{q}_i^T \Theta_{i,2}^T N^T (G_{i,2} + H_{i,2}) N \Theta_{i,2} \dot{q}_i$$

Partial differentiating Eq. 42 with respect to \dot{q}_i^T gives

$$\frac{\partial KE_i}{\partial \dot{q}_i^T} = \frac{1}{2} \frac{\partial(m_i \dot{q}_i)}{\partial \dot{q}_i^T} \dot{q}_i = \frac{\partial KE_{i,e}}{\partial \dot{q}_i^T} + \frac{\partial KE_{i,1}}{\partial \dot{q}_i^T} + 2 \frac{\partial KE_{i,2}}{\partial \dot{q}_i^T} \quad (44)$$

where the first term vanishes because $m_{i,e}$ in Eq. 43 is a constant matrix. Referring to Eq. 34, matrices $H_{i,1}$, $H_{i,2}$, and $H_{i,3}$ are redefined in the following forms, as

$$\begin{aligned} H_{i,1} &= \Gamma^T(q_i) \otimes \begin{bmatrix} B_{11} & B_{12} & B_{13} \\ B_{21} & B_{22} & B_{23} \\ B_{31} & B_{32} & B_{33} \end{bmatrix} \otimes \Gamma(q_i) \\ &= [H_{i,1,1} \ H_{i,1,2} \ H_{i,1,3}] \end{aligned} \quad (45)$$

$$\begin{aligned} H_{i,2} &= \begin{bmatrix} D_{11} & D_{12} & D_{13} \\ D_{21} & D_{22} & D_{23} \\ D_{31} & D_{32} & D_{33} \end{bmatrix} \otimes \Gamma(q_i) \\ &= [H_{i,2,1} \ H_{i,2,2} \ H_{i,2,3}] \end{aligned} \quad (46)$$

$$H_{i,3} = [H_{i,3,1} \ H_{i,3,2} \ H_{i,3,3}]^T = \begin{bmatrix} q_i^T E_1^T \\ q_i^T E_2^T \\ q_i^T E_3^T \end{bmatrix} \quad (47)$$

Thus, the second term in Eq. 44 can be written as

$$\begin{aligned} \frac{\partial KE_{i,1}}{\partial \dot{q}_i^T} &= \frac{\partial(N \Theta_{i,1} \dot{q}_i)}{\partial \dot{q}_i^T} (G_{i,1} - H_{i,1} + H_{i,2}) N \Theta_{i,1} \dot{q}_i - \\ &\quad \frac{1}{2} \left[\frac{\partial(H_{i,1,1} - H_{i,2,1})}{\partial \dot{q}_i^T} N \Theta_{i,1} \dot{q}_i, \right. \\ &\quad \frac{\partial(H_{i,1,2} - H_{i,2,2})}{\partial \dot{q}_i^T} N \Theta_{i,1} \dot{q}_i, \\ &\quad \left. \frac{\partial(H_{i,1,3} - H_{i,2,3})}{\partial \dot{q}_i^T} N \Theta_{i,1} \dot{q}_i, \right] N \Theta_{i,1} \dot{q}_i \\ &= [1] - [2] \end{aligned} \quad (48)$$

where [1] corresponds the first term and [2] represents the second term. Then,

$$\begin{aligned} [1] &= \frac{\partial N_1}{\partial \dot{q}_i^T} \Theta_{i,1} \dot{q}_i + \frac{\partial N_2}{\partial \dot{q}_i^T} \Theta_{i,2} \dot{q}_i + \frac{\partial N_3}{\partial \dot{q}_i^T} \Theta_{i,3} \dot{q}_i \\ &\quad (G_{i,1} - H_{i,1} + H_{i,2}) N \Theta_{i,1} \dot{q}_i \\ [2] &= \frac{1}{2} \sum_{j=1}^3 \frac{\partial(H_{i,1,j} - H_{i,2,j})}{\partial \dot{q}_i^T} N \Theta_{i,1} \dot{q}_i N_j^T \Theta_{i,j} \dot{q}_i \\ &= \frac{1}{2} \sum_{j=1}^3 [3] N \Theta_{i,1} \dot{q}_i N_j^T \Theta_{i,j} \dot{q}_i \end{aligned}$$

where [3] represents the partial differentiation in [2], which is then written as

$$\begin{aligned} [3] &= \frac{\partial}{\partial \dot{q}_i^T} \left(\begin{bmatrix} q_i^T B_{12} q_i \\ q_i^T B_{22} q_i \\ q_i^T B_{32} q_i \end{bmatrix} - \begin{bmatrix} D_{12} q_i \\ D_{22} q_i \\ D_{32} q_i \end{bmatrix} \right) \\ &= \begin{bmatrix} (B_{12} - B_{22}) q_i - D_{12}^T \\ (B_{22} - B_{32}) q_i - D_{22}^T \\ (B_{32} - B_{33}) q_i - D_{32}^T \end{bmatrix} \end{aligned}$$

where $B_{\alpha\beta}^T = B_{\beta\alpha}$ ($\alpha = 1, 2, 3$) and $D_{\alpha\beta} = D_{\beta\alpha}$ ($\alpha = 1, 2, 3$). Substituting the expressions of [3] into [2] gives

$$\begin{aligned} [2] &= \frac{1}{2} \sum_{j=1}^3 \sum_{\alpha=1}^3 \{ (B_{\alpha\beta} - B_{\beta\alpha}) q_i - D_{\alpha\beta}^T \} \\ &\quad q_i^T \Theta_{i,1}^T N_{\alpha} N_j^T \Theta_{i,j} \dot{q}_i \end{aligned}$$

Substituting the expressions of [1] and [2] into Eq. 48 yields

$$\begin{aligned} \frac{\partial KE_{i,1}}{\partial \dot{q}_i^T} &= \left(\frac{\partial N_1}{\partial \dot{q}_i^T} \Theta_{i,1} \dot{q}_i + \frac{\partial N_2}{\partial \dot{q}_i^T} \Theta_{i,2} \dot{q}_i + \frac{\partial N_3}{\partial \dot{q}_i^T} \Theta_{i,3} \dot{q}_i \right) \\ &\quad (G_{i,1} + H_{i,1} - H_{i,2}) N \Theta_{i,1} \dot{q}_i - \\ &\quad \frac{1}{2} \sum_{j=1}^3 \sum_{\alpha=1}^3 \{ (B_{\alpha\beta} + B_{\beta\alpha}) q_i - D_{\alpha\beta}^T \} \\ &\quad q_i^T \Theta_{i,1}^T N_{\alpha} N_j^T \Theta_{i,j} \dot{q}_i \end{aligned} \quad (49)$$

The last term in Eq. 44 can be written as

$$\begin{aligned} 2 \frac{\partial K E_{12}}{\partial \dot{q}_i} &= \frac{\partial (N \Theta_{1,2} \dot{q}_i)}{\partial \dot{q}_i} (G_{1,2} - H_{1,2}) \Theta_{1,2} \dot{q}_i - \\ &\quad \frac{\partial \{ (G_{1,2} - H_{1,2}) \Theta_{1,2} \dot{q}_i \}}{\partial \dot{q}_i} N \Theta_{1,2} \dot{q}_i \\ &= \left[\frac{\partial N_1}{\partial \dot{q}_i} \Theta_{1,2} \dot{q}_i + \frac{\partial N_2}{\partial \dot{q}_i} \Theta_{1,2} \dot{q}_i + \frac{\partial N_3}{\partial \dot{q}_i} \Theta_{1,2} \dot{q}_i \right] \\ &\quad (G_{1,2} - H_{1,2}) \Theta_{1,2} \dot{q}_i - \\ &\quad [E_1^T \Theta_{1,2} \dot{q}_i + E_2^T \Theta_{1,2} \dot{q}_i + E_3^T \Theta_{1,2} \dot{q}_i] \\ &\quad N \Theta_{1,2} \dot{q}_i \end{aligned} \quad (50)$$

Substituting Eqs. 49 and 50 into Eq. 44 will result in the following final expression of the matrix partial differentiation, as

$$\begin{aligned} \frac{1}{2} \frac{\partial (m_i \dot{q}_i)}{\partial \dot{q}_i} &= \\ &\quad \left[\frac{\partial N_1}{\partial \dot{q}_i} \Theta_{1,2} \dot{q}_i + \frac{\partial N_2}{\partial \dot{q}_i} \Theta_{1,2} \dot{q}_i + \frac{\partial N_3}{\partial \dot{q}_i} \Theta_{1,2} \dot{q}_i \right] \\ &\quad \{ (G_{1,2} - H_{1,2}) \Theta_{1,2} \dot{q}_i - (G_{1,2} - H_{1,2}) \Theta_{1,2} \dot{q}_i \} - \\ &\quad [E_1^T \Theta_{1,2} \dot{q}_i + E_2^T \Theta_{1,2} \dot{q}_i + E_3^T \Theta_{1,2} \dot{q}_i] N \Theta_{1,2} \dot{q}_i - \\ &\quad \frac{1}{2} \sum_{j=1}^3 \sum_{k=1}^3 \{ (B_{j,k} - B_{k,j}) \dot{q}_j - D_{j,k} \} \\ &\quad \dot{q}_j^T \Theta_{1,2}^T N_2 N_3^T \Theta_{1,2} \dot{q}_i \end{aligned} \quad (51)$$

GLOBAL LEVEL MOTION EQUATIONS

In the previous sections, the local level equations of motion have been derived for an arbitrary elastic beam. In order that those generalized coordinates at the common connecting boundaries are compact for the adjacent beams, it is necessary to include the kinematic constraints in the equations of motion. The concept of the compatibility matrix is employed in the assembly process so that the coefficient matrices and the generalized force vectors of each subsystem are compatible. A set of global generalized coordinates is selected among the local generalized coordinates of each subsystem such that the global generalized coordinates are independent of each other.

Compatibility Matrix

A matrix which linearly relates the local generalized coordinates to the global generalized coordinates is called the compatibility matrix. For a system with n global generalized coordinates q , the local generalized coordinates q_i with m components can be expressed as

$$q_i = \Phi_i q \quad (i = 1, 2, \dots, N) \quad (52)$$

where the compatibility matrix Φ_i is an $m \times n$ matrix which is in general a time-varying function of the rigid body generalized coordinates. N is the total number of the subsystems under consideration. It is noticed that the compatibility matrix contains the information of the geometric boundary conditions which describe the kinematic constraints for those adjacent subsystems.

Assembly of Motion Equations

Differentiating Eq. 52 with respect to time gives

$$\dot{q}_i = \Phi_i \dot{q} + \dot{\Phi}_i q \quad (53)$$

$$\ddot{q}_i = \Phi_i \ddot{q} + 2\dot{\Phi}_i \dot{q} + \ddot{\Phi}_i q \quad (54)$$

Rearranging the local level equations of motion, one can show that Eq. 39 takes the following standard form as

$$m_i \ddot{q}_i + c_i \dot{q}_i + k_i q_i = F_i \quad (55)$$

where c_i is a damping matrix, k_i is a stiffness matrix, F_i is a generalized force vector, and they are formulated as

$$c_i = \dot{m}_i - \frac{1}{2} \frac{\partial (m_i \dot{q}_i)}{\partial \dot{q}_i}$$

$$k_i = k_{i1} - \frac{\partial F_i}{\partial \dot{q}_i}$$

$$F_i = Q_i - f_i - \frac{\partial V_i}{\partial \dot{q}_i}$$

Substituting Eqs. 53 and 54 into Eq. 55 followed by premultiplying Eq. 55 with the transpose compatibility matrix Φ_i^T will result in the following global equations of motion as

$$M \ddot{q} + C \dot{q} + K q = F \quad (56)$$

where the global mass, damping, and stiffness matrices and the global generalized force vector are formulated as follows:

$$\begin{aligned} M &= \sum_{i=1}^N \Phi_i^T m_i \Phi_i \\ C &= \sum_{i=1}^N (\Phi_i^T c_i \Phi_i - 2\dot{\Phi}_i^T m_i \dot{\Phi}_i) \\ K &= \sum_{i=1}^N (\Phi_i^T k_i \Phi_i - \dot{\Phi}_i^T c_i \dot{\Phi}_i - \ddot{\Phi}_i^T m_i \ddot{\Phi}_i) \\ F &= \sum_{i=1}^N \Phi_i^T F_i \end{aligned} \quad (57)$$

Structural and/or fluid viscous damping terms can be added in each c_i matrix. The internal connecting force terms in each F_i vector vanishes automatically during the process of matrix assembly.

CONCLUSIONS

A systematic mathematical model predicting the motion of a multi-body system with elastic members has been fully developed in the current paper. The mutually coupled rigid body and elastic motions are revealed by including the rigid body generalized coordinates which have not been considered as the unknown degrees of freedom until very recent years. The significant complexity in mathematical formulation arises because of the involvement of the unknown rigid body DOF. Nonlinear coupling terms due to Coriolis and centrifugal forces, which were neglected historically, are completely taken into account and are derived explicitly in matrix form. The conventional finite element analysis cooperated with the direct stiffness method is used in the discretization of the elastic members. A third order polynomial function is adopted in the finite element shape function in order to exclude these negligible effect of longitudinal displacement and axial twisting which are usually of higher order in magnitude compared with the other deformations in most flexible structures. The Lagrange's equation is employed in which both the rigid body and the elastic DOF are treated as unknown generalized coordinates of the system. The elastic deformations of every element in each elastic beam are measured in the local reference frame so that they are compatible at the local level. The position vector as well as the velocity vector are formulated in terms of the moving frame instead of the usual inertial frame. This results in simple mathematical operations in finding kinetic and potential energies.

The final form of the system dynamic equations of motion is expressed in a closed form which shows high nonlinearity and strong contributions of the coupling terms in the time-varying coefficient matrices and generalized force terms. The procedure and methodology developed herein are applicable to the dynamic modeling of

the planar mechanisms, as well as the spatial unconstrained structures. The application of the theory presented in the current paper is demonstrated and implemented in Part II. The extensive simulation results and the experimental data are also included in Part II of this work. Numerical techniques which resolve the difficulty in solving nonlinear differential equations involving mixed rigid body variables with large overall motion and elastic variables with small vibration are investigated and are presented under a separate paper in which Newmark predictor-corrector integration schemes are developed.

ACKNOWLEDGMENT

The authors would like to acknowledge the financial support of the Air Force Office of Scientific Research under Grant No. AFOSR-89-0403.

References

- [1] Sunada, W.H. and Dubowsky, S., 1981, "The Application of Finite Element Methods to the Dynamic Analysis of Flexible Spatial and Co-Planar Linkage Systems," *ASME Journal of Mechanical Design*, Vol. 103, pp. 643-651.
- [2] Sunada, W.H. and Dubowsky, S., 1983, "On the Dynamic Analysis and Behavior of Industrial Robotic Manipulators with Elastic Members," *ASME Journal of Mechanisms, Transmissions, and Automation in Design*, Vol. 105, pp. 42-51.
- [3] Naganathan, G. and Soni, A.H., 1986, "Non-Linear Flexibility Studies for Spatial Manipulators," *IEEE International Conference on Decision and Control*, Vol. 1, pp. 373-378.
- [4] Naganathan, G. and Soni, A.H., 1987, "Coupling Effects of Kinematics and Flexibility in Manipulators," *MIT The International Journal of Robotics Research*, Vol. 6, No. 1, pp. 75-84.
- [5] Naganathan, G. and Soni, A.H., 1987, "An Analytical and Experimental Investigation of Flexible Manipulator Performance," *IEEE International Conference on Robotics and Automation*, Vol. 1, pp. 767-773.
- [6] Naganathan, G. and Soni, A.H., 1988, "Nonlinear Modeling of Kinematic and Flexibility Effects in Manipulator Design," *ASME Journal of Mechanisms, Transmissions, and Automation Design*, Vol. 110, pp. 243-254.
- [7] Naganathan, G. and Soni, A.H., "Dynamic Response of a Manipulator," *ASME 9th Applied Mechanisms Conference Proceedings*, Kansas City, Missouri, Vol. 2, Session XII.A, pp. III.1-6.
- [8] Simo, J.C. and Vu-Quoc, L., 1986, "On The Dynamics of Flexible Beams Under Large Overall Motions-The Plane Case: Part I," *ASME Journal of Applied Mechanics*, Vol. 53, pp. 849-854.
- [9] Simo, J.C. and Vu-Quoc, L., 1986, "On The Dynamics of Flexible Beams Under Large Overall Motions-The Plane Case: Part II," *ASME Journal of Applied Mechanics*, Vol. 53, pp. 855-863.
- [10] Sadler, J.P., Yang, Z., and Rouch, K.E., 1988, "The Use of ANSYS for the Analysis of Flexible Four-Bar Linkages," *ASME Trends and Developments in Mechanisms, Machines, and Robots-1988*, ASMEDE-Vol. 15-2, pp. 441-447.
- [11] Yang, Z. and Sadler, J.P., 1990, "Large Displacement Finite Element Analysis of flexible Linkages," *ASME Journal of Mechanical Design*, Vol. 112, pp. 175-182.
- [12] Yang, Z. and Sadler, J.P., 1990, "Finite Element Modeling of Spatial Robot Manipulators," *ASME 21st Mechanisms, Machines, and Robots Conference Proceedings*, September, 1990, Chicago, IL.
- [13] Nagarajan, S. and Turcic, D.A., 1990, "Lagrangian Formulation of the Equations of Motion for Elastic Mechanisms With Mutual Dependence Between Rigid Body and Elastic Motions. Part I: Element Level Equations," *ASME Journal of Dynamic Systems, Measurement, and Control*, Vol. 112, pp. 203-214.
- [14] Nagarajan, S. and Turcic, D.A., 1990, "Lagrangian Formulation of the Equations of Motion for Elastic Mechanisms With Mutual Dependence Between Rigid Body and Elastic Motions. Part II: System Equations," *ASME Journal of Dynamic Systems, Measurement, and Control*, Vol. 112, pp. 215-224.
- [15] Gaultier, P.E. and Clegorn, W.L., 1989, "Modeling of Flexible Manipulator Dynamics: A Literature Survey," *The 1st National Conference on Applied Mechanisms and Robotics*, Cincinnati, Ohio, 89AMR-2C-3, pp. 1-10.
- [16] Low, K.H., 1987, "A Systematic Formulation of Dynamic Equations for Robot Manipulators with Elastic Links," *Journal of Robotic Systems*, Vol. 4(3), pp. 435-456.
- [17] Low, K.H., 1989, "Solution Schemes for The System Equations of Flexible Robots," *Journal of Robotic Systems*, Vol. 6(4), pp. 383-405.
- [18] Logan, D.L., 1986, *A First Course in The Finite Element Analysis*, PWS Publishers.
- [19] Timoshenko, S. and Gere, J., 1972, *Mechanics of Materials*, Van Nostrand Reinhold Company.

APPENDIX

Coefficient Matrices

$$Y = \begin{bmatrix} 1 & D_1 \\ 0 & 0 \\ 0 & D_2 \\ 0 & 0 \end{bmatrix} \quad Z = \begin{bmatrix} 0 & 0 \\ I' & D_3 \\ 0 & 0 \\ 0 & D_4 \end{bmatrix} \quad I' = \begin{bmatrix} 1 & 0 \\ 0 & -1 \end{bmatrix}$$

$$k_1 = \begin{bmatrix} 12 & 6l & -12 & 6l \\ & 4l^2 & -6l & 2l^2 \\ \text{Sym} & & 12 & -6l \\ & & & 4l^2 \end{bmatrix} \quad D_1 = \begin{bmatrix} -\frac{3}{2} & \frac{2}{3} \\ -\frac{2}{3} & \frac{1}{2} \end{bmatrix}$$

$$k_2 = \begin{bmatrix} 12 & -6l & -12 & -6l \\ & 4l^2 & 6l & 2l^2 \\ \text{Sym} & & 12 & 6l \\ & & & 4l^2 \end{bmatrix} \quad D_2 = \begin{bmatrix} \frac{3}{2} & -\frac{2}{3} \\ -\frac{2}{3} & \frac{1}{2} \end{bmatrix}$$

$$D_3 = \begin{bmatrix} -\frac{3}{2} & \frac{2}{3} \\ \frac{2}{3} & -\frac{1}{2} \end{bmatrix} \quad D_4 = \begin{bmatrix} \frac{3}{2} & -\frac{2}{3} \\ \frac{2}{3} & -\frac{1}{2} \end{bmatrix}$$

$$J_1 = \begin{bmatrix} 1 & 0 & 0 & 0 \\ 0 & 0 & 1 & 0 \end{bmatrix} \quad J_2 = \begin{bmatrix} 0 & 1 & 0 & 0 \\ 0 & 0 & 0 & 1 \end{bmatrix}$$

where I is a 2×2 unit matrix and 0 is a 2×2 zero matrix.

Skew-Symmetric Matrix and Properties

For a given vector $\bar{\Omega}$, a corresponding skew-symmetric matrix $\hat{\Omega}$ associated with the vector $\bar{\Omega}$ is defined as

$$\hat{\Omega} = \begin{bmatrix} 0 & -\Omega_3 & \Omega_2 \\ \Omega_3 & 0 & -\Omega_1 \\ -\Omega_2 & \Omega_1 & 0 \end{bmatrix}$$

where $\Omega_i (i = 1, 2, 3)$ are the components of the vector $\bar{\Omega}$. In an analogy, a skew-symmetric matrix \hat{d} associated with a given matrix d is defined as

$$\hat{d} = \begin{bmatrix} 0 & -d_3 & d_2 \\ d_3 & 0 & -d_1 \\ -d_2 & d_1 & 0 \end{bmatrix}$$

where d is partitioned as $d = [d_1^T d_2^T d_3^T]^T$.

For simplicity, two special matrix product operators \otimes and Γ are introduced in the current paper. These special operators have the higher priority over all other matrix operations, and they are defined as

$$\begin{aligned} A \otimes \Gamma(B) &= [A_{ij} B] \text{ for each submatrix} \\ \Gamma(B) \otimes A &= [B A_{ij}] \text{ for each submatrix} \\ \Gamma^T(B) &= \Gamma(B^T) \end{aligned}$$

where A is a partitioned matrix with the following form as

$$A = \begin{bmatrix} A_{11} & \dots & \dots & A_{1n} \\ \vdots & & & \vdots \\ \vdots & & A_{mj} & \vdots \\ A_{m1} & \dots & \dots & A_{mn} \end{bmatrix}$$

and the number of column of each A_{ij} ($i = 1, \dots, m$; $j = 1, \dots, n$) must be equal to the number of row of matrix B so that they are compatible in matrix operating.

If q is an n dimensional vector, and a scalar Φ and an m dimensional vector a are the functions of q , the following matrix partial derivatives are defined.

$$\frac{\partial \Phi}{\partial q^T} = \left\{ \frac{\partial \Phi}{\partial q_i} \right\}; \quad \frac{\partial a}{\partial q^T} = \left[\frac{\partial a_j}{\partial q_i} \right]$$

($i = 1, \dots, n$; $j = 1, \dots, m$)

where $\{\partial \Phi / \partial q_i\}$ is an n dimensional vector, and $[\partial a_j / \partial q_i]$ is an $n \times m$ matrix in which i determines a row and j determines a column for the matrix. The following properties of matrix partial derivatives are derived from the above definitions.

$$\begin{aligned} \frac{\partial}{\partial q^T} (a^T b) &= \frac{\partial a}{\partial q^T} b + \frac{\partial b}{\partial q^T} a \\ \frac{\partial}{\partial q^T} (C q) &= C^T \\ \frac{\partial}{\partial q^T} (q^T C q) &= (C + C^T) q \\ \frac{\partial}{\partial q^T} (\Phi_1 \Phi_2) &= \frac{\partial \Phi_1}{\partial q^T} \Phi_2 + \Phi_1 \frac{\partial \Phi_2}{\partial q^T} \\ \frac{\partial}{\partial q^T} (B a) &= \frac{\partial B}{\partial q^T} a + \left[\frac{\partial b_1}{\partial q^T} a \quad \dots \quad \frac{\partial b_n}{\partial q^T} a \right] \end{aligned}$$

where $B = [b_1 \dots b_n]^T$, a , b , Φ_1 , Φ_2 , and B are the functions of q , C is a constant matrix, and b_i ($i = 1, \dots, n$) are the subvectors in B .

**APPENDIX E. Modeling of Multibody Flexible Articulated Structures
with Mutually Coupled Motions: Part II - Application and Results.**

MODELING OF MULTIBODY FLEXIBLE ARTICULATED STRUCTURES WITH MUTUALLY COUPLED MOTIONS: PART II — APPLICATION AND RESULTS

Jiechi Xu and Joseph R. Baumgarten
Department of Mechanical Engineering
Iowa State University
Ames, Iowa

ABSTRACT

The application of the systematic procedures in the derivation of the equations of motion proposed in Part I of this work is demonstrated and implemented in detail. The equations of motion for each subsystem are derived individually and are assembled under the concept of compatibility between the local kinematic properties of the elastic degrees of freedom of those connected elastic members. The specific structure under consideration is characterized as an open loop system with spherical unconstrained chains being capable of rotating about a Hooke's or universal joint. The rigid body motion, due to two unknown rotations, and the elastic degrees of freedom are mutually coupled and influence each other. The traditional motion superposition approach is no longer applicable herein. Numerical examples for several cases are presented. These simulations are compared with the experimental data and good agreement is indicated.

INTRODUCTION

Part I of this work presents the development of the equations of motion for an arbitrary elastic beam in a flexible structural system containing both the rigid and elastic bodies. In part II of the paper the theories developed in part I are applied to a specific problem. The structural system is characterized as an open loop system with spherical unconstrained chains being capable of rotational motion. The equations of motion for the rigid bodies in the system are derived in a fashion similar to the derivation of the equations of motion for the elastic beams. The influence of the elastic deformations preceding the rigid body is considered. The strategy in the derivation is first to obtain the local level dynamic equations and then to assemble the equations at the global level. The geometric boundary conditions are implemented to ensure the compatibility between the local displacement, velocity and acceleration of the elastic degrees of freedom that are common to two or more members. Fig. 1 shows a satellite test rig built by Cowles [1] and Anderson [2] at the Iowa State University. A corresponding schematic drawing of the dynamic part of the test rig is shown in Fig. 2. A lower shaft supports an upper rotating structure and is driven by a DC motor through a driving chain. An upper shaft is connected to the lower shaft by a Hooke's type universal joint. A cross bar is fixed on the top of the upper shaft to balance the coning motion. An upper assembly is defined as those parts of the structure that are supported by the universal joint, except the upper shaft and the cross bar. The configuration of the entire rotating upper assembly is axisymmetric about the spin



Figure 1: A test rig

axis of the lower shaft.

COORDINATE SYSTEMS

Fig. 3 shows the coordinate systems associated with the structural model of the test rig to assist analyzing the dynamic response of the structural system. Point O is a universal joint at which the origin of a set of inertial coordinates ($\hat{e}_1, \hat{e}_2, \hat{e}_3$) is located. In addition, coordinates ($\hat{i}_b, \hat{j}_b, \hat{k}_b$), named moving coordinates, are also settled at point O . These moving coordinates are initially aligned with the inertial coordinates but are attached to the upper assembly and are then rotated with the assembly. Three successive rotating angles are defined between these two sets of coordinates. One set of coordinates is defined for each beam, elastic or rigid, and each tank, with the corresponding origins located at each proximal end of the beams and at each geometric center of the tanks, respectively. All of the coordinates are locally defined with their i coordinates being selected such that they coincide with the center lines of the undeformed beams or they are initially pointed to the opposite direction of one of the moving coordinates, \hat{k}_b , for each tank.

Three Successive Rotating Angles

A set of three successive rotating angles about the universal joint

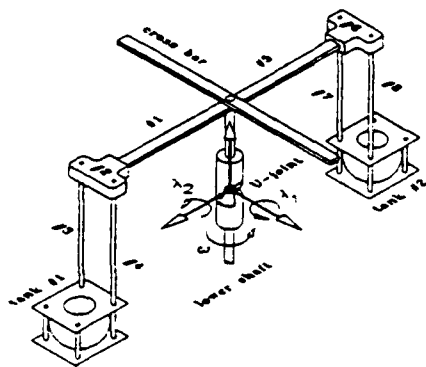


Figure 2: Schematic of the test rig

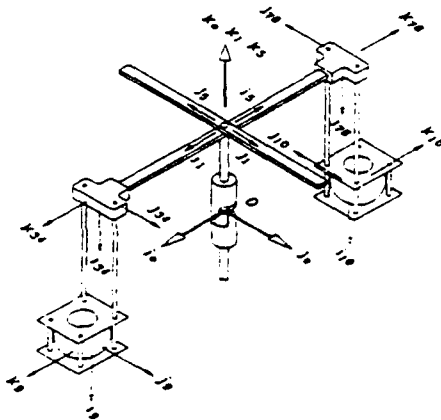


Figure 3: Coordinate systems

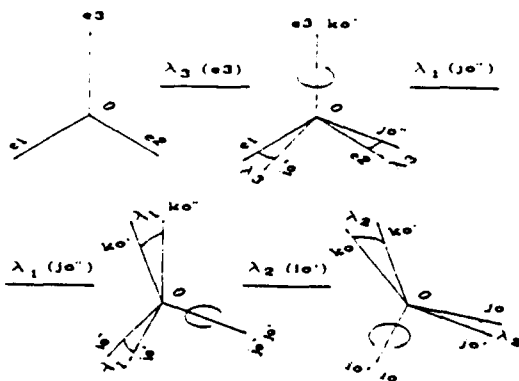


Figure 4: Three successive rotating angles

is defined between the inertial and moving coordinates as shown in Fig. 4. Firstly, the upper shaft spins about the \hat{e}_3 axis of the inertial coordinates with an angle of λ_3 to reach a first intermediate system $(\hat{i}_0, \hat{j}_0, \hat{k}_0)$. Secondly, the upper assembly nutates about the \hat{j}_0 axis of the first intermediate system with an angle of λ_1 to reach a second intermediate system $(\hat{i}_1, \hat{j}_1, \hat{k}_1)$. Finally, the upper assembly rotates an angle of λ_2 about the \hat{i}_1 axis of the second intermediate system to reach the final moving coordinates $(\hat{i}_2, \hat{j}_2, \hat{k}_2)$. These three successive rotating angles constitute the base of the rigid body gross motion which is essential in analyzing the structural deflections and rotations.

Rigid Body Angular Velocity

Referring to Fig. 4, the rigid body angular velocity $\vec{\Omega}$, interpolated as the angular velocity of the moving frame, can be found by means of the superposition principle of angular velocity, as

$$\vec{\Omega} = \lambda_3 \hat{e}_3 - \lambda_1 \hat{j}_0 - \lambda_2 \hat{i}_1 \quad (1)$$

where $\lambda_i (i = 1, 2, 3)$ are the corresponding time rates of three successive rotating angles $\lambda_i (i = 1, 2, 3)$. By observing the rotations, it is found that the following unit vectors are identical, i.e.

$$\hat{e}_3 = \hat{k}_0, \quad \hat{j}_0 = \hat{j}_1, \quad \hat{i}_1 = \hat{i}_2$$

Substituting above three identities into Eq. 1 gives

$$\vec{\Omega} = \lambda_3 \hat{k}_0 - \lambda_1 \hat{j}_0 - \lambda_2 \hat{i}_0 \quad (2)$$

The objective is to transfer \hat{k}_0 and \hat{j}_0 coordinates into $(\hat{i}_2, \hat{j}_2, \hat{k}_2)$ system. From Appendix , this can be easily resolved and the final expression can be shown as

$$\vec{\Omega} = \vec{e}_2^T \Omega \quad (3)$$

where $\vec{e}_2^T = (\hat{i}_2, \hat{j}_2, \hat{k}_2)$, a set of unit vectors of the moving coordinates, and Ω is an angular velocity vector which can be written as

$$\Omega = N \dot{\lambda} \quad (4)$$

where $\dot{\lambda} = \{\dot{\lambda}_1, \dot{\lambda}_2, \dot{\lambda}_3\}^T$, and N is a coefficient matrix containing the information of three successive rotations and is defined as

$$N = \begin{bmatrix} N_{11}^T \\ N_{21}^T \\ N_{31}^T \end{bmatrix} = \begin{bmatrix} 0 & 1 & -\sin \lambda_1 \\ \cos \lambda_2 & 0 & \cos \lambda_1 \sin \lambda_2 \\ -\sin \lambda_2 & 0 & \cos \lambda_1 \cos \lambda_2 \end{bmatrix} \quad (5)$$

It has been shown that the configurations of the structure are axisymmetric. This does not imply, however, the symmetry of the inertial forces about the spin axis, which induce elastic deformations. From a static force analysis, it is found that the tangential inertial forces are non-symmetric about the spin axis in three orthogonal Cartesian planes. Each elastic beam must be therefore discretized using the different generalized coordinates.

TANK DYNAMICS

Referring to Fig. 2, a tank assembly or a tank for simplicity, constructed of a spherical plastic container, liquid within the container, two clamping steel plates which hold the spherical tank, and some clamping bolts, is considered as a rigid body system. One tank is placed on each side of the test rig axisymmetrically. Liquid sloshing within the tank is modeled by Computational Fluid Dynamics (CFD) [3]. The interaction mechanisms between the structure and liquid are investigated in a joint efforts from the flexible structure model and the CFD model. The results are published under a separate paper [4]. Due to the special construction of the tank assembly, some elastic degrees of freedom of the supporting flexible

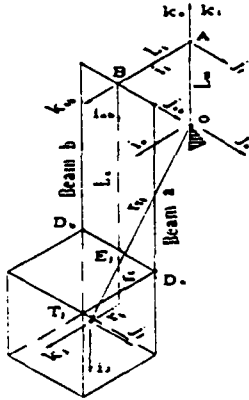


Figure 5: Tank assembly

beams connecting the tank assembly are constrained. The geometric constraints are revealed explicitly prior to defining tank generalized coordinates. Tank equations of motion are derived in such a way that one model accommodates two tanks in terms of proper substitutions of the corresponding transformation matrices between the participated coordinates. A position vector of the tank is formulated first followed by the derivation of a velocity vector at the mass center of the tank assembly by differentiating the position vector with respect to time. The vector expressions are all relative to the moving coordinates. The tank translational kinetic energy are found by using a standard formula involving a velocity squared term. The tank angular velocity and the inertia dyadic about the mass center are formulated prior to calculating tank rotational kinetic energy. Gravity is the only external loading under consideration. The instantaneous liquid free surface shape and its orientation within the tank are supplied by the output of the CFD modeling. Liquid inertia dyadic is updated so as to update the tank kinetic energy. The mass center of sloshing liquid is calculated relative to the geometric center of the tank. The coefficient mass, damping, and stiffness matrices and the generalized force vectors are formulated by applying Lagrange's equation. The derivation of the tank dynamic equations can therefore be accomplished.

Geometric Constraints

Fig. 5 depicts the tank assembly and its associated structures. Beams *a* and *b* are two flexible beams which connect the rigid tank assembly at the clamped points, D_1 and D_2 . The transverse deflections of these two beams in the \hat{j}_{ab} direction are equal to each other. The rotation of beam *a* about the \hat{j}_{ab} axis at point D_1 is equal to the corresponding rotation of beam *b* about the same axis at point D_2 . The rotations of the beams about the \hat{k}_{ab} axis at points D_1 and D_2 are zero because these points are clamped on the tank. Therefore, the following four geometric boundary conditions are concluded.

$$\begin{aligned} d_{1my} &= d_{2my}; & \phi_{1my} &= \phi_{2my} \\ \phi_{1mz} &= 0; & \phi_{2mz} &= 0 \end{aligned} \quad (6)$$

where the second subscript *m* denotes the last finite element node (for both beams) which coincides with either the point D_1 or the point D_2 , d_{1my} and d_{2my} are the deflections of beams *a* and *b* in the \hat{j}_{ab} direction, ϕ_{1my} and ϕ_{2my} are the rotations about the \hat{j}_{ab} axis, and ϕ_{1mz} and ϕ_{2mz} are the rotations about the \hat{k}_{ab} axis.

The local generalized coordinates of the tank assembly include the

rigid body degrees of freedom, which result from three rotations about the universal joint, and the elastic degrees of freedom, which are due to the elastic deformations at the distal end B_1 of beam *a* and the elastic deformations at the points D_1 and D_2 . By applying four geometric boundary conditions stated in Eq. 6, a set of local generalized coordinates is defined as

$$q_i = \{\lambda^T d_i^T\}^T \quad (7)$$

where

$$d_i^T = \{d_{1my}\phi_{1mz}d_{1mz}\phi_{1my}d_{2my}d_{2mz}\phi_{2my}d_{2mz}\} \quad (8)$$

Thus,

$$\begin{aligned} \lambda &= \Theta_{i\lambda} q_i \\ d_i &= \Theta_{id} q_i \end{aligned} \quad (9)$$

where the coefficient matrices $\Theta_{i\lambda}$ and Θ_{id} can be easily found by their definitions.

Tank Position and Velocity Vectors

Referring to Fig. 5 again, point T_1 is a mass center of the corresponding tank assembly, and the vector \vec{r}_{T_1} is the position vector of the mass center. Thus,

$$\begin{aligned} \vec{r}_{T_1} &= L_{01}\hat{k}_1 - L_{11}\hat{i}_1 - d_{1my}\hat{j}_1 - d_{1mz}\hat{k}_1 - \\ &L_{21}\hat{i}_2 - d_{2my}\hat{j}_2 - \frac{1}{2}(d_{2mz} - d_{3mz})\hat{k}_2 - \\ &r_{11}\hat{i}_1 - r_{12}\hat{j}_1 - \Delta_1\hat{i}_1 - \Delta_2\hat{j}_1 - \Delta_3\hat{k}_1 \end{aligned} \quad (10)$$

where the Δ 's are the relative coordinates of the instantaneous mass center deviated from the initial position during the tank motion. It should be noticed that the first four terms in the above equation determine the position vector of point B_1 after elastic deflections of beam *a*, the next four terms relate a relative position vector of point E_1 to point B_1 , and the last five terms establish a relative position vector of the mass center T_1 to point E_1 on the tank. After transferring the local coordinates to the moving coordinates, it can be shown that Eq. 10, in matrix form, becomes

$$\begin{aligned} \vec{r}_{T_1} &= \begin{Bmatrix} 0 \\ 0 \\ L_{01} \end{Bmatrix} - T_{01} \begin{Bmatrix} L_{11} \\ d_{1my} \\ d_{1mz} \end{Bmatrix} - \\ &T_{02} \begin{Bmatrix} L_{21} \\ d_{2my} \\ \frac{1}{2}(d_{2mz} - d_{3mz}) \end{Bmatrix} - \\ &T_{03} T_{11} \begin{Bmatrix} r_{11} - \Delta_1 \\ \Delta_1 \\ r_{12} - \Delta_2 \end{Bmatrix} \end{aligned} \quad (11)$$

where the matrices T_{01} , T_{02} and T_{11} are the rotational transformation matrices (see Appendix) wherein T_{01} is a constant matrix and T_{02} is a time-varying matrix. Physically, beam *a* is much stiffer than beams *a* and *b*, and hence the T_{02} matrix is approximately constant. Differentiating the above equation with respect to time yields a velocity vector as

$$\begin{aligned} \dot{\vec{r}}_{T_1} &= T_{01} \begin{Bmatrix} 0 \\ \dot{d}_{1my} \\ \dot{d}_{1mz} \end{Bmatrix} - T_{02} \begin{Bmatrix} 0 \\ \dot{d}_{2my} \\ \frac{1}{2}(\dot{d}_{2mz} - \dot{d}_{3mz}) \end{Bmatrix} \\ &- T_{02} \dot{T}_{11} \begin{Bmatrix} r_{11} + \Delta_1 \\ \Delta_1 \\ r_{12} + \Delta_2 \end{Bmatrix} \\ &- T_{02} T_{11} \begin{Bmatrix} \dot{\Delta}_1 \\ \dot{\Delta}_2 \\ \dot{\Delta}_3 \end{Bmatrix} - \dot{T}_{11} \vec{r}_{T_1} \end{aligned} \quad (12)$$

where the Δ 's are the relative velocity components of the tank mass center, which are small compared with the tank overall motion. The term associated with these components can then be neglected in the above velocity equation. $\tilde{\Omega}$ is a skew-symmetric matrix derived from the corresponding rigid body angular velocity $\tilde{\Omega}$.

Tank Angular Velocity

The tank angular velocity $\tilde{\Omega}$ is a vector summation of the following three angular velocities,

1. $\tilde{\Omega}$, a rigid body angular velocity ($\dot{\hat{e}}_0$ relative to \hat{e}_0)
2. $\tilde{\omega}_{ab}$, a rigid beam angular velocity ($\dot{\hat{e}}_{ab}$ relative to \hat{e}_0)
3. $\tilde{\omega}_l$, a tank local angular velocity ($\dot{\hat{e}}_l$ relative to \hat{e}_{ab})

Referring to Fig. 5, it can be shown that the tank angular velocity $\tilde{\Omega}$, takes the following matrix form as

$$\tilde{\Omega} = \hat{e}_0^T \left(\tilde{\Omega} - T_{\alpha} \begin{Bmatrix} \phi_{lmy} \phi_{lms} \\ \phi_{lmy} \\ \phi_{lms} \end{Bmatrix} - T_{ab} \begin{Bmatrix} 0 \\ \phi_{amy} \\ 0 \end{Bmatrix} \right) \quad (13)$$

The local inertia dyadic of the tank assembly about the mass center of the tank can be written as

$$\tilde{I}_l = \hat{e}_l^T I_l \hat{e}_l \quad (14)$$

where I_l is a local inertia matrix about the local tank coordinates. Substituting the transformation matrices between the moving frame and the tank local frame ($\hat{i}_l, \hat{j}_l, \hat{k}_l$) into the above equation yields

$$\tilde{I}_l = \hat{e}_0^T I_l \hat{e}_0 \quad (15)$$

where

$$I_l = T_{ab} T_{ab}^T I_l T_{\alpha}^T T_{\alpha}^T \quad (16)$$

Kinetic Energy

The tank kinetic energy, translational and rotational, can be formulated as

$$KE = \frac{1}{2} m_t \dot{\hat{e}}_0^T \dot{\hat{e}}_0 - \frac{1}{2} \tilde{\Omega} \cdot \tilde{I}_l \cdot \tilde{\Omega} \quad (17)$$

Substituting Eqs. 9, 12-15, and the expression of $\tilde{\Omega}$ into Eq. 17, one can find that the kinetic energy of the tank assembly becomes

$$KE = \frac{1}{2} \dot{q}_j^T m_j \dot{q}_j \quad (18)$$

where the mass matrix m_j is written as

$$\begin{aligned} m_j &= m_t \hat{e}_0^T N^T (G_{j1} + H_{j1} - H_{j2} - \frac{1}{m_j} I_l) \cdot \\ &N \hat{e}_0 + \hat{e}_0^T G_{j3} \hat{e}_0 - m_{je} - \\ &m_t \hat{e}_0^T (G_{j2} - H_{j2} - \frac{1}{m_j} H_{j4}) N \hat{e}_0 - \\ &m_t \hat{e}_0^T N^T (G_{j2}^T - H_{j2}^T - \frac{1}{m_j} H_{j4}^T) \hat{e}_0 \end{aligned} \quad (19)$$

where m_j is the total mass of the tank, m_{je} is an instantaneous constant mass matrix, G_{j1} , G_{j2} , and G_{j3} are the instantaneous constant coefficient matrices, H_{j1} and H_{j2} are the time-varying symmetric matrices, and H_{j3} and H_{j4} are time-varying rectangular matrices. All these matrices are similar to the corresponding ones listed in

Part I. Partial differentiating Eq. 18 with respect to q_j , and partial differentiating Eq. 18 with respect to \dot{q}_j , followed by differentiating the result with respect to time will result in the following damping matrix, as

$$c_j = \dot{m}_j - \frac{1}{2} \frac{\partial(m_j \dot{q}_j)}{\partial \dot{q}_j^T} \quad (20)$$

where the partial differentiation can be obtained following the same derivation demonstrated in Part I.

Potential Energy

The tank potential energy is constituted of only the tank elevation in the gravitational field. Following the same procedure in Part I one can find that the potential energy takes a similar formulation as

$$PE = V_j - h_j^T q_j \quad (21)$$

where the potential function V_j and the force coefficient vector h_j , are the functions of the local generalized coordinates q_j . Partial differentiating the above potential energy equation with respect to q_j yields the following generalized force vectors and stiffness matrix as

$$f_j = -\frac{\partial V_j}{\partial q_j} - h_j; \quad k_j = \frac{\partial h_j}{\partial q_j} \quad (22)$$

where the matrix partial differentiations can also be obtained in a similar way as demonstrated in Part I.

Tank Equations of Motion

The equations of motion of the tank can now be written in a standard form as

$$m_j \ddot{q}_j + c_j \dot{q}_j + k_j q_j = f_j \quad (23)$$

where all the coefficient matrices and the generalized force vectors are already derived in the previous sections. Particularly, the mass matrix m_j , the stiffness matrix k_j , and the generalized force vector f_j are the functions of the generalized coordinates q_j only while the damping matrix c_j is a function of both the generalized coordinates q_j and velocities \dot{q}_j .

RIGID BEAM DYNAMICS

Beams 2 and 6 (see Fig. 3) are modeled as the rigid bodies because they are much more rigid in resisting deflections than other beams. Following the same concept in the tank dynamics, only one model is developed to accommodate two rigid beams.

Velocity Vector

As shown in Fig. 6, point B, is the mass center of the rigid beam after the deflections and rotations of the preceding elastic beam. Point O is the universal joint at which the moving frame is located. A position vector of the mass center of the rigid beam is then written as

$$\vec{r}_B = L_u \hat{k}_0 - L_l \hat{i}_l - d_{my} \hat{j}_l - d_{mz} \hat{k}_l \quad (24)$$

where L_u is the length of the upper shaft, L_l is the length of the preceding elastic beam, and d_{my} and d_{mz} are the elastic deflections at the distal end of the preceding elastic beam. The above vectorial equation can be rewritten in the matrix form as

$$\vec{r}_B = \begin{Bmatrix} 0 \\ 0 \\ L_u \end{Bmatrix} - T_{\alpha} \begin{Bmatrix} L_l \\ d_{my} \\ d_{mz} \end{Bmatrix} \quad (25)$$

The local generalized coordinates of the rigid beam are defined as

$$q_l^T = \lambda^T \quad d^T \quad (26)$$

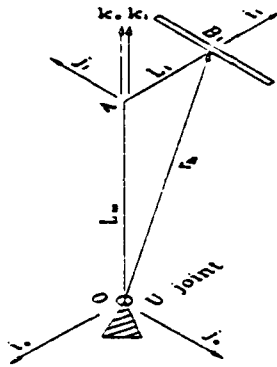


Figure 6: Rigid beam schematic

where d_i , the elastic generalized coordinates of the preceding elastic beam, are defined as

$$d_i^T = \{d_{1m_y}, \phi_{1m_z}, d_{1m_z}, \phi_{1m_y}\} \quad (27)$$

Differentiating Eq. 25 with respect to time yields the following velocity vector, as

$$\dot{r}_{B1} = T_n \left\{ \begin{array}{c} 0 \\ \dot{d}_{1m_y} \\ \dot{d}_{1m_z} \end{array} \right\} - \bar{\Omega} r_{B1} \quad (28)$$

Inertia Dyadic and Angular Velocity

The inertia dyadic of the rigid beam about its mass center B_1 is formulated in the following, as

$$\bar{I}_1 = \bar{e}_1^T T_n I_1 T_n^T \bar{e}_1 \quad (29)$$

where $I_1 (i = 1, 2, 3)$ is a local inertia matrix about the $\bar{i}_1, \bar{j}_1, \bar{k}_1$ coordinates. The angular velocity of the rigid beam can be written as

$$\begin{aligned} \bar{\Omega}_1 &= \bar{\Omega} - \bar{\omega}_1 \\ &= \bar{e}_1^T \left(\bar{\Omega} - T_n \left\{ \begin{array}{c} \phi_{1m_y} \dot{\phi}_{1m_z} \\ \phi_{1m_y} \\ \phi_{1m_z} \end{array} \right\} \right) \end{aligned} \quad (30)$$

where $\bar{\omega}_1$ is a local angular velocity accounting for the rotations, ϕ_{1m_y} and ϕ_{1m_z} , of the preceding elastic beam.

Rigid Beam Equations of Motion

Following the same procedures stated in the previous sections, one first formulates the kinetic and potential energies in terms of Eqs. 26 - 30, then derives the mass, damping, and stiffness matrices and the generalized force vectors by differentiating the kinetic energy and potential energy terms with respect to the corresponding quantities, generalized coordinates, velocities, and time. Finally, one can obtain the equations of motion of the rigid beam in the following form as

$$m_1 \ddot{q}_1 + c_1 \dot{q}_1 + k_1 q_1 = f_1 \quad (31)$$

where m_1 , k_1 , and f_1 are the functions of q_1 only, and c_1 is a function of \dot{q}_1 and \ddot{q}_1 . These matrices and vectors are similar to those derived in the tank dynamics.

DYNAMICS OF A BAR-SHAFT ASSEMBLY

The cross bar, the lower shaft, and the upper shaft (see Fig. 2) construct a bar-shaft assembly. Following the same procedures in Lagrange's approach, it can be shown that the kinetic and potential energies of the assembly take the following forms, as

$$\begin{aligned} KE_o &= \frac{1}{2} (I_{L1} \dot{\lambda}_1^2 - \dot{\lambda}^T m_{u1} \dot{\lambda} - \dot{\lambda}^T m_{c1} \dot{\lambda}) \\ PE_o &= -m_{L1} G L_{L1} - \left(\frac{1}{2} m_{u1} - m_{c1} \right) G L_{u1} T_{o33} \end{aligned} \quad (32)$$

where I_{L1} is the moment of inertia of the lower shaft about its spin axis, m_{u1} and m_{c1} are the mass matrices of the upper shaft and the cross bar, respectively, m_{L1} , m_{u1} , and m_{c1} are the corresponding masses of the lower shaft, the upper shaft, and the cross bar. L_{L1} is the length between the universal joint and the mass center of the lower shaft, and T_{o33} is an element of the transformation matrix T_o which relates the inertial frame to the moving frame. Substituting above equations into Lagrange's formula gives the following dynamic equations of the bar-shaft assembly, as

$$\begin{aligned} (m_{oe} - m_{oe}) \ddot{\lambda} - c_o \dot{\lambda} \\ = f_o - \left(\frac{1}{2} m_{u1} - m_{c1} \right) G L_{u1} \frac{\partial T_{o33}}{\partial \lambda^T} \end{aligned} \quad (33)$$

where m_{oe} is a 3×3 null matrix except the element at the 3rd row and the 3rd column with the value of I_{L1} , f_o is a zero force vector except the 3rd component which reflects the unknown input torque about the vertical axis \bar{e}_3 applied on the lower shaft. The time-varying mass matrix m_{oe} and damping matrix c_o can be expressed as

$$\begin{aligned} m_{oe} &= m_{u1} - m_{c1} \\ c_o &= \dot{m}_{oe} - \frac{1}{2} \frac{\partial (m_{oe} \dot{\lambda})}{\partial \lambda^T} \end{aligned} \quad (34)$$

where $m_{oe} = m_{u1} - m_{c1}$.

SYSTEM MOTION EQUATIONS

The equations of motion for the elastic beams are derived in Part I. The total degrees of freedom of the system are nineteen if each elastic beam is modeled by one finite element. Three of the generalized coordinates result from the rigid body motion and the rest are due to the elastic deformations. If each elastic beam is modeled by two elements the total number of degrees of freedom then increases to forty three.

Global and Local Generalized Coordinates

By using one element for each elastic beam, the global generalized coordinates are selected as

$$q = \{ \lambda^T, d_{1m_y} \phi_{1m_z} d_{1m_z} \phi_{1m_y}, d_{3m_y} \phi_{3m_z} d_{3m_z} \phi_{3m_y}, d_{3m_y} d_{3m_z} \phi_{3m_y} d_{4m_z}, d_{7m_y} d_{7m_z} \phi_{7m_y} d_{8m_z} \}^T \quad (35)$$

where the first subscripts of each elastic variable denote the corresponding elastic beams, and the second subscripts m denotes the last node. Accordingly, the local generalized coordinates are defined in the follows:

$$\begin{aligned} q_1^T &= \{ \lambda^T | 0 | d_{1m_y} \phi_{1m_z} d_{1m_z} \phi_{1m_y} \} \\ q_2^T &= \{ \lambda^T | 0 | d_{3m_y} \phi_{3m_z} d_{3m_z} \phi_{3m_y} \} \\ q_3^T &= \{ \lambda^T | 0 | d_{3m_y} \phi_{3m_z} d_{3m_z} \phi_{3m_y} \} \\ q_4^T &= \{ \lambda^T | 0 | d_{4m_y} \phi_{4m_z} d_{4m_z} \phi_{4m_y} \} \end{aligned}$$

$$\begin{aligned}
\bar{q}_1^T &= \{\lambda^T \ 0 \ d_{7my} \phi_{7mz} \ d_{7mz} \ \phi_{7my}\} \\
\bar{q}_2^T &= \{\lambda^T \ 0 \ d_{8my} \phi_{8mz} \ d_{8mz} \ \phi_{8my}\} \\
\bar{q}_3^T &= \{\lambda^T\} \\
\bar{q}_4^T &= \{\lambda^T \mid d_{1my} \phi_{1mz} \ d_{1mz} \ \phi_{1my}\} \\
\bar{q}_5^T &= \{\lambda^T \mid d_{3my} \phi_{3mz} \ d_{3mz} \ \phi_{3my}\} \\
\bar{q}_6^T &= \{\lambda^T \mid d_{1my} \phi_{1mz} \ d_{1mz} \ \phi_{1my} \mid \\
&\quad \mid d_{3my} \phi_{3mz} \ d_{3mz} \ \phi_{3my} \mid \\
\bar{q}_{10}^T &= \{\lambda^T \mid d_{5my} \phi_{5mz} \ d_{5mz} \ \phi_{5my} \mid \\
&\quad \mid d_{7my} \phi_{7mz} \ d_{7mz} \ \phi_{7my} \mid \\
&\quad \mid d_{8my} \phi_{8mz} \ d_{8mz} \ \phi_{8my}\}
\end{aligned} \quad (36)$$

where q_1, q_5, q_3, q_4, q_7 , and q_8 are the generalized coordinates for the corresponding elastic beams, q_0 are for the bar-shaft assembly, q_2 and q_6 are for the rigid beams, and q_9 and q_{10} are for the tanks. The null vector 0, containing four components, appears in each set of the generalized coordinates for the elastic beams because the proximal ends are all clamped in this particular structure.

Compatibility Matrices

By comparing Eq. 36 with Eq. 35, the corresponding compatibility matrices for each subsystem can be found as

$$\begin{aligned}
\bar{\Phi}_1 &= \begin{bmatrix} I_3 & 0 & 0 \\ 0 & 0 & 0 \\ 0 & I_4 & 0 \end{bmatrix} \\
\bar{\Phi}_2 &= \begin{bmatrix} I_3 & 0 & 0 & 0 \\ 0 & 0 & 0 & 0 \\ 0 & 0 & I_4 & 0 \end{bmatrix} \\
\bar{\Phi}_3 &= \begin{bmatrix} I_3 & 0 & 0 & 0 \\ 0 & 0 & 0 & 0 \\ 0 & 0 & I_2' & 0 \end{bmatrix} \\
\bar{\Phi}_4 &= \begin{bmatrix} I_3 & 0 & 0 & 0 \\ 0 & 0 & 0 & 0 \\ 0 & 0 & I_4'' & 0 \end{bmatrix} \\
\bar{\Phi}_7 &= \begin{bmatrix} I_3 & 0 & 0 \\ 0 & 0 & 0 \\ 0 & 0 & I_4' \end{bmatrix} \\
\bar{\Phi}_8 &= \begin{bmatrix} I_3 & 0 & 0 \\ 0 & 0 & 0 \\ 0 & 0 & I_4'' \end{bmatrix} \\
\bar{\Phi}_9 &= [I_3 \ 0] \\
\bar{\Phi}_{10} &= \begin{bmatrix} I_3 & 0 & 0 \\ 0 & I_4 & 0 \\ 0 & 0 & 0 & I_4 & 0 \end{bmatrix} \\
\bar{\Phi}_{10} &= \begin{bmatrix} I_3 & 0 & 0 & 0 & 0 \\ 0 & I_4 & 0 & 0 & 0 \\ 0 & 0 & 0 & I_4 & 0 \\ 0 & 0 & 0 & 0 & I_4 \end{bmatrix}
\end{aligned} \quad (37)$$

where 0 's are the null matrices, I_3 is a 3×3 identity matrix, I_4 is a 4×4 identity matrix, and I_2' and I_4' are defined as

$$I_4' = \begin{bmatrix} 1 & 0 & 0 & 0 \\ 0 & 0 & 0 & 0 \\ 0 & 1 & 0 & 0 \\ 0 & 0 & 1 & 0 \end{bmatrix}$$

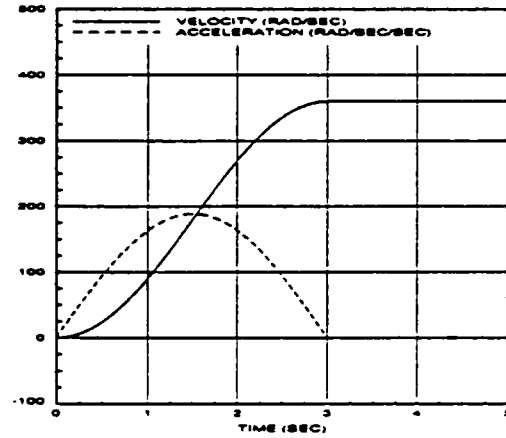


Figure 7: Spin profile

$$I_d'' = \begin{bmatrix} 1 & 0 & 0 & 0 \\ 0 & 0 & 0 & 0 \\ 0 & 0 & 0 & 1 \\ 0 & 0 & 1 & 0 \end{bmatrix} \quad (38)$$

Assembly of Equations

The time rates of the compatibility matrices are zero because they are constant. Following the same procedure developed in Part I, one can conclude that the global mass, damping, and stiffness matrices and generalized force vectors can be written as

$$\begin{aligned}
M &= \sum_{i=0}^{10} \bar{\Phi}_i^T m_i \bar{\Phi}_i \\
C &= \sum_{i=0}^{10} \bar{\Phi}_i^T c_i \bar{\Phi}_i \\
K &= \sum_{i=0}^{10} \bar{\Phi}_i^T k_i \bar{\Phi}_i \\
F &= \sum_{i=0}^{10} \bar{\Phi}_i^T f_i
\end{aligned} \quad (39)$$

The system equations are therefore given as

$$M \ddot{q} - C \dot{q} - K q = F \quad (40)$$

Integrating the above system equations numerically will yield the solutions of the system dynamic responses which are illustrated in the following section. A detailed numerical integration method is developed and is to be published under a separate paper.

SIMULATION RESULTS

The following structure configurations and material properties are used in the simulation of dynamic response. The mass density and the Young's modulus are $0.7833 \times 10^6 (km)$ and $0.21 \times 10^{12} (Pa)$, respectively, for all the members, elastic and rigid. The units of the length (L) and cross-sectional area (A) are (m) and (m^2), respectively.

The specific values for each of the members are listed in the follows:

$$\begin{aligned} L_1 &= L_2 = 0.165; A_1 = A_2 = 0.72 \times 10^{-4} \\ L_3 &= L_4 = 0.104; A_3 = A_4 = 0.019 \times 0.019 \\ L_5 &= L_6 = L_7 = L_8 = 0.29; \\ D_3 &= D_4 = D_7 = D_8 = 0.0037(\text{diameter}) \\ L_{11} &= 0.940; D = 0.0254 \\ L_{12} &= 0.127; D = 0.0254 \\ L_{13} &= 1.219; A_{13} = 0.00635 \times 0.0254 \\ \text{Tank} &= 0.165 \times 0.165 \times 0.114 \end{aligned}$$

The total mass of the tank, including the solid structure and liquid, is 1.96(km).

The input spin velocity of the lower shaft and its corresponding angular acceleration profile are shown in Fig. 7. A sinusoidal function is adopted in the angular velocity profile in which the speed of the lower shaft increases gradually from zero to 60RPM after 3 seconds. In one case, the upper shaft is driven by the lower shaft through the universal joint without any initial tilt while in another case the λ_1 angle of the upper shaft is tilted 1 degree initially from the spin axis. The results from these two runs are compared with in Fig. 3. The top figure shows the time domain plots of the rigid body angles in which two angles are varying in a range of several degrees for the tilted case (the angle magnitudes for the non-tilt case are too small to show up in the current scale). The influence of the rigid body motion to the elastic deformations clearly shows up in three figures following the top figure. This effect is expected and accounted for in the dynamic modeling. In the third case (see Fig. 9), one of the tanks is thrust upward by an impulse of 1N after the lower shaft spins 1.3 seconds. The spin profiles are the same as those in case 1 and case 2 except that it takes only 1 second to drive the lower shaft from zero to 60RPM. The upper shaft experiences a relatively large nutation before it regains stability as evidenced by the large variations of the rotation angles of λ_1 and λ_2 , and the tank vertical position relative to the universal joint shown in the top figure. The effects of the rigid body motion is very significant to the elastic deflections and rotations in this case. The following three figures show the comparisons of the beam tangential, vertical, and radial deflections between the axisymmetric points on the tanks and the rigid beams. The most significant deformation, overall radial deflection at the tank center accounting for all the possible elastic deflections and rotations preceding the tank, is calculated and compared with the experiment measurement. A measured actual profile of the spin velocity is used in the computer simulation and the computed result matches the experimental data very well as illustrated in Fig. 10.

CONCLUSIONS

It is recalled that in the proposed approach the inherent character of mutual influence between the rigid and elastic motions is revealed by including the rigid body degrees of freedom in the system generalized coordinates. This approach results in equations of motion with highly nonlinear coupling terms, especially those associated with the time rate vector of the generalized coordinates. The equations of motion for each rigid subsystem are derived individually and are assembled along with the equations of motion for the elastic beams to obtain the system equations. The elastic deformations are completely considered in the dynamic response for the subsystems down the chain due to the nature of the open loop system. The numerical simulations clearly show a good indication that the predicted results from numerical integration match the measured experimental data very well. A detailed numerical method is discussed and developed in a forthcoming publication.

ACKNOWLEDGMENT

The authors would like to acknowledge the financial support of the

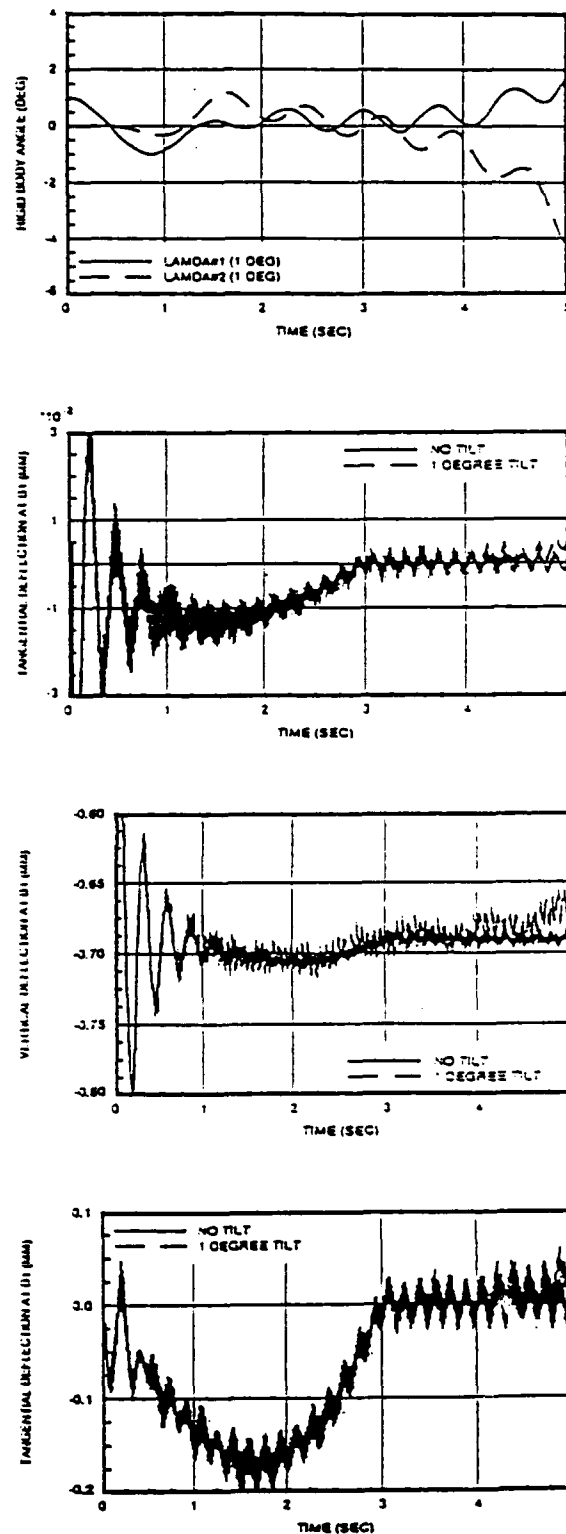


Figure 8: Case = 1 and = 2

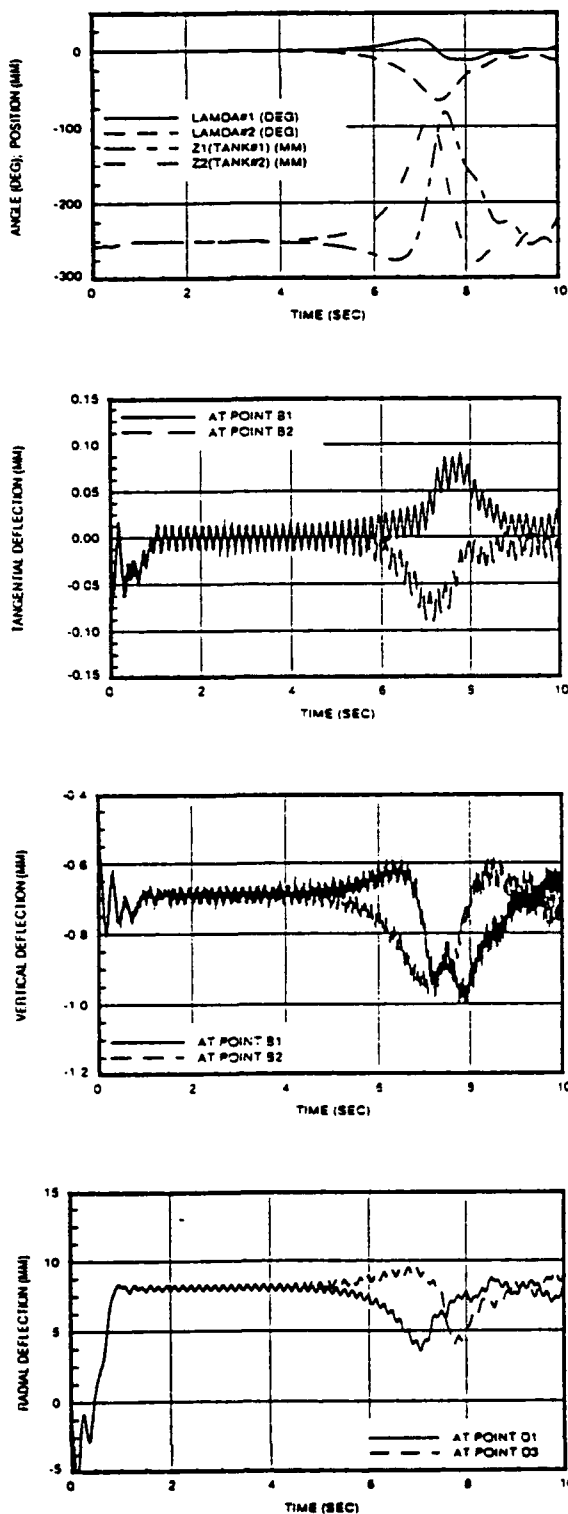


Figure 9: Case# 3 (with impulse)

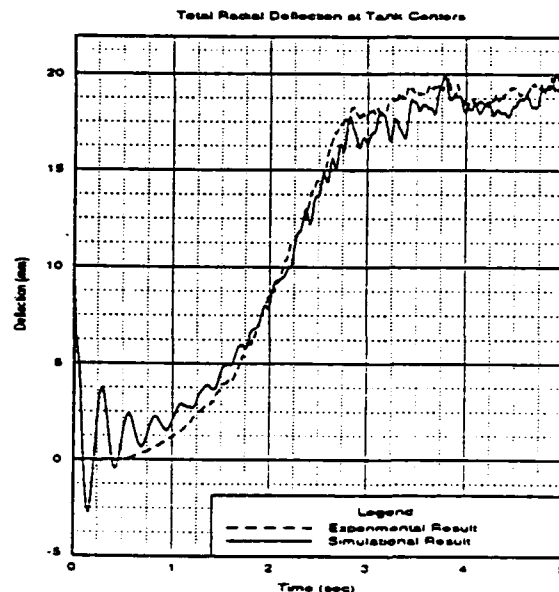


Figure 10: Overall deformation at tank center

Air Force Office of Scientific Research under Grant No. AFOSR-89-0403.

References

- [1] Cowles, D.S., 1987. "Design of A Spin-Stabilized Spacecraft Simulator with Liquid Fuel Stores." M.S. Thesis, Iowa State University, Ames, Iowa.
- [2] Anderson, M.D., 1988. "Instrumentation of A Spin-Stabilized Spacecraft Simulator with Liquid Fuel Stores." M.S. Thesis, Iowa State University, Ames, Iowa.
- [3] Chen, K.-H. and Pletcher, R.H., 1990. "A Primitive Variable, Strongly Implicit Calculation Procedure for Viscous Flows at All Speeds." AIAA-90-1521. *AIAA 21th Fluid Dynamics, Plasma Dynamics, and Lasers Conference*, June 18-20, Seattle, WA.
- [4] Kececy, F.J., Sethuramin, B., Xu, J., et al 1992. "Three-Dimensional Liquid Sloshing in A rotating Spherical Container: Accounting for The Fluid-Structure Interaction", *Symposium on High-Performance Computing for flight Vehicles*, December 7-9, Washington, D.C.

APPENDIX

If $(\hat{i}, \hat{j}, \hat{k})$ is a Cartesian coordinate system and $(\hat{e}_1, \hat{e}_2, \hat{e}_3)$ is another Cartesian coordinate system after rotating an arbitrary angle Θ about one of the axes of the system $(\hat{i}, \hat{j}, \hat{k})$, the following three rotational transformation matrices are defined, as

$$T(\Theta_x) = \begin{bmatrix} 1 & 0 & 0 \\ 0 & \cos\Theta_x & -\sin\Theta_x \\ 0 & \sin\Theta_x & \cos\Theta_x \end{bmatrix}$$

$$T(\Theta_y) = \begin{bmatrix} \cos\Theta_y & 0 & \sin\Theta_y \\ 0 & 1 & 0 \\ -\sin\Theta_y & 0 & \cos\Theta_y \end{bmatrix}$$

$$T(\Theta_k) = \begin{bmatrix} \cos\Theta_k & -\sin\Theta_k & 0 \\ \sin\Theta_k & \cos\Theta_k & 0 \\ 0 & 0 & 1 \end{bmatrix}$$

where Θ_i , Θ_j , Θ_k are the rotating angles about the \hat{i} , \hat{j} , and \hat{k} axes respectively.

Three transformation matrices encountered in the current paper are formulated as

$$\begin{aligned} T_{\alpha} &= \begin{bmatrix} T_{11} & 0 & 0 \\ 0 & T_{22} & 0 \\ 0 & 0 & T_{33} \end{bmatrix} \\ T_{\alpha\beta} &= \begin{bmatrix} 0 & 0 & t_{13} \\ 0 & t_{22} & 0 \\ t_{31} & 0 & 0 \end{bmatrix} \\ T_{\alpha\beta\gamma} &= \begin{bmatrix} 1 & 0 & \phi_{\alpha\beta\gamma} \\ 0 & 1 & -\Theta \\ -\phi_{\alpha\beta\gamma} & \Theta & 1 \end{bmatrix} \end{aligned}$$

where T_{ij} and t_{ij} are equal to either 1 or -1, and the twisting angle Θ is defined as

$$\Theta = \frac{1}{L_j}(d_{\alpha m_2} - d_{\beta m_2})$$

**APPENDIX F. A Sequential Implicit-Explicit Integration Method in
Solving Nonlinear Differential Equations from Flexible System Modeling.**

A SEQUENTIAL IMPLICIT-EXPLICIT INTEGRATION METHOD IN SOLVING NONLINEAR DIFFERENTIAL EQUATIONS FROM FLEXIBLE SYSTEM MODELING

Jiechi Xu and Joseph R. Baumgarten
Department of Mechanical Engineering
Iowa State University
Ames, Iowa

ABSTRACT

The dynamic equations of motion obtained in the modeling of flexible structural systems with unknown rigid body gross motion are often highly nonlinear and possess time-varying coefficient matrices. The inherent characters of nonlinear large overall rigid body motion and linear small vibration are also involved in the system equations. Neither the implicit nor the explicit algorithm seems optimally suited and efficient by itself in dealing with these kinds of equations. This paper, therefore, presents a sequential implicit-explicit method in which it is attempted to achieve the attributes of both classes of algorithms. The equation system expressed in matrix form is first mapped to a subsystem in which the specified generalized coordinates are eliminated. The subsystem is then partitioned into two sets of coupled equations. One set of equations, describing the elastic motion, is linear with respect to the elastic generalized coordinates and is integrated implicitly. The other set of equations, governing the rigid body motion, contains the highly nonlinear coupling terms and is integrated explicitly with the back substitutions of the elastic kinematic properties already calculated in solving the first set of equations. A Newmark algorithm is employed to integrate the second order system of differential equations directly. A predictor-corrector scheme also coming from the Newmark algorithm is applied to the explicit integration. The procedures developed in the current paper are applied to simulating dynamic response of a complicated flexible system with mutually dependent rigid body unconstrained spherical motion and small elastic deformation.

INTRODUCTION

Traditionally, the dynamic modeling for the flexible systems involving elastic bodies is focused on these problems in which the gross, or nominal, rigid body motion is predefined or can be derived. The resulting system equations, therefore, only include the elastic generalized coordinates. The mutually coupled terms between the rigid body and elastic motions are missed or neglected by assuming them small. However, for those problems with unknown rigid body motion, the corresponding rigid body degrees of freedom must also be included in the system generalized coordinates, and two motions are therefore influenced and dependent of each other. Consequently, difficulties arise in the numerical analysis. The inherent kinematic facts, reflecting the large overall nonlinear rigid body motion and small linear vibration, need to be accounted for at each time step in the integration. Basically, there are two classes of algorithms for the time integration for dynamic problems: implicit and explicit. Im-

plicit methods are usually stable numerically, permitting large time steps, and are effective for linear systems. Explicit methods, on the other hand, tend to be effective for nonlinear systems with low natural frequencies in assuring the numerical stability which depends on the highest natural frequency of the system. However, neither class seems very efficient by itself in dealing with the systems with mixed properties arising from the nonlinear and linear motions.

In analogy to the problems under investigation in this work, many methods have been developed in which it is attempted to simultaneously achieve the attributes of both classes of methods in a single algorithm. In the time integration of structure-media problems, Belytschko *et al.* [1] have presented three techniques for enhancing computational efficiency: explicit-explicit(E-E) partitions, explicit-implicit(E-I) partitions, and implicit-implicit(I-I) partitions. The mesh, resulted from the discretization in space by the finite element method, is subdivided into two subdomains in which each domain is integrated by a different method. The nodes are partitioned into two groups, explicit and implicit; and the elements are partitioned into three groups, explicit, implicit, and interface, accordingly. In the E-I partitions, the explicit subdomain is integrated first and the results are subsequently used as boundary conditions for the integration of the implicit subdomain. In the E-E and I-I partitions, either the interpolation or the extrapolation must be performed, respectively.

Hughes and Liu [2,3] introduced a simplified method in which the mesh is grouped into explicit and implicit elements only. The notions of interface elements and the node categories are avoided. The improved implicit-explicit algorithms are claimed to be amenable to stability and accuracy analysis, and, at the same time, be simply and concisely implemented. The stability analyses are also carried out for the implicit, explicit, and implicit-explicit algorithms. In their formulation, the Newmark family of methods is used to define the implicit method. A predictor-corrector scheme, constructed from the Newmark family, is employed in defining the explicit method. The developments described in their papers are restricted to linear structural dynamics. In a later paper published by Hughes *et al.* [4], the implicit-explicit finite element concept is extended to nonlinear transient analysis. An effective static problem is formed in the iterative procedures in terms of the unknown displacement, which is in turn linearized. A predictor-multicorrector scheme is proposed to achieve second order accuracy.

In an effort contributed by Chang and Hamilton [5] [6], a method for simulating systems with two internally coupled motions, a slow motion and a fast motion, is presented. The concept of implicit-

explicit algorithm is applied to integrating the coupled system in a sequential fashion. The fast motion equations are integrated first by the implicit method in which an effective static problem is also formed in terms of displacement. By assuming the negligible changes of variables of slow motions for each time step, the time-varying coefficient matrices are replaced by the corresponding ones at the previous time step. The slow motion is updated by integrating the nonlinear equations explicitly, in which a predictor-corrector scheme is employed.

The current paper proposes an implicit-explicit sequential time integration method. This is designed to simulate systems with mutually coupled large overall nonlinear rigid body motion and small linear elastic motion arising in the dynamic modeling of flexible structural systems. The original differential equation system, which is capable of handling the forward and inverse dynamic analyses, is mapped into a subsystem by eliminating these specified rigid body degrees of freedom in a forward like dynamic analysis. The subsystem is then partitioned into two equation groups, suggested by the inherent characteristic of the flexible dynamic motion. One group is defined to describe the linear elastic motion and the other group is derived by including the nonlinear rigid body motion and the coupling terms. The Newmark implicit algorithm is applied to the first set of equations to integrate the elastic motion. Two distinct schemes, direct and iterative integrations, are introduced. The direct integration leads to a direct substitution of the displacement and velocity in the equations in terms of the acceleration, and the values of the coefficients at $(t - \Delta t)$ are replaced by the predicted values based on the current time. The iterative integration, on the other hand, leads to an effective linear problem in terms of the acceleration, which is in turn linearized. A predictor-multicorrector scheme is employed to enhance a second order accuracy without adverse effect on the stability condition. The explicit algorithm, incorporated with a single pass predictor-corrector scheme, is proposed to integrate the second set of nonlinear rigid body equations of motion. The elastic quantities involved in the coupling terms are back substituted by the values calculated from the first set of elastic equations of motion. The rigid body variables at the future time step are substituted by the predicted values accordingly and are corrected using the same Newmark algorithm. The method developed in this paper possesses improved implementation properties and is aimed to be applicable to any dynamic systems with the mixed rigid body and elastic degrees of freedom.

DYNAMIC EQUATIONS

A standard form of the structural dynamic equations can be written in the following matrix form, as

$$M(p)\ddot{p} - C(p, \dot{p})\dot{p} - K(p)p = F(p) \quad (1)$$

where the mass matrix M is usually a symmetric matrix and is a function of the generalized coordinates p which include the rigid body and elastic degrees of freedom. The damping matrix C , resulted from the Coriolis and centrifugal accelerations, is a nonsymmetric matrix and is a function of both the generalized coordinates and their time rates \dot{p} . The stiffness matrix K is a nonsymmetric matrix and is a function of the generalized coordinates only. The generalized force vector F is also a function of generalized coordinates in general and includes the external loadings which initiate the motion and drive the system. In an inverse dynamic analysis the driving forces are specified and the rigid body motion is to be determined. The above equations of motion need not to be modified because the force terms appear at the right hand side of the equations and the number of generalized coordinates is equal to the number of the equations. In a forward-like dynamic analysis, however, the rigid body degrees of freedom, are partially or totally specified

and the corresponding driving forces become unknown. The number of unknown generalized coordinates is less than the number of the equations though the total number of unknown variables still equals the number of the equations. The equation system can not be integrated directly and must be restructured to be suited for the direct integration.

System Mapping

Eq. 1 can be rewritten in the following sub-matrix form, as

$$\begin{bmatrix} M_{11} & M_{12} & M_{13} \\ M_{21} & M_{22} & M_{23} \\ M_{31} & M_{32} & M_{33} \end{bmatrix} \begin{Bmatrix} \ddot{p}_1 \\ \ddot{p}_2 \\ \ddot{p}_3 \end{Bmatrix} - \begin{bmatrix} C_{11} & C_{12} & C_{13} \\ C_{21} & C_{22} & C_{23} \\ C_{31} & C_{32} & C_{33} \end{bmatrix} \begin{Bmatrix} \dot{p}_1 \\ \dot{p}_2 \\ \dot{p}_3 \end{Bmatrix} - \begin{bmatrix} K_{11} & K_{12} & K_{13} \\ K_{21} & K_{22} & K_{23} \\ K_{31} & K_{32} & K_{33} \end{bmatrix} \begin{Bmatrix} p_1 \\ p_2 \\ p_3 \end{Bmatrix} = \begin{Bmatrix} F_1 \\ F_2 \\ F_3 \end{Bmatrix} \quad (2)$$

where the generalized sub-coordinates p_2 are supposed to be those specified degrees of freedom of the rigid body motion, and the unknown driving forces are involved in F_2 . It can be easily shown that Eq. 2 could be mapped to the following system which includes two sets of equations as

$$\begin{bmatrix} M_{11} & M_{13} \\ M_{31} & M_{33} \end{bmatrix} \begin{Bmatrix} \ddot{p}_1 \\ \ddot{p}_3 \end{Bmatrix} - \begin{bmatrix} C_{11} & C_{13} \\ C_{31} & C_{33} \end{bmatrix} \begin{Bmatrix} \dot{p}_1 \\ \dot{p}_3 \end{Bmatrix} - \begin{bmatrix} K_{11} & K_{13} \\ K_{31} & K_{33} \end{bmatrix} \begin{Bmatrix} p_1 \\ p_3 \end{Bmatrix} = \begin{Bmatrix} F_1 - M_{12}\ddot{p}_2 - C_{12}\dot{p}_2 - K_{12}p_2 \\ F_3 - M_{32}\ddot{p}_2 - C_{32}\dot{p}_2 - K_{32}p_2 \end{Bmatrix} \quad (3)$$

and

$$F_2 = \sum_{i=1}^3 (M_{2i}\ddot{p}_i - C_{2i}\dot{p}_i - K_{2i}p_i) \quad (4)$$

Eq. 3 can be solved first by the proposed integration algorithms in the following sections. The results are subsequently used for the vectors \ddot{p}_i , \dot{p}_i , and p_i ($i = 1, 2, 3$) in Eq. 4 to determine the unknown driving forces involved in the force vector F_2 .

Subsystem Partition

In Lagrange's approach, the formula of kinetic energy can be written in a standard matrix form as

$$KE = \frac{1}{2} \dot{p}^T M \dot{p} \quad (5)$$

where M is a symmetric mass matrix, \dot{p} is a vector resulted from the derivatives of the generalized coordinates with respect to time. The damping matrix can be derived and expressed as

$$C = \dot{M} - \tilde{M} \quad (6)$$

where \dot{M} are the time rates of the mass matrix M , and \tilde{M} is a nonsymmetric matrix which is defined as

$$\tilde{M} = -\frac{1}{2} \frac{\partial}{\partial \dot{p}^T} (M \dot{p}) \quad (7)$$

Therefore, the damping matrix C is a nonsymmetric matrix wherein \tilde{M} is a symmetric matrix. The viscous damping matrix can be added

to \dot{M} matrix. In analogy to Eq. 3, the system equations can be partitioned in the following form as

$$\begin{bmatrix} M_{rr} & M_{re} \\ M_{er} & M_{ee} \end{bmatrix} \begin{Bmatrix} \ddot{q}_r \\ \ddot{q}_e \end{Bmatrix} = \begin{bmatrix} \dot{M}_{rr} - \ddot{M}_{rr} & \dot{M}_{re} - \ddot{M}_{re} \\ \dot{M}_{er} - \ddot{M}_{er} & \dot{M}_{ee} - \ddot{M}_{ee} \end{bmatrix} \begin{Bmatrix} \dot{q}_r \\ \dot{q}_e \end{Bmatrix} - \begin{bmatrix} 0 & K_{re} \\ 0 & K_{ee} \end{bmatrix} \begin{Bmatrix} q_r \\ q_e \end{Bmatrix} = \begin{Bmatrix} Q_r \\ Q_e \end{Bmatrix} \quad (8)$$

where q_r are the rigid body generalized coordinates, q_e are the elastic generalized coordinates, and K_{ee} is a symmetric structural stiffness matrix. The sub-matrices associated with the rigid body generalized coordinates in the system stiffness matrix are null because there is no stiffness for the rigid body motion. The above equations can be separated into two sets of equations as shown below.

$$M_{rr}\ddot{q}_r - M_{re}\ddot{q}_e = f_r \quad (9)$$

$$M_{er}\ddot{q}_r - M_{ee}\ddot{q}_e - \dot{M}_{ee}\dot{q}_e - K_{ee}q_e = f_e \quad (10)$$

where

$$\begin{aligned} f_r &= Q_r - (\dot{M}_{rr} - \ddot{M}_{rr})\dot{q}_r \\ &\quad - (\dot{M}_{re} - \ddot{M}_{re})\dot{q}_e - K_{re}q_e \\ f_e &= Q_e - (\dot{M}_{er} - \ddot{M}_{er})\dot{q}_r - \dot{M}_{ee}\dot{q}_e \end{aligned} \quad (11)$$

Rewriting Eq. 9 in the following form as

$$\ddot{q}_r = M_{rr}^{-1}(f_r - M_{re}\ddot{q}_e) \quad (12)$$

and substituting the above result into Eq. 10 will yield

$$M_{es}\ddot{q}_e - \dot{M}_{ee}\dot{q}_e - K_{ee}q_e = f_{es} \quad (13)$$

where

$$M_{es} = M_{ee} - M_{er}M_{rr}^{-1}M_{re} \quad (14)$$

and

$$f_{es} = f_e - M_{er}M_{rr}^{-1}f_r \quad (15)$$

The modified system therefore takes the following form as:

$$M_{rr}\ddot{q}_r - M_{re}\ddot{q}_e = f_r \quad (16)$$

$$M_{es}\ddot{q}_e - \dot{M}_{ee}\dot{q}_e - K_{ee}q_e = f_{es} \quad (17)$$

In general, the mass submatrices M_{rr} , M_{re} , and M_{es} are nonlinear functions of q_r and q_e ; matrix \dot{M}_{ee} is a nonlinear function of \dot{q}_e and q_e ; the structural stiffness matrix K_{ee} is a constant matrix; the generalized force vectors f_r and f_{es} include not only the external loading but also the Coriolis and centrifugal forces and are nonlinear functions of q_r , q_e , \dot{q}_r , and \dot{q}_e . The above two sets of equations are coupled through the inertia matrix M_{es} and the force terms. Eq. 16, which governs the rigid body motion, is nonlinear with respect to q_r and q_e while Eq. 17, which governs the elastic motion, is linear with respect to q_e .

ALGORITHM DEVELOPMENT

In the following sections an implicit-explicit sequential time integration algorithm will be developed to solve the system with coupled nonlinear second order ordinary differential equations as expressed in Eqs. 16 and 17. Eq. 17 is numerically integrated first by an implicit method to find the kinematic values of the elastic motion. The results are subsequently used in integrating Eq. 16 to update the rigid body motion.

Implicit phase

Two implicit algorithms, direct and iterative, are demonstrated in the following two sections. In the direct method the values of the displacement and velocity at the future time step are replaced by the predicted values and Eq. 17 is integrated in terms of the acceleration. The displacement and velocity are in turn corrected by a Newmark algorithm, but the acceleration is not corrected. In the iterative method the values of the displacement and velocity are predicted first. Eq. 17 is then integrated by forming an effective linear problem in terms of the acceleration. All the variables are finally corrected by the Newmark algorithm also. Multiple iterations can be performed to increase the accuracy.

Direct method: The Newmark algorithms can be written in the following forms as

$$d_{t+\Delta t} = \ddot{d}_{t+\Delta t} - \Delta t^2 3\ddot{d}_{t+\Delta t} \quad (18)$$

$$\dot{d}_{t+\Delta t} = \dot{\ddot{d}}_{t+\Delta t} - \Delta t 7\ddot{d}_{t+\Delta t} \quad (19)$$

and

$$\ddot{d}_{t+\Delta t} = \ddot{d}_t - \Delta t \ddot{d}_t - \frac{1}{2} \Delta t^2 (1 - 2\beta) \ddot{d}_t \quad (20)$$

$$\dot{\ddot{d}}_{t+\Delta t} = \dot{\ddot{d}}_t + \Delta t (1 - \gamma) \ddot{d}_t \quad (21)$$

where Δt is the size of time step, the subscripts t and $t + \Delta t$ denote the current and future time, β and γ are two Newmark parameters, d , \dot{d} , and \ddot{d} are the displacement, velocity, and acceleration vectors, respectively, and \ddot{d} and $\dot{\ddot{d}}$ are the predicted displacement and velocity vectors. The values of the matrices M_{es} and \dot{M}_{ee} and the vector f_{es} in Eq. 17 at the future time $t + \Delta t$ can be evaluated by the substitutions of the predicted values as shown in Eqs. 20 and 21. Substituting Eqs. 18 and 19 into Eq. 17 results in the following equation as

$$M_{es,t+\Delta t} \ddot{q}_{e,t+\Delta t} = f_{es,t+\Delta t} \quad (22)$$

where M_{es} and f_{es} are the effective inertia matrix and the effective force vector, respectively, and they are defined as

$$M_{es,t+\Delta t} = \ddot{M}_{es,t+\Delta t} - \Delta t \gamma \dot{\ddot{M}}_{es,t+\Delta t} - \Delta t^2 3\ddot{K}_{ee,t+\Delta t} \quad (23)$$

$$f_{es,t+\Delta t} = \ddot{f}_{es,t+\Delta t} - \dot{\ddot{M}}_{ee,t+\Delta t} \dot{\ddot{q}}_{e,t+\Delta t} - \ddot{K}_{ee,t+\Delta t} \ddot{q}_{e,t+\Delta t} \quad (24)$$

Once the acceleration vector is solved from Eq. 22, the displacement and velocity vectors can be corrected from Eqs. 18 and 19. This leads to updating the rigid body motion by explicitly integrating Eq. 16 and to advance to the next time step.

Iterative method: The accuracy can be improved by using the iterative method with the trade off of performing iterations. The superscript notation (i) is used in the following quantities to denote the iteration. The same Newmark algorithms are employed in the development of a predictor-multicorrector scheme.

Before iteration $(i = 0)$, the predicted values of the displacement and velocity are assigned as the initial values for the future time while the corresponding initial acceleration can be obtained by integrating Eq. 17, i.e.

$$i = 0 \quad (25)$$

$$q_{e,t+\Delta t}^{(i)} = \ddot{q}_{e,t+\Delta t} \quad (26)$$

$$\dot{q}_{e,t+\Delta t}^{(i)} = \dot{\ddot{q}}_{e,t+\Delta t} \quad (27)$$

$$\ddot{q}_{e,t+\Delta t}^{(i)} = \ddot{M}_{es,t+\Delta t}^{-1} (\ddot{f}_{es,t+\Delta t} - \dot{\ddot{M}}_{ee,t+\Delta t} \dot{\ddot{q}}_{e,t+\Delta t} - \ddot{K}_{ee,t+\Delta t} \ddot{q}_{e,t+\Delta t}) \quad (28)$$

Substituting Eqs. 13 and 19 into Eq. 17 yields

$$M^* \ddot{q}_{e,i+\Delta t}^{(i)} = f_{es,i+\Delta t}^{(i)} - \dot{M}_{ee,i+\Delta t}^{(i)} \dot{q}_{e,i+\Delta t}^{(i)} - K_{ee,i+\Delta t}^{(i)} \dot{q}_{e,i+\Delta t}^{(i)} \quad (29)$$

where M^* is an effective inertia matrix which can be expressed as

$$M^* = M_{es,i+\Delta t}^{(i)} + \Delta t \gamma \dot{M}_{ee,i+\Delta t}^{(i)} + \Delta t^2 \beta K_{ee,i+\Delta t}^{(i)} \quad (30)$$

Let $\Delta \ddot{q}_e$ be an acceleration increment during each iteration, i.e.

$$\Delta \ddot{q}_e = \ddot{q}_{e,i+\Delta t}^{(i)} - \ddot{q}_{e,i+\Delta t}^{(i-1)} \quad (31)$$

and Δf be an effective force increment during the same interval of iteration, i.e.

$$\Delta f = f_{es,i+\Delta t}^{(i)} - M_{es,i+\Delta t}^{(i)} \ddot{q}_{e,i+\Delta t}^{(i-1)} - \dot{M}_{ee,i+\Delta t}^{(i)} \dot{q}_{e,i+\Delta t}^{(i-1)} - K_{ee,i+\Delta t}^{(i)} \dot{q}_{e,i+\Delta t}^{(i-1)} \quad (32)$$

Eq. 29 can then be rewritten as

$$M^* \Delta \ddot{q}_e = \Delta f \quad (33)$$

Solving Eq. 33 gives the values of the acceleration increment $\Delta \ddot{q}_e$. The results are then subsequently used to find the corrected values of the displacement, velocity, and acceleration, i.e.

$$\ddot{q}_{e,i+\Delta t}^{(i-1)} = \ddot{q}_{e,i+\Delta t}^{(i)} - \Delta \ddot{q}_e \quad (34)$$

$$\dot{q}_{e,i+\Delta t}^{(i-1)} = \dot{q}_{e,i+\Delta t}^{(i)} - \Delta t \gamma \ddot{q}_{e,i+\Delta t}^{(i-1)} \quad (35)$$

$$q_{e,i+\Delta t}^{(i-1)} = q_{e,i+\Delta t}^{(i)} - \Delta t^2 \beta \ddot{q}_{e,i+\Delta t}^{(i-1)} \quad (36)$$

In summary, Eqs. 25-28 construct a predictor phase, Eqs. 30, 32, and 33 form an effective linear problem, and Eqs. 34-36 construct a corrector phase. If additional iterations are to be performed, i is replaced by $i-1$, and calculations resume with Eq. 30. Either a fixed number of iterations may be performed, or iterating may be terminated when $\Delta \ddot{q}_e$ or Δf satisfy presigned convergence conditions. When the iterative phase is completed, the solution at the future time $t + \Delta t$ is defined by the last iterated values. At this point, the current time t is replaced by the future time $t + \Delta t$, and calculations for the next time step may begin.

Explicit Phase

After performing the implicit integration for Eq. 17, the kinematic values of the elastic displacement, velocity, and acceleration at the future time are obtained, and the results can be substituted into Eq. 16. The rigid body displacement and velocity vectors at the future time can be predicted using the following formulas as:

$$\ddot{q}_{r,i+\Delta t} = \ddot{q}_{r,i} - \Delta t \ddot{q}_{r,i} - \frac{1}{2} \Delta t^2 (1 - 2\beta) \ddot{q}_{r,i} \quad (37)$$

$$\dot{q}_{r,i+\Delta t} = \dot{q}_{r,i} + \Delta t (1 - \gamma) \ddot{q}_{r,i} \quad (38)$$

It is noticed that Eqs. 37 and 38 are analogous to Eqs. 20 and 21. By substituting the above predictor vectors along with the results from solving Eq. 17, the acceleration vector of the rigid body motion in Eq. 16 can be solved through the following equations, as

$$M_{rr,i+\Delta t} \ddot{q}_{r,i+\Delta t} = f_{re,i+\Delta t} \quad (39)$$

where

$$f_{re,i+\Delta t} = f_{r,i+\Delta t} - M_{re,i+\Delta t} \ddot{q}_{e,i+\Delta t} \quad (40)$$

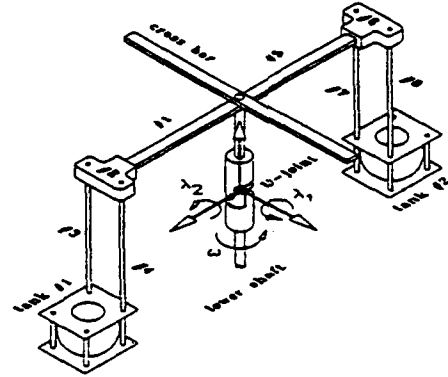


Figure 1: Schematic of A Rotating System

Once again, the rigid body displacement and velocity vectors are ready to be corrected as follows:

$$q_{r,i+\Delta t} = q_{r,i+\Delta t} - \Delta t^2 \beta \ddot{q}_{r,i+\Delta t} \quad (41)$$

$$\dot{q}_{r,i+\Delta t} = \dot{q}_{r,i+\Delta t} - \Delta t \gamma \ddot{q}_{r,i+\Delta t} \quad (42)$$

where the acceleration vector $\ddot{q}_{r,i+\Delta t}$ is solved in Eq. 39. The procedures in the explicit phase are summarized as predicting the values through Eqs. 37 and 38, solving Eq. 39 for the acceleration vector, and correcting the values through Eqs. 41 and 42.

At this point, the implicit-explicit sequential time integration algorithms introduced to solve the equation system, Eqs. 16 and 17, are derived completely. The solutions of the original dynamic equations, Eq. 1, are hence obtained.

NUMERICAL RESULTS

A Fortran computer code has been written to simulate the dynamic response of a spatial structure system with the implementation of the numerical algorithms developed in this work. In the analyses to follow, the direct method, rather than the more accurate iterative method, is employed in the implicit phase because of the limitations in computing storage and time. Illustrated in Fig. 1, the dynamic part of the structure under consideration in the model is supported by a Hooke's type universal joint at point O . The lower shaft connected to the joint, driven by a D.C. motor, spins vertically about its own central axis. The structure rotates about the joint with two unknown rigid body rotating angles λ_1 and λ_2 . Tanks 1 and 2 are two rigid body assemblies which contain the sloshing liquid. Beams 1, 3, 4, 5, 7, and 8 are modeled as elastic bodies while beams 2 and 6 and the cross bar are treated as rigid bodies. More detailed modeling and application are referred to Xu and Baumgarten [7][8][9].

A modal analysis for the structure model has been accomplished using the MSC/NASTRAN finite element package. The natural frequencies range from 23 Hz to over 1000 Hz. The critical size of the time step with γ being equal to 0.5 is about 0.0002 seconds, if using the explicit integration method only (see Hughes and Liu [2]). By considering the accuracy in showing the effect of the highest natural frequency, the time step size could be as small as 0.0001 seconds. Based on the sequential implicit-explicit time integration method, a time interval of 0.005 seconds is chosen for integration. The simulations are performed on a networked DECstation 3100 workstation using the MIPS Fortran 77 compiler running under RISC-based ULTRIX 4.1. It takes about 5.21 seconds of CPU time for one real-

time step. The total number of the degrees of freedom of the model is equal to nineteen, in which each elastic beam is modeled by one beam element with a third order polynomial shape function.

A sinusoidal function is used as a spin profile of the lower shaft in the simulation. Starting from zero, the angular velocity increases gradually and reaches 60 RPM over the time base t_p . In Case #1, an initial tilt of $\lambda_1 = 1$ degree is set to induce off balanced rotation, and t_p is set to 3 seconds in the spin profile. The numerical results of two rigid body rotating angles and velocities are compared with for the rigid and flexible models. As shown in Fig. 2, the values of the flexible model (dashed line) deviate significantly from the corresponding values of the rigid body model (solid line) after a few seconds. Another run with an impulse acting on one of the tanks but with no initial tilt is performed; here $t_p = 1$ second is used in the spin profile. The impulse is applied vertically after 1.5 seconds with the magnitude of 1 N. This run lasts for 10 seconds in order that the peak value of off balanced motion is developed thoroughly. The solid lines represent the results with Newmark parameters of $\gamma = 0.6$ and $\beta = 0.303$ while the dashed lines are for $\gamma = 0.5$ and $\beta = 0.25$. A phenomenon of "numerical damping" is reconfirmed in the plots in Fig. 3. By increasing γ to 0.6, the high frequencies engendered by the stiff components are damped out. $D1Y$ and $D3Y$ are the circumferential deflections of beam 1 and beam 3 at the distal ends, respectively (note the different scales in the figures). $D1Z$ is the vertical deflection of beam 1 while $D3Z$ is the radial deflection of beam 3. The initial elastic deformations for each flexible beam are set to zero to avoid over estimation in the simulation.

CONCLUSION

An implicit-explicit sequential time integration algorithm has been developed in the present paper. The method is intended to solve second order nonlinear ordinary differential equations derived from the modeling of flexible structural systems with mutually dependent rigid body and elastic motions. The original dynamic equations are transferred to a subsystem which is composed of two coupled sets of motion equations. One set of equations governs the nonlinear rigid body motion while another set of equations is defined to describe the linear elastic vibration. Two algorithms, implicit and explicit, are proposed to integrate the subsystem, in which the elastic vibration is solved first during the implicit phase, and the rigid body motion is then updated subsequently during the explicit phase. The Newmark algorithm family is employed in both the implicit and explicit integrations in which a multiple pass predictor-corrector scheme is used in the implicit method while a single pass predictor-corrector scheme is used in the explicit method. An example is presented in simulating dynamic response of a spatial system with unknown rigid body motion. The numerical integrations are carried out, and the results are compared with for a rigid body model and a flexible model. In the second run case an impulse is applied on the structure to excite the elastic beam oscillations in which the higher frequencies can be damped out by increasing the value of γ Newmark parameter. The computation efficiency is demonstrated using the current method. The accuracy (which is at most the second order herein) can be further improved by introducing higher order predictor-corrector schemes.

ACKNOWLEDGMENT

The authors would like to acknowledge the financial support of the Air Force Office of Scientific Research under Grant No. AFOSR-89-0403.

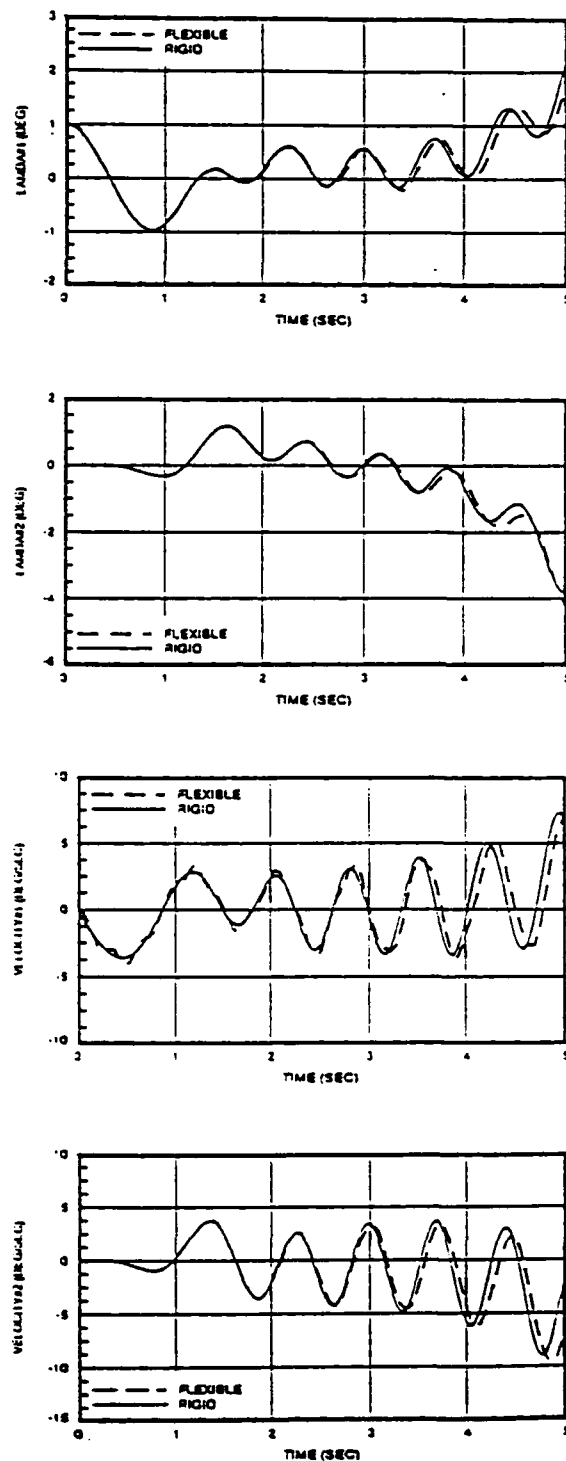


Figure 2: Case #1

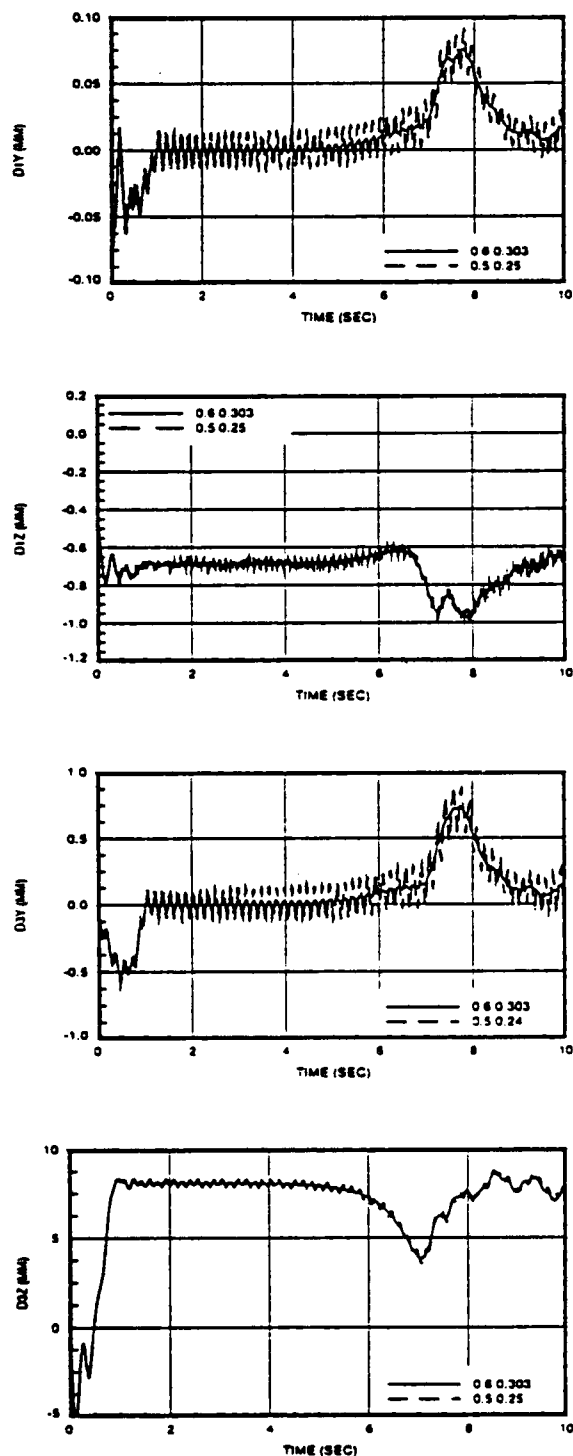


Figure 3: Case#2

References

- [1] Belytschko, T., Yen, H.J., and Mullen, R. 1979, "Mixed Method for Time Integration," *Computer Method in Applied Mechanics and Engineering*, Vol. 17/18, pp. 259-275.
- [2] Hughes, T.J.R. and Liu, W.K., 1978, "Implicit-Explicit Finite Elements in Transient Analysis: Stability Theory," *ASME Journal of Applied Mechanics*, Vol. 45, pp. 371-374.
- [3] Hughes, T.J.R. and Liu, W.K., 1978, "Implicit-Explicit Finite Elements in Transient Analysis: Implementation and Numerical Examples," *ASME Journal of Applied Mechanics*, Vol. 45, pp. 375-378.
- [4] Hughes, T.J.R., Pister, K.S., and Taylor, R.L., 1979, "Implicit-Explicit Finite Elements in Nonlinear Transient Analysis," *Computer Method in Applied Mechanics and Engineering*, Vol. 17/18, pp. 159-182.
- [5] Chang, L.-W. and Hamilton, J.F., 1988, "A Sequential Integration Method," *ASME Journal of Dynamic Systems, Measurement, and Control*, Vol. 110, pp. 382-388.
- [6] Chang, L.-W. and Hamilton, J.F., 1991, "Simulation of Flexible-Link Manipulators Applying Sequential Integration Method," *ASME Journal of Dynamic Systems, Measurement, and Control*, Vol. 113, pp. 175-178.
- [7] Xu, J. and Baumgarten, J. R., 1991, "A Finite Element/Lagrangian Formulation of Dynamic Motion Prediction for A Flexible Satellite Simulator with Both Rigid and Elastic Bodies," *Proceedings of the 2nd National Applied Mechanisms and Robotics Conference*, Cincinnati, Ohio, November 3-6, 91AMR-VIIB-5, pp. 1-8.
- [8] Xu, J. and Baumgarten, J. R., 1992, "Modeling of Multibody Flexible Articulated Structures with Mutually Coupled Motions. Part I: General Theory," *Proceedings of the 22nd ASME Mechanisms Conference*, Scottsdale, AZ, September 13-16.
- [9] Xu, J. and Baumgarten, J. R., 1992, "Modeling of Multibody Flexible Articulated Structures with Mutually Coupled Motions. Part II: Application and Results," *Proceedings of the 22nd ASME Mechanisms Conference*, Scottsdale, AZ, September 13-16.

**APPENDIX G. A Primitive Variable, Strongly Implicit Calculation
Procedure for Viscous Flows at All Speeds.**

Primitive Variable, Strongly Implicit Calculation Procedure for Viscous Flows at All Speeds

K.-H. Chen* and R. H. Pletcher†

Iowa State University, Ames, Iowa 50011

A coupled solution procedure is described for solving the compressible form of the time-dependent, two-dimensional Navier-Stokes equations in body-fitted curvilinear coordinates. This approach employs the strong conservation form of the governing equations but uses primitive variables (u, v, p, T) rather than the more traditional conservative variables ($p, \rho u, \rho v, e$) as unknowns. A coupled modified strongly implicit procedure (CMSIP) is used to efficiently solve the Newton-linearized algebraic equations. It appears that this procedure is effective for Mach numbers ranging from the incompressible limit ($M_\infty \rightarrow 0.01$) to supersonic. Generally, smoothing was not needed to control spatial oscillations in pressure for subsonic flows despite the use of central differences. Dual-time stepping was found to further accelerate convergence for steady flows. Sample calculations, including steady and unsteady low-Mach-number internal and external flows and a steady shock-boundary-layer interaction flow, illustrate the capability of the present solution algorithm.

Introduction

OVER the past two decades, a number of different finite-difference schemes have been proposed to solve the Navier-Stokes equations.¹ Traditionally, they have been classified as methods for either compressible or incompressible flows. Most of the formulations for compressible flows have utilized conservative variables,^{2,3} which include density, instead of pressure, as a primary variable, and the equations have generally been solved in a coupled (simultaneous) manner. An exception to this is the recent work of Karki and Patankar⁴ and Van Doormaal et al.⁵

Methods for incompressible flows, on the other hand, have employed a wider range of dependent variables, including derived as well as primitive, and the equations have generally been solved in a segregated (one variable at a time) manner. The derived variable approaches usually either involve more unknowns than contained in the original Navier-Stokes equations or become too complicated to easily extend to three-dimensional flow calculations.

Numerical methods developed for compressible flows are not, in general, suitable for efficiently solving low-Mach-number or incompressible flows. The reasons usually offered for this are 1) roundoff error due to using density as a primary variable,⁶ 2) truncation errors due to applying approximate factorization in multiple dimensional problems,⁷ and 3) a time step (or CFL number) constraint due to near infinite acoustic speed.¹

To circumvent some of the above problems, pressure can be chosen as a primary variable instead of density because the variation of pressure is generally significant for all flow regimes. This idea has been used⁸ in solving low-Mach-number steady flows by a coupled space marching procedure that involves using multiple sweeps to account for the upstream

propagation of pressure signals. But this space marching procedure is only effective for flows within a dominant flow direction. Recently, a similar idea, although different in detail, was proposed to alleviate the above problems using a segregated algorithm.⁹ Feng and Merkle⁹ also employed pressure as a primary variable in a scheme that utilized a preconditioning technique to scale all eigenvalues of the coupled system of equations to the same order of magnitude in order to accelerate convergence for low-Mach-number steady flows.

The approximate factorization procedure was avoided in the present work by using a modified form of Stone's strongly implicit procedure (SIP)¹⁰ to solve the algebraic equations in the plane. The modified form of the SIP algorithm (MSIP) proposed by Schneider and Zedan¹¹ exhibits faster convergence and less sensitivity to the relaxation-type parameter of the method than the original SIP algorithm. The MSIP algorithm was extended to handle a coupled 4×4 block system in the present work.

There are many applications in which it would be convenient to use the same algorithm for Mach numbers ranging from incompressible to transonic. The search for an algorithm suitable for all speeds goes back at least to the work of Harlow and Amsden.¹² More recent work on the subject includes contributions from Karki and Patankar⁴ and Van Doormaal et al.⁵ The main contribution of the present work is to point out a solution strategy that could be applied to a number of difference formulations to permit efficient computation over a wider range of Mach numbers. The specific difference stencil used in the present work may not be optimum for all cases (particularly at very high Reynolds number), and can clearly be improved. The form used, however, does serve to illustrate the advantages of the overall approach.

In the present paper, a coupled strongly implicit procedure for solving the two-dimensional unsteady compressible conservation-law form of the Navier-Stokes equations with primitive variables, i.e., u and v velocity components, pressure, and temperature, is described. Incompressible test cases are computed from this formulation simply by setting the Mach number to a very low value. Since all variables, including pressure, are computed simultaneously in the algorithm, there is no need to use a separate pressure Poisson equation, and the continuity equation is automatically satisfied. Some convergence enhancement techniques for steady-state solutions will also be described. Several steady-state results including two low-Mach-number incompressible flows and one supersonic flow will be given. One unsteady subsonic flow is also discussed.

Presented as Paper 90-1521 at the AIAA 21st Fluid Dynamics, Plasma Dynamics, and Lasers Conference, Seattle, WA, June 18-20, 1990; received June 25, 1990; revision received Dec. 18, 1990; accepted for publication Dec. 27, 1990. Copyright © 1990 by the authors. Published by the American Institute of Aeronautics and Astronautics, Inc., with permission.

*Research Assistant, Department of Mechanical Engineering and Computational Fluid Dynamics Center, 2025 H. M. Black Engineering Building; currently at the University of Toledo/NASA Lewis Research Center, Cleveland, OH. Member AIAA.

†Professor, Department of Mechanical Engineering and Computational Fluid Dynamics Center, 2025 H. M. Black Engineering Building. Member AIAA.

Numerical Approach

Governing Equations

After replacing the density by pressure and temperature using the equation of state ($\rho = p/RT$), the nondimensional form of the unsteady, two-dimensional compressible Navier-Stokes equations can be written in generalized nonorthogonal coordinates¹ as

$$\frac{\partial Q(q)}{\partial \tau} + \frac{\partial E(q)}{\partial \xi} + \frac{\partial F(q)}{\partial \eta} = 0 \quad (1)$$

where

$$q = \begin{pmatrix} u \\ v \\ p \\ T \end{pmatrix}$$

$$Q = \frac{1}{J} \begin{pmatrix} \frac{\rho u}{T} \\ \frac{\rho v}{T} \\ \frac{p}{T} \\ (C_p - R)p - \frac{1}{2} \frac{\rho u^2}{T} - \frac{1}{2} \frac{\rho v^2}{T} \end{pmatrix}$$

$$E = \frac{1}{J} \begin{pmatrix} \frac{\rho}{T} u U + R p \xi_x - (\xi_x \tau_{xx} + \xi_v \tau_{xv}) \\ \frac{\rho}{T} v U + R p \xi_v - (\xi_x \tau_{xv} + \xi_v \tau_{vv}) \\ \frac{\rho}{T} U \left(C_p p - \frac{\rho}{T} \frac{u^2}{2} - \frac{\rho}{T} \frac{v^2}{2} \right) U \\ - \xi_x u \tau_{xx} - (\xi_x v + \xi_v u) \tau_{xv} - \xi_v v \tau_{vv} \\ - \frac{R C_p \mu}{Pr Re} [(\xi_x^2 - \xi_v^2) T_t + (\xi_x \eta_x - \xi_v \eta_v) T_n] \end{pmatrix}$$

$$F = \frac{1}{J} \begin{pmatrix} \frac{\rho}{T} u V - R p \eta_x - (\eta_x \tau_{xx} + \eta_v \tau_{xv}) \\ \frac{\rho}{T} u V - R p \eta_v - (\eta_x \tau_{xv} + \eta_v \tau_{vv}) \\ \frac{\rho}{T} V \left(C_p p - \frac{\rho}{T} \frac{u^2}{2} - \frac{\rho}{T} \frac{v^2}{2} \right) V \\ - \eta_u u \tau_{xx} - (\eta_x v + \eta_v u) \tau_{xv} - \eta_v v \tau_{vv} \\ - \frac{R C_p \mu}{Pr Re} [(\xi_x \eta_x + \xi_v \eta_v) T_t + (\eta_x^2 + \eta_v^2) T_n] \end{pmatrix}$$

$$\tau_{xx} = \frac{2 R \mu}{3 Re} [2(\xi_x \mu_t + \eta_v \mu_n) - (\xi_v \nu_t + \eta_v \nu_n)]$$

$$\tau_{xv} = \frac{2 R \mu}{3 Re} [2(\xi_x \nu_t + \eta_v \nu_n) - (\xi_v \mu_t + \eta_v \mu_n)]$$

$$\tau_{vv} = \frac{R \mu}{Re} [(\xi_x \mu_t + \eta_v \mu_n) - (\xi_v \nu_t + \eta_v \nu_n)]$$

$$U = \xi_x u + \xi_v v \quad V = \eta_x u + \eta_v v$$

Laminar flow was assumed and the viscosity for air was determined by the Sutherland formula¹ as follows:

$$\mu = \frac{C_1 T^{3/2}}{(T + C_2)} \quad (2)$$

The above nondimensional variables were defined in the following manner (dimensional quantities are indicated by a tilde):

$$t = \frac{\tilde{t}}{L_{ref} \tilde{u}_{ref}}, \quad x = \frac{\tilde{x}}{L_{ref}}, \quad y = \frac{\tilde{y}}{L_{ref}}, \quad u = \frac{\tilde{u}}{\tilde{u}_{ref}}$$

$$v = \frac{\tilde{v}}{\tilde{u}_{ref}}, \quad \rho = \frac{\tilde{\rho}}{\rho_{ref}}, \quad p = \frac{\tilde{p}}{(\rho_{ref} \tilde{u}_{ref}^2)}, \quad T = \frac{\tilde{T}}{T_{ref}}$$

$$\mu = \frac{\tilde{\mu}}{\mu_{ref}}, \quad C_1 = \tilde{C}_1 \frac{T_{ref}^2}{\mu_{ref}}, \quad C_2 = \frac{\tilde{C}_2}{T_{ref}}$$

$$R = \frac{\tilde{R}}{(\tilde{u}_{ref}^2 / T_{ref})} = \frac{1}{\gamma M_\infty^2}$$

$$C_p = \frac{\tilde{C}_p}{(\tilde{u}_{ref}^2 / T_{ref})} = \frac{1}{(\gamma - 1) M_\infty^2}$$

The Reynolds number, Mach number, and Prandtl number were defined as

$$Re = \frac{\rho_{ref} \tilde{u}_{ref} L_{ref}}{\mu_{ref}}, \quad M_\infty = \frac{\tilde{u}_{ref}}{\sqrt{\gamma R T_{ref}}}, \quad Pr = \frac{\tilde{C}_p \tilde{\mu}}{k}$$

Here, L_{ref} is a flowfield characteristic length; x and y are the Cartesian coordinates; u and v are the respective Cartesian velocity components; ρ is the density; p is the static pressure; μ is the dynamic viscosity; T is the static temperature; R is the gas constant; C_p is the constant pressure specific heat; k is the thermal conductivity; γ is the specific heat ratio; and C_1 and C_2 are the Sutherland constants. The subscript "ref" denotes the reference quantities that are the upstream bulk properties for internal flow cases, or the freestream properties for external flow cases.

All sample calculations were performed for dry air at ambient temperature and pressure using the following fluid property constants.

$$\tilde{R} = 287 \text{ m}^2/(\text{s}^2 \text{ K}), \quad \gamma = 1.4$$

$$\tilde{C}_1 = 1.458 \times 10^{-6} \text{ kg}/(\text{m s} \sqrt{\text{K}}), \quad \tilde{C}_2 = 110.4 \text{ K}$$

Discretization of the Equations

The discretization will be described for the form of the equations given by Eq. (1). A first-order forward difference was used for the time terms. Central differences, in general, were used for the spatial derivative terms in the equations. For example, the first-order spatial derivative term of the continuity equation in the ξ direction was differenced by

$$\frac{\partial}{\partial \xi} \left(\frac{\rho U}{JT} \right)_{i,j}^{n+1} = \frac{1}{2} \left[\left(\frac{\rho U}{JT} \right)_{i+1,j}^{n+1} - \left(\frac{\rho U}{JT} \right)_{i-1,j}^{n+1} \right]$$

where, $\Delta \xi = 1$ was assumed. However, the deferred correction formula proposed by Khosla and Rubin¹³ was also used for the convective terms in the momentum and energy equations for one of the cases presented in this paper (driven cavity flow). For example,

$$\frac{\partial}{\partial \xi} \left(\frac{\rho u U}{JT} \right)_{i,j}^{n+1,k+1} = \left[\left(\frac{\rho u U}{JT} \right)_{i,j}^{n+1,k+1} - \left(\frac{\rho u U}{JT} \right)_{i-1,j}^{n+1,k+1} \right] - \frac{1}{2} \left[\left(\frac{\rho u U}{JT} \right)_{i+1,j}^{n+1,k} - 2 \left(\frac{\rho u U}{JT} \right)_{i,j}^{n+1,k} + \left(\frac{\rho u U}{JT} \right)_{i-1,j}^{n+1,k} \right]$$

for $U > 0$ (3)

$$\begin{aligned} \frac{\partial}{\partial \xi} \left(\frac{\rho u U}{JT} \right)_{i,j}^{n+1,k+1} &= \left[\left(\frac{\rho u U}{JT} \right)_{i+1,j}^{n+1,k+1} \right. \\ &\quad - \left. \left(\frac{\rho u U}{JT} \right)_{i,j}^{n+1,k+1} \right] - \frac{1}{2} \left[\left(\frac{\rho u U}{JT} \right)_{i+1,j}^{n+1,k} - 2 \left(\frac{\rho u U}{JT} \right)_{i,j}^{n+1,k} \right. \\ &\quad \left. + \left(\frac{\rho u U}{JT} \right)_{i-1,j}^{n+1,k} \right] \quad \text{for } U < 0 \quad (4) \end{aligned}$$

The upwind-differencing part of the above expression was evaluated implicitly on the left-hand side of the equations and the central-differencing part was evaluated explicitly on the right-hand side of the equations. When the solution converges, the second-order central difference is recovered.

The second-order spatial derivative terms in the ξ direction were differenced as

$$\frac{\partial}{\partial \xi} \left(a \frac{\partial \phi}{\partial \xi} \right)_{i,j}^{n+1} = \left(a \frac{\partial \phi}{\partial \xi} \right)_{i+1/2,j}^{n+1} - \left(a \frac{\partial \phi}{\partial \xi} \right)_{i-1/2,j}^{n+1}$$

where ϕ is the dependent variable, a represents a combination of metric terms and viscosity in the viscous terms in the momentum equations and the coefficient to the conduction terms in the energy equation. $(i - 1/2)$ indicates a location halfway between i and $(i - 1)$, and $(i + 1/2)$ denotes a location halfway between $(i + 1)$ and i . The values of $a_{i-1/2,j}$ and $a_{i+1/2,j}$ were determined as

$$a_{i-1/2,j} = \frac{1}{2}(a_{i,j} + a_{i-1,j}), \quad a_{i+1/2,j} = \frac{1}{2}(a_{i,j} + a_{i+1,j})$$

and the first-order derivative terms at the half-nodal point were evaluated as

$$\begin{aligned} \left(\frac{\partial \phi}{\partial \xi} \right)_{i+1/2,j}^{n+1} &= \phi_{i+1,j}^{n+1} - \phi_{i,j}^{n+1} \\ \left(\frac{\partial \phi}{\partial \xi} \right)_{i-1/2,j}^{n+1} &= \phi_{i,j}^{n+1} - \phi_{i-1,j}^{n+1} \end{aligned}$$

Similar expressions for the terms in the η direction are evaluated in the same way. The second-order spatial cross derivative terms are expressed as

$$\frac{\partial \phi}{\partial \xi} \left(\frac{\partial \phi}{\partial \eta} \right)_{i,j}^{n+1} = \frac{1}{2} (\phi_{i+1,j+1}^{n+1} - \phi_{i+1,j-1}^{n+1} - \phi_{i-1,j+1}^{n+1} + \phi_{i-1,j-1}^{n+1})$$

The above central-difference representations for the spatial derivative terms can also be interpreted as evaluating the flux quantities $[E$ and F in the Eq. (1)] at the face of control volume by simply averaging the flux quantities at two nodal points, e.g., $E_{i+1/2,j} = \frac{1}{2}(E_{i+1,j} + E_{i,j})$. All metric terms of the transformation at the interior points were evaluated by second-order central differences satisfying the geometric conservation law.¹⁴

After differencing, all nonlinear terms were linearized by a Newton method.¹ However, it should be noted that an equivalent formulation can be developed using conventional Jacobian matrices.¹⁵ The representations for two typical nonlinear terms, such as the time term in the continuity equation and one of the convective terms in the momentum equations, are illustrated as

$$\begin{aligned} \left(\frac{\rho}{T} \right)_{i,j}^{n+1,k+1} &= \left(\frac{\rho}{T} \right)_{i,j}^{n+1,k} \rho^{n+1,k+1} \\ &\quad - \left(\frac{\rho}{T} \right)_{i,j}^{n+1,k} T^{n+1,k+1} - \left(\frac{\rho}{T} \right)_{i,j}^{n+1,k} \end{aligned} \quad (5)$$

$$\begin{aligned} \left(\frac{\rho u U}{JT} \right)_{i,j}^{n+1,k+1} &= \left(\frac{\rho U}{JT} + \frac{\rho u}{T} y_\eta \right)_{i,j}^{n+1,k} u^{n+1,k+1} \\ &\quad - \left(\frac{\rho u}{T} x_\eta \right)_{i,j}^{n+1,k} v^{n+1,k+1} - \left(\frac{u U}{JT} \right)_{i,j}^{n+1,k} \rho^{n+1,k+1} \\ &\quad - \left(\frac{\rho u U}{JT^2} \right)_{i,j}^{n+1,k} T^{n+1,k+1} - \left(\frac{\rho u U}{JT} \right)_{i,j}^{n+1,k} \end{aligned} \quad (6)$$

where k is the iteration index and n indicates the time level.

For time-accurate calculations, the linearization error can be effectively removed by iterating at each time level. For steady-state calculations, iterations were not required at each time step since the time marching scheme is itself a relaxation procedure. All terms were treated in an implicit way (at level $n + 1, k + 1$) except the viscous dissipation terms (in the energy equation) that were evaluated at the level $(n + 1, k)$. After linearization, the four variables, u, v, ρ , and T , appear in all of the equations and the resulting equations takes the following form:

$$\begin{aligned} A_{i,j}^6 q_{i-1,j-1} + A_{i,j}^5 q_{i+1,j-1} + A_{i,j}^4 q_{i-1,j+1} + A_{i,j}^3 q_{i+1,j+1} \\ + A_{i,j}^2 q_{i,j} + A_{i,j}^1 q_{i,j} - A_{i,j}^0 q_{i-1,j-1} \\ - A_{i,j}^1 q_{i,j-1} + A_{i,j}^2 q_{i-1,j+1} = b_{i,j} \end{aligned} \quad (7)$$

and can be expressed in a matrix form as

$$[A]q = b \quad (8)$$

where

$$[A] = \begin{bmatrix} A_{i,j}^6 & A_{i,j}^5 & A_{i,j}^4 & A_{i,j}^3 & A_{i,j}^2 & A_{i,j}^1 & A_{i,j}^0 \\ A_{i,j}^0 & A_{i,j}^1 & A_{i,j}^2 & A_{i,j}^3 & A_{i,j}^4 & A_{i,j}^5 & A_{i,j}^6 \\ A_{i,j}^6 & A_{i,j}^5 & A_{i,j}^4 & A_{i,j}^3 & A_{i,j}^2 & A_{i,j}^1 & A_{i,j}^0 \end{bmatrix}$$

is the coefficient matrix with a 4×4 block in each element and

$$\begin{aligned} q &= [(u, v, \rho, T)_{i,j}^T, \dots, (u, v, \rho, T)_{i,j}^T, \dots, (u, v, \rho, T)_{i,j}^T]^T \\ b &= [(b_u, b_v, b_\rho, b_T)_{i,j}^T, \dots, (b_u, b_v, b_\rho, b_T)_{i,j}^T, \dots, \\ &\quad (b_u, b_v, b_\rho, b_T)_{i,j}^T]^T \end{aligned}$$

are the unknown vector and the right-hand side vector, respectively. Figure 1 shows the computational molecule for A^1, A^2, A^3, \dots and A^6 .

Boundary Conditions

All boundary conditions were treated implicitly. In general, except for noslip boundaries, the governing equations were written on boundary points. This procedure usually needs field variables at the points outside the domain. The way the unknowns at these extra points are determined varies with the boundary and flow types. The various boundary conditions are discussed as follows:

Inflow Boundary

For subsonic flows, u, v , and T were specified. Pressure was extrapolated from interior points. For supersonic flows, all variables must be specified.

Outflow Boundary

For subsonic flows, pressure was specified at this boundary and extrapolation was used to obtain other variables. For supersonic flows, all variables were extrapolated from interior points.

Far-Field Boundary

For subsonic flows, freestream velocity, pressure, and temperature were specified and the v component of velocity was

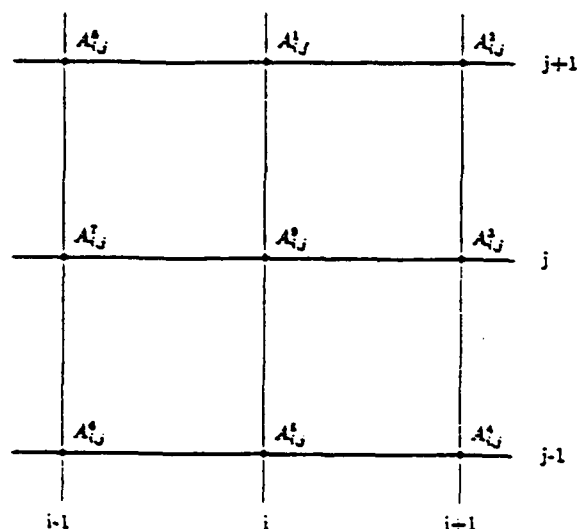


Fig. 1 Computational molecule for $A_{i,j}^{n+1,k+1}, A_{i,j}^{n+1,k}, \dots, A_{i,j}^{n,k}$.

obtained by extrapolation from interior points. For supersonic flows reported in this paper, all variables were specified.

Symmetry Boundary

The governing equations were written at this boundary as described above. All variables at the points outside the domain were obtained by the symmetry condition for u , p , and T and the antisymmetry condition for v .

Wall Boundary

Instead of writing the governing equations at this boundary, noslip conditions were used for velocity components. Either isothermal or a heat flux condition was used for the boundary condition for T . For pressure, the favored treatment is to write the normal momentum equation at this boundary and apply the noslip conditions to simplify it. The resulting equation will relate the normal derivative of pressure to velocity derivative terms. The treatment will become more complicated for irregular or curvilinear boundaries but it may enhance the coupling between the pressure and velocity fields and avoid spurious pressure solutions. This idea will be discussed further in the results section.

For internal steady-flow calculations, the treatment for the pressure boundary condition at the inflow and outflow deserves special attention. For a compressible formulation used in this study, the pressure level calculated at the inflow boundary must be adjusted (due to density variation) as the calculation proceeds if the specified Reynolds number is to be maintained. The same adjustment must be applied to the pressure everywhere, including the outflow pressure. This pressure adjustment procedure maintains a constant and predetermined mass flow rate. Without this adjustment, the Reynolds number of the final converged solution may drift from the desired value. This drift was found to be more severe for low-Reynolds-number flows.

CMSIP Solution Procedure

The above algebraic equations with the specified boundary conditions, which has a 4×4 block in each element, were solved by the CMSIP procedure. This procedure introduces an auxiliary matrix $[P]$ to both sides of the above matrix equation [Eq. (8)] as

$$[A + P]q^{n+1,k+1} = [P]q^{n+1,k} + b \quad (9)$$

where $[A + P]$ can be conveniently decomposed into lower-

and upper-block triangular matrices, each of which has only five nonzero diagonals. The following procedure was used to obtain the unknown vector q . Letting $\delta^{n+1,k+1} = q^{n+1,k+1} - q^{n+1,k}$ and a residual vector $R^{n+1,k} = b - [A]q^{n+1,k}$, Eq. (9) becomes

$$[A + P]\delta^{n+1,k+1} = R^{n+1,k} \quad (10)$$

Replacing $[A + P]$ by the $[L][U]$ product gives

$$[L][U]\delta^{n+1,k+1} = R^{n+1,k} \quad (11)$$

Defining a provisional vector W by $W^{n+1,k+1} = [U]\delta^{n+1,k+1}$, the solution procedure can be written in two steps:

Step 1:

$$[L]W^{n+1,k+1} = R^{n+1,k} \quad (12)$$

Step 2:

$$[U]\delta^{n+1,k+1} = W^{n+1,k+1} \quad (13)$$

The detailed formulation of this procedure can be found in Andersen et al.,¹ Stone's original paper,¹⁰ and Schneider and Zedan¹¹ for scalar equations. The coupled formula, which is a straightforward extension from its scalar counterpart, can be obtained from Chen¹² or Zedan and Schneider.¹⁶ This procedure treats the unknowns for the entire domain in a strongly implicit manner that enhances the robustness of the solution algorithm. It should be noted that the present work may be one of the first attempts to solve compressible Navier-Stokes equations by the CMSIP scheme. Application of the CMSIP scheme to hyperbolic equations has been studied by Walters et al.¹⁷, where a stability analysis showed that the SIP scheme was unconditionally stable for the three-dimensional wave equation.

Smoothing

When a nonstaggered (collocated) grid arrangement is used with central differences, a spatial oscillation in pressure due to pressure-velocity decoupling has frequently been reported in the literature¹⁸ for low-Mach-number and incompressible flows. This type of high-frequency oscillation is also found near a shock wave in supersonic flows. In most cases, for low-Mach-number flow calculations, it appears that this pressure oscillation can be removed by proper treatment of the boundary conditions and the form of governing equations used, although the generality of this finding is still being studied. If the pressure decoupling occurs, the following explicit smoothing procedure (or "filter"¹⁹) is suggested:

$$\phi^{n+1} = \phi^{old} + \omega \left(\frac{\partial^2 \phi^{old}}{\partial \xi^2} + \frac{\partial^2 \phi^{old}}{\partial \eta^2} \right) \quad (14)$$

where ϕ is the variable to be smoothed.

Smoothing was generally not needed in the subsonic flow calculations. The exception was for the cylinder cases where smoothing was required for the pressure. For those cases, the pressure boundary conditions were obtained by setting the pressure derivative normal to the body equal to zero rather than the more usual procedure of evaluating the pressure derivative from the momentum equations. A value of ω between 0.05 and 0.2 was found to be satisfactory. For the supersonic case, all dependent variables were smoothed using $\omega = 0.005$. The widely used implicit smoothing method⁴ was also tried and it was found that the present explicit smoothing was less sensitive to the smoothing parameter ω .

Convergence Criterion

The convergence criterion was based on the norm of all variables in a coupled sense. This criterion is as follows:

$$\left(\frac{\sum_{i,j=1}^{im,jm} \sum_{n=1}^{n-1} \left| \frac{q_n^{k+1} - q_n^k}{q_n^{k+1}} \right|^{0.5}}{4 \times im \times jm} \right) \leq \epsilon \quad (15)$$

where k is the iteration level, n the variable index, im the number of grid points in the x direction, jm the number of grid points in the y direction, q_n a component of the unknown vector q , and $q_{n,rms}$ the root-mean-square value of q_n . The criterion ϵ was generally set equal to 1.0×10^{-4} .

Convergence Acceleration Technique

As with most central-difference schemes, the time term serves to enhance the diagonal dominance, especially if the continuity equation is solved coupled with the system. When central differences are applied to the spatial derivative terms in the continuity equation, the time term must be retained to avoid a singularity in the matrix system. Unlike the momentum and energy equations that possess nonzero diagonal terms from the diffusion and conduction terms, the time term in the continuity equation bears all of the burden of providing the diagonal dominance in this equation. Although the present method solves equations in a coupled manner, and the resulting coefficient matrix is in block form, the diagonal dominance requirement for a single equation can still provide a good guidelines to assure convergence of the coupled equations. Golub and Van Loan²⁰ provide the definition of the diagonal dominance for a block system, but it was found impractical to use in the present work.

Consistent with the above observations, the present authors found that if the steady-state solution is the only concern, dual time can be used to accelerate the convergence rate for low-Mach-number flow calculations when an isothermal condition is assumed. This dual-time technique applies a much smaller time step for the continuity equation than for momentum equations. For this current formulation, the time step for the continuity equation was about the order of W_0^2 for low-Mach-number flows. This dual-time procedure is equivalent to using different relaxation factors for different equations. This technique assures that the rapidly propagating pressure signal in low-Mach-number flows is resolved by the smaller time step used in the continuity equation, which can be thought as an equation for pressure.

The local time step¹⁵ was also used in the momentum and energy equations to further accelerate the convergence for steady state calculations.

Sample Results

Sample results are presented for four subsonic cases and one supersonic case. The four subsonic cases include two steady-state internal flows, one steady-state external flow, and one unsteady external flow. The results for these five test cases are briefly described in the next several sections.

Subsonic Steady-State Flows

Developing Flow in a Channel

Because of the symmetrical nature of this problem, only the upper half-channel was calculated. Four cases with Reynolds numbers of 0.5, 10, 75, and 7500 and a Mach number of 0.05 was studied. The Reynolds number is based on the inlet velocity, bulk density, and half-width of the channel. Grids of 21×11 , 21×11 , 31×11 , and 41×11 points and nondimensional channel lengths of 2, 4, 30, and 3000 were used for Reynolds numbers of 0.5, 10, 75, and 7500, respectively. The grid points were clustered near the inlet and the upper wall. The centerline velocity distribution along the flow-development region is shown in Fig. 2. The agreement between the present results and those by TenPas and Pletcher,²¹

Moriwara and Cheng,²¹ McDonald et al.,²² and Bodoia and Osterle²³ is good. The convergence history of these four cases is shown in Fig. 3. It should be noted that for steady-state calculations, iterations were not used at each time step so that the number of iterations shown in the figure is equal to the number of time steps. Heat transfer at $Re = 500$ and $Pr = 0.72$ was also studied for this case. The results have been reported in Chen and Pletcher²⁴ and will not be presented here.

Driven Cavity Flow

The two-dimensional driven cavity problem was studied very extensively and served as a benchmark test case for the incompressible Navier-Stokes calculations. Results were obtained for Reynolds numbers of 100, 1000, and 3200, respectively, under an isothermal condition and a Mach number of 0.05. Figure 4 shows the u velocity component along the vertical centerline, and Fig. 5 shows the v velocity component along the horizontal centerline for these three Reynolds numbers. The agreement with the results by Ghia et al.²⁵ and Goodrich and Soh²⁶ is excellent for $Re = 100$ and 1000 and is good for $Re = 3200$. The effects of grid refinement are also shown. Figure 6 compares the pressure distribution along the stationary wall obtained by the present method with those obtained by Ghia et al.²⁷ The abscissa in Fig. 6 represents distance along the parameter of the cavity, measured as indicated in the insert.

The streamline pattern, pressure contours, the velocity vectors for $Re = 3200$ are shown in Fig. 7. For the grid points used (indicated in the figures), the convergence rate for Re

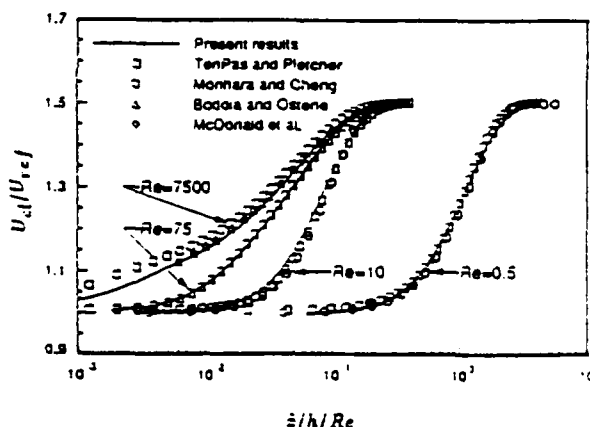


Fig. 2 Predicted centerline velocity distribution for developing flow in a two-dimensional channel inlet.

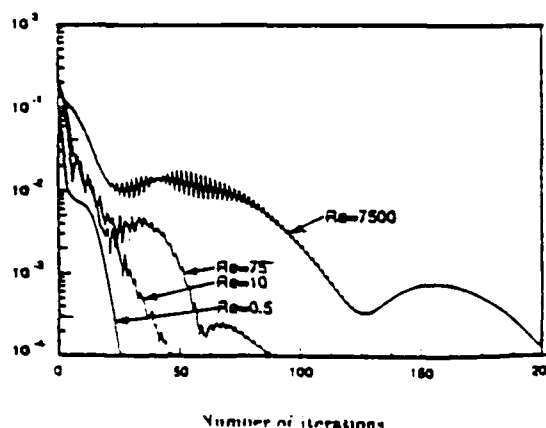


Fig. 3 Convergence history for developing flow in a two-dimensional channel inlet.

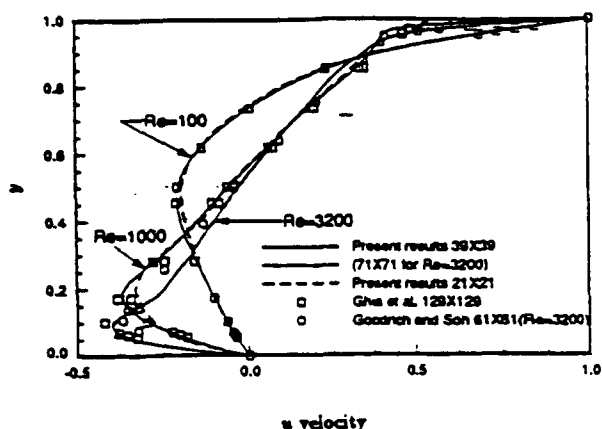


Fig. 4 Predicted u velocity component along the vertical centerline of the two-dimensional driven cavity for $Re = 100$, 1000, and 3200.

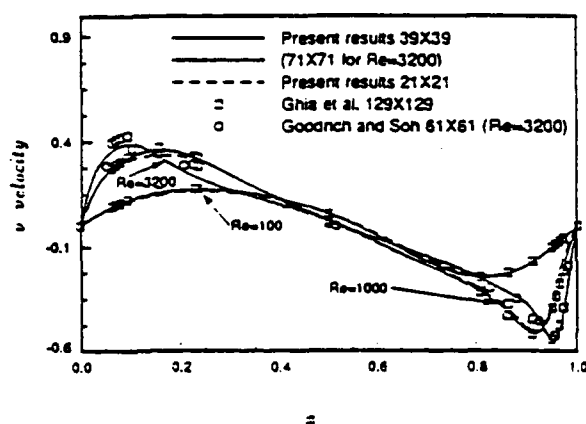


Fig. 5 Predicted v velocity component along the horizontal centerline of the two-dimensional driven cavity for $Re = 100$, 1000, and 3200.

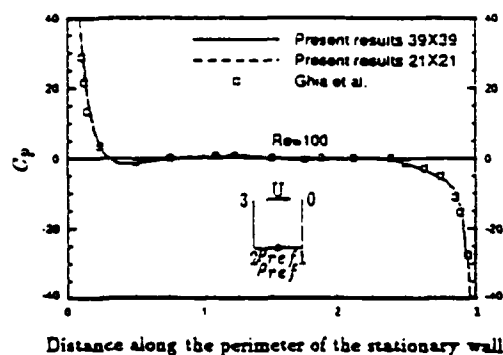


Fig. 6 Predicted pressure coefficient C_p along the stationary walls of the two-dimensional driven cavity for $Re = 100$ ($C_p = Re \times (\bar{p} - \bar{p}_{ref})/(\bar{\rho} U^2)$).

$Re = 100$ and 1000 compares very favorably with that reported by Mansour and Hamed²⁸ where a coupled scheme in primitive variables was used for the incompressible Navier-Stokes equations. Usually less than 200 iterations were sufficient. For the $Re = 3200$ case, slow convergence for a 71×71 grids was encountered. A similar difficulty at this Reynolds number was also reported by Napolitano and Walters.²⁹ It is suspected that the slow convergence at this Reynolds number is due to the strong transient nature of the flow where several significant secondary flows appear and interact with the main circulating vortex. Goodrich et al.³⁰ have found the flow to be unsteady at $Re = 5000$.

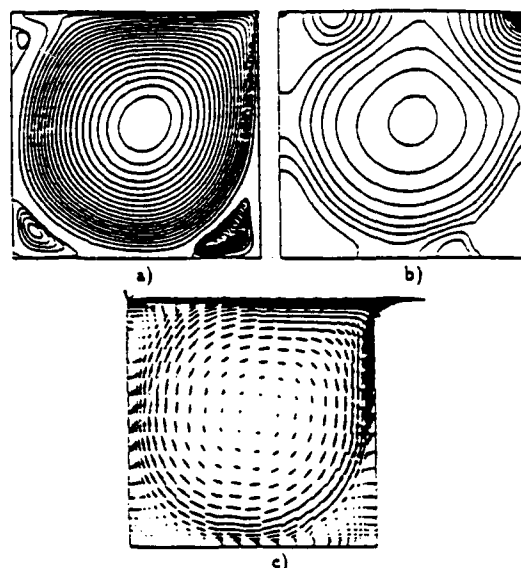


Fig. 7 Results for the two-dimensional driven cavity flow for $Re = 3200$: a) streamlines, b) pressure contours, and c) velocity vectors.

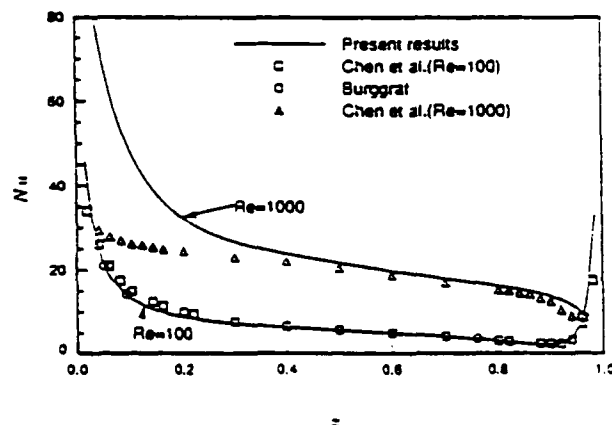


Fig. 8 Local Nusselt number at the top moving wall of the two-dimensional driven cavity.

Table 1 Mach number effect for cavity flow
 $Re = 100$, 21×21 grid

Mach number	0.2	0.1	0.05	10^{-2}	10^{-1}	10^{-4}
No. of iterations	25	27	33	85	85	85

Heat-transfer results were obtained for Reynolds numbers of 100 and 1000, respectively, and a Mach number of 0.05. Figure 8 shows the local Nusselt number along the top moving wall that is hotter than the stationary wall for $Re = 100$ and 1000 with $Pr = 1.0$. The results for $Re = 100$ were compared with those obtained by Chen et al.³¹ and Burggraf.³² The good agreement is obvious. The results for $Re = 1000$, however, do not agree well with those of Chen et al.³¹ near the left corner of the top wall. Further research is needed to resolve this discrepancy.

In order to study the effect of Mach number, the driven cavity case for $Re = 100$ with a 21×21 grid was computed with Mach numbers ranging from 10^{-4} –0.2 and an isothermal condition. The number of iterations (time steps) for all Mach numbers is listed in Table 1. It shows that for Mach number lower than 10^{-2} the number of iterations required increases by a factor of more than two. Even with this increase, this algorithm is still very efficient for this range of low-Mach-

number cases, at least compared with the results reported by Mansour and Hamed.²³ The solutions for the above Mach numbers were almost identical.

For all cases computed for the cavity flow, no pressure oscillation was detected using central difference even for the high Reynolds number case. This unexpected result might be attributed to 1) usage of the compressible form that contains the pressure information in the time and the first-order derivative terms and 2) the treatment of the pressure boundary condition at the wall, which employs the momentum equations to evaluate the pressure derivative at the wall in an implicit manner. Both of these procedures enhance the pressure-velocity coupling, thus tending to remove the pressure oscillation. The present authors also found the above procedures successful in removing the pressure oscillation in three-dimensional cavity flow, although the three-dimensional cavity results will not be presented here.

Unsteady Flow over a Circular Cylinder, $Re = 100$

Before solving this unsteady vortex shedding flow, the present algorithm has been tested for a flow over a circular cylinder with Reynolds number of 40 (based on diameter), which is considered³³ as the upper limit for a steady-state flow to exist for this flow configuration. The solution and efficiency of the present algorithm for this case has been discussed by Chen and Fletcher²⁴ and will not be included here.

This vortex shedding case was used to demonstrate the application of the present procedure for unsteady flows. This flow has been studied very extensively in the literature.^{34,35} An O-type 81×101 grid was used with mesh clustering near the wall and in the wake region. The outer boundary was located 20 diameters from the cylinder. Since the final periodic unsteady solution was of primary interest, the initial condition was efficiently generated by the steady-state technique that quickly set up a flow pattern with a little asymmetry. The asymmetric trigger technique suggested by Leconte and Piquet³⁵ was not needed. Starting from this initial solution, a constant nondimensional time step of 0.02 was used to march the solution in time. Iterations were used at each time step to eliminate the linearization error. Initially about 15 iterations were needed per time step but this number quickly dropped to two for most of the time marching history. The computation was stopped after several periodic cycles were observed. Figure 9 shows the final four cycles of the lift coefficient having a constant amplitude of about 0.31, which is almost identical to the result reported by Visbal.³⁶ The Strouhal number based on this is about 0.167. This result is located within the experimental range 0.16 ~ 0.17 reported by Roshko.³⁷

Figure 10 shows the results for streamlines and vorticity contours, respectively, in the final cycle. The Mach number used was 0.2.

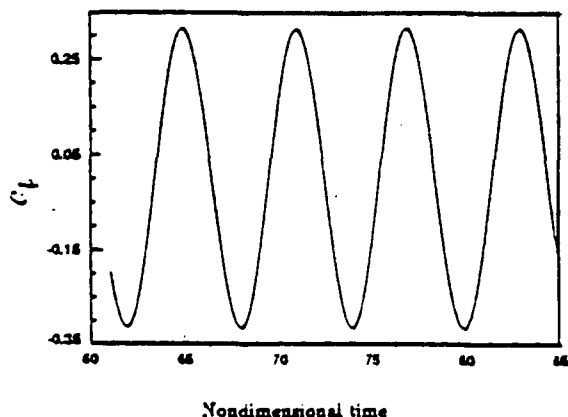
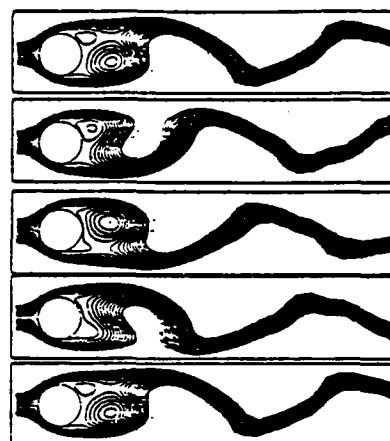
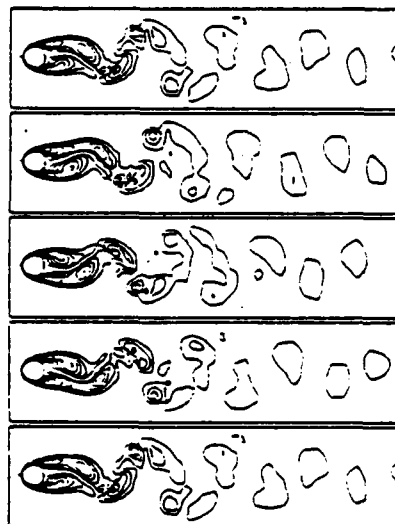


Fig. 9 Time history of the lift coefficient for the final four cycles of the vortex shedding patterns for $Re = 100$.



a) Streamlines



b) Vorticity contours

Fig. 10 Vortex shedding pattern for the final cycle for $Re = 100$: a) streamlines, and b) vorticity contours.

Shock-Boundary-Layer Interaction Problem

This case demonstrates the shock-capturing capability of the present procedure. This case has been studied by several other researchers,^{3,3} and a more detailed description of this problem can be obtained from their work. The freestream Mach number is 2 and Reynolds number, based on the distance from the leading edge to the point at which the impinging shock intersected the plate, is 0.296×10^6 . The strength of the impinging shock is strong enough to cause the laminar boundary layer to separate. The angle of this impinging shock is 32.6 deg. An 81×81 grid was used.

The grid was uniform in the main flow direction and stretched in the cross-stream direction with the minimum nondimensional grid increment of 1.0×10^{-4} next to the wall. The computational domain began five grid points ahead of the leading edge of the plate, and top boundary extended far enough to allow the leading-edge shock to pass through the outflow boundary. This treatment eliminates the need for using nonreflective boundary conditions at the top boundary.

Freestream conditions were specified at the inlet boundary below the impinging shock. The postshock conditions were specified at the inlet boundary above the impinging shock and along the top boundary. Extrapolation was used at the outflow boundary. Nonslip conditions, zero normal pressure gradient, and an adiabatic wall temperature were used at the wall.

The results are shown for wall-pressure and skin-friction distributions in Figs. 11 and 12, respectively. The pressure contours are shown in Fig. 13. The above results compare reasonably well with the results in the literature^{3,34-37} and

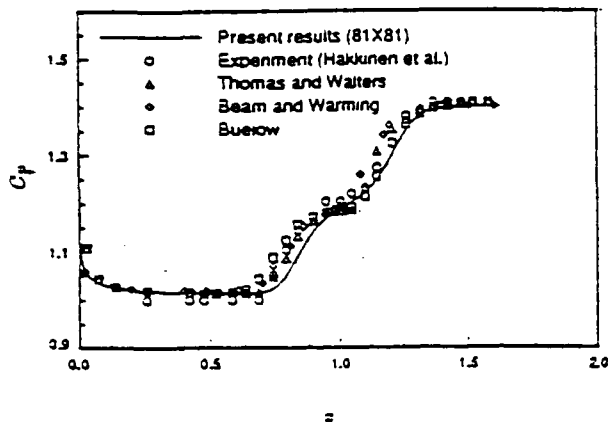


Fig. 11 Pressure-coefficient, $C_p (= \bar{p}/\bar{p}_\infty)$, distribution along the wall.

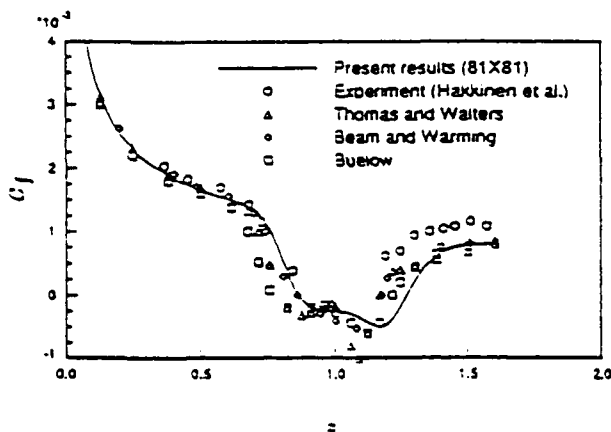


Fig. 12 Skin-friction coefficient, $C_f (= \tau/\bar{p}_\infty)$, distribution along the wall.

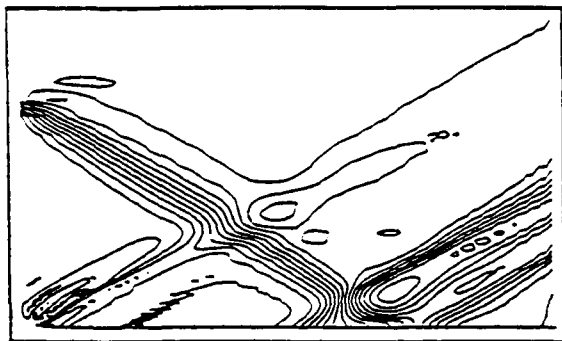


Fig. 13 Pressure contours for shock-boundary-layer interaction problem.

demonstrate the shock-capturing capability of the present scheme. About 1000 iterations were required to obtain the present converged solutions.

For this supersonic case, smoothing was needed for all variables instead of pressure only as for low-Mach-number cases. Clearly, the shock resolution obtained by this method can be improved, but the present results suggest that the formulation of the scheme is fundamentally correct and sufficient for capturing shocks.

Most of the above calculations were performed on the Apollo DN 10,000 workstation. The CPU time was approximately 0.0048 s/node/iteration.

Conclusions

A coupled solution strategy for the time-dependent compressible form of the Navier-Stokes equations that appears to be effective for Mach numbers ranging from the incompressible limit ($M_\infty \sim 0.01$) to supersonic has been developed. The approach employs the strong conservation form of the governing equations but uses primitive (u, v, p, T) variables rather than the more traditional conserved ($\rho, \rho u, \rho v, e$) variables as unknowns. This choice of variables simplifies the treatment of viscous terms and enhances effectiveness at low Mach numbers by allowing the density to be removed from the difference equations. A coupled modified strongly implicit procedure was used to efficiently solve the Newton-linearized algebraic equations. Generally, it was found that smoothing was not needed to control spatial oscillations in pressure for subsonic flows despite the use of central differences. Dual-time stepping was found to further accelerate convergence for steady flows. Generally good agreement between the predictions and results in the literature was observed for several test cases including steady and unsteady low-Mach-number internal and external flows and a steady shock-boundary-layer interaction flow on a flat plate in a supersonic stream. The extension of this algorithm to three-dimensional flow calculations is currently being investigated.

Acknowledgments

This research was partially supported by the Air Force Office of Scientific Research through Grant AFOSR-89-0403. The authors are also grateful for support received through a block grant from the Iowa State University Computation Center.

References

- Anderson, D. A., Tannehill, J. C., and Pletcher, R. H., *Computational Fluid Mechanics and Heat Transfer*, Hemisphere, New York, 1984, Chaps. 7, 9.
- Beam, R. M., and Warming, R. F., "An implicit Factored Scheme for the Compressible Navier-Stokes Equations," *AIAA Journal*, Vol. 16, No. 4, 1978, pp. 393-402.
- Liou, M.-S., "Newton/Upwind Method and Numerical Study of Shock-Wave/Boundary-Layer Interactions," *International Journal for Numerical Methods in Fluids*, Vol. 9, No. 7, 1989, pp. 747-761.
- Karki, K. C., and Parankar, S. V., "Pressure-Based Calculation Procedure for Viscous Flows at All Speeds in Arbitrary Configurations," *AIAA Journal*, Vol. 27, No. 9, 1989, pp. 1167-1174.
- Van Doornmal, J. P., Raithby, G. D., and McDonald, B. H., "The Segregated Approach to Predicting Viscous Compressible Fluid Flows," *Journal of Turbomachinery, Transactions of the ASME*, Vol. 109, No. 2, April 1987, pp. 268-277.
- Issa, R. L., "Numerical Methods for Two- and Three-Dimensional Recirculating Flows," *Computational Methods for Turbulent, Transonic and Viscous Flows*, edited by J. A., Elsevier, Hemisphere, New York, 1983.
- Merkle, C. L., and Choi, Y.-H., "Computation of Compressible Flows at Very Low Mach Numbers," *AIAA Paper 86-0351*, Jan. 1986.
- TenPas, P. W., and Pletcher, R. H., "Coupled Space-Marching Method for the Navier-Stokes Equations for Subsonic Flows," *AIAA Journal*, Vol. 29, No. 2, 1991, pp. 219-226.
- Feng, J., and Merkle, C. L., "Evaluation of Preconditioning Methods for Time-Marching Systems," *AIAA Paper 90-0016*, 1990.
- Stone, H. L., "Iterative Solution of Implicit Approximations of Multidimensional Partial Differential Equations," *SIAM Journal of Numerical Analysis*, Vol. 5, No. 3, 1968, pp. 530-558.
- Schneider, G. E., and Zedan, M., "A Modified Strongly Implicit Procedure for the Numerical Solution of Field Problems," *Numerical Heat Transfer*, Vol. 4, No. 1, 1981, pp. 1-19.
- Harlow, F. H., and Amsden, A. A., "Numerical Calculation of Almost Incompressible Flow," *Journal of Computational Physics*, Vol. 3, No. 1, 1968, pp. 80-93.
- Khosla, P. K., and Ruin, S. G., "Diagonally Dominant Second-Order Accurate Implicit Scheme," *Computers and Fluids*, Vol. 2, No. 2, 1974, pp. 207-209.

- ¹⁴Hindman, R. G., "Generalized Coordinate Forms of Governing Fluid Equations and Associated Geometrically Induced Errors," *AIAA Journal*, Vol. 20, No. 10, 1982, pp. 1359-1367.
- ¹⁵Chen, K.-H., *A Primitive Variable, Strongly Implicit Calculation Procedure for Two- and Three-Dimensional Unsteady Viscous Flows: Applications to Compressible and Incompressible Flows Including Flows with Free Surfaces*, Ph.D. Dissertation, Iowa State Univ., Ames, IA, 1990.
- ¹⁶Zedan, M., and Schneider, G. E., "A Coupled Strongly Implicit Procedure for Velocity and Pressure Calculation in Fluid Flow Problems," *Numerical Heat Transfer*, Vol. 8, No. 5, 1985, pp. 537-557.
- ¹⁷Walters, R. W., Dwyer, D. L., and Hassan, H. A., "A Strongly Implicit Procedure for the Compressible Navier-Stokes Equations," *AIAA Journal*, Vol. 24, No. 1, 1986, pp. 6-12.
- ¹⁸Patankar, S. V., *Numerical Heat Transfer and Fluid Flow*, Hemisphere, New York, 1981, Chapter 6.
- ¹⁹Peyret, R., and Taylor, T. D., *Computational Methods for Fluid Flow*, Springer-Verlag, New York, 1983, pp. 104-105.
- ²⁰Golub, G. H., and Van Loan, C. F., *Matrix Computations*, Johns Hopkins Univ. Press, Baltimore, MD, 1983, Chap. 4.
- ²¹Monihara, H., and Cheng, R. T., "Numerical Solution of the Viscous Flow in Entrance Region of Parallel Plates," *Journal of Computational Physics*, Vol. 11, No. 4, 1973, pp. 550-572.
- ²²McDonald, J. W., Denny, V. E., and Mills, A. F., "Numerical Solutions of the Navier-Stokes Equations in Inlet Regions," *Journal of Applied Mechanics, Series E*, Vol. 39, Dec. 1972, pp. 373-378.
- ²³Bodoia, J. R., and Osterle, J. F., "Finite-Difference Analysis of Plane Poiseuille and Couette Flow Development," *Applied Scientific Research, Sec. A*, Vol. 10, No. 3-4, 1961, pp. 265-276.
- ²⁴Chen, K.-H., and Fletcher, R. H., "A Primitive Variable, Strongly Implicit Calculation Procedure for Viscous Flows at All Speeds," AIAA Paper 90-1521, June 1990.
- ²⁵Ghia, U., Ghia, K. N., and Shin, C. T., "High-Re Solutions for Incompressible Flow Using the Navier-Stokes Equations and a Multigrid Method," *Journal of Computational Physics*, Vol. 48, No. 3, 1982, pp. 387-411.
- ²⁶Goodrich, J. W., and Soh, W. Y., "Time-Dependent Viscous Incompressible Navier-Stokes Equations: The Finite-Difference Galerkin Formulation and Streamfunction Algorithm," *Journal of Computational Physics*, Vol. 34, No. 1, Sept. 1989, pp. 207-241.
- ²⁷Ghia, K. N., Hankey, W. L., Jr., and Hodge, J. K., "Study of Incompressible Navier-Stokes Equations in Primitive Variables Using Implicit Numerical Technique," AIAA Paper 77-648, June 1977.
- ²⁸Mansour, M. L., and Hamed, A., "Implicit Solutions of the Incompressible Navier-Stokes Equations in Primitive Variables," AIAA Paper 87-0717, August 1987.
- ²⁹Napolitano, M., and Walters, R. W., "An Incremental Block-Line Gauss-Seidel Method for the Navier-Stokes Equations," *AIAA Journal*, Vol. 24, No. 5, 1986, pp. 770-776.
- ³⁰Goodrich, J. W., Gustafson, K., and Halasi, K., "Hopf Bifurcation in the Driven Cavity," NASA TM-102334 (or ICOMP-89-21), Oct. 1989.
- ³¹Chen, C.-J., Ho, K.-S., and Cheng, W.-S., "The Finite Analytic Method," Vol. 5, IIHR Rept. 232-V, Iowa Inst. of Hydraulic Research, Univ. of Iowa, Iowa City, IA, 1982.
- ³²Burggraf, O. R., "Analytic and Numerical Studies of the Structure of Steady Separated Flows," *Journal of Fluid Mechanics*, Vol. 24, Pt. 1, 1966, pp. 113-151.
- ³³Forberg, B., "A Numerical Study of Steady Viscous Flow Past a Circular Cylinder," *Journal of Fluid Mechanics*, Vol. 98, Pt. 4, 1980, pp. 319-355.
- ³⁴Rogers, S. E., and Kwak, D., "An Upwind-Differencing Schemes for the Time-Accurate Incompressible Navier-Stokes Equations," AIAA Paper 88-2583, June 1988.
- ³⁵Lecointre, Y., and Piquet, J., "On the Use of Several Compact Methods for the Study of Unsteady Incompressible Viscous Flow Around a Circular Cylinder," *Computers and Fluids*, Vol. 12, No. 4, 1984, pp. 255-280.
- ³⁶Visbal, M. R., "Evaluation of an Implicit Navier-Stokes Solver for Some Unsteady Separated Flows," AIAA Paper 86-1053, May 1986.
- ³⁷Roshko, A., "On the Development of Turbulent Wakes from Vortex Streets," NACA TN-2913, 1953.
- ³⁸Thomas, J. L., and Walters, R. W., "Upwind Relaxation Algorithms for the Navier-Stokes Equations," AIAA Paper 85-1501, 1985.
- ³⁹Buelow, P. E., *Comparison of TVD Schemes Applied to the Navier-Stokes Equations*, Master Thesis, Iowa State Univ., Ames, IA, 1988.
- ⁴⁰Hakkinen, R. J., Greber, L., Trilling, L., and Arbarbanel, S. S., "The Interaction of an Oblique Shock Wave with a Laminar Boundary Layer," NASA Memo-2-18-59W, March 1959.

**APPENDIX H. Simulation of Three-Dimensional Liquid Sloshing
Flows Using a Strongly Implicit Calculation Procedure.**

NOTE: This paper, which has been accepted for publication by the *AIAA Journal*, is a revision of AIAA Paper No. 91-1661, which was presented at the AIAA 22nd Fluid Dynamics, Plasma Dynamics, and Lasers Conference, Honolulu, HA, 1991.

SIMULATION OF THREE-DIMENSIONAL LIQUID SLOSHING FLOWS USING A STRONGLY IMPLICIT CALCULATION PROCEDURE

Kuo-Huey Chen*

The University of Toledo/NASA Lewis Research Center, Cleveland, Ohio, 44135

and

Richard H. Pletcher[†]

Iowa State University, Ames, Iowa 50011

Abstract

A coupled strongly implicit solution strategy for unsteady three-dimensional free surface flows has been developed based on an artificial compressibility formulation for the incompressible Navier-Stokes equations. A pseudotime term has been used in the continuity equation to permit time accurate calculations to be achieved. The scheme appears capable of tracking the free surface reasonably accurately inside a partially-filled spherical container undergoing a general rotating motion characteristic of that experienced by a spin-stabilized satellite. Five different free surface calculations have been presented. Some of the results exhibit an interesting Reynolds number dependent oscillatory behavior which is believed to be physical although no experimental results appear to be available for verification to date.

Introduction

The liquid sloshing motion inside a container has long been of interest to engineers and researchers. Liquid sloshing occurs in many important practical applications such as in oil tankers, railroad tank cars, missiles, satellites and spacecraft^{1,2,3}. A particular goal of the present study has been the simulation of sloshing motion in a spherical container undergoing motion characteristic of that experienced aboard a spin-stabilized satellite. The major concern about the liquid sloshing motion within a container is that a substantial periodic force may be generated which may affect the stability of the moving vehicle. If the sloshing frequency is near the natural frequency of the vehicle structure, resonance may increase the likelihood of structural damage or instability

*Senior Research Associate, Member AIAA, Mailing address: Ohio Aerospace Inst. 2001 Aerospace Parkway, Brook Park, OH 44142.

[†]Professor, Department of Mechanical Engineering, Member AIAA.

resulting from the motion.

The sloshing motion of liquid usually involves the presence of a free surface which is the interface between the liquid and air or other type of gas. The presence of the free surface adds another difficulty in analysis to an already complicated fluid motion, since the free surface position usually is not known *a priori* and has to be determined as part of the solution. The container may undergo several different kinds of motion ranging from a simple linear acceleration or rotation to more complicated combinations of these. To conveniently analyze the motion, it is usually necessary to transform the governing equations to a non-inertial coordinate system⁴. The motion of the liquid is generally three-dimensional, time-dependent and sufficiently complex that no major simplification to the general equations (incompressible Navier-Stokes equations) is possible. The accurate simulation of such motion is a formidable problem primarily because of the computational resources required, and few, if any, three-dimensional time-dependent simulations have been reported in the literature.

Chakravarthy⁵ investigated laminar incompressible flow within rotating liquid filled shells under rotation but without the presence of free surfaces. Vaughn, Oberkampf and Wolfe⁴ solved the three-dimensional incompressible Navier-Stokes equations for a fluid-filled cylindrical canister that was spinning and nutating. In their work, the equations were transformed to a non-inertial frame. Again, the container was completely filled with liquid and no free surface was present. In a review of the literature, very few articles dealing with the liquid sloshing within a spherical container were found. Perhaps most relevant to the present study is the work of Kassinos and Prusa⁶, where a general motion of a spherical container was accounted for by a complete coordinate transformation using several successive axis rotations and a translation. Some liquid spin-up problems have been restricted to either the rectangular⁷ or the cylindrical⁸ configurations.

The present study utilizes a surface fitting approach^{6,9,10} for the free surface and the artificial compressibility formulation of the equations. In this method a fictitious time derivative of pressure is added to the continuity equation so that the solution of the set of conservation equations can be marched in time. Originally, this method was thought to be only applicable to steady flow problems¹¹. For these, the entire time dependence was fictitious, but the solution approached the correct steady state solution asymptotically with time. More recently, investigators^{12,13,14} have suggested that the procedure can be made accurate with respect to time by considering the

time like variable appearing in the fictitious time term added to the continuity equation to be a pseudotime. For each physical time step, the pseudotime is advanced several increments in an iterative fashion. When the variables no longer change with pseudotime, the fictitious time term is zero and the equations satisfy the compatibility condition for incompressible flow at the specified physical time. The coordinate treatment of Kassinos and Prusa⁶, which is applicable to sloshing phenomena under a variety of conditions, is adopted in this study. A coupled strongly implicit procedure (CSIP), initially proposed by Stone^{15,16}, is used to solve the resulting algebraic system of equations with the specified boundary conditions. A similar solution procedure has been used previously by the present authors to solve coupled two-dimensional equations and was found to be efficient and robust for several diverse problems¹⁷. Unsteady results for five liquid sloshing problems in a rotating half-filled spherical container are presented. In the following sections, the mathematical formulation, boundary conditions, numerical solution algorithm and the results will be discussed in detail.

Mathematical Formulation

Governing equations

The incompressible Navier-Stokes equations with an isothermal condition can be written as:

$$\frac{\partial u_i}{\partial x_i} = 0 \quad (1)$$

$$\frac{\partial u_i}{\partial t} + u_j \frac{\partial u_i}{\partial x_j} = -\frac{1}{\rho} \frac{\partial p}{\partial x_i} + \nu \frac{\partial^2 u_i}{\partial x_j \partial x_j} - g_i \quad (2)$$

where u_i is the velocity component, p is the thermodynamic pressure, g_i is the acceleration of gravity, ρ is the density (constant), ν is the kinematic viscosity and x_i represents the spatial coordinates.

At least two different approaches can be used to formulate this problem for numerical solution. First, the above equations can be solved in the form indicated above together with the proper treatment of the boundary conditions in accordance with the rotating-nutating motion of the container at any instant of time. Ideally, this treatment is workable for a simple motion of the container, but will become impractical and difficult for describing the motion and interpreting the results if a general rotating-nutating motion is encountered. Actually, such a general motion can

arise in the interaction between a satellite structure and the liquid sloshing in a partially filled container. Therefore, it is more appropriate to handle the general motion of the container with terms within the equations themselves. That is, the motion of the container relative to an inertial frame can be implicitly accounted for by proper coordinate transformations. This is the second approach and the one that will be adopted in this study. A schematic diagram of the partially filled rotating-nutating container is shown in Fig. 1.

Following the approach outlined in Kassinos and Prusa⁶, several steps are needed to transform the governing equations from an inertial frame to a non-inertial frame. They are described in the following several sections. In addition to those transformations, a generalized nonorthogonal coordinate transformation is applied to the resulting equations to handle the irregular geometry of the boundaries.

The rotating-nutating coordinates: x_2 coordinate system The original three-dimensional incompressible equations will be labeled with a subscript 0 to indicate that they are in x_0 inertial frame and rewritten as

$$\frac{\partial u_{0i}}{\partial x_{0i}} = 0 \quad (3)$$

$$\frac{\partial u_{0i}}{\partial t_0} + u_{0j} \frac{\partial u_{0i}}{\partial x_{0j}} = -\frac{1}{\rho} \frac{\partial p}{\partial x_{0i}} + \nu \frac{\partial^2 u_{0i}}{\partial x_{0j} \partial x_{0j}} - g_{0i} \quad (4)$$

The container may undergo a motion with nonzero angular velocities or accelerations with respect to each axis at any instant of time. If a coordinate frame, x_1 , is attached to the spacecraft (or other vehicle) undergoing this general motion, then three successive coordinate rotations will reflect this motion. The procedure to perform the three coordinate rotations is described in detail in Chen¹⁸ and Chen and Pletcher¹⁹. Also, since the container may be attached to another structure (satellite or spacecraft, for example) by an elastic bar, another translation is required to move the origin of the x_1 coordinate to the location of the container by the length of the elastic bar h_i . After combining the three successive rotations and the translation, The relationship between x_0 and x_2 is

$$x_{2i} = \alpha_{ji} x_{0j} - h_i \quad \text{or} \quad x_{0i} = \alpha_{ij} (x_{2j} + h_j) \quad (5)$$

where α_{ij} represents the elements of a 3×3 transformation matrix, $[T]$, between x_0 and x_1 frames, resulting from the above successive rotations. The transformation matrix, $[T]$, is expressed as

follows:

$$[T] = \begin{bmatrix} C_2 C_3 & S_1 S_2 C_3 - C_1 S_3 & C_1 C_3 S_2 + S_1 S_3 \\ C_2 S_3 & S_1 S_2 S_3 + C_1 C_3 & C_1 S_2 S_3 - S_1 C_3 \\ -S_2 & S_1 C_2 & C_1 C_2 \end{bmatrix}$$

where $C_i = \cos \psi_i$ and $S_i = \sin \psi_i$.

After applying the chain rule to the derivative terms in Eqs. (3) and (4) using Eq. (5), the governing equations in the x_2 frame can be expressed as:

$$\frac{\partial u_{2i}}{\partial x_{2i}} = 0 \quad (6)$$

$$\frac{\partial u_{2l}}{\partial t_2} - \dot{\alpha}_{il} \alpha_{ij} u_{2j} + [\dot{\alpha}_{ji} \alpha_{jk} (x_{2k} + h_k) - \dot{h}_i + u_{2i}] \frac{\partial u_{2l}}{\partial x_{2i}} = -\frac{1}{\rho} \frac{\partial p}{\partial x_{2l}} + \nu \frac{\partial^2 u_{2l}}{\partial x_{2j} \partial x_{2j}} - g_{2l} \quad (7)$$

where $u_{2i} = \alpha_{ji} u_{0j}$, $g_{2l} = \alpha_{il} g_{0l}$, $\dot{h}_i = dh_i/dt$ and $\dot{\alpha}_{il} = d\alpha_{il}/dt$.

To more conveniently describe the solutions and apply the boundary conditions, a new relative velocity is defined as follows:

$$u_{2l'} = u_{2l} + \dot{\alpha}_{ji} \alpha_{jk} (x_{2k} + h_k) - \dot{h}_i$$

This new relative velocity is always zero at the wall of the container no matter what kind of motion the container may undergo. The introduction of this new relative velocity can greatly simplify the treatment of the boundary conditions. Substituting the above definition of the relative velocity into Eqs. (6) and (7) and omitting the primes, we have the following equations written in terms of relative velocity components:

$$\frac{\partial u_{2i}}{\partial x_{2i}} = 0 \quad (8)$$

$$\begin{aligned} \frac{\partial u_{2l}}{\partial t_2} + u_{2i} \frac{\partial u_{2l}}{\partial x_{2i}} - 2\beta_{cr,li} u_{2i} - \beta_{t,li} (x_{2i} + h_i) - \beta_{cp,li} (x_{2i} + h_i) \\ = -\frac{1}{\rho} \frac{\partial p}{\partial x_{2l}} + \nu \frac{\partial^2 u_{2l}}{\partial x_{2j} \partial x_{2j}} - g_{2l} + E_l \end{aligned} \quad (9)$$

where $\beta_{cr,li} = \dot{\alpha}_{jl} \alpha_{ji}$, $\beta_{t,li} = \ddot{\alpha}_{jl} \alpha_{ji}$, $\beta_{cp,li} = \dot{\alpha}_{kl} \dot{\alpha}_{ki} - \dot{\alpha}_{kl} \dot{\alpha}_{nj} \alpha_{kj} \alpha_{ni}$, $E_l = 2\dot{\alpha}_{il} \alpha_{ij} \dot{h}_j - \ddot{h}_l$, $\ddot{h}_l = d^2 h_l / dt^2$ and $\ddot{\alpha}_{jl} = d^2 \alpha_{jl} / dt^2$.

Free surface tracking coordinates: x_3 coordinate system When the container undergoes a rotating-nutating motion, the free surface shape will change continuously with time. Equations

(8) and (9) can be used to model this motion; however, a third coordinate rotation is preferred in this study for the following two reasons. First, the kinematic equation which is used in this study to update the free surface at each time step requires that the free surface height be a single-valued function of the other two coordinates. Therefore it is important to keep this free surface a single-valued function by rotating the coordinates as required at each computational time step. Second, rotating the coordinates in response to changes in the orientation of the free surface facilitates the establishment of the computational grid by the present algebraic grid generation scheme.

At any instant of time, the free surface may move to a new position with respect to the x_2 coordinates as shown in Fig. 2. It is desirable to have the x_{23} axis remain normal to the free surface in an average sense. One way to accomplish this is to let the x_2 coordinates rotate an angle ϕ_r counterclockwise about the x_{22} axis and a successive counterclockwise rotation angle, ϕ'_r , about the x'_{31} axis as shown in Fig. 2. A transformation matrix, $[S]$, is required to transform from the x_2 to the x_3 coordinates. The expression for this transformation matrix, $[S]$, is:

$$[S] = \begin{bmatrix} \cos \phi_r & \sin \phi_r \sin \phi'_r & -\sin \phi_r \cos \phi'_r \\ 0 & \cos \phi'_r & \sin \phi'_r \\ \sin \phi_r & -\cos \phi_r \sin \phi'_r & \cos \phi_r \cos \phi'_r \end{bmatrix}$$

The relationship between the x_2 and x_3 coordinates is:

$$x_{2i} = s_{ij}x_{3j} \quad (10)$$

where s_{ij} is an element of $[S]$.

The chain rule is then applied to Eqs. (8) and (9) using Eq. (10) and the resulting governing equations in the x_3 coordinates are:

$$\frac{\partial u_{3i}}{\partial x_{3i}} = 0 \quad (11)$$

$$\begin{aligned} \frac{\partial u_{3n}}{\partial t_3} + (u_{3i} + f_{ij}x_{3j})\frac{\partial u_{3n}}{\partial x_{3i}} - (f_{ni} + 2\lambda_{ni})u_{3i} - \tau_{1,ni}x_{3i} - \tau_{2,ni}h_i \\ = -\frac{1}{\rho}\frac{\partial p}{\partial x_{3n}} + \nu\frac{\partial^2 u_{3n}}{\partial x_{3j}\partial x_{3j}} - g_{3n} + E_n \end{aligned} \quad (12)$$

where $u_{3j} = s_{ij}u_{2i}$, $g_{3n} = s_{ln}g_{2l}$, $f_{ij} = s_{ki}s_{kj}$, $\lambda_{ni} = \beta_{cr,lj}s_{ji}s_{ln}$, $\tau_{1,ni} = (\beta_{t,lj} + \beta_{cp,lj})s_{ln}s_{ji}$, $\tau_{2,ni} = (\beta_{t,li} + \beta_{cp,li})s_{ln}$ and $E_n = s_{ln}E_l$

Generalized nonorthogonal coordinates: z coordinate system It is desirable to establish a new coordinate system having the property that the coordinate lines fit the boundaries of the problem domain of interest, i.e., the liquid itself enclosed by the container wall and the free surface. Let this new coordinate system be designated by (τ, z_i) . The relationship between the (t_3, x_{3i}) and (τ, z_i) coordinate systems can be expressed as:

$$\tau = t_3 \quad z_i = z_i(x_{31}, x_{32}, x_{33}, t_3)$$

By applying the chain rule to the time and spatial derivative terms, the final governing equations in generalized nonorthogonal coordinates can be written as:

$$\eta_{j,i} \frac{\partial u_{3i}}{\partial z_j} = 0 \quad (13)$$

$$\begin{aligned} \frac{\partial u_{3n}}{\partial \tau} + (\dot{z}_j + \eta_{j,i} u_{3i} + \eta_{j,i} f_{ik} x_{3k}) \frac{\partial u_{3n}}{\partial z_j} - (f_{ni} + 2\lambda_{ni}) u_{3i} + \eta_{j,n} \frac{\partial p}{\partial z_j} \\ - \frac{1}{Re} (\eta_{j,i} \eta_{k,i} \frac{\partial^2 u_{3n}}{\partial z_j \partial z_k} + \eta_{k,ii} \frac{\partial u_{3n}}{\partial z_k}) = \tau_{1,ni} x_{3i} + \tau_{2,ni} h_i - g_{3n} + E_n \end{aligned} \quad (14)$$

where $\eta_{i,j} = \partial z_i / \partial x_{3j}$ and $\eta_{i,jj} = \partial^2 z_i / \partial x_{3j} \partial x_{3j}$ are the metric terms and $\dot{z}_i = \partial z_i / \partial t_3$ is the grid speed term. The detailed expressions for the metric terms and the grid speed terms are documented in Chen¹⁸. It should be noted that Eqs. (13) and (14) have been nondimensionalized before performing the generalized nonorthogonal coordinates transformation by the following nondimensional quantities:

$$x_{3i}^* = \frac{x_{3i}}{L_{ref}}, \quad u_{3i}^* = \frac{u_{3i}}{V_{ref}}, \quad t^* = \frac{t}{t_{ref}}, \quad p^* = \frac{p - p_0}{p_{ref}} \quad (15)$$

where L_{ref} is the radius of the sphere, V_{ref} is the reference velocity (will be defined later), $p_{ref} = \rho V_{ref}^2$, $t_{ref} = L_{ref} / V_{ref}$ and p_0 = atmospheric pressure or saturated vapor pressure above the free surface. The superscript * has been dropped for convenience in Eqs. (13) and (14) and the Reynolds number, Re , in Eq. (14) is defined as:

$$Re = \frac{V_{ref} L_{ref}}{\nu}$$

Boundary Conditions

All boundary conditions are treated implicitly. In general, except for noslip boundaries, the governing equations are written at boundary points. There are only two types of boundaries for this three-dimensional configuration (see Fig. 3.) They are the solid wall of the container and the free surface. Four boundary equations are required at each boundary to close the system of equations.

At the wall of the spherical container, a noslip condition is used for three velocities ($u_{3i} = 0$) and the normal momentum equation for pressure. The normal momentum equation is formed by performing the inner product of the *local* unit normal vector and the three momentum equations, Eq. (14). The resulting normal momentum equation after simplifying with the noslip condition can be found in Chen¹⁸ and Chen and Pletcher¹⁹.

At the free surface, strictly speaking, five equations are needed at this boundary since one more equation is required for an additional unknown, i.e., the free surface position, which is part of the solution. The so-called dynamic equations will be discussed first. These equations, which will be coupled with the Navier-Stokes equations for the interior points, are derived based on the following conditions. First, it is assumed that the two tangential shear stresses along the free surface are zero since no external tangential forces are applied to the surface. Second, the normal shear stress must be continuous across the free surface boundary, and finally, the continuity equation must be satisfied at this boundary. For the continuous normal stress condition, a further assumption for air is made to only retain the pressure contribution to the normal stress equation, since the viscous stress contribution is small for air compared with the corresponding terms for the liquid.

These four equations in nondimensional form are:

1. *Continuity equation*

$$\eta_{j,i} \frac{\partial u_{3i}}{\partial z_j} = 0 \quad (16)$$

2. *Zero tangential shear stress (two equations)*

$$\frac{\partial U_n}{\partial \tau_1} + \frac{\partial U_\tau}{\partial n} + U_\tau \kappa_1 = 0 \quad (17)$$

$$\frac{\partial U_n}{\partial \tau_2} + \frac{\partial U_\tau}{\partial n} + U_\tau \kappa_2 = 0 \quad (18)$$

3. *Continuous normal shear stress*

$$p - \frac{2}{Re} \frac{\partial U_n}{\partial n} - \frac{1}{We} \kappa = 0 \quad (19)$$

where n , τ_1 and τ_2 denote distances normal to the free surface and along the 1st and 2nd tangential directions at the free surface respectively. U_n , U_{τ_1} and U_{τ_2} denote velocity components along the \vec{n} , $\vec{\tau}_1$ and $\vec{\tau}_2$ directions, respectively, at the free surface. The κ_1 , κ_2 and κ denote *local* curvature terms and We is the Weber number defined as

$$We = \frac{\rho V_{ref}^2 L_{ref}}{\Gamma}$$

where Γ is the surface tension coefficient. The detailed derivation of the above quantities can be found in Chen¹⁸.

Finally, the additional unknown, i.e., free surface position, is determined from the kinematic equation which is derived from the Lagrangian point of view²⁰. Basically, it represents the fact that fluid particles which lie on the free surface must remain on it. Letting F be the free surface height which is a function of time, and the x_{31} and x_{32} coordinates, the condition that a particle on the free surface must remain on the free surface can be written as:

$$\frac{D}{Dt_2} \{F(x_{31}, x_{32}, t_3) - x_{33}\} = 0$$

Using the chain rule to express this in terms of the generalized nonorthogonal coordinates gives the following representation for the free surface kinematic condition:

$$\begin{aligned} \frac{\partial F}{\partial \tau} &= \{u_{33} + f_{3k}x_{3k}\} \\ &\quad - \{\dot{z}_1 + (u_{31} + f_{1k}x_{3k})\eta_{1,1} + (u_{32} + f_{2k}x_{3k})\eta_{1,2}\} \frac{\partial F}{\partial z_1} \\ &\quad - \{\dot{z}_2 + (u_{31} + f_{1k}x_{3k})\eta_{2,1} + (u_{32} + f_{2k}x_{3k})\eta_{2,2}\} \frac{\partial F}{\partial z_2} \end{aligned} \quad (20)$$

In the above equation, the free surface coincides with the $z_3 = \text{constant}$ surface (see Fig. 3).

The free surface kinematic equation, Eq. (20), was used to explicitly establish a new free surface position after the flow solution for the entire domain was obtained. Central differences were used to represent the spatial derivative terms in Eq. (20). Equation (20) is only valid for the interior points. At the edge of the free surface, i.e., $i = 1, i_{max}$, $j = j_{max}$ and $k = k_{max}$, the second-order Lagrangian extrapolation formula was used in the physical domain in the z_2 (radial) direction to obtain the free surface positions for all θ directions from the free surface position at the interior points.

The implementation of the boundary "equations" discussed in this section is not trivial and can be seen in detail in Chen¹⁸. Also, there were several types of singularities in this coordinate system (see Fig. 3) where special treatment was necessary^{18,19}.

Numerical Solution Algorithm

The artificial compressibility method

The final governing equations, Eqs. (13) and (14) together with the boundary equations at the wall and at the free surface, Eqs. (16) to (19), close the system of equations once the free surface position is updated by the kinematic equation, Eq. (20). In this study, a form of the artificial compressibility method (first proposed by Chorin¹¹) was used to solve these equations. The four unknowns, u_{3i} and p , are obtained simultaneously by this procedure.

The first step is to add an artificial time derivative of pressure, $\partial p / \partial \tau^*$, to the continuity equation. This artificial pressure term not only provides a linkage between the time variation of pressure and the divergence of the velocity, but also ensures that the coupled system is nonsingular if central differences are used in the continuity equation. The final equations become:

$$\frac{\partial p}{\partial \tau^*} + \eta_{j,i} \frac{\partial u_{3i}}{\partial z_j} = 0 \quad (21)$$

and

$$\begin{aligned} \frac{\partial u_{3n}}{\partial \tau} + (\dot{z}_j + \eta_{j,i} u_{3i} + \eta_{j,i} f_{ik} x_{3k}) \frac{\partial u_{3n}}{\partial z_j} - (f_{ni} + 2\lambda_{ni}) u_{3i} + \eta_{j,n} \frac{\partial p}{\partial z_j} \\ - \frac{1}{Re} (\eta_{j,i} \eta_{k,i} \frac{\partial^2 u_{3n}}{\partial z_j \partial z_k} + \eta_{k,ii} \frac{\partial u_{3n}}{\partial z_k}) = \tau_{1,ni} x_{3i} + \tau_{2,ni} h_i - g_{3n} + E_n \end{aligned} \quad (22)$$

where τ^* is a pseudotime. Note that this pseudotime is also added to the free surface continuity equation, Eq. (16).

It is important to add this artificial time term to the continuity equation after the generalized coordinate transformation is applied instead of before if the grid is moving in time. Pan and Chakravarthy⁵ have pointed out that for a moving grid system the divergence of the velocity would not be zero if this term was added before the generalized coordinate transformation even in steady state calculations.

Discretization of the equations

The discretization will be described for the form of the equations given by Eq. (22). A first-order forward difference was used for the time terms. Central differences were used for the spatial derivative terms in the equations. All metric terms of the transformation were evaluated by second-order central differences satisfying the geometric conservation law²¹. The grid speed terms were evaluated by a first-order forward difference. All nonlinear terms were linearized by a Newton method²². The representation for the nonlinear convective term is illustrated as:

$$(u_{3i} \frac{\partial u_{3n}}{\partial z_j})^{n+1} \simeq (\bar{u}_{3i})^{n+1} (\frac{\partial u_{3n}}{\partial z_j})^{n+1} + (\frac{\partial \bar{u}_{3n}}{\partial z_j})^{n+1} (u_{3i})^{n+1} - (\bar{u}_{3i} \frac{\partial \bar{u}_{3n}}{\partial z_j})^{n+1} \quad (23)$$

where $(\bar{u}_{3i})^{n+1}$ and $(\frac{\partial \bar{u}_{3n}}{\partial z_j})^{n+1}$ are the values from the previous iteration level of the current time level, $n + 1$. The linearization error was effectively removed by doing subiterations at each time level. After linearization, the four variables, u_{3i} and p , appear in all the equations and the resulting system of equations takes the following form:

$$A_{i,j,k}^b \vec{q}_{i,j,k-1} + A_{i,j,k}^s \vec{q}_{i,j-1,k} + A_{i,j,k}^w \vec{q}_{i-1,j,k} + A_{i,j,k}^p \vec{q}_{i,j,k} \\ + A_{i,j,k}^e \vec{q}_{i+1,j,k} + A_{i,j,k}^n \vec{q}_{i,j+1,k} + A_{i,j,k}^t \vec{q}_{i,j,k+1} = \vec{b}_{i,j,k} \quad (24)$$

which can be rewritten in vector form as:

$$[A] \vec{q} = \vec{b} \quad (25)$$

where the coefficients A^b to A^t are 4×4 matrices and \vec{q} is the vector of unknowns (dependent variables), $(u_{3i}, p)^T$, and \vec{b} is the RHS vector. The difference molecule can be seen in Fig. 4. The A's are the coefficient matrices for the unknowns at the positions indicated in the figures. The resulting algebraic system of equations, Eq. (25), coupled with the boundary equations was solved by the CSIP method which will be described below.

Coupled strongly implicit procedure

Following Stone¹⁵, a general iterative formula for Eq. (25) may be obtained by adding an auxiliary matrix $[P]$ to each side of Eq. (25) and adding iteration numbers to \vec{q} as:

$$[A + P] \vec{q}^{n+1,k+1} = [P] \vec{q}^{n+1,k} + \vec{b} \quad (26)$$

where n is the time level and k is the iteration level. In the Stone's SIP method^{15,16}, $[P]$ is chosen that $[A + P]$ can be decomposed as:

$$[A + P] = [L][U] \quad (27)$$

where $[L]$ and $[U]$ are, respectively, lower and upper triangular matrices, each of which has only four nonzero elements for the three-dimensional 7-point formula in each row. A partial cancellation parameter was introduced to reduce the influence of this extra $[P]$ matrix by a Taylor series expansion (see details in Stone^{15,16}). After $[L]$ and $[U]$ are obtained, the following procedure is used to obtain the unknown vector \vec{q} .

Letting $\vec{\delta}^{n+1,k+1} = \vec{q}^{n+1,k+1} - \vec{q}^{n+1,k}$ and a residual vector $\vec{R}^{n+1,k} = \vec{b} - [A]\vec{q}^{n+1,k}$, Eq. (26) can be written as

$$[L][U]\vec{\delta}^{n+1,k+1} = \vec{R}^{n+1,k} \quad (28)$$

Defining a provisional vector \vec{W} by $\vec{W}^{n+1,k+1} = [U]\vec{\delta}^{n+1,k+1}$, the solution procedure can be written in two steps:

Step 1:

$$[L]\vec{W}^{n+1,k+1} = \vec{R}^{n+1,k} \quad (29)$$

Step 2:

$$[U]\vec{\delta}^{n+1,k+1} = \vec{W}^{n+1,k+1} \quad (30)$$

The process represented by Eqs. (29) and (30) consists of a forward substitution to determine $\vec{W}^{n+1,k+1}$ followed by a backward substitution to obtain $\vec{\delta}^{n+1,k+1}$. The coefficient matrix $[A]$, and so the $[L]$ and $[U]$ matrices, need to be updated at each iteration since they contain unknowns due to the linearization procedure.

In the artificial compressibility method, the time term in the continuity equation is artificial (in pseudotime) even for time accurate calculations. It was found that convergence was enhanced by using a *local* pseudotime. This local pseudotime was determined based on the following criterion:

$$(\Delta\tau^*)_{i,j,k} \simeq \frac{\sigma}{\sum |\lambda_{i,j,k}|} \quad (31)$$

where $\lambda_{i,j,k}$ are the off-diagonal coefficient terms in the continuity equation and the summation is over the six neighboring points at each i, j, k location. The $\Delta\tau^*$ is a local value and varies in space. The σ is a constant to further control the time step. The choice of σ is problem-dependent. Usually a value of the order of one will give satisfactory results.

The convergence at each physical time step was based on the maximum value of the divergence of the velocity field. For the results presented here, this criterion is

$$|\nabla \cdot \vec{V}| = |\eta_{j,i} \frac{\partial u_{3i}}{\partial z_j}| \leq 5 \times 10^{-4} \quad (32)$$

The solution procedure for the three-dimensional liquid sloshing flow calculations can be summarized as follows:

1. Set initial conditions.
2. Update the free surface position at each time step by the kinematic equation based on the flow solution at the previous time step.
3. Generate the grid under the new free surface position.
4. Construct the coefficient matrix $[A]$ and the right-hand-side vector \vec{b} .
5. Call the CSIP solver to update solution (u_{3i}, p) ; go back to step 4 and subiterate (until convergence) to create a divergence-free field at each time step.
6. Go back to step 2 and move to the next time step.

Results and Discussion

Before solving the more complicated three-dimensional unsteady liquid sloshing problems, the present algorithm was evaluated by solving the 3-D driven cavity problem for a Reynolds number of 100. The steady state results were compared against the data in the literature and satisfactory agreement was observed¹⁸. Several cases for which the steady state solution is known analytically will be discussed in the following sections.

Axisymmetric spin-up

Three axisymmetric spin-up problems were studied. For this type of spin-up, the tank rotates with respect to its own axis of symmetry ($h_i=0$). Due to the symmetry of this problem, the solution should be independent of position in the circumferential direction. This provides one easy check on the validity of the code. As the spinning is initiated, the liquid and free surface begin to

move relative to the container and eventually reach a steady-state equilibrium condition in which solid-body rotation prevails. Computations were made for three different types of spin-up, all for normal earth gravitational acceleration. The three types of spin-up are described as follows:

1. **Initially capped spin-up:** Initially, the spherical container half-filled with a liquid has been spun about a specified rotation axis in a constant rotational speed and has reached a solid-body rotation. A cap covers the liquid surface to prevent it from rising up. At time zero, the cap is suddenly removed (or broken) and the liquid surface starts to rise (or drop) until another equilibrium position is reached. The initial absolute velocity is distributed according to the condition of the solid-body rotation. This case was computed for two values of Reynolds number.
2. **Gradual spin-up:** At time zero, the spherical container half-filled with a liquid gradually starts to rotate with the rotational speed from zero to a desired constant value about a specified rotation axis. The initial absolute velocity is zero everywhere.
3. **Impulsive spin-up:** At time zero, the spherical container half-filled with a liquid impulsively starts to rotate with a constant rotational speed about a specified rotation axis (the axis of symmetry of the container, for the axisymmetric spin-up case). The initial absolute velocity is zero everywhere except at the wall of the container.

For the same rotational speed of 60 rpm, the spin-up phenomena were found to be quite different for these three spin-up types. Results for these three axisymmetric spin-up cases are given below.

Initially capped spin-up This case was computed for two Reynolds numbers, $Re=21.9$ and 2254.7 , where the Reynolds number is based on the radius of the sphere and a reference velocity equal to the radius times the rotational speed in radians per second. These two Reynolds numbers can be achieved through the rotation of a sphere 6.4 cm in radius at 60 rpm using glycerin and kerosene as the fluids, so the two cases will be referred to as the glycerin and kerosene cases. Other characteristic dimensionless parameters of the problem include the Froude and Weber numbers. The Weber number has been defined previously. The Froude number is $Fr=V_{ref}/\sqrt{gh}$, where V_{ref} is the same as used in the Reynolds number, h is the initial maximum free surface depth and g is the acceleration of gravity. The Froude number was 0.51 for both of these initially capped

cases. For the $Re=21.9$ case, $We=207.6$ and for $Re=2254.7$, $We=284.9$. The capped spherical container was initially spun about its axis of symmetry at a constant rotational speed until solid body rotation prevailed in the liquid. Since the liquid surface was covered by a cap, there was no free surface motion at all. The initial absolute velocity distribution is as follows:

$$V_r = 0 \quad V_\theta = r\omega \quad V_z = 0$$

where V_r is the velocity component in the radial direction, V_θ is the velocity component in the circumferential direction, V_z is the velocity component in the direction normal to the previous two directions, r is the distance in the radial direction away from the line of symmetry and ω is the rotational speed (60 rpm) (w.r.t. x_{23} axis). It should be noted that the governing equations were expressed in terms of the relative velocity (relative to the final solid-body rotation) and therefore $u_{3i}=0$ was actually used as the initial condition for velocities.

At time zero, the cap is suddenly removed (or broken) and the free surface starts to rise, from its initial position, near the wall of the container and drop near at the center of the free surface in response to the sudden change of the pressure field. Some selected velocity vector plots illustrating the general flow pattern at different times are shown in Fig. 5. The results shown are in the $x_{22} = 0$ plane. The time shown on the figures has been nondimensionalized using a characteristic time based on the radius of the container and the rotational speed at the wall. The dotted lines inserted in Fig. 5 indicate the analytical steady state equilibrium (relative to the x_2 frame) free surface position. The analytical steady state equilibrium free surface solutions were derived by the present authors and are listed in Chen¹⁸. The velocities are largest near the free surface and significantly smaller near the bottom of the container. As time continues, the fluid eventually passes (or overshoots) the equilibrium position. By time $\tau = 1.62$, the magnitude of the flow has been reduced and the flow pattern has begun to reverse itself. This can be seen in Fig. 5b and more clearly in Fig. 5c. This flow continues to oscillate about the equilibrium position but damps very quickly until the new equilibrium position is reached at about $\tau = 15.96$ in Fig. 5d (see also Fig. 6). It should be noted that the magnitude of the velocities in Fig. 5d has become very small as the final solid-body rotation is approached. The velocities shown here are relative to the solid-body rotation expected at steady state, as pointed out in a previous section. The steady-state numerical free surface position matches exceptionally well with the analytical solution.

To permit a more detailed analysis of the flow pattern under this spin-up condition, the time

histories of the free surface positions at the wall of the container and at the center of the free surface and the x_{23} component of the velocity were recorded for three different grids, i.e., $11 \times 11 \times 11$, $21 \times 11 \times 21$, $31 \times 11 \times 31$. Figure 6 shows the free surface position at the wall and at the center of the free surface for glycerin during the spin-up process. The free surface position can be seen to oscillate about the equilibrium position. This oscillation is damped out quickly by the viscosity of the fluid. Figure 7 illustrates the same phenomena but shows the time evolution of the component of the velocity normal (x_{23} component) to the free surface at the center of the container. The grid refinement study indicated in Figs. 6 and 7 shows that the unsteady free surface positions and velocity were relatively insensitive to the grid distribution in the circumferential and height (vertical) directions. It is well known that for viscous free surface flow simulations, there exists an extremely thin boundary layer (or singularity) near the liquid-gas-solid contact line. In our grid refinement study, the effect of this singularity tended to become more evident and eventually caused the numerical calculations to break down as the grid spacing in the radial direction was refined.

For this spin-up problem, the number of subiterations at the first time step was about 50 but then quickly dropped to less than 10 after 20 time steps and finally became 1 as the solution approached the final steady state. It took about 2 hours CPU time on the Apollo DN 10,000 workstation for the course grid case. A nondimensional time step of 0.015 was used throughout the calculation.

The initially capped spin-up calculations were repeated for a Reynolds number of 2254.7. This was achieved by keeping all rotation parameters the same and decreasing the kinematic viscosity of the fluid by a factor of about 100 to a value corresponding to the viscosity of kerosene. The final analytical equilibrium free surface position is then expected to be the same as for the glycerin case. With this less viscous fluid, the flow pattern was found quite similar to the previous case and will not be repeated here; however several interesting results deserve further discussion.

Figure 8 indicates the variation of the free surface position at the wall and tank center as a function of nondimensional time during the spin-up process for kerosene. Since the viscosity of kerosene is a factor of 100 less than that of glycerin, the free surface oscillations appear to damp out much more slowly than was observed for glycerin. This behavior is believed to be real although no experimental data had been found to date to clarify this point. The final computed steady state position of the free surface agrees reasonably well with the analytical solution. Figure

9 shows the computed velocity component normal to the free surface at the center of the container as a function of time. Slowly damped oscillatory motion is evident. The spin-up with kerosene took about four times longer than that with glycerin to reach final steady state solid-body rotation (Both cases had the same reference time and this was estimated from the plots shown previously).

The kerosene calculations were made with the same grid as used to obtain the glycerin results. During the course of early computations, it was found that the free surface developed a saw-toothed profile of small amplitude in the radial direction which appeared to slow convergence at each time step. The saw-toothed profile might have been due to the use of central differences in the spatial derivative terms in the kinematic equation at the higher Reynolds number. If the use of central differences at high Reynolds numbers was the source of the problem, it could have been remedied by the use of a finer grid which, of course, would have increased the required computational effort considerably. Instead, a small amount of smoothing was added to remove this undesired profile and stabilize the calculation. The smoothing was of the following form:

$$F^{new} = F^{old} + s \left(\frac{\partial^2 F^{old}}{\partial z_2^2} \right) \quad (33)$$

where s is the smoothing parameter, F is the free surface height function (see free surface kinematic equation) and z_2 is the radial direction. A value of $s = 9 \times 10^{-3}$ was used for this case. The second derivative in the expression above was represented, of course, in difference form. It should be noted that the use of the smoothing of the free surface height function, F , for this calculation resulted in less than 1% loss of the initial total volume. Although this discrepancy may be considered insignificant for most purposes, ways of avoiding this loss deserve further study in the future.

Gradual spin-up; liquid: glycerin As mentioned before, the high frequency free surface oscillations were possibly due to natural overshoots arising from the sudden removal of the cap during the spin-up process. To further understand this phenomenon, a third test for this configuration was conducted for glycerin again in the following way. The container was spun up with the rotational speed being gradually increased from 0 to 60 rpm by a sine function of time during the nondimensional time interval from zero to five. This rotational speed was specified as:

$$\omega = 30(\sin \theta + 1) \text{ rpm}, \quad \text{for } 0 \leq \tau \leq 5$$

$$\text{where } \theta = \frac{\pi}{5}\tau - \frac{\pi}{2}$$

and

$$\omega = 60 \text{ rpm,} \quad \text{for } \tau > 5$$

Figure 10 indicates the variation of the free surface position at the wall and tank center as a function of nondimensional time during the gradual spin-up process. The oscillatory phenomena in Fig. 6 disappeared and instead, a nonoscillatory ramp-up of the free surface at the wall and drop at the tank center was observed. The final steady state free surface positions agree very well the analytical solution.

Impulsive spin-up; liquid: glycerin At time zero, the spherical container half-filled with glycerin impulsively starts to rotate about its axis of symmetry. The initial absolute velocity was zero everywhere except at the wall of the container at which a rotational speed of 60 rpm was suddenly applied. Due to the use of the relative velocity in the formulation, a negative distribution of the solid-body rotation velocity was specified everywhere initially except at the wall where a zero relative velocity was specified. A $11 \times 11 \times 11$ grid was used again for this case. The free surface positions at the wall of the container and at the center of the free surface are shown in Fig. 11. No free surface overshoots were observed in this case. Being spun up impulsively, the flow reached the final steady state equilibrium position earlier than for the previous gradual spin-up case.

Asymmetric spin-up

When the rotation arm, h_i , is nonzero, the solutions will no longer be symmetric. A schematic diagram for this type of spin-up is shown in Fig. 12. This case belongs to the initially capped spin-up type as explained in the previous section. The same container as before was half filled again with glycerin. It was initially covered by a cap and rotated in an orbit with a constant rotational speed under the condition of solid-body rotation. At time zero, the cap was removed to allow the liquid surface to move under this spinning condition. The rotational speed was 30 rpm and the rotational arm, h_1 (x_{21} component of h_i), was 12.8 cm which was twice of the radius of the container. Based on the above physical quantities, the characteristic nondimensional parameters are:

$$Re = 21.9 \quad Fr = 0.51 \quad We = 207.6$$

where the reference velocity, V_{ref} , was based on the rotational speed of the center of the container, i.e., $V_{ref} = \omega h_1$.

A $41 \times 11 \times 11$ grid was used to compute this case with the 41 points being placed in the circumferential direction. A constant nondimensional time step of 0.01 was used for this calculation. At the first time step, 170 subiterations were required for convergence, but the number of subiterations required dropped rapidly and varied between 10 and 15 for most of the calculation. Compared with the previous axisymmetric cases, this calculation was more difficult in two respects. First, the free surface was asymmetric and more grid points were required to resolve the solution in the circumferential direction. The solution would sometimes diverge suddenly if the resolution of the grid was not fine enough or if the grid distribution after the grid adaptation procedure contained a locally steep slope. Second, more computational effort was required to obtain the solution at each time step.

In this calculation, the value of ϕ_r in the free surface tracking coordinates was no longer zero. Therefore, the present test case also served as a check for this transformation. For this case, the computation was carried out until the final solid-body steady state solutions were obtained.

In Fig. 13 a series of results showing the free surface position at different instants of time are presented. The centrifugal force is larger at the right hand side (RHS) (far away from the spin axis) of the tank in Fig. 13 than at the left hand side (LHS) (closer to the spin axis). In response to this sudden change, the free surface begins to rise at the RHS and to depress at the LHS from its initial position, becoming curved as can be seen in Figs. 13d-13f and finally assumes a parabolic equilibrium shape at about $\tau = 7.2$.

Some selected velocity vector plots for different times in the $x_{22}=0$ plane are shown in Fig. 14 with the analytical equilibrium free surface position¹⁸ superimposed. The largest velocity vectors occurred near the free surface. The computation was carried out until the nondimensional time equaled 7.2 at which time solid-body rotation prevailed. The final free surface position can be seen to agree fairly well with the analytical solution.

Again, the numerical steady state free surface positions at the wall of the container were plotted against the analytical solution. Figure 15 shows the time evolution of the free surface position at the wall for positions of 0 (LHS) and 180 (RHS) degrees (see also Fig. 12). This plot indicates the free surface rise at the RHS and drop at the LHS from its initial position (equal to zero for

half full container). The small discrepancy between the current numerical solution for the free surface position and the analytical solution is probably due to the relatively coarse grid used in this calculation. Further studies with a finer grid may help to resolve this discrepancy. This calculation took about 22 hours of CPU time on the Apollo DN 10,000 workstation.

Conclusions

A coupled strongly implicit solution strategy for unsteady three-dimensional free surface flows has been developed based on an artificial compressibility formulation for the Navier-Stokes equations. A pseudotime term has been used in the continuity equation to permit time accurate calculations to be achieved. The scheme appears capable of tracking the free surface reasonably accurately although further verification of the procedure is desirable. An algebraic procedure for adjusting the grid between time steps has proven to be adequate. Five different free surface calculations have been reported. The initially capped cases exhibited an interesting Reynolds number dependent oscillatory behavior which is believed to be physical although no experimental results appear to be available for verification to date.

Acknowledgments

This research was supported by the Air Force Office of Scientific Research through Grant No. AFOSR-89-0403.

References

1. Peterson, L. D., Crawley, E. F. and Hansman, R. J., "Nonlinear Fluid Slosh Coupled to the Dynamics of a Spacecraft," *AIAA Journal*, Vol. 27, No. 9, 1989, pp. 1230-1240.
2. Kana, D. D., "Validated Spherical Pendulum Model for Rotary Liquid Slosh," *Journal of Spacecraft and Rockets*, Vol. 26, No. 3, 1989, pp. 188-195.
3. Van Schoor M. C., Peterson, L. D. and Crawley, E. F., "The Coupled Nonlinear Dynamic Characteristics of Contained Fluids in Zero Gravity," AIAA paper 90-0996-CP, 1990.
4. Vaughn, H. R., Oberkampf, W. L. and Wolfe W. P., "Fluid Motion Inside a Spinning Nutating Cylinder," *Journal of Fluid Mechanics*, Vol. 150, Jan. 1985, pp. 121-138.
5. Chakravarthy, S. R., "Numerical Simulation of Laminar, Incompressible Flow within Liquid filled Shells," US Army Research and Development Command, Ballistic Research Laboratory, Contract Report ARBRL-CR-00491, 1982.
6. Kassinos, A. C. and Prusa, J. M., "A Numerical Model for 3-D Viscous Sloshing in Moving Containers," *Proceedings of the ASME Winter Annual Meeting*, Symposium on Recent Advances and Application in CFD, 1990, pp. 75-86.
7. Hirt, C. W. and Nichols, B. D., "Volume of Fluid (VOF) Method for the Dynamics of Free Boundaries," *Journal of Computational Physics*, Vol. 39, No. 1, 1981, pp. 201-225.
8. Holler, H. and Ranov, T., "Unsteady Rotating Flow in a Cylinder with a Free Surface," ASME Paper 68-FE-13, 1968.
9. Miyata H., "Finite-Difference Simulation of Breaking Waves," *Journal of Computational Physics*, Vol. 65, No. 1, 1986, pp. 179-214.
10. Miyata H., Sato T. and Baba N., "Difference Solution of a Viscous Flow with Free-Surface Wave about an Advancing Ship," *Journal of Computational Physics*, Vol. 72, No. 2, 1987, pp. 393-421.
11. Chorin, A. J., "A Numerical Method for Solving Incompressible Viscous Flows Problems," *Journal of Computational Physics*, Vol. 2, No. 1, 1967, pp. 12-26.
12. Rogers, S. E. and Kwak, D., "An Upwind Differencing Schemes for the Time-Accurate Incompressible Navier-Stokes Equations," AIAA paper 88-2583, 1988.

13. Merkle, C. L. and Athavale, M., "Time-Accurate Unsteady Incompressible Flow Algorithm Based on Artificial Compressibility," AIAA paper 87-1137, 1987.
14. Pan, D. and Chakravarthy S., "Unified Formulation for Incompressible Flows," AIAA paper 89-0122, 1989.
15. Stone, H. L., "Iterative Solution of Implicit Approximations of Multi-dimensional Partial Differential Equations," *SIAM Journal of Numerical Analysis*, Vol. 5, No. 3, 1968, pp. 530-558.
16. Weinstein, H. G., Stone, H. L. and Kwan, T. V., "Iterative Procedure for Solution of Systems of Parabolic and Elliptic Equations in Three Dimensions," *I & EC Fundamentals*, Vol. 8, No. 2, 1969, pp. 281-287.
17. Chen, K.-H. and Pletcher, R. H., "A Primitive Variable, Strongly Implicit Calculation Procedure for Viscous Flows at All Speeds," *AIAA Journal*, Vol. 29, No. 8, 1991, pp. 1241-1249.
18. Chen, K.-H., A Primitive Variable, Strongly Implicit Calculation Procedure for Two and Three-Dimensional Unsteady Viscous Flows: Applications to Compressible and Incompressible Flows Including Flows with Free Surfaces, Ph.D dissertation, Iowa State University, Ames, Iowa, 1990.
19. Chen, K.-H. and Pletcher, R. H., "Simulation of Three-Dimensional Liquid Sloshing Flows Using a Strongly Implicit Calculation Procedure," AIAA paper 91-1661, 1991.
20. Lamb, H., *Hydrodynamics*, Dover Publications, 1945.
21. Hindmann, R. G., "Generalized Coordinate Forms of Governing Fluid Equations and Associated Geometrically Induced Errors," *AIAA Journal*, Vol. 20, No. 10, 1982, pp. 1359-1367.
22. Anderson, D. A., Tannehill, J. C., and Fletcher, R. H., *Computational Fluid Mechanics and Heat Transfer*, McGraw-Hill Book Co., New York, 1984.

List of figures

- Fig. 1 Schematic of a partially filled rotating-nutating container moving relative to an inertial frame.
- Fig. 2 Notation for the S transformation.
- Fig. 3 Coordinate system for liquid sloshing problem.
- Fig. 4 Three-dimensional computational molecule for $A_{i,j,k}^e$, $A_{i,j,k}^w, \dots, A_{i,j,k}^p$.
- Fig. 5 Selected velocity vector plots at $x_{22}=0$ plane for the axisymmetric initially capped spin-up of a spherical container half-filled with glycerin (The dotted line indicates the steady state analytical free surface position).
- Fig. 6 Time history of the nondimensional free surface height for the axisymmetric initially capped spin-up of a spherical container half-filled with glycerin ($Re=21.9$).
- Fig. 7 Time history of the u_{23} velocity component on the free surface at the center of rotation for the axisymmetric initially capped spin-up of a spherical container half-filled with glycerin ($Re=21.9$).
- Fig. 8 Time history of the nondimensional free surface height for the axisymmetric initially capped spin-up of a spherical container half-filled with kerosene ($Re=2254.7$).
- Fig. 9 Time history of the u_{23} velocity component on the free surface at the center of rotation for the axisymmetric initially capped spin-up of the a spherical container half-filled with kerosene ($Re=2254.7$).
- Fig. 10 Time history of the nondimensional free surface height for the axisymmetric gradual spin-up of a spherical container half-filled with glycerin ($Re=21.9$).
- Fig. 11 Time history of the nondimensional free surface height for the axisymmetric impulsive spin-up of a spherical container half-filled with glycerin ($Re=21.9$).
- Fig. 12 Schematic for asymmetric spin-up; container half-filled with glycerin.
- Fig. 13 Selected free surface plots for the asymmetric initially capped spin-up of a spherical container half-filled with glycerin.
- Fig. 14 Selected velocity vector plots at $x_{22}=0$ plane for the asymmetric initially capped spin-up of a spherical container half-filled with glycerin (The dotted line indicates the steady state analytical free surface position).
- Fig. 15 Time history of the nondimensional free surface height for the asymmetric initially capped spin-up of a spherical container half filled with glycerin.

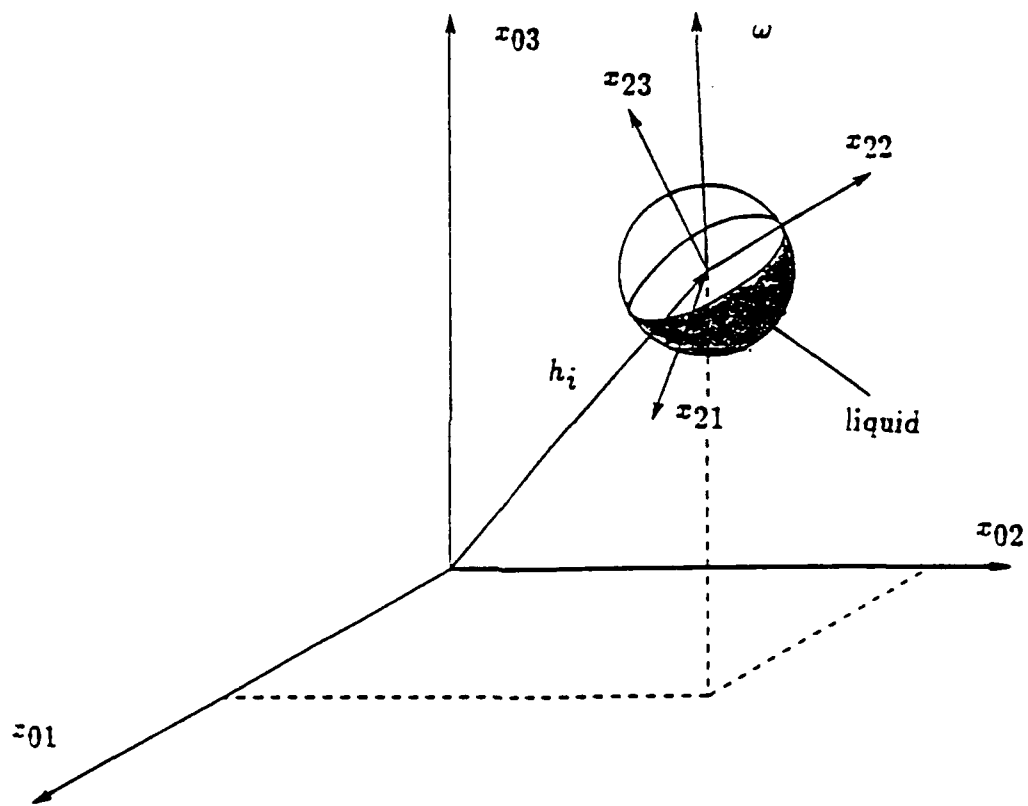


Fig. 1

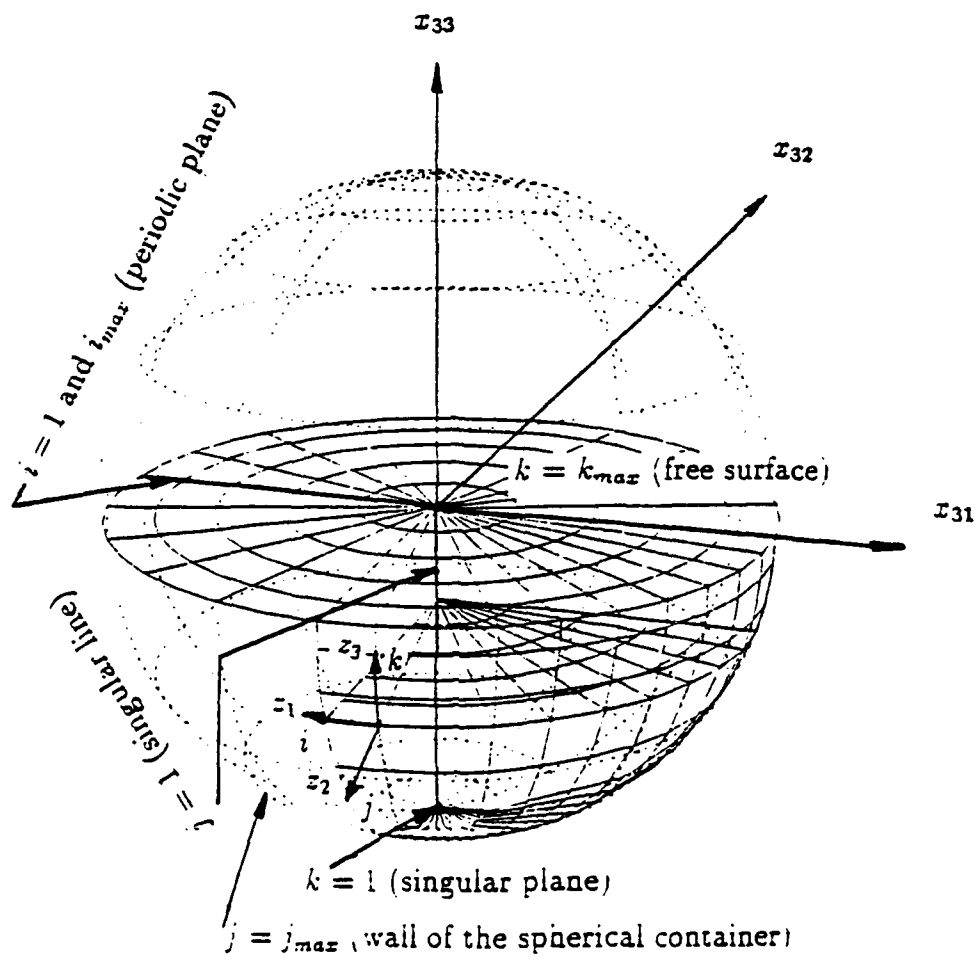


Fig. 3

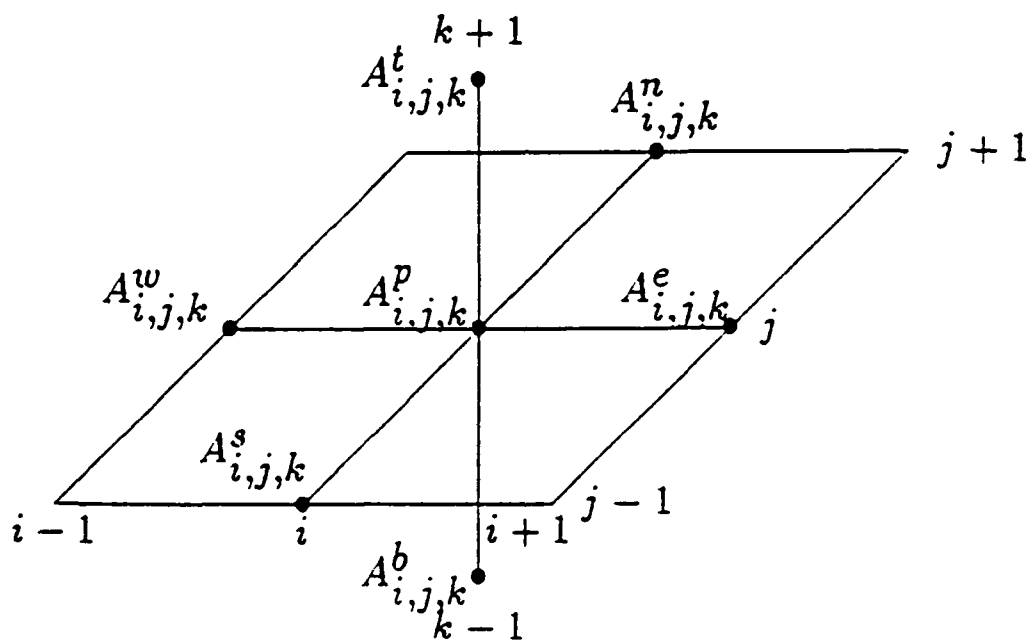


Fig. 4

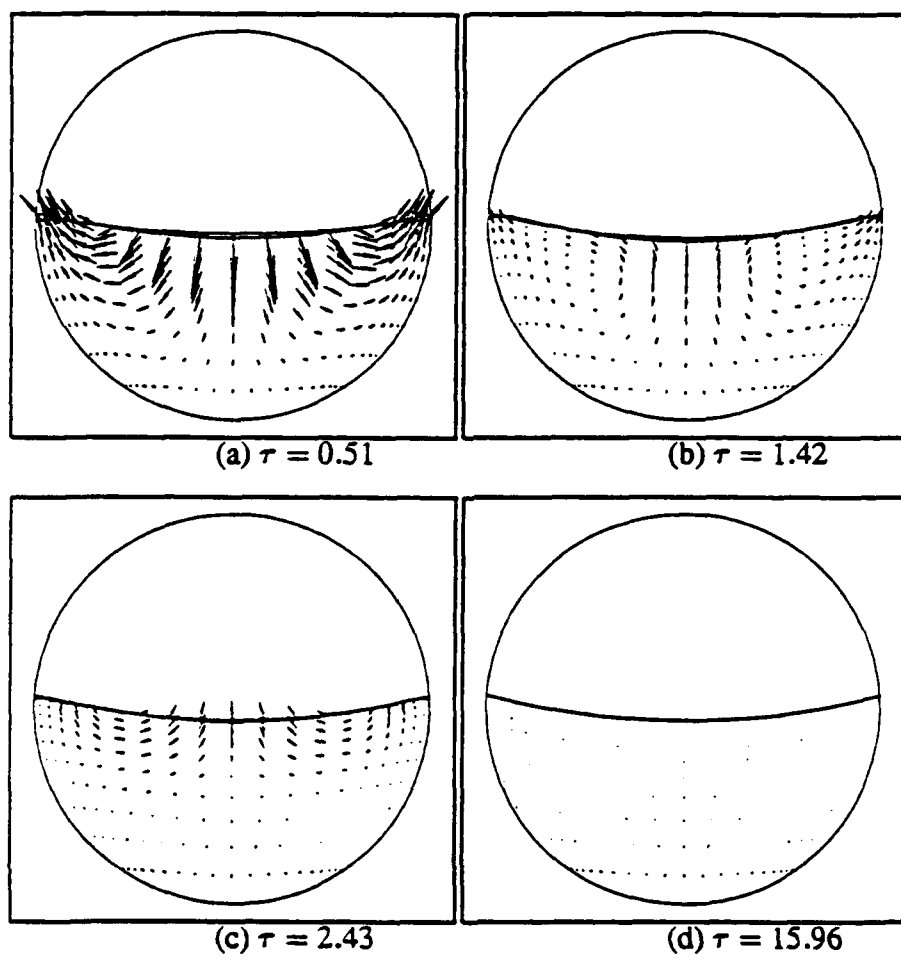


Fig. 5

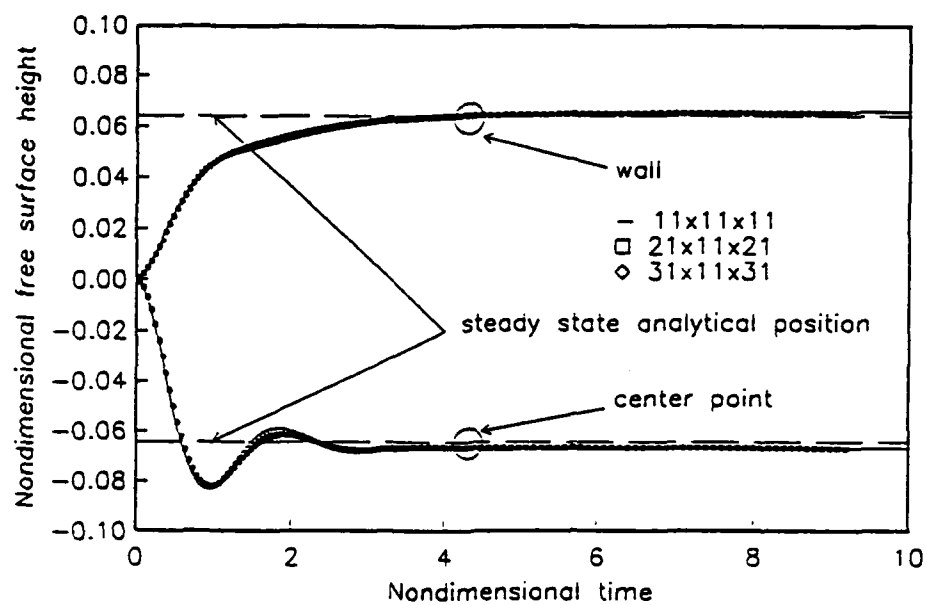


Fig. 6

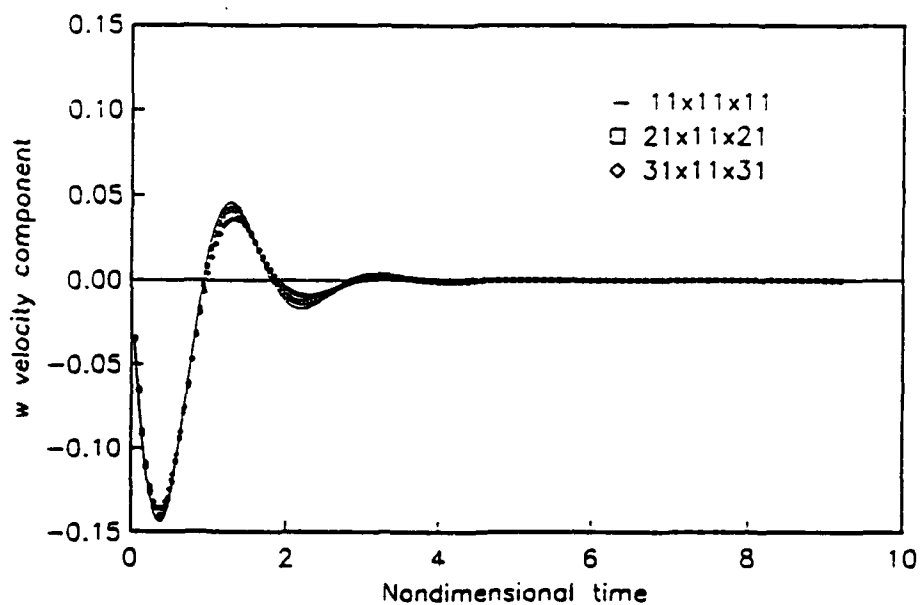


Fig. 7

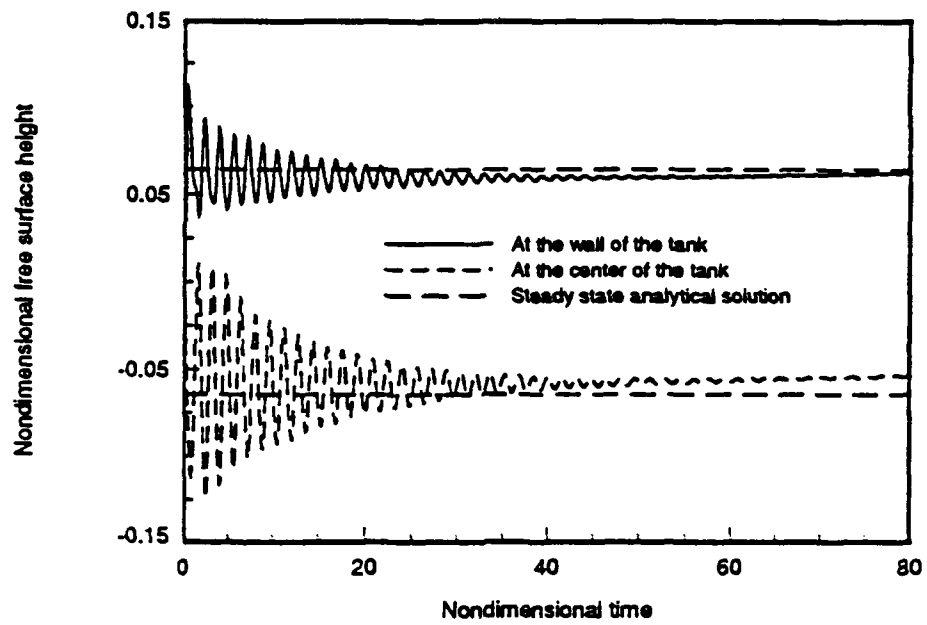


Fig. 8

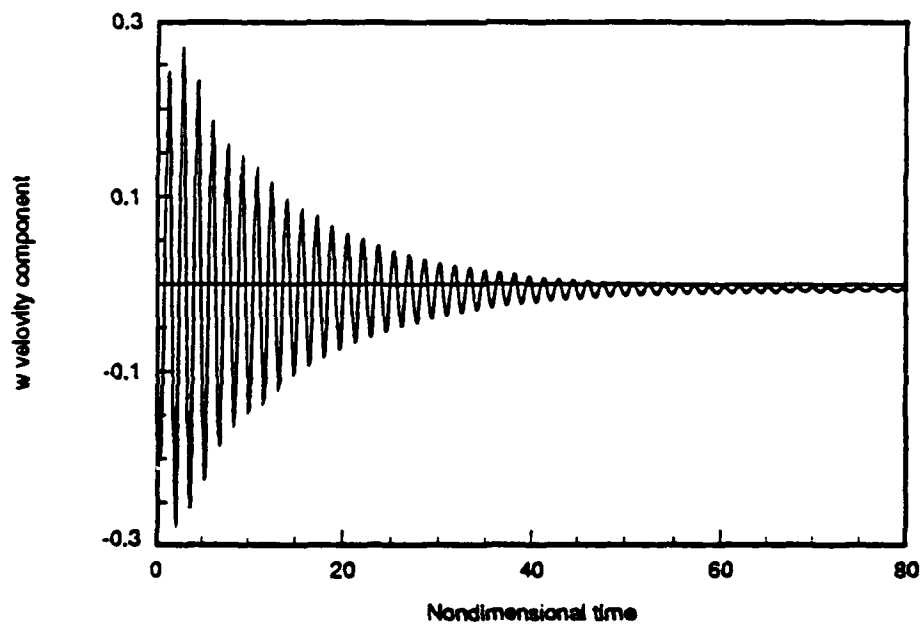


Fig. 9

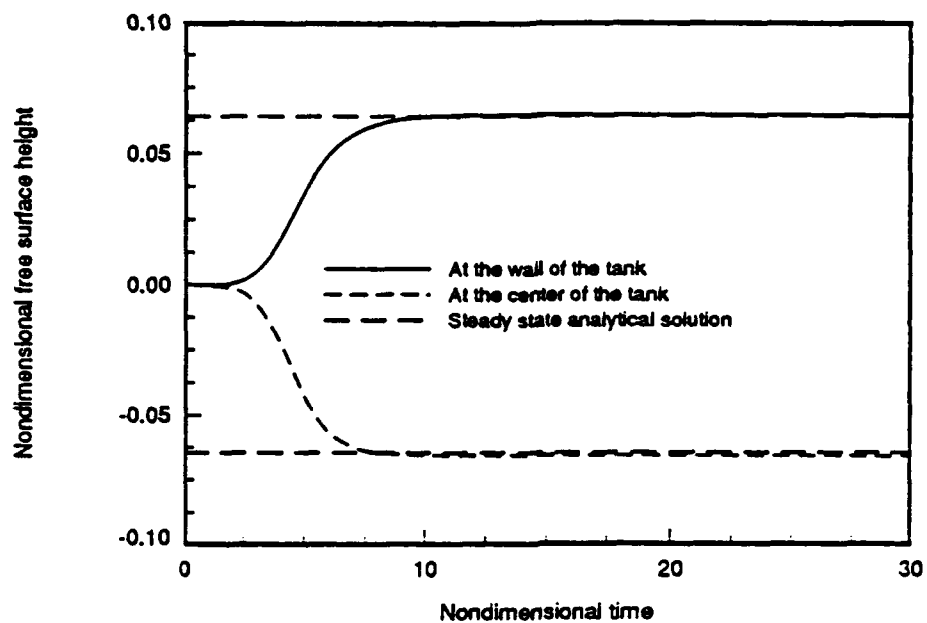


Fig. 10

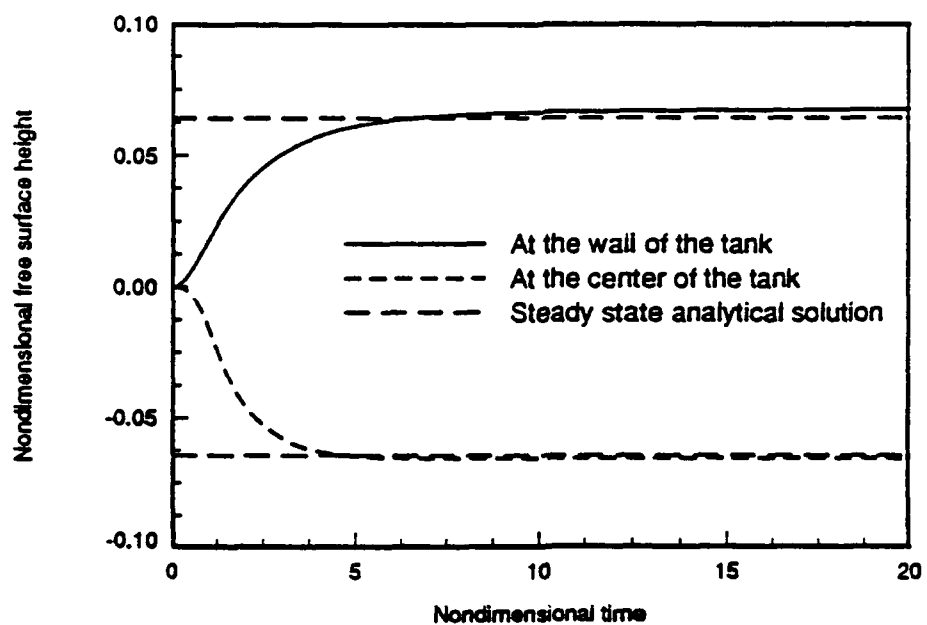


Fig. 11

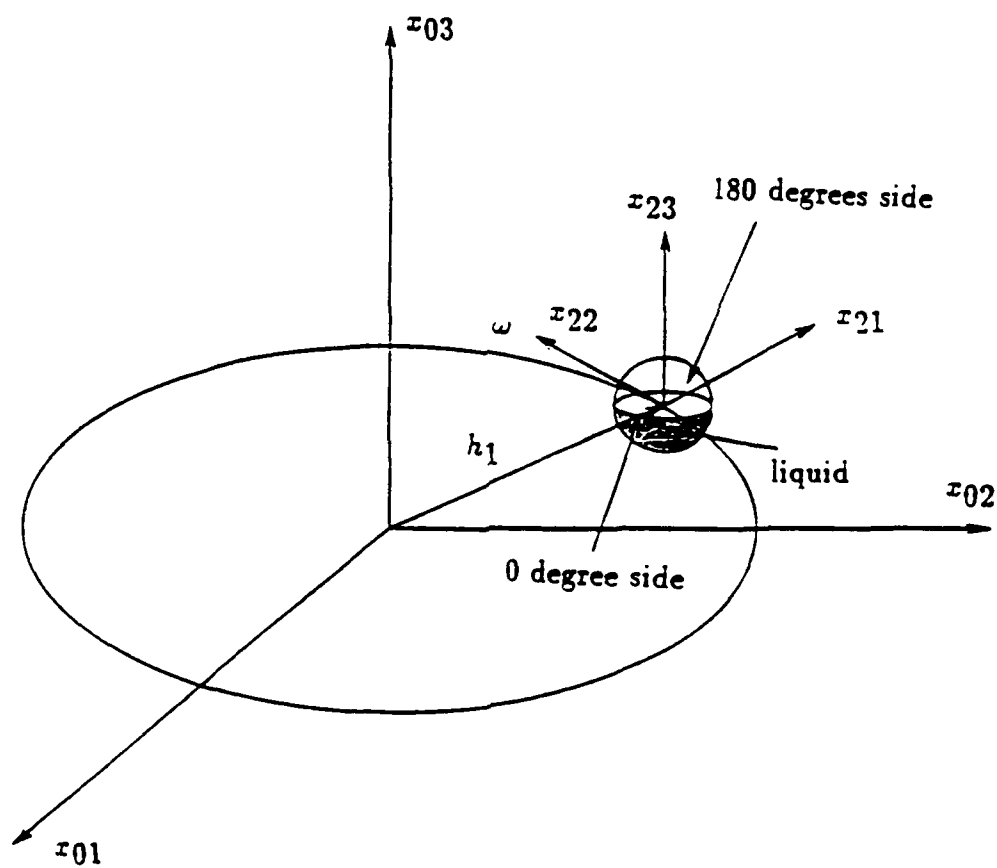


Fig. 12

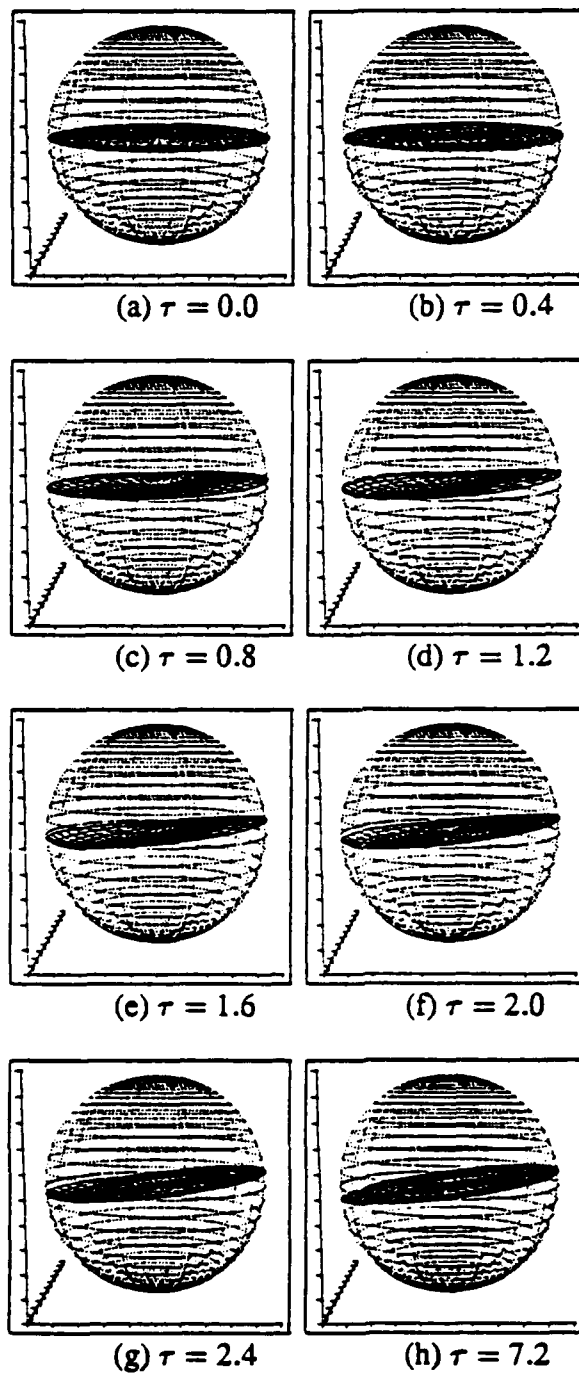


Fig. 13

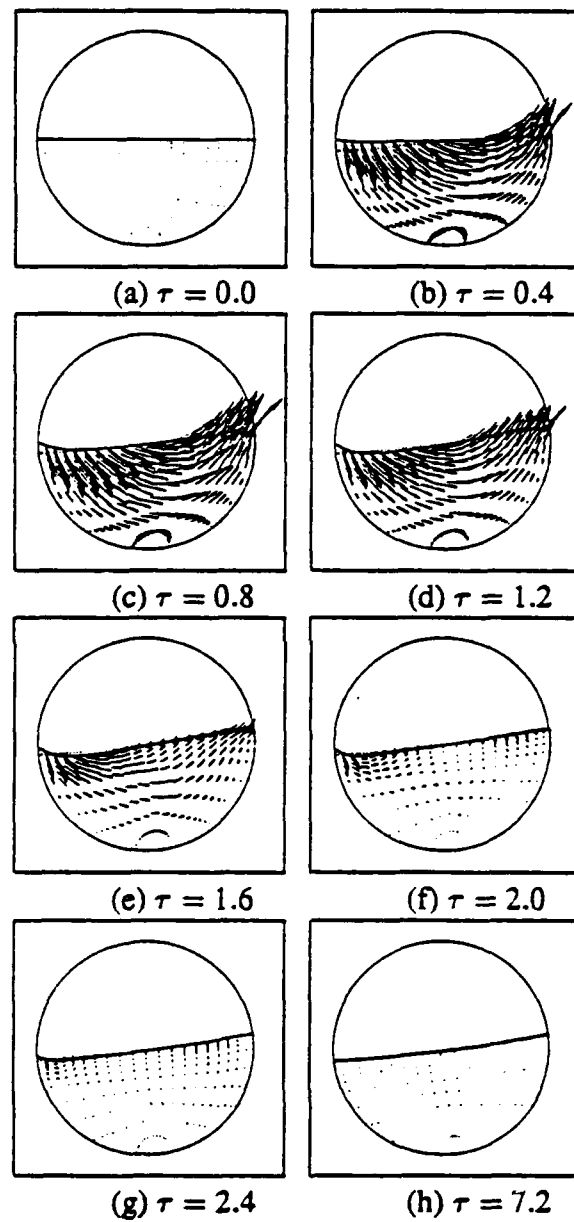


Fig. 14

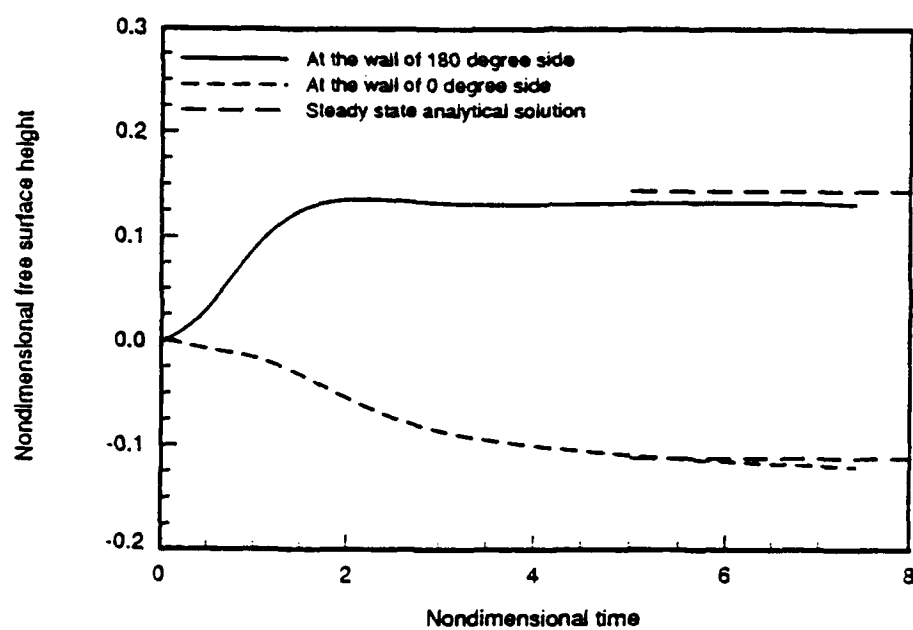


Fig. 15

**APPENDIX I. A Numerical and Experimental Study of
Three-Dimensional Liquid Sloshing in a Rotating Spherical Container.**



AIAA 92-0829

A Numerical and Experimental Study of Three-Dimensional Liquid Sloshing in a Rotating Spherical Container

K.-H. Chen

The University of Toledo

NASA Lewis Research Center, Cleveland, Ohio

and

F. J. Kelecy and R. H. Pletcher

Iowa State University

Ames, Iowa

**30th Aerospace Sciences
Meeting & Exhibit
January 6-9, 1992 / Reno, NV**

A Numerical and Experimental Study of Three-Dimensional Liquid Sloshing in a Rotating Spherical Container

Kuo-Huey Chen*

The University of Toledo/NASA Lewis Research Center, Cleveland, Ohio

and

Franklyn J. Kelecy[†] and Richard H. Fletcher[‡]

Iowa State University, Ames, Iowa 50011

Abstract

A numerical and experimental study of three dimensional liquid sloshing inside a partially-filled spherical container undergoing an orbital rotating motion is described. Solutions of the unsteady, three-dimensional Navier-Stokes equations for the case of a gradual spin-up from rest are compared with experimental data obtained using a rotating test rig fitted with two liquid-filled spherical tanks. Data gathered from several experiments are reduced in terms of a dimensionless free surface height for comparison with transient results from the numerical simulations. The numerical solutions are found to compare favorably with the experimental data.

Introduction

The motion of a sloshing liquid inside a moving container has long been of interest to engineers and researchers. Liquid sloshing arises in many important practical applications, including the design of oil tankers, railroad tank cars, missiles, satellites, and spacecraft^{1,2,3,4,5}. The present study is concerned with sloshing flows inside spherical containers undergoing motions characteristic of spin-stabilized satellites. Previous research⁶ in this area has shown that satellites containing partially-filled liquid stores can exhibit an unstable coning motion shortly after being released in space. This instability is thought to arise from the sloshing force induced by the free surface motion inside the fuel stores themselves.

One of the distinguishing characteristics of sloshing flows is the presence of one or more free surfaces. A free surface, in the present context, is defined as the interface between the liquid and another fluid (usually a gas) which fills the regions not occupied by the fluid. The free surface adds an additional difficulty to the analysis of the fluid motion since its position is usually not known a priori, and thus must be computed as part of the solution.

The motion of the liquid is governed by the three-dimensional, incompressible Navier-Stokes equations. To conveniently analyze the fluid motion, one can employ a coordinate transformation which takes a moving, non-inertial coordinate system in physical space to a non-moving coordinate system in computational space. The free surface is then placed at one boundary of the computational domain (a practice known as "surface fitting"). Both the coordinate transformation and the desire to accommodate arbitrary motions of the container ultimately give rise to a large number of terms in the governing equations⁷. As a result, unsteady

calculations based on this approach require enormous computational resources in order to obtain accurate solutions in both time and space.

A numerical model has been developed by the present authors⁸ for studying complicated three-dimensional liquid sloshing flows in rotating spherical containers. This model employs the coordinate transformation/surface fitting approach described above in conjunction with the artificial compressibility formulation for incompressible flows⁹. The resulting system of discrete equations is solved using a coupled strongly implicit (CSIP) procedure. Some results obtained with this model have been presented in Ref. 8. Although these results appear qualitatively correct, a rigorous assessment of their accuracy has not been made due to the lack of reliable experimental (or other numerical) data.

To date, only a few three-dimensional, transient free surface simulations using the incompressible Navier-Stokes equations have been reported in the open literature. Partom¹⁰ discussed the numerical simulation of three dimensional flow in a partially-filled cylinder. His work employed a three-dimensional extension of the volume of fluid (VOF) method of Hirt and Nichols¹¹. Some results for several cases (both with and without the influence of gravity) were presented; however, no comparisons with experimental data were made. Sicilian and Tegart¹² described transient free surface results for free surface motion in a partially-filled container during a controlled free fall. Although their predicted forces agreed with the trends in the measured data, significant discrepancies still existed.

In an effort to provide data for the present study, use was made of an existing experimental facility which was originally developed to study the kinematics and dynamics of spin-stabilized satellites¹³. The facility consisted of a motor-driven rotating shaft on which two liquid-filled spherical containers were mounted. The instrumentation included sensors for measuring the transient free surface position at the walls of the containers. It was recognized that data obtained with these sensors could be directly compared to numerical results, thereby providing a means of validating the numerical model.

In the following sections, the mathematical formulation of the numerical model are briefly discussed, along with an overview of the numerical solution algorithm. Additional details of the formulation and algorithm are provided in Ref. 8. The experimental setup and test procedure are then described, followed by a presentation of some numerical and experimental results.

*Senior Research Associate, Member AIAA.

[†]Research Assistant, Department of Mechanical Engineering.

[‡]Professor, Department of Mechanical Engineering, Member AIAA.

Copyright ©1991 by the authors. Published by the American Institute of Aeronautics and Astronautics, Inc. with permission.

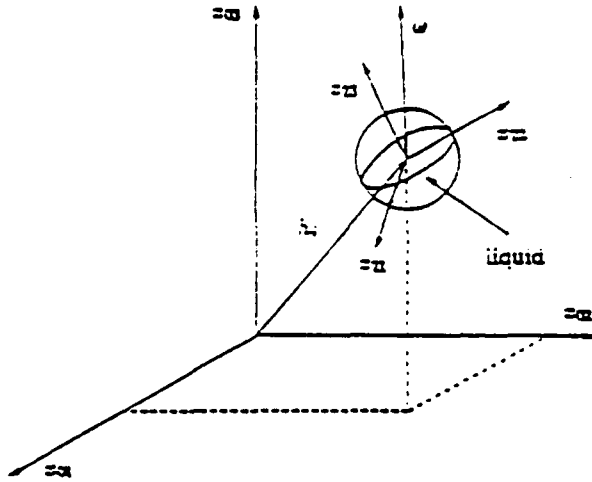


Figure 1: Schematic of a partially filled rotating-nutating container moving relative to an inertial frame.

Mathematical Formulation

Governing equations

The incompressible Navier-Stokes equations for an isothermal, laminar flow can be written as

$$\frac{\partial u_i}{\partial x_i} = 0 \quad (1)$$

$$\frac{\partial u_i}{\partial t} + u_j \frac{\partial u_i}{\partial x_j} = -\frac{1}{\rho} \frac{\partial p}{\partial x_i} - \nu \frac{\partial^2 u_i}{\partial x_j \partial x_j} - g_i \quad (2)$$

where u_i are the velocity components, p is the thermodynamic pressure, g_i is the acceleration due to gravity, ρ is the density, ν is the kinematic viscosity, and x_i are the spatial coordinates. As mentioned previously, several transformations of the governing equations are required in order to accommodate both the free surface and a general motion of the container with respect to an inertial coordinate system (see Fig. 1). These transformations are well documented in Refs. 7 and 8, and therefore will not be repeated here. The final governing equations, written in a generalized non-orthogonal coordinates with respect to a non-inertial reference frame, are

$$\frac{\partial p}{\partial \tau} + \eta_{j,i} \frac{\partial u_{3i}}{\partial z_j} = 0 \quad (3)$$

$$\begin{aligned} & \frac{\partial u_{3n}}{\partial \tau} + (\dot{z}_j + \eta_{j,i} u_{3i} + \eta_{j,i} f_{ik} z_{3k}) \frac{\partial u_{3n}}{\partial z_j} \\ & - (f_{ni} + 2\lambda_{ni}) u_{3i} + \eta_{j,n} \frac{\partial p}{\partial z_j} - \frac{1}{Re} (\eta_{j,i} \eta_{k,i} \frac{\partial^2 u_{3n}}{\partial z_j \partial z_k} \\ & + \eta_{k,ii} \frac{\partial u_{3n}}{\partial z_k}) = \tau_{i,ni} z_{3i} + \tau_{i,ni} h_i - g_{3n} + E_n \end{aligned} \quad (4)$$

where u_{3i} is the relative velocity component in z_i coordinate system (see Fig. 1). Re is the Reynolds number based on the radius of the spherical container and the rotational speed, z_j

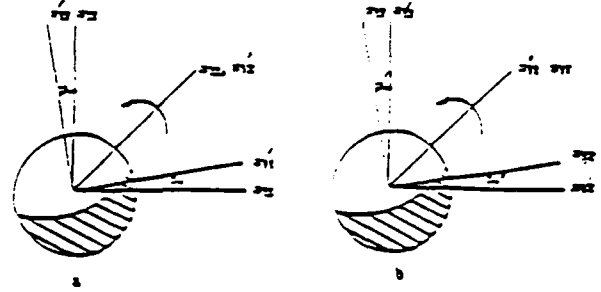


Figure 2: Notation for the S transformation.

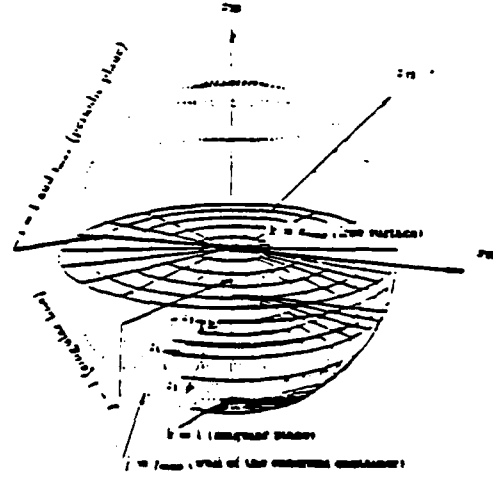


Figure 3: Coordinate system for liquid sloshing problem.

are the generalized coordinates, τ is the physical time, τ^* is the pseudotime employed in the artificial compressibility method, $\eta_{i,j}$ and $\eta_{i,jj}$ are metric terms, and \dot{z}_i is the grid speed. Other quantities appearing in the above equations can be attributed to the transformation of the governing equations from an inertial to a non-inertial frame. Additional details are given in Refs. 7 and 8. It should be noted that the free surface tracking coordinate transformation described in Ref. 8 has been modified in this paper to account for tangential free surface deformation (which appears in the cases examined in the present study). The new transformation matrix $[S]$ is defined as follows:

$$[S] = \begin{bmatrix} \cos \phi_r & \sin \phi_r \sin \phi'_r & -\sin \phi_r \cos \phi'_r \\ 0 & \cos \phi'_r & \sin \phi'_r \\ \sin \phi_r & -\cos \phi_r \sin \phi'_r & \cos \phi_r \cos \phi'_r \end{bmatrix}$$

The notation for this new transformation is shown in Figure 2.

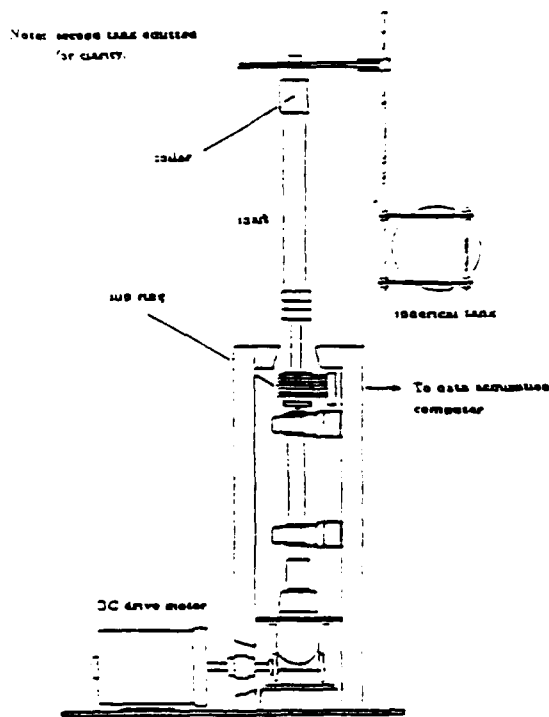


Figure 5: Illustration of current satellite test rig configuration.

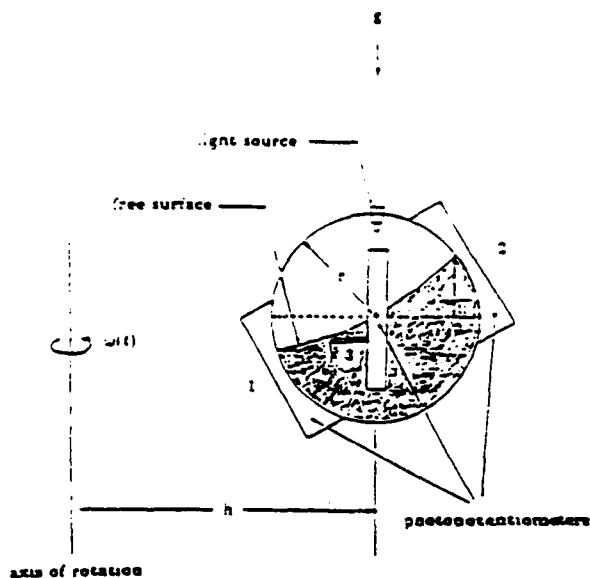


Figure 6: Schematic of spherical container and instrumentation.

The spherical containers were spun in a simple orbital motion about the axis of rotation (the drive shaft) by a DC motor connected through a series of gear boxes. The plane of this orbital motion was kept normal to the axis as shown. The rotational speed was controlled manually using a transformer, and was measured by a tachometer connected to the motor drive train.

The instrumentation for a typical spherical container is illustrated in Fig. 6. Each sphere was fitted with three light-sensitive photopotentiometers to sense the inboard (1), outboard (2) and tangential (3) free surface positions at the wall of the container. All three photopotentiometers were oriented normal to the equatorial plane of the sphere at the indicated circumferential positions (90 degrees apart). By tinting the liquid to block light transmission, the voltage output from the photopotentiometers was made proportional to the fraction of photopotentiometer surface covered by the liquid. The sensitivity of this arrangement was enhanced by a 6 volt light source located at the top of the spherical container.

All data were collected and stored using a microcomputer outfitted with a high speed data acquisition board. The data acquisition hardware was configured to accept eight channels of bipolar voltage signals, with maximum sampling rate of 90000 samples per second.

The photopotentiometers were dynamically calibrated to obtain a voltage versus free surface height relationship for use in data reduction. This calibration was accomplished by spinning the rig up to a specified rotational speed, waiting for steady state conditions to be established, and recording the output voltage produced by the photopotentiometers. The steady state position of the free surface (which was determined from the analytical solution for a given rotational speed) was then correlated with the known circumferential positions of the photopotentiometers.

Results and Discussion

Computations were carried out for the two types of spin-up described below. In both cases, terrestrial gravity was included in the acceleration field.

1. **Initially capped spin-up:** A spherical container half-filled with a liquid is spun about a specified axis of rotation at a constant rotational speed until solid-body rotation of the liquid is achieved. A cap covers the liquid surface to prevent it from rising up. At time zero, the cap is suddenly removed (or broken) and the liquid surface starts to rise (or drop) until another equilibrium position is reached. The initial absolute velocity is distributed according to the condition of solid-body rotation.
2. **Gradual spin-up:** A spherical container half-filled with a liquid is gradually spun up from rest to a prescribed steady state rotational speed. The plane of the motion is normal to the axis of rotation. This case corresponds to the conditions of the experimental study.

Initially-capped spin-up

A schematic of this case is shown in Fig. 7. The radius of the container is 7.62 cm, and the distance from the axis of rotation to the center of the container is 44.7 cm. The fluid is prescribed as glycerin at room temperature.

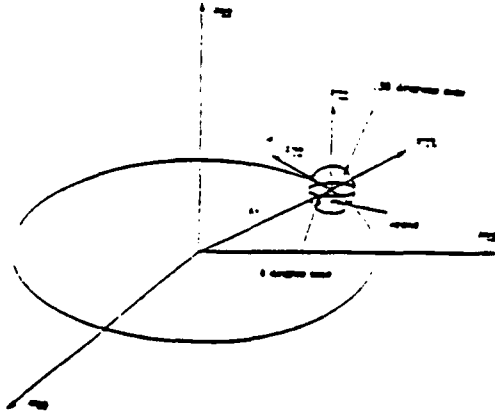


Figure 7: Schematic for asymmetric spin-up: container half-filled with glycerin.

The characteristic nondimensional parameters for this situation are:

$$Re = 181.4 \quad Fr = 3.25 \quad We = 12002.1$$

where Re is the Reynolds number, Fr is the Froude number, and We is the Weber number. The Froude and Weber numbers are defined as

$$Fr = V_{ref} / \sqrt{gh}$$

$$We = \rho V_{ref} L_{ref} / \Gamma$$

where V_{ref} is the same as used in the Reynolds number, h is the initial maximum free surface depth, g is the acceleration due to gravity, and Γ is the surface tension coefficient. Since the liquid surface was covered by a cap, there was no initial free surface motion. However, it should be noted that while the initial relative velocity was zero everywhere, the absolute velocity was nonzero and distributed according to the condition of solid-body rotation.

A $51 \times 11 \times 11$ grid (51 points in the circumferential direction), and a constant non-dimensional time step of 0.01 were used for this calculation. The extremely high centrifugal force field associated with this case caused the free surface to rise (drop) almost to the top (bottom) of the tank during the transient. In addition, the motion of the free surface appeared to be more abrupt than in the cases reported by Ref. 8. This abrupt free surface motion gave rise to numerical instabilities which, in turn, resulted in a sudden divergence of the solution after a long period of time in the calculation. Upon investigating the cause of these instabilities, the following remedies were introduced into the algorithm.

First, it was found that the free surface tracking angle, ϕ_s , must be handled carefully (ϕ_s' is zero in this case, since there is no tangential acceleration). As described in Ref. 8, the purpose of the tracking angle is to both facilitate the present grid generation procedure and to keep the free surface height function, F , single-valued. The influence of the tracking angle (and its time rate of change) is contained in various terms of the transformed governing equations. For this particular case, it was observed that the free surface (and also ϕ_s) tended to oscillate after nondimensional time, $\tau = 1.8$, whereupon the time rate of ϕ_s (ϕ_s') began to grow rapidly. The magnitude of the terms influenced by ϕ_s in the

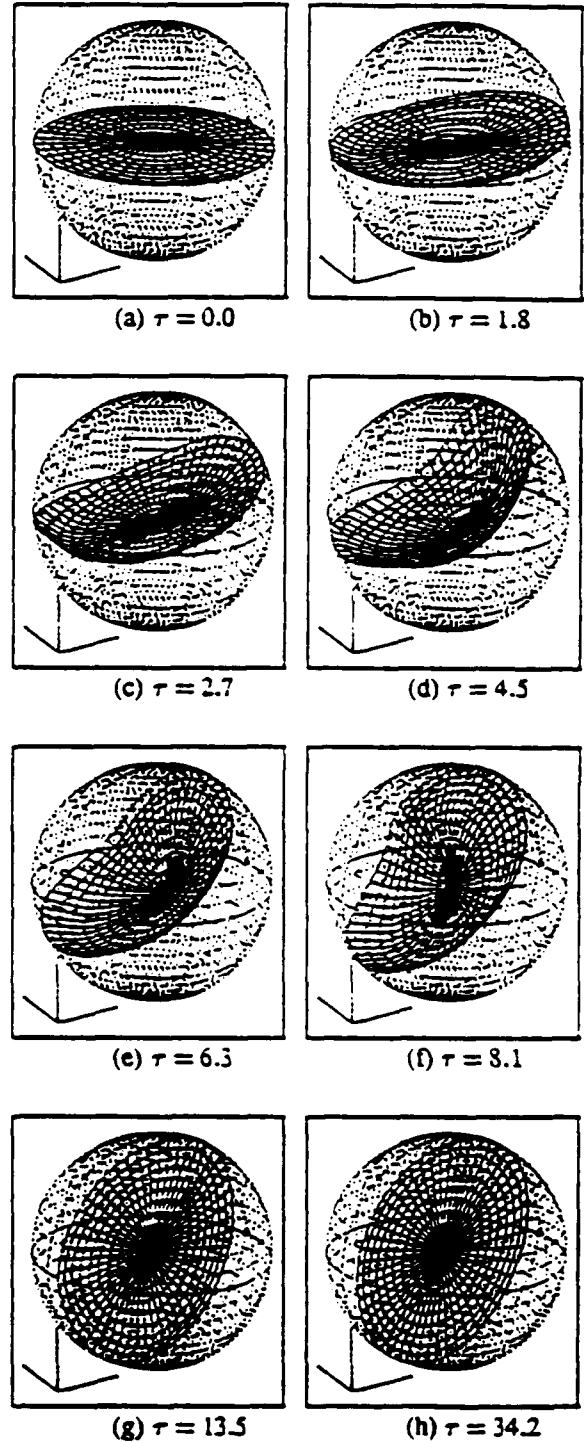


Figure 8: Selected free surface plots for the initially capped spin-up of a spherical container half-filled with glycerin.

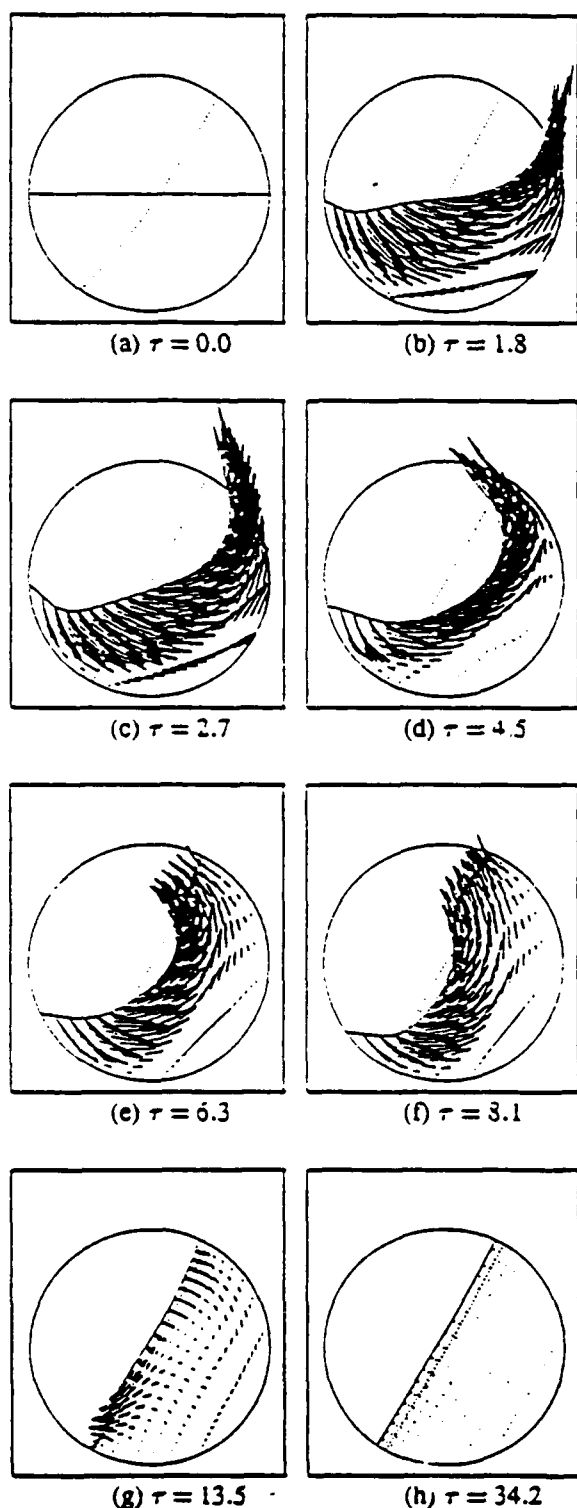


Figure 9: Selected velocity vector plots at $x-z=0$ plane for the initially capped spin-up of a spherical container half filled with glycerin (The dotted line indicates the steady state analytical free surface position)

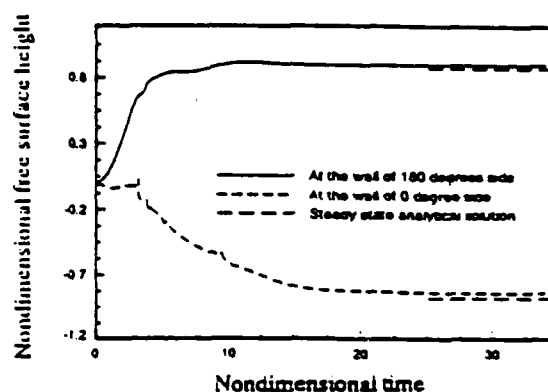


Figure 10: The time history of the nondimensional free surface height for the initially capped spin-up of a spherical container half filled with glycerin.

governing equations finally became dominant and resulted in the solution diverging. To reduce the sensitivity of the solution to this effect, the calculation of ϕ_s was modified by averaging angles at two time levels. This treatment smoothed out the temporal variations in both ϕ_s and ϕ_r , which, in turn, helped eliminate the potential for unstable behavior.

Another phenomenon observed in the present case was the appearance of a local saw-toothed profile in the free surface at a non-dimensional time of $\tau=2.6$. This profile propagated to neighboring points, which eventually resulted in a very unfavorable grid distribution, and ultimately to solution divergence. The cure for this problem was to employ first-order upwind approximations to the spatial derivative terms in the free surface kinematic equation rather than central differences.

The final calculations for this case were carried out on an Apollo DN10000 workstation, and required about 58 hours of CPU time to reach steady state. The computed solution is presented in Figs. 8-11. A series of results showing the free surface position at different instants of time are shown in Fig. 8. Final steady state conditions are achieved at about $\tau=34$, which corresponds to approximately one revolution (orbit) of the container. The velocity vectors are presented in a similar fashion in Fig. 9.

The free surface position at the wall is shown in Fig. 10. The analytical free surface position for the steady state, solid-body rotation condition was obtained from Ref. 7. It can be seen that some discrepancy exists between the computed steady state free surface position and the analytical solution. It is believed that this discrepancy is either due to the use of first-order upwind differencing in the kinematic equation or to the linear interpolation procedure used to transfer the free surface points from the old grid to the new grid. Ways of eliminating these problems are currently being investigated.

The number of subiterations required at each time step is plotted in Fig. 11. The sudden increase in subiterations at nondimensional times between 3 and 5 was found to be the result of the free surface angle oscillation described above. For the majority of the computation, however, less than 10 subiterations were needed.

Gradual spin-up

A series of experiments were carried out with the test rig to examine a gradual spin-up from rest. The variation of

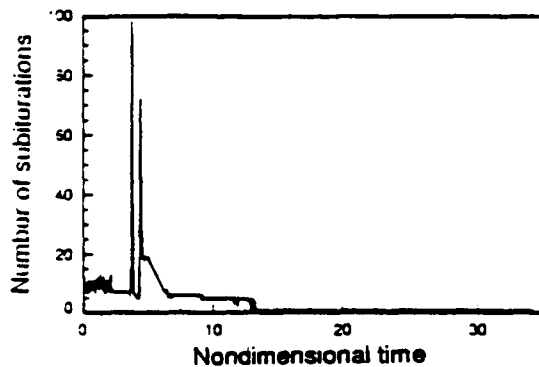


Figure 11: The time history of the number of subiterations at each time step for the initially capped spin-up of a spherical container half filled with glycerin.

the rotational speed was controlled manually with the aim of producing a transient of about one to two seconds. The recorded rotational speeds (obtained from the tachometer) were then used as input to the computer program.

Due to the symmetry of the configuration, photopotentiometer data were obtained for one sphere only. During the course of calibration, it was found that the signal from the tangential photopotentiometer (#3) was too small to provide a reliable indication of the free surface level. This was due primarily to the small free surface deflection at that position for the tests conducted. Also, the length of the photopotentiometers (as well as other effects) limited the range of free surface deflection for which reliable calibrations of the other photopotentiometers could be obtained. Ways of extending the sensitivity and range of the photopotentiometers are currently being studied.

Two sets of data (three runs per set) were obtained for nominal steady state speeds of 30 rpm and 60 rpm. One run from each set was then selected for simulation with the computer program. Appropriate initial and boundary conditions were prescribed for each case, and the rotational speed as a function of time was specified using the tachometer data from the experiment. It should be noted that the tachometer data were smoothed prior to use in the program in order to filter out the noise in the signal. The resulting smoothed and unsmoothed (raw) data are shown in Figs. 12-13.

The numerical solutions were performed using a $41 \times 11 \times 11$ grid (41 grid points in the circumferential direction) for 3000 non-dimensional time steps ($\Delta \tau = 0.03$). Both solutions were initiated at a physical time of 1 second (the time at which the sphere begins to move in the experimental time frame). The total elapsed physical time was about 4 seconds. The calculations were carried out on a DECstation 5000/200, and consumed about 23 hours of CPU time in both cases.

For comparison with the experiment, a non-dimensional free surface height, l/r , was defined, where l is the height of the free surface above the equatorial plane (see Fig. 6). Values of l/r at the inboard and outboard positions were computed and stored at prescribed time intervals for later analysis. For the cases discussed below, the maximum experimental uncertainty in the values of l/r was estimated to be between 2×10^{-2} and 3×10^{-2} .

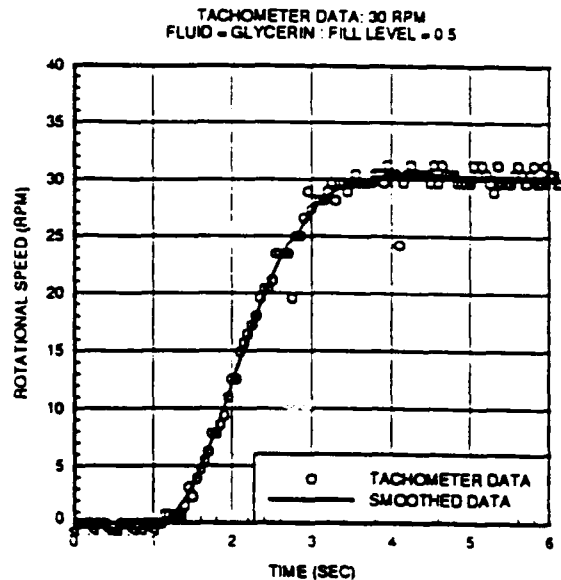


Figure 12: The transient rotational speed curve for the gradual spin-up of a spherical container half filled with glycerin : 30 rpm case.

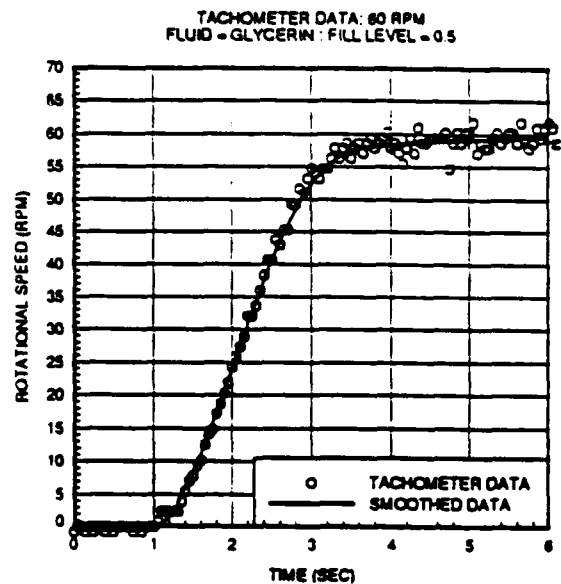


Figure 13: The transient rotational speed curve for the gradual spin-up of a spherical container half filled with glycerin : 60 rpm case.

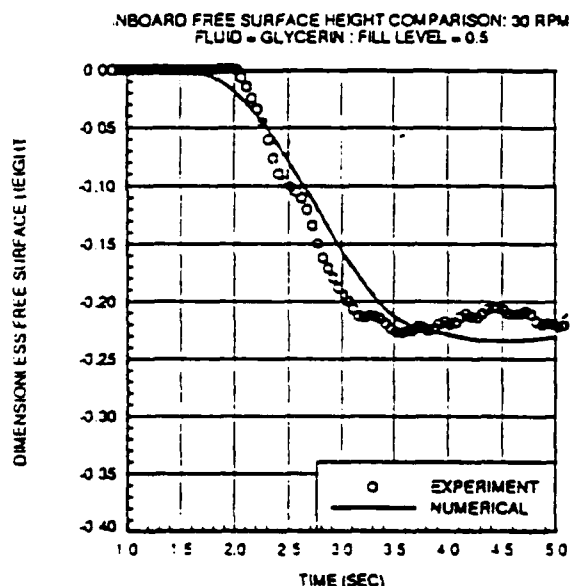


Figure 14: The time history of the nondimensional inboard free surface height for the gradual spin-up of a spherical container half filled with glycerin : 30 rpm case.

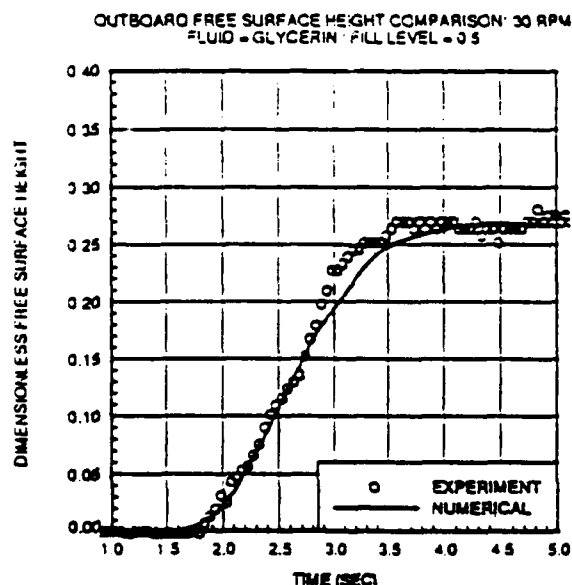


Figure 15: The time history of the nondimensional outboard free surface height for the gradual spin-up of a spherical container half filled with glycerin : 30 rpm case.

OUTBOARD FREE SURFACE HEIGHT COMPARISON: 60 RPM
FLUID = GLYCERIN : FILL LEVEL = 0.5

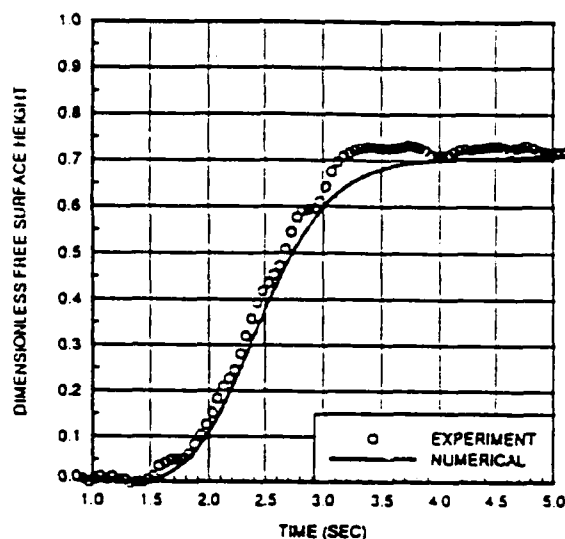


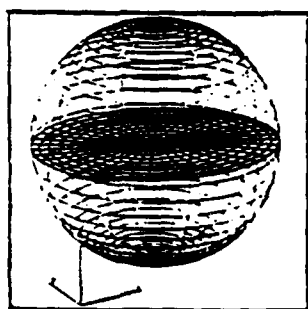
Figure 16: The time history of the nondimensional outboard free surface height for the gradual spin-up of a spherical container half filled with glycerin : 60 rpm case.

The solution for 30 rpm case is presented in Figs. 14-15. In Figs. 14-15, the computed inboard and outboard free surface heights are compared with their experimental counterparts. It can be seen that the computed results are in reasonable agreement with the experimental data. In particular, the delay between the initiation of the rotation and the response of the free surface appears to be well predicted, as is the general rate of change of the free surface position with time. There does, however, appear to be some smoothing of the numerical response relative to the experimental data. The differences between the numerical and experimental results are attributed to both the coarse grid used in the numerical simulation and the uncertainties inherent in the experimental data.

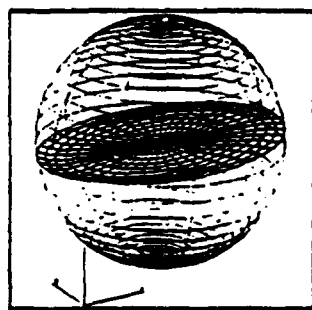
The solution for the 60 rpm case is presented in Figs. 16-18. For this case, the deflection of the free surface at the inboard position exceeded the calibration range, and thus could not be used. A comparison of the computed outboard free surface height response with the experimental data is shown in Fig. 16. Again, the agreement of the computations with experiment is generally good, although, as in the 30 rpm case, the response appears somewhat smooth.

It is observed in both cases that the free surface transient roughly corresponds to the transient in the rotational speed. This behavior is the result of the high viscosity of the test fluid (glycerin), the geometry and rotational speeds employed in the tests, and the length of the rotational speed transient. For less viscous fluids or faster transients, the motion will become more complex, with noticeable secondary oscillations persisting for some time after the steady state rotational speed has been achieved.

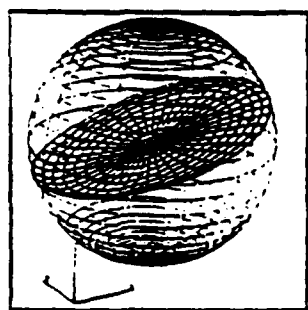
Selected plots of the free surface and velocity fields are presented in Figs. 17-18. As the container begins to accelerate, the fluid initially sloshes both tangentially (rearward) and radially (outward), thus creating a highly distorted free surface topology. Eventually, as the steady state conditions are approached, the free surface flattens out into its steady



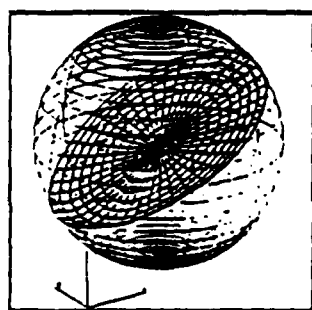
(a) $t=1.498$ sec



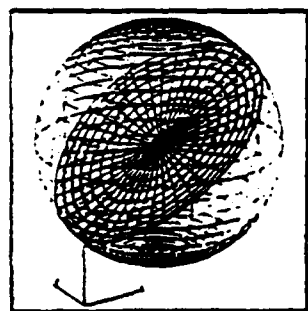
(b) $t=1.996$ sec



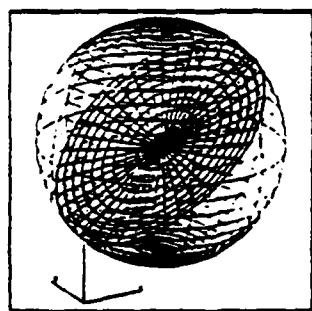
(c) $t=2.494$ sec



(d) $t=2.991$ sec

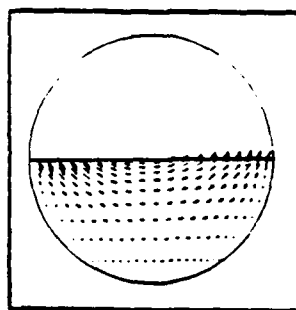


(e) $t=3.489$ sec

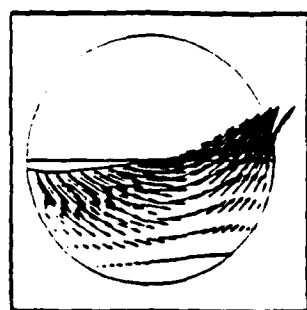


(f) $t=3.989$ sec

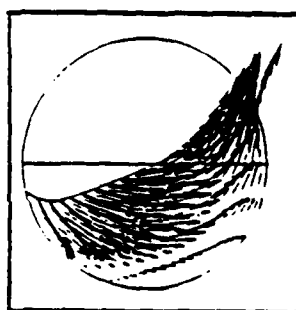
Figure 17: Selected free surface plots for the gradual spin-up of a spherical container half-filled with glycerin : 60 rpm case.



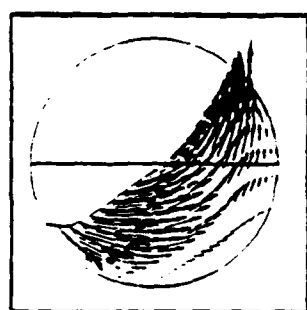
(a) $t=1.498$ sec



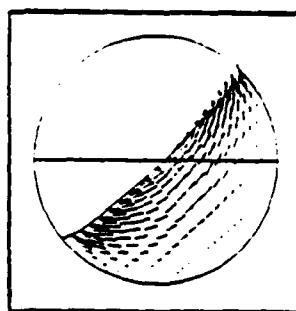
(b) $t=1.996$ sec



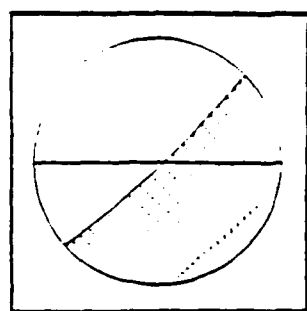
(c) $t=2.494$ sec



(d) $t=2.991$ sec



(e) $t=3.489$ sec



(f) $t=3.989$ sec

Figure 18: Selected velocity vector plots at $x_{22}=0$ plane for the gradual spin-up of a spherical container half filled with glycerin : 60 rpm case (The dotted line indicates the initial free surface position).

state configuration.

Conclusions

Numerical solutions for two classes of three-dimensional sloshing flows inside partially-filled spherical containers were presented. The calculated transient free surface positions for the gradual spin-up case were compared with corresponding experimental data, and found to be in reasonable agreement. Discrepancies between the numerical and experimental results were attributed to both numerical errors and experimental uncertainty. Despite these discrepancies, however, the essential behavior of the fluid appeared to be well predicted by the present numerical model.

Work is in progress to improve both the numerical and experimental results presented in this paper. Specifically, the numerical solution procedure is being developed further so that accurate solutions can be obtained on finer grids. Particular attention is being focused on the vectorization of the CSIP algorithm. Improvements in the present experimental facility will include extending the accuracy and range of the photopotentiometers, and installing additional instrumentation (such as pressure transducers) at selected positions on the spherical container.

Acknowledgments

This research was supported by the Air Force Office of Scientific Research through Grant No. AFOSR-89-0403.

References

1. Peterson, L. D., Crawley, E. F., and Hansman, R. J., "Nonlinear Fluid Slosh Coupled to the Dynamics of a Spacecraft," *AIAA Journal*, 27, No. 9, pp. 1230-1240, 1989.
2. Kana, D. D., "Validated Spherical Pendulum Model for Rotary Liquid Slosh," No. 3, *Journal Spacecraft*, pp. 188-195, 1989.
3. Van Schoor M. C., Peterson, L. D. and Crawley, E. F., "The Coupled Nonlinear Dynamic Characteristics of Contained Fluids in Zero Gravity," AIAA 90-0996-CP, 1990.
4. Ramaswamy, B., "Numerical Simulation of Unsteady Viscous Free Surface Flow," *Journal of Computational Physics*, 90, pp. 396-430, 1990.
5. Vaughn, H. R., Oberkampf, W. L. and Wolfe W. P., "Fluid Motion Inside a Spinning Nutating Cylinder," *Journal Fluid Mechanics*, 150, pp. 121-138, 1985.
6. Baumgarten, J. R., Flugrad, D. R., and Prusa, J. M., "Investigation of Liquid Sloshing in Spin-Stabilized Satellites," ISU-ERI-Ames-90401, Iowa State University, 1989.
7. Chen, K.-H., *A Primitive Variable, Strongly Implicit Calculation Procedure for Two and Three-Dimensional Unsteady Viscous Flows: Applications to Compressible and Incompressible Flows Including Flows with Free Surfaces*, Ph.D dissertation, Iowa State University, Ames, Iowa, 1990.
8. Chen, K.-H. and Pletcher, R. H., "Simulation of Three-Dimensional Liquid Sloshing Flows Using a Strongly Implicit Calculation Procedure," AIAA-91-1661, 1991.
9. Chorin, A. J., "A Numerical Method for Solving Incompressible Viscous Flows Problems," *Journal of Computational Physics*, 2, pp. 12-26, 1967.
10. Partom, I. S., "Application of the VOF Method to the Sloshing of a Fluid in a Partially Filled Cylindrical Container," *International Journal for Numerical Methods in Fluid Mechanics*, 7, pp. 535-550, 1987.
11. Hirt, C. W., and Nichols, B. D., "Volume of Fluid (VOF) Method for the Dynamics of Free Boundaries," *Journal of Computational Physics*, 39, pp. 201-225, 1981.
12. Sicilian, J. M. and Tegar, J. R., "Comparison of FLOW-3D Calculations with Very Large Amplitude Slosh Data," PVP-Vol. 176, Computational Experiments, pp. 23-30, Presented at the 1989 ASME Pressure Vessels and Piping Conference, Honolulu, Hawaii, July 23-27, 1989.
13. Anderson, M. D., *Motion Study of a Spin Stabilized Satellite Test Rig*, Master thesis, Iowa State University, 1988.
14. Lamb, H., *Hydrodynamics*, Dover Publications, 1945.
15. Hindman R. G., "Generalized Coordinate Forms of Governing Fluid Equations and Associated Geometrically Induced Errors," *AIAA Journal*, 20, No. 10, pp. 1359-1367, 1982.
16. Anderson, D. A., Tannehill, J. C., and Pletcher, R. H., *Computational Fluid Mechanics and Heat Transfer*, McGraw-Hill Book Co., New York, 1984.